Unconventional magnetic properties of low-dimensional antiferromagnets $BaNi_2V_2O_8$ and $BaCu_2V_2O_8$

vorgelegt von
M.Sc. Ekaterina Klyushina
aus Leningrad

Von der Fakultät II - Mathematik und Naturwissenschaften
der Technischen Universität Berlin
zur Erlangung des akademischen Grades
Doktor der Naturwissenschaften
Dr. rer. nat.

g e n e h m i g t e D i s s e r t a t i o n

Promotionsausschuss:

Vorsitzender: Prof. Dr. Wolf-Christian Müller
Gutachterin: Prof. Dr. Bella Lake
Gutachter: Prof. Dr. Jon Goff
Gutachter: Prof. Dr. Kim Lefmann

Tag der wissenschaftlichen Aussprache: 17.05.2017

Berlin 2017

Abstract

This work explores the magnetic properties of two novel compounds $BaCu_2V_2O_8$ and $BaNi_2V_2O_8$ which both provide rare physical realizations of model magnetic systems that are characterized by unconventional magnetic behaviour at finite temperatures. $BaNi_2V_2O_8$ has an ideal honeycomb crystal structure where S=1 nickel magnetic ions are arranged on well isolated honeycomb layers. The nearest neighbour magnetic ions within the plane interact with each other via the dominant antiferromagnetic exchange interaction while the interaction between the honeycomb planes is found to be very weak. The spins develop long-range magnetic order in their ground state and lie entirely within the honeycomb plane forming collinear arrangement so that each spin is antiparallel to its 3 nearest neighbours. The crystal and magnetic structure of $BaNi_2V_2O_8$ imply that this compound is a two-dimensional planar antiferromagnet. The magnetic properties of this compound were explored using DC susceptibility, powder and single crystal inelastic neutron scattering measurements as well as single crystal neutron diffraction measurements whose results were analysed using different theoretical approaches. The single crystal measurements at base temperature reveal a spin-wave magnetic excitation spectrum which disperses within the honeycomb plane but is completely dispersionless in the out-of-plane direction confirming the strongly two-dimensional magnetic behaviour of this compound. The dispersion of the magnetic excitation spectrum at base temperature was analysed using linear spin-wave theory which allowed the Hamiltonian of $BaNi_2V_2O_8$ to be solved. The critical phenomena in $BaNi_2V_2O_8$ were explored by performing the neutron diffraction measurements at finite temperatures both below and above the ordering temperature T_N. The extracted critical exponents reveal that $BaNi_2V_2O_8$ behaves as a two-dimensional antiferromagnet over the whole explored temperature range displaying the crossovers from 2D Ising like to 2D XY and then to 2D Heisenberg magnetic behaviour with increasing temperature.

The second compound is $BaCu_2V_2O_8$ which has tetragonal symmetry where the magnetic S=$\frac{1}{2}$ Cu^{2+} ions form screw chains along the c-axis. The DC susceptibility data reveal a non-magnetic ground state and were fitted well by the dimer-model which allows the magnetic intra- and interdimer exchange constants to be estimated. The single crystal inelastic neutron scattering measurements of $BaCu_2V_2O_8$ reveal that the magnetic excitation spectrum is gapped and characterized by a high ratio of the gap to the bandwidth which equals 3.6 indicating a strong dimerization. The magnetic excitations disperse along the chain direction but are completely dispersionless within the tetragonal plane implying that $BaCu_2V_2O_8$ is a strongly dimerized 1D chain where the dimers are coupled together along the c-axis. The magnetic excitation spectrum was analysed using the theoretical model for the 1D alternating chain which allowed the Hamiltonian of $BaCu_2V_2O_8$ to be solved. The results were verified by comparison with theoretical simulations of the spectra using this Hamiltonian. The strong dimerization of $BaCu_2V_2O_8$ makes this compound a good candidate for the observation and detailed investigation of strongly correlated phenomena at finite temperatures. The thermal behaviour of the magnetic excitations in $BaCu_2V_2O_8$ were explored by analysing of the temperature dependence of their lineshape at finite temperatures over a wide temperature range. The analysis was performed using a new fitting function and revealed the extraordinary coherence of the magnetic excitations in $BaCu_2V_2O_8$ at finite temperatures which manifests itself in an asymmetric thermal lineshape broadening in contrast to the Lorentzian lineshapes observed in conventional magnets. The observed results were verified by comparison with the results of theoretical simulations of the magnetic excitations at finite temperature in $BaCu_2V_2O_8$ which were performed using both numerical and analytical theoretical approaches.

Zusammenfassung

In dieser Arbeit werden die magnetischen Eigenschaften von zwei neuen Verbindungen untersucht, $BaNi_2V_2O_8$ und $BaCu_2V_2O_8$. Beide Substanzen zeichnen sich durch ihren besonderen Modellcharakter aus der schon bei endlicher Temperatur zu ungewöhnlichen magnetischen Verhalten führt. $BaNi_2V_2O_8$ kristallisiert mit einer bienenwaben Struktur in der sich die magnetischen, S=1 Ni^{2+} - Ionen anordnen. Die bienenwaben Ebenen sind voneinander gut getrennt. In der Ebene besteht zwischen den magnetischen Ionen eine dominante antiferromagnetische Wechselwirkung zu den nächsten Nachbarn, die Wechselwirkung zwischen den Ebenen ist sehr schwach. Die Momente zeigen im Grundzustand langreichweitige Ordnung. Sie sind vollständig in der bienenwaben Ebene angeordnet mit einer kollinearen Ausrichtung, jeder Spin ist antiparallel zu den drei nächsten Nachbarn ausgerichtet. Die chemische und magnetische Struktur von $BaNi_2V_2O_8$ kann als zwei - dimensionaler (2D), planarer Antiferromagnet verstanden werden. Die magnetischen Eigenschaften dieser Verbindung wurden mit statischen Magnetisierungsmessungen, sowie inelastischer Neutronenstreuung an Pulver- und Einkristallproben als auch mit elastischer Neutronenstreuung an Einkristallen untersucht. Die Ergebnisse werden mit verschiedenen theoretischen Ansätzen analysiert. Die inelastischen Messungen mit Neutronenstreuung bei Basistemperatur zeigen Dispersion in der bienenwaben Ebene, während senkrecht zu den Ebenen keine Dispersion beobachtet wird. Dies zeigt den stark zwei - dimensionalen Charakter dieser Verbindung. Die Dispersion der magnetischen Anregungen bei Basistemperatur wird anhand von linearer Spin - Wellen Theorie untersucht, damit kann der Hamiltonian von $BaNi_2V_2O_8$ bestimmt werden. Das kritische Verhalten von $BaNi_2V_2O_8$ wird mit Neutronenstreuung unter- und oberhalb der Ordnungstemperatur T_N untersucht. Die dabei bestimmten kritischen Exponenten zeigen, dass sich $BaNi_2V_2O_8$ über den gesamten untersuchten Temperaturbereich wie ein zwei - dimensionaler Antiferromagnet verhält mit Übergängen bei steigender Temperatur von 2D - Ising zu 2D - XY hin zu 2D - Heisenberg Verhalten.
Die zweite Verbindung, $BaCu_2V_2O_8$, hat eine tetragonale Symmetrie und die magnetischen S=$\frac{1}{2}$ Cu^{2+} - Ionen bilden eine schraubenförmige Kette längs der c-Achse. Die statische Suszeptibilität zeigt einen unmagnetischen Grundzustand. Die Daten werden mit einem Dimer Modell gefittet, daraus kann die Dimer - Wechselwirkung und die Wechselwirkung zwischen den Dimeren bestimmt werden. Die inelastische Neutronenstreuung an Einkristallen zeigt eine Energielücke der magnetischen Anregungen. Das Verhältnis zwischen der Energielücke und der Breite des magnetischen Spektrums beträgt 3.6. Dies ist ein Hinweis auf starke Dimerisierung. Die magnetischen Anregungen zeigen Dispersion entlang der Spinketten. In der tetragonalen Ebene zeigt das Spektrum keine Dispersion. Daher ist $BaCu_2V_2O_8$ eine stark dimerisierte 1D-Spinkette in der die Dimere längs der c-Achse wechselwirken. Das Spektrum der magnetischen Anregungen wird mit einem Modell für die 1D alternierende Spinkette untersucht, damit konnte die Hamilton Funktion von $BaCu_2V_2O_8$ bestimmt werden. Die Ergebnisse werden verifiziert durch Vergleich der gemessenen Spektren mit Simulationen der Spektren. Die starke Dimerisierung von $BaCu_2V_2O_8$ macht diese Substanz zu einem guten Modellsystem für hochkorrelierte Phänomene bei endlichen Temperaturen, sowohl in experimenteller wie auch theoretischer Hinsicht. Das thermische Verhalten der magnetischen Anregungen von $BaCu_2V_2O_8$ wird untersucht mit der Linienform der Anregungen über einen großen Temperaturbereich. Die Analyse benutzt eine neue Funktion zur Anpassung der Linienform im Gegensatz zum Lorentz Verhalten, das gewöhnlich in magnetischen Substanzen gefunden wird. Es zeigt sich - bei endlichen Temperaturen - eine außerordentlich hohe Kohärenz der magnetischen Anregungen, die sich in einer asymmetrischen, Linienform manifestiert. Diese Ergebnisse werden verifiziert durch den Vergleich theoretischer Spektren bei endlicher Temperatur, die mit numerischen und analytischen Methoden gewonnen werden.

Acknowledgments

The presented results took long time of measurements, data analysis, thinking under results and finally writing more than 160 pages of this thesis. And during all this time I have never been alone. This is why I would like to start this thesis with the acknowledgement to people who helped me and supported me during all the time.
I would like to thank my supervisor Bella Lake for two incredibly interesting projects and for that opportunities and experience which I got working under them. She introduced me to a scientific world which consists of the experiments on the best research facilities, participation in the international conferences, collaborations with other scientist and learning new skills in research schools. I am eternally grateful to her for being always open for questions and discussions and for readiness to help in case of difficulties. Thank you very much for that, Bella!
I would like to thank Konrad for being always tolerant and kind. His scientific experience and knowledge in experimental physics simplify my life in this place so much while his care about the instruments in our department leads to the smoothly run experiments with clear results. I am especially grateful to him for his review of my drafts and for the useful advises and corrections.
I also would like to thank to Nazmul for the wonderful samples which he has grown especially for these projects and whose perfect quality allows these projects to be done. I also would like to thank to current and former members of this group for creating and keeping an unique homely and warm atmosphere. I am gratitude for fresh discussions during daily lunches which bring us together, for good sense of humor and for coffee with homemade cookies and cakes. Anup, Jianhui, Christian, Alexandros , Shravani, Nazmul and Konrad, thank you all for this fun!
Finally, I would like to thank my family for their infinite patience and support. I am gratitude to my parents for encouraging of all my scientific adventures. I am especially gratitude to my husband for his help and patience to me and to my work. Thank you very much for always being nearby when it was needed!

Contents

1 Introduction

"Explore the world. Nearly everything is really interesting if you go into it deeply enough"

Richard Feynman , Nobel Prize laureate in physics

The investigation of compounds which display low-dimensional magnetic properties allows a wide range of the theoretically predicted intriguing magnetic phenomena to be experimentally observed. Because the magnetic exchange interactions in low-dimensional magnetic systems are usually very weak, the magnetic excitations in these systems are conventionally explored at very low temperatures where they are not affected (destroyed) by thermal fluctuations (thermal effects). However, in particular systems, increasing temperatures might induce unconventional magnetic behaviours such as exotic phase transition to the spin vortex - anti vortex quasi -ordered state. This transition is known as the Berezinskii - Kosterlitz - Thouless phase transition and was theoretically predicted for the two-dimensional (2D) XY planar magnetic system. Another example is the strongly correlated behaviour of certain magnetic excitations at elevated temperatures which was theoretically predicted for one-dimensional (1D) gapped quantum antiferromagnets. This extraordinary coherence of the magnetic excitations was detected for first time in strongly dimerized one-dimensional Heisenberg chains and was later confirmed in a three-dimensional (3D) dimerized Heisenberg magnet. These exotic thermally induced magnetic behaviours have received little experimental exploration because solid state compounds which behave as ideal low-dimensional magnetic model systems are very rare. This makes the search for and investigation of compounds which are physical realizations of the magnetic models an important scientific task of condensed matter physics.

In this work two compounds $BaCu_2V_2O_8$ and $BaNi_2V_2O_8$, which are both supposed to be good physical realizations of these rare magnetic models, are explored.

$BaNi_2V_2O_8$ has an ideal crystal structure where the S=1 Ni^{2+} magnetic ions are arranged in a honeycomb lattice so that all distances between them are equivalent. The dominant magnetic exchange interaction within the honeycomb plane is antiferromagnetic and realized between the nearest neighbour magnetic ions. These honeycomb layers are well separated within the crystal structure by a distance which is much larger than the distance between the nearest neighbour magnetic ions within the plane. Thus, the magnetic exchange interaction between the layers is very weak and is of the order of 10^{-4}-10^{-5} times weaker than the dominant exchange coupling within the plane. The system is characterized by both easy-plane and easy-axis single-ion anisotropies due to crystal field effects. The combination of

these anisotropies with the weak interplane exchange coupling leads to a phase transition to a long-range magnetically ordered state at low temperatures. In the ground state each spin is antiparallel to its 3 nearest neighbors and lies within the plane along the crystal axis due to the weak easy-axis anisotropy. Just above the ordering temperature the spins are confined to the 2D plane due to the easy-plane anisotropy which makes this compound a promising candidate to search for Berezinskii - Kosterlitz - Thousless behaviour.
The second compound is $BaCu_2V_2O_8$ which has a tetragonal crystal structure where S=$\frac{1}{2}$ Cu^{2+} magnetic ions are surrounded by the oxygen ions forming double copper-oxygen plaquettes. The magnetic exchange interaction between the copper ions within the plaquettes is weak and ferromagnetic which is in agreement with the Goodenough - Kanamori rules. The copper-oxygen plaquettes are strongly coupled by the dominant antiferromagnetic exchange interaction along the c-axis forming ferromagnetic-antiferromagnetic alternating screw chains. These chains do not interact with each other which makes $BaCu_2V_2O_8$ a purely one-dimensional magnetic system. This 1D magnetic system is strongly dimerized because the dominant antiferromagnetic exchange interaction is four times stronger than the ferromagnetic one. The magnetic excitation spectrum forms a gapped band with the ratio of the gap to the bandwidth equals to 3.5 and the energy gap equals to 35.5 meV. The magnetic excitations are hard-core bosons which interact strongly with each other via the hard-core constraint which allows only one excitation per dimer site. The magnetic properties are characterized by the singlet non-magnetic ground state and the excited S=1 triplet state. The magnetic excitations retain their coherence at finite temperatures and interact with each other in a correlated manner because the phase space of the available states is restricted due to the hard-core constraint. This makes $BaCu_2V_2O_8$ a promising candidate to experimentally explore strongly correlated behaviour at finite temperatures while the energy scale of the excitations allows this phenomenon to be explored over a wide temperature range.
Chapter 2 of this thesis gives an *"Introduction to low-dimensional quantum magnetism"*. At the beginning of this Chapter the origin of magnetism in free magnetic ions is explained and then the crystal field effects are described since all explored compounds in this work have a strong crystal field. Chapter 3 gives an overview of *Experimental Techniques*. The main part of this Chapter describes the theoretical principles and technical realization of DC magnetic susceptibility and inelastic neutron scattering measurements since these are the main techniques used in this work.
Chapter 4 and Chapter 5 present the results of the thermodynamic and inelastic neutron scattering measurements of $BaNi_2V_2O_8$ at base and finite temperatures, respectively. Chapter 4 starts from the analysis of the bulk properties of $BaNi_2V_2O_8$ which was done using several theoretical approaches and allows the energy range of the magnetic exchange interactions to be estimated. Using this range as a constraint, the analysis of the single crystal magnetic excitation spectra was performed within linear spin-wave theory which allows the Hamiltonian of $BaNi_2V_2O_8$ to be solved. After that, the critical phenomena in $BaNi_2V_2O_8$

both below and above the ordering temperature T_N was precisely explored in Chapter 5 to characterize the magnetic behaviour of $BaNi_2V_2O_8$ over a wide temperature range. Evidence for a free vortex state was found in a narrow temperature range just above T_N.
The magnetic properties of $BaCu_2V_2O_8$ at both base and finite temperatures are explored in Chapter 6 and Chapter 7, respectively. The investigation of the Hamiltonian of $BaCu_2V_2O_8$ starts from the analysis of the DC susceptibility data which suggests a strongly dimerized system and estimates the type and values of the magnetic exchange interactions within this model. The analysis of the magnetic excitations observed in the magnetic excitation spectra of single crystal $BaCu_2V_2O_8$ proposes two possible solutions for the Hamiltonian of this compound which were distinguished via comparison with the results of a theoretical simulation performed for each solution. At the end of Chapter 6 the magnetic exchange paths which are responsible for the extracted magnetic exchange interactions were distinguished by the analysis of the intensity distribution of the magnetic excitation spectra.
Having established the Hamiltonian of $BaCu_2V_2O_8$, Chapter 7 explores the magnetic behaviour of $BaCu_2V_2O_8$ at finite temperatures. For this, the temperature dependence of the line shape of the magnetic excitations was analysed using a fitting function which was developed for the first time in this project. The extracted results were compared with two different theoretical approaches. The lineshape was found to broaden asymmetrilly with increasing temperature in contrast to the symmetric Lorentzian broadening observed in conventional magnets. This results suggests that $BaNi_2V_2O_8$ remains strongly correlated to elevated temperatures in general agreement with the theoretical approaches.
Finally Chapter 8 *"Results and conclusions"* summarizes the results obtained in this thesis and gives an overview of the perspectives for future investigations of $BaCu_2V_2O_8$ and $BaNi_2V_2O_8$.

2 Introduction to low dimensional quantum magnetism

2.1 Introduction

This chapter summarizes the theoretical background behind the presented research. The Chapter starts by describing the magnetic ions whose unpaired electrons are responsible for the magnetic moments in a crystal. First, a single magnetic ion is discussed, and then the effects of crystal field are introduced. Because the magnetic properties of a compound mainly depend on the interactions between the magnetic ions, the various types of the magnetic exchange interactions are discussed.
A magnetic system can be described by different magnetic models depending on the crystal lattice, the strength of the magnetic exchange interactions and the dimensionality of the magnetic moments as well as the presence of magnetic anisotropy. Because this work explore the compounds $BaNi_2V_2O_8$ and $BaCu_2V_2O_8$ which respectively belong to two different models, the description of these modes finalizes this Chapter.

2.2 Free Magnetic Ion

The state of an electron in an atom is characterized by the four quantum numbers which are n, l, m_l and m_s. These numbers respectively describe the *energy shell* and *orbital angular momentum* of the electron and the projections of its *spin* and *orbital angular momentum* on a given axis z. These numbers are connected with each other by the relations l=0,1,2,3,..,$n-1$ and $|m_l| \leqslant l$ where n can take any natural number.
The electronic states are combined into the electronic shells $K(\mathrm{n}=1)$, $L(\mathrm{n}=2)$, $M(\mathrm{n}=3)$,... so that each shell consists of electronic states which are characterized by the same quantum number n. The number of the states in one shell is restricted by the Pauli principle which prohibits two electrons to be in the same state. Therefore, all states should be characterized by unique set of the quantum numbers.
The spin- and angular- momenta have magnetic moments which equal

$$\vec{\mu}_l = -\mu_B \cdot \vec{\boldsymbol{l}} \quad \vec{\mu_s} = -g_s \cdot \mu_B \cdot \vec{\boldsymbol{s}} \tag{2.1}$$

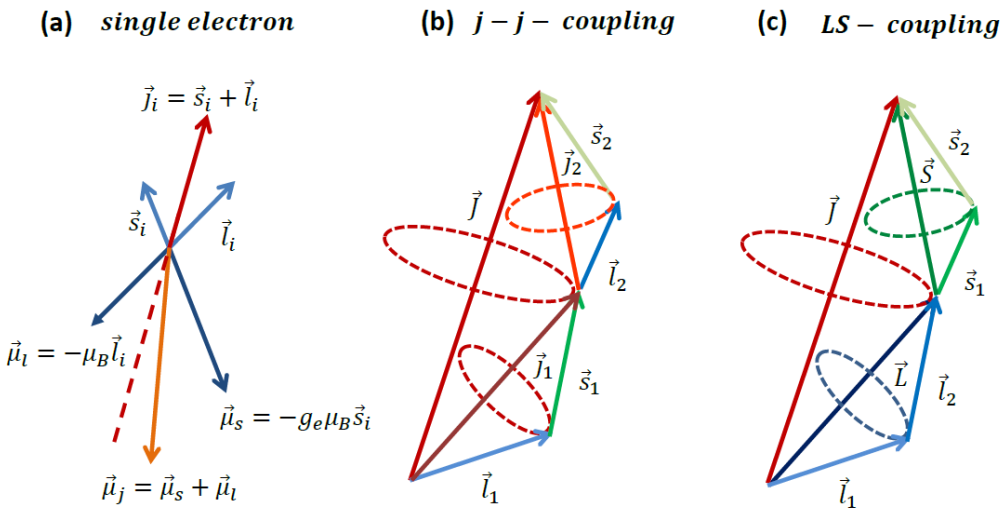

Figure 2.1: (a) Vector model of the electron spin, orbital and total angular momentum and the magnetic moments associated with them. (b) Vector model of the total electron angular momentum within $\boldsymbol{j-j}$ coupling approach and (c) $\boldsymbol{LS}$-coupling approach

Here μ_B is the Bohr magneton and g_s is the gyromagnetic ratio which is g_s=2 for a free electron. Thus, the single electron has a *total angular momentum* $\vec{\boldsymbol{j}}=\vec{\boldsymbol{s}}+\vec{\boldsymbol{l}}$ with the associated magnetic moment $\vec{\mu}_j = \vec{\mu}_l + \vec{\mu}_s$ whose absolute value $|\vec{\mu}_j|$ equals $|\vec{\mu}_j| = g_j \cdot \mu_B \sqrt{j(j+1)}$. Here g_j is an Landé - $\boldsymbol{g}$ factor which equals:

$$g_j = g_l \frac{j(j+1) - s(s+1) + l(l+1)}{2j(j+1)} + g_s \frac{j(j+1) + s(s+1) - l(l+1)}{2j(j+1)} \tag{2.2}$$

The *total angular momentum* $\vec{\boldsymbol{j}}$ of the electron is not parallel to the associated *total magnetic momentum* $\vec{\boldsymbol{\mu}}$ because the spin and orbital magnetic moments have a different coefficient of proportionality to the spin and orbital angular momentum, respectively (Fig.2.1 (a)) [1].

2.2.1 LS-coupling and j-j coupling

The definition of the total electronic angular momentum is clear when an atom has only a single electron. However, when the atom contains several electrons there are two ways to calculate the total angular momentum of the electronic system $\vec{\boldsymbol{J}}$. The option that is realized depends on the strength of the *spin - orbit coupling* which defines the interaction between the spin and orbital angular momenta $\vec{\boldsymbol{s}}$ and $\vec{\boldsymbol{l}}$.

Spin - orbit coupling $\vec{\boldsymbol{s}} \cdot \vec{\boldsymbol{l}}$ arises from the motion of the nucleus in the reference frame of the electron and can be understood via the classical analogy that the circular movement of the electrical charge of the nucleus produces an magnetic field which interacts with the electronic

spin [2]. The energy of this interaction is $E = \lambda \vec{s} \cdot \vec{l}$ where λ is a spin - orbit coupling constant. When the *spin - orbit coupling* is comparable to other energies in the system the total angular momentum should be calculated as a sum of the total angular momenta of all individual electrons according to the *j-j - coupling* scheme (Fig. 2.1(b)):

$$\vec{J} = \sum_i \vec{j_i} \tag{2.3}$$

However, the energy of the *spin - orbit coupling* is only significant for heavy atoms because it is proportional to Z^4 and for most of the atoms it can be considered as a weak perturbation with respect to the other energy terms in the Hamiltonian. In this case the total angular momentum $\vec{J}$ can be calculated according to the $\boldsymbol{LS}$-coupling (or Russell - Saunders coupling) rule (Fig. 2.1(c)):

$$\vec{J} = \vec{L} + \vec{S} \tag{2.4}$$

Here $\vec{S}$ and $\vec{L}$ are the total electronic spin and orbital angular momentum, respectively, which are given by the relations:

$$\vec{S} = \sum_i \vec{s_i} \quad \vec{L} = \sum_i \vec{l_i} \tag{2.5}$$

where $\vec{s_i}$ and $\vec{l_i}$ are the spin and orbital angular momenta, respectively, of the i^{th} electron which process around the total spin $\vec{S}$ and the total orbital angular momenta $\vec{L}$, respectively [2]. The quantum number J corresponds to the total angular momentum $\vec{J}$ and takes the values from the range |L-S|$\leqslant J \leqslant$|L+S|. The multiplicity of a given J equals to 2J+1 and describes the number of the electronic states which are characterized by the quantum numbers J and M_J where M_J determines the component of the total angular momentum $\vec{J}$ along a particular axis such as the direction of the applied field or symmetry axis of the crystal field [3].

Due to the spherical symmetry of the atomic Coulomb potential, the total spin and orbital momentum of the fully occupied electronic shell equals zero. Therefore, the total magnetic moment (or *effective magnetic moment*) of the atom is determined by the sum of the total spin and orbital angular momenta of the electrons in the partially filled electronic shell:

$$\begin{aligned} \vec{\mu}_{eff} &= \vec{\mu}_L + \vec{\mu}_S \\ |\vec{\mu}|_{eff} &= g_J \cdot \mu_B \sqrt{J(J+1)} \end{aligned} \tag{2.6}$$

Here g_J is a Landé g-factor which should be calculated using the (eq. 2.2) where the electronic spin $\vec{s}$ and orbital angular momentum $\vec{l}$ are replaced by the total spin $\vec{S}$ and total orbital angular momentum $\vec{L}$ of the electronic system. L-S coupling is relevant to the light transition

metal ions Ni^{2+} and Cu^{2+} which are studied in this thesis.

2.2.2 Hund's rules

As was shown above, the effective magnetic moment of the magnetic ion is determined by the total angular momentum $\vec{J}$ of the partially filled electronic shell. Therefore, to accurately calculate $\vec{J}$ the electronic configuration of this shell is required.
The electronic configuration of the partially filled electronic shell in the L-S coupling scheme can be found using Hund's rules [3; 4]. According to these rules the electrons will fill the unclosed electronic shell by:

1. achieving the maximum possible value of total spin $\vec{S}$
2. achieving the maximum possible value of total orbital momentum $\vec{L}$

The first rule has priority over the second rule and the total angular momentum quantum number J in the ground state should be calculated depending on the conditions:

1. if the electronic subshell is less than half full then J=|L-S|
2. if the electronic subshell is more than half full then J=L+S

Thus, Hund's rules allow the ground state of the electronic configuration to be defined unambiguously by the *S, L* and *J* quantum numbers. The conventional notation is $^{2S+1}L_J$ where L is given by a corresponding letter in analogy to the notation of the electronic orbitals [3].
The ground states of the isolated Ni^{2+} and Cu^{2+} ions can be indeed calculated according to the Hund's rules. The electronic configuration of Ni^{2+} is $[Ar]3d^8$ where the maximum achievable value of the total spin is S=1 and corresponds to the electronic configuration of 8 electrons on the fivefold degenerate d-electronic orbitals so that three d-electronic orbitals are fully occupied and two are half-filled. The maximum achievable value of the total orbital angular momentum is L=3 and corresponds to the electronic configuration where two half-filled d-electronic orbitals are characterized by m_l=1 and m_l=2. Because the d-electronic orbitals with 8 electrons are more than half-filled, the value of the total angular momentum is J=4. Therefore the ground state of the Ni^{2+} is given by the term $^3D_4$.
The ground state of free Cu^{2+} ion can be calculated in a similar way. The electronic configuration of Cu^{2+} is $[Ar]3d^9$. There is only one possible value of the total spin quantum number which is S=$\frac{1}{2}$ because there is only one unoccupied vacancy on the 3d-orbitals left. The maximum achievable value of the total orbital angular momentum is L=2 and corresponds to the case when the half-filled d-orbital is characterized by m_l=2. Because the 3d-electronic orbital with 9 electrons is more than half-filled, J=3. Thus, the ground state of the Cu^{2+} free ion is characterized by the term $^2P_3$.
However, when a magnetic ion is surrounded by a very strong crystal field, Hund's rules do

not always work. If the energy splitting of the electronic orbitals is large enough due to the crystal field, the higher orbital will be filled only after a lower orbital is fully occupied, in this situation S is not maximized [1; 5]. Hund's second rule can also be broken by quenching of the total orbital angular momentum which forces the electronic configuration to have no defined orientation of the orbital angular momentum [5].

2.3 Crystal field

A crystal is a many-body system which contains many atoms with their nuclei surrounded by many electrons. Therefore, the total system should be described by a many-particle wave function $\Psi(\boldsymbol{r_1}, \boldsymbol{r_2}, ..., \boldsymbol{r_n})$ where $\boldsymbol{r_n}$ is the coordinate of the n^{th} electron. This wave function depends only on the coordinates of the electrons because the nuclei are supposed to move much slower than the electrons and, therefore, can be considered as providing only a fixed potential [6].
The ground state of this system should be found by solving the many-body Schrödinger equation:

$$\hat{\boldsymbol{H}}\Psi(\boldsymbol{r_1}, \boldsymbol{r_2}, ..., \boldsymbol{r_n}) = E\Psi(\boldsymbol{r_1}, \boldsymbol{r_2}, ..., \boldsymbol{r_n}) \tag{2.7}$$

with an appropriate Hamiltonian $\hat{\boldsymbol{H}}$ which is:

$$\begin{aligned}\hat{\boldsymbol{H}} &= -\frac{\hbar}{2m_e}\sum_{i}^{N_e}\bigtriangledown_i^2 - \sum_{i}^{N_e}\sum_{j}^{N_n}\frac{Z_j}{|\vec{r_i} - \vec{R_j}|} + \frac{1}{2}\sum_{i}^{N_e}\sum_{j\neq i}^{N_e}\frac{1}{|\vec{r_i} - \vec{r_j}|} + \frac{1}{2}\sum_{i}^{N_n}\sum_{j\neq i}^{N_n}\frac{Z_i Z_j}{|\vec{R_i} - \vec{R_j}|} \\ &= \hat{T}_e + \hat{V}_{ne} + \hat{V}_{ee} + \hat{V}_{nn}\end{aligned} \tag{2.8}$$

Here, the first term $\hat{T}_e$ is the kinetic energy of an electron and the second $\hat{V}_{ne}$ and third $\hat{V}_{ee}$ terms describe the electron-nuclear and electron-electron interactions, respectively. The last term $\hat{V}_{nn}$ describes the nuclear - nuclear interaction and can be considered as a constant term which is usually weak.
Although the terms $\hat{T}_e$ and $\hat{V}_{ne}$ are the single-electron operators, the term $\hat{V}_{ee}$ describes an double-electron interaction making the Schrödinger equation with this straightforward Hamiltonian (Eq. 2.8) analytically unsolvable for a system with more than two electrons. Because of the large number of electrons in solid systems, it is also difficult for numerical computations.

2.3.1 Hartree-Fock approach

This many-particle problem can be solved using the Hartree-Fock approach which suggests that the electron within the crystal can be described by the single-electron wave-function $\psi(\boldsymbol{r_n})$ within the averaged effective potential V_{eff} caused by the presence of other electrons

[4]. This effective potential is defined as:

$$V_{eff} = \int \frac{\rho(\boldsymbol{r'})}{|\boldsymbol{r} - \boldsymbol{r'}|} dr' \tag{2.9}$$

Here $\rho(\boldsymbol{r'})$ is the electron density distribution of the other electrons in the system. This effective potential is called the *Hartree potential* [4; 6].
The total many-particle wave function of the system $\Psi(\boldsymbol{r_1}, \boldsymbol{r_2}, ..., \boldsymbol{r_n})$ is a linear combination of the product of the single electron wave-functions $\psi_i(\boldsymbol{r_n})$:

$$\Psi(\boldsymbol{r_1}, \boldsymbol{r_2}, ..., \boldsymbol{r_n}) = \frac{1}{\sqrt{N!}} \sum_{i}^{N!} (-1)^{P(i_1, i_2, .., i_N)} \psi_{i_1}(\boldsymbol{r_1}) \cdot \psi_{i_2}(\boldsymbol{r_2}) \cdot ... \cdot \psi_{i_N}(\boldsymbol{r_N}) \tag{2.10}$$

where $P(i)$ is permutation operator which makes the total wave function asymmetric as is required according to the Pauli exclusion principle.
Due to the spherical symmetry of the Coulomb potential the one-electron wave function can be divided into radial and angular parts:

$$\psi(\boldsymbol{r_n}) = R_{nl}(\boldsymbol{r_n}) Y_{l,m_l}(\theta, \phi) \tag{2.11}$$

Here, $\mathrm{Y}_{l,m_l}(\theta, \phi)$ are the spherical harmonics which are normalized Legendre Polynomials whose squares determine the electron density distribution within the atom or, in another words, the shape of the electronic orbitals which contain the electrons with the same quantum number l.
Using the introduced wave-function (2.10) and replacing the term $\hat{V}_{ee}$ in the Hamiltonian (2.8) by the $\hat{V}_{eff}$, the many-particle Schrödinger equation will be split into N single particle Schrödinger equations. These equations, however, should be solved self-consistently because the effective potential depends on the one-electron wave-function. Indeed, the introduced electron density distribution $\rho(\boldsymbol{r})$ is connected with the one-electron wave-functions $\psi(\boldsymbol{r})$ by the relation:

$$\rho(\boldsymbol{r}) = \sum_{i}^{N} |\psi_i(\boldsymbol{r})|^2 \tag{2.12}$$

While the one-electron wave-function $\psi_i(\boldsymbol{r})$ comes from the solution of the N single-particle Schrödinger equations, the electron density distribution $\rho(\boldsymbol{r})$, which is used in the $\hat{V}_{eff}$, was initially guessed. If the initial guess of the $\rho(\boldsymbol{r})$ is close enough to the real distribution, it will consistent with the $\rho(\boldsymbol{r})$ calculated by substitution of the solved wave-functions $\psi(\boldsymbol{r})$ into eq. 2.12, otherwise the N single-particle Schrödinger equations can be solved again using the $\rho(\boldsymbol{r})$ based on the previous solutions. The calculation must be performed interatively

until the initial $\rho(\boldsymbol{r})$ and calculated $\rho(\boldsymbol{r})$ are consist within the determined error. Therefore, an accurate initial guess of $\rho(\boldsymbol{r})$ is very important and is the main difficulty in using of the Hartree-Fock approach based on the self-consistent field.

2.3.2 Molecular orbitals

To estimate the effect of crystal field on the atomic electronic orbitals of a magnetic ion, it is not always necessary to treat a whole crystal structure but can be enough to consider only the symmetry of the nearest neighbour ions [7]. Indeed, for the free magnetic ion the electronic orbitals have spherical symmetry due to the spherical symmetry of the Coulomb potential. However, when this ion is placed into the local crystal environment which has a lower symmetry, the symmetry of the electron orbitals of the magnetic ion is also reduced which leads to the energy splitting of the degenerate energy levels. In particular, the electronic orbitals overlap with the orbitals of the neighbouring ions (ligands) forming molecular bonds whose symmetry corresponds to the symmetry of the local crystal environment. The energy of these molecular orbitals and hence the size of the crystal field splitting depends on degree of overlap between the electronic orbitals of the ligand and magnetic ion.
In $BaNi_2V_2O_8$ each Ni^{2+} ion is surrounded by an octahedra of oxygen ligands. Therefore, the partially occupied $3d^8$ electronic orbitals of the Ni^{2+} are splitted by this octahedral local crystal field these ligands.
Figure 2.2 shows the energy splitting of the d-electronic orbitals by the octahedral (Fig. 2.2(c)) and tetrahedral (Fig. 2.2(d)) crystal fields which are characterized by O_h and T_d point groups symmetry, respectively . Both fields split the fivefold degenerate d-electronic orbitals into the triply degenerate t_{2g} orbitals and doubly degenerate e_g orbitals. This splitting of the d orbitals is based on the equivalence of the electron space density distribution. Indeed, the t_{2g} molecular orbital consists of the d_{xy}, d_{xz} and d_{zy} d-orbitals which all have obviously an equivalent electron space density distribution (Fig. 2.2(a)). The e_g molecular orbital consists of the $d_{x^2-y^2}$ and d_{z^2} d-orbitals which, at first glance, are completely different. However, because d_{z^2} can be represented as a linear combination of the $d_{z^2-y^2}$ and $d_{z^2-x^2}$ orbitals they also have equivalent electron space density distribution.
In the octahedral crystal field the e_g orbital is less energetically preferable than t_{2g} because they involve stronger overlapping with the electronic orbitals of the ligands. Indeed, the $d_{x^2-y^2}$ and d_{z^2} electronic orbitals in the octahedral environment point in the direction of the surrounding ions, maximizing the overlapping of their electronic orbitals. The d_{xy}, d_{xz} and d_{zy} orbitals are in contrast oriented in the directions between the neighbour ions. The Ni^{2+} ions in $BaNi_2V_2O_8$ which have 8 electrons in their 3d shell will have completely filled t_{2g} orbitals and half filled e_g orbitals. Thus, it is the e_g orbitals which are responsible for the magnetic properties of this compound.
In the tetrahedral crystal field the splitting is inversed and the t_{2g} molecular orbital is less

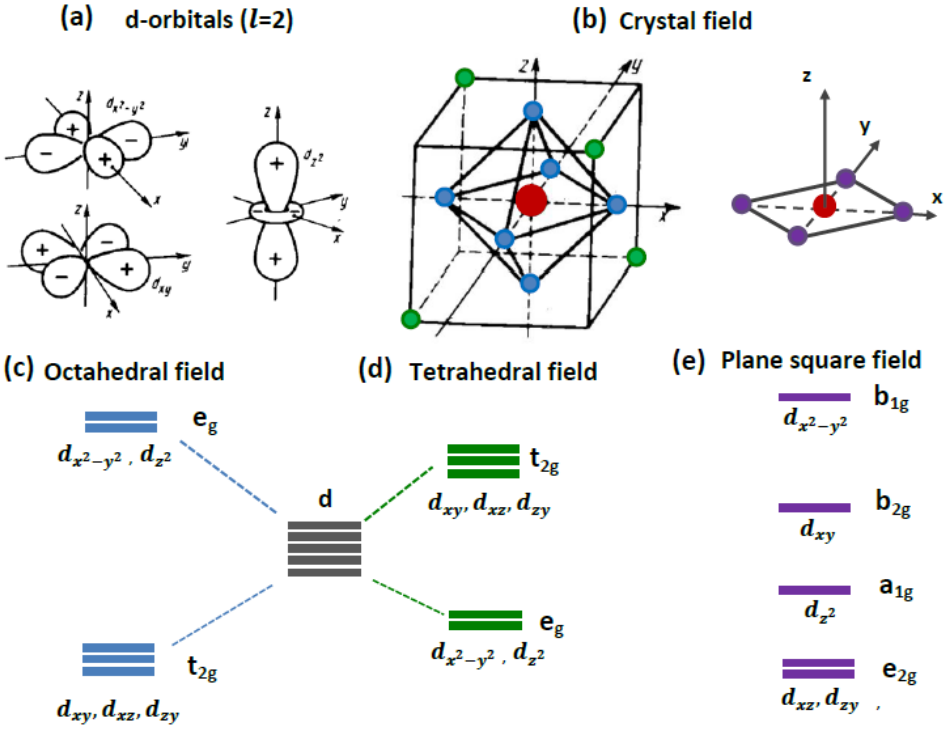

Figure 2.2: (a) The spherical harmonics of the d-electronic orbitals, (b) the octahedral (blue circles), tetrahedral (green circles) and planar (purple circles) surrounding of the ion (red circle). The energy splitting of the d-electronic orbitals in the (c) octahedral, (d) tetrahedral and (e) planar crystal fields [7].

energetically preferable than e_g. Indeed, the d_{xy}, d_{xz} and d_{zy} orbitals point towards the ligands which lie on the tetrahedral verticies. $d_{x^2-y^2}$ and d_{z^2} are, in contrast, along to the x and y axis which are between the neighbour ions.

In $BaCu_2V_2O_8$ the symmetry of the local crystal environment of the Cu^{2+} magnetic ions is much lower than in $BaNi_2V_2O_8$. Indeed, in $BaCu_2V_2O_8$ there are double copper-oxygen plaquettes where each plaquettes is formed by a square of oxygen ions surrounding the Cu^{2+} ion at the centre (Fig. 2.2(b)). Both plaquettes share two oxygens forming the flat double copper-oxygen plaquettes. Therefore, the $3d^9$ electronic orbitals of each Cu^{2+} ion are splitted under effect of this square planar crystal field which is characterized by D_{4h} point group symmetry.

Figure 2.2 (e) shows the diagram of the energy splitting of the 3d electron orbitals in the plane square crystal field. Applying the same logic to the planar square field as for the octahedral and tetrahedral crystal fields, brings to the conclusion that d_{xz} and d_{zy} d-orbitals produce the weakest overlapping with p-orbitals of the ligands. Indeed, the p-orbitals of the ligands point along the diagonals of the square within the plane while the d_{xz} and d_{zy} d-orbitals are along out of plane directions. The next energy level corresponds to the d_{z^2} orbital which has

part of its electron density distribution within the plane which can overlap with the orbitals of the ligands. Because d_{xy} and $d_{x^2-y^2}$ lie within the square plane they overlap considerably with the p-orbitals of the ligands. The d_{xy} orbital which is oriented towards the sides of the square overlaps more weakly with the p-orbitals of oxygen than the $d_{x^2-y^2}$ orbital which pointes along the diagonals straight towards the ligand ions. The Cu^{2+} ions in $BaCu_2V_2O_8$ have 9 electrons in their 3d shell. Thus it is the $d_{x^2-y^2}$ orbital that will be half filled and is responsible for the magnetic properties of this compound.

2.3.3 Quenching of the total orbital angular momentum

One of the consequences of a presence of the strong crystal field environment is a total or partial quenching of the total orbital angular momentum of the magnetic ion. Indeed, the quantum orbital angular-momentum operator is a Hermitian operator that means that its non-trivial eigenvalues are real. Since the quantum orbital angular-momentum operator is $\hat{L}=-i\hbar\vec{\boldsymbol{r}}\times\frac{d}{dr}$ when it acts on a real function only a zero value for the component of the orbital angular momentum along any axis is allowed, $M_l = 0$. It easy to prove that the wave-function of a non-degenerate state is a real function. Therefore, in the non-degenerate molecular orbital the orbital angular momentum is totally quenched [5]. This crystal field effect can be observed for the $3d^9$ Cu^{2+} electron orbitals which are split in planar crystal field as it is shown in Fig. 2.2(e). The upper unfilled molecular orbital b_{1g} is non-degenerate, therefore, the orbital angular momentum of Cu^{2+} magnetic ion in $BaCu_2V_2O_8$ is completely quenched and does not contribute to the total angular momentum $\boldsymbol{J}$. Thus, $BaCu_2V_2O_8$ has a total angular momentum: $\vec{\boldsymbol{J}} = \vec{\boldsymbol{S}}$.

In general, the total orbital angular momentum of the magnetic ion in a degenerate ground state is not quenched. However, quenching of the total orbital angular momentum strongly depends on the point-symmetry group of the particular local crystal field environment which, in some cases, can lead to quenching of the total orbital angular momentum even for degenerate orbitals.

In $BaNi_2V_2O_8$ 3d electronic orbitals of the Ni^{2+} magnetic ion are split into the three-fold degenerate t_{2g} and two-fold degenerate e_g orbitals on the octahedral crystal field and e_g orbital is half-occupied in the ground state.

To explore the effect of this octahedral crystal field on the Ni^{2+} magnetic ion a local crystal-field potential is introduced [1; 5]:

$$V_{crystal} = \sum_{i}^{6} \frac{e_i}{|\boldsymbol{r} - \boldsymbol{R}_i|} \tag{2.13}$$

Here $\boldsymbol{R}_i$ is the position of the i^{th} ligand which is treated as a point charge e_i . Using spherical coordinates (R_i,θ_i,ψ_i) and (r,θ_i,ψ_i) for $\boldsymbol{R}_i$ and $\boldsymbol{r}$, respectively, this potential is expanded into

a series of the spherical harmonics:

$$V_{crystal} = \sum_{l} \sum_{m=-l}^{l} K_{lm} r^l P_l^{|m|}(cos(\theta)) e^{im\psi} \tag{2.14}$$

where $P_l^m(\cos(\theta))$ are associated Legendre polynomials in spherical coordinate system, and coefficients K_{lm} are given by the relation:

$$K_{lm} = \frac{(l-|m|)!}{(l+|m|)!} \sum_i \frac{e_i}{R_i^{l+1}} P_l^{|m|}(cos(\theta_i)) e^{-im\psi_i} \tag{2.15}$$

For the d-electrons it is enough to consider expansion up to fourth order (l=4 in eq.2.14 and eq.2.15). The symmetry of the series expansion of $V_{crystal}$ should match the initial symmetry of $V_{crystal}$ which is octahedral, therefore only even indexes $K_{2,0}$,$K_{2,2}$,$K_{4,0}$,$K_{4,2}$ and $K_{4,4}$ will appear in the expansion. The direct substitution of the parameterized Legendre polynomials $P_l^m(\cos(\theta_i))$ into the eq.2.15 and their further summation over all ligands reveals that coefficients $K_{2,0}$,$K_{2,2}$ and $K_{4,2}$ equal zero and only $K_{4,0}$, $K_{4,4}$ will survive in the expansion eq.2.14. Reducing the similar terms after a substitution of the $K_{4,0}$, $K_{4,4}$ coefficients together with corresponding Legendre polynomials $P_l^m(\cos(\theta_i))$ into the expansion eq.2.14, the crystal-field potential is simplified to the equation [1; 5]:

$$V_{crystal} = \frac{5}{2} K_{4,0}(x^4 + y^4 + z^4 - \frac{3}{5} r^2) \tag{2.16}$$

and electrostatic crystal-field Hamiltonian:

$$H_{crystal} = -e \sum_i V_{crystal}(\boldsymbol{r}_i) \tag{2.17}$$

Because the crystal field potential is given by a real function its eigenfunctions are also real and, therefore, the total orbital angular momentum is quenched. Thus, the total angular momentum of the Ni^{2+} magnetic ion in the octahedral crystal field surrounding is expected to be quenched.

However, the total angular momentum can be partially restored due to the spin-orbit coupling which was not taken into account so far. Indeed, since e_g is doubly degenerate and consists of two orbitals they can be mixed with each other via spin-orbit coupling. If they are combined using imaginary coefficients the orbital moment can be partially restored [5]. This scenario may be energetically favourable because the crystal can then lower its energy by aligning the spin moment parallel to the orbital moment giving a negative spin-orbit energy. This prefered spin direction makes the spin moments anisotropic.

This was observed in $BaNi_2V_2O_8$ where the spin anisotropy was detected and the effective

magnetic moment was found to be slightly bigger than that expected for $\vec{\boldsymbol{J}}$=$\vec{\boldsymbol{S}}$ implying that the $\vec{\boldsymbol{L}}$ is not fully quenched. The details are given in Chapter 4.

2.4 Magnetic exchange interactions

In magnetic materials the magnetic electrons interact with each other via exchange interactions. This happens both between the electrons on the same magnetic ion and also between electrons on different magnetic ions. The magnetic exchange interactions between the magnetic ions can be described by the reduced Hamiltonian which is spin-dependent part of the total Hamiltonian of the system and can be written in a simple form [7; 3]:

$$\hat{\boldsymbol{H}}_s = -\sum_{i,j} J_{i,j} \boldsymbol{S_i} \cdot \boldsymbol{S_j} \tag{2.18}$$

Here $\boldsymbol{S}_i$ is a spin of the i^{th} magnetic ion and $J_{i,j}$ is the magnetic exchange interaction between the magnetic ions. There are several types of the magnetic exchange interactions which arise from the different physical mechanisms.
The first one is a *direct exchange interaction* between the electrons on the same ion. In this case the interaction $J_{i,j}$ is given by the exchange integral [4; 8]:

$$J_{i,j} = \int \phi_i^*(\boldsymbol{r_i}) \cdot \phi_j^*(\boldsymbol{r_j}) \frac{1}{|\boldsymbol{r_i} - \boldsymbol{r_j}|} \phi_i(\boldsymbol{r_i}) \cdot \phi_j(\boldsymbol{r_j}) dr_i dr_j \tag{2.19}$$

Here ϕ_j^* is the wave-function of the electrons and $\boldsymbol{r}_i$ are their coordinates. This integral minimizes the total energy of the system when the spins are parallel or ferromagnetically aligned. Indeed, when the spins are parallel they cannot occupy the same orbital due to the Pauli principle and, therefore, the effect of the strong intra-orbital Coulomb repulsion is reduced. This is the explanation of the first Hund's rule which states that on the same electronic subshell the elections have a configuration which maximizes a total $\boldsymbol{S}$. Because this integral is always positive, the magnetic exchange interaction J_{FM}, which corresponds to the ferromagnetic spin alignment, has a positive sign.
Another mechanism of the exchange interaction is the *kinetic exchange interaction*. This mechanism is based on the minimizing of the kinetic energy of the tunnelling electrons due to their spatial delocalization in the bonding state and is the source of interactions between magnetic ions [3; 8].
When two magnetic ions have per one electron on site, the total wave function is asymmetric and is given by the linear combination of the product of their single states:

$$\Psi(\boldsymbol{r_1}, \boldsymbol{r_2}) = \frac{1}{\sqrt{2}} [\psi_a(\boldsymbol{r_1}) \psi_b(\boldsymbol{r_2}) \pm \psi_a(\boldsymbol{r_2}) \psi_b(\boldsymbol{r_1})] \boldsymbol{\sigma} \tag{2.20}$$

Here, $\boldsymbol{\sigma}$ is the spin part of the total wave function which satisfies the condition for the asymmetry of $\Psi(\boldsymbol{r_1},\boldsymbol{r_2})$. For the symmetric spatial part $\frac{1}{\sqrt{2}}[\psi_a(\boldsymbol{r_1})\psi_b(\boldsymbol{r_2})+\psi_a(\boldsymbol{r_2})\psi_b(\boldsymbol{r_1})]$ of the total wave function, spin part should be asymmetric which is provided by the following linear combination of the spin states (total spin is zero) [7]:

$$\boldsymbol{\sigma}_{asym} = \frac{1}{\sqrt{2}}[(|\uparrow,\downarrow\rangle - |\downarrow,\uparrow\rangle)] \tag{2.21}$$

When the spatial part of the total wave function is asymmetric $\frac{1}{\sqrt{2}}[\psi_a(\boldsymbol{r_1})\psi_b(\boldsymbol{r_2})$-$\psi_a(\boldsymbol{r_2})\psi_b(\boldsymbol{r_1})]$, the spin part σ should be symmetric which is realized by the one of the triplet states $|\uparrow,\uparrow\rangle$, $|\downarrow,\downarrow\rangle$ and $\frac{1}{\sqrt{2}}[(|\uparrow,\downarrow\rangle+|\downarrow,\uparrow\rangle)]$ with total spin 1.
The total wave function with the symmetric and asymmetric spatial parts are calling 'bonding' and 'antibonding' orbitals, respectively and it can be shown that the bonding state is more energetically favoured [4].
The energy difference between these states are:

$$E_s - E_{as} = 2\int \psi_a^*(\boldsymbol{r_1})\psi_b^*(\boldsymbol{r_2})\hat{H}\psi_a(\boldsymbol{r_2})\psi_b(\boldsymbol{r_1}) \tag{2.22}$$

And the exchange integral J is defined as:

$$J = \frac{E_s - E_{as}}{2} \tag{2.23}$$

Because E_s<E_{as} the exchange constant has a negative sign and is thus antiferromagnetic favouring antiparallel spin alignment. This exchange mechanism is responsible for direct exchange interactions between two different magnetic ions. It can also lead to ferromagnetic exchange when a partially filled orbital on one ion overlaps with an unfilled orbital on the neighbouring ion.

2.4.1 Goodenough - Kanamori rules

When the magnetic ions are well separated from each other the overlap of their electronic orbitals becomes very weak which reduces the direct and kinetic exchange interactions between the ions. In this case the magnetic ions can interact with each other via *superexchange interaction* [7; 3]. This interaction exists between two magnetic ions which are separated by a ligand which forms bonds with both of them. The physical mechanism of this interaction is the same as in the *kinetic exchange* interaction and based on the hopping of the electron via the bonding orbitals. However, in contrast to the direct exchange interaction, two bonds are involved and the electrons mediate between three ions. Therefore, for the *superexchange interaction* the spatial arrangement of the interacting magnetic ions with respect to the ligand ion is very imporant. In particular, the strength and sign of the *superexchange interaction*

depends on the angle between the bonds which the ligands form with the magnetic ions. This dependence was formulated by Goodenough and Kanamori and is known as the *Goodenough-Kanamori rules* [9; 10]. According to these rules if the two magnetic ions and a ligand, which is placed between them, form a linear system so that their electronic orbitals overlap under 180° this results in strong antiferromagnetic exchange interaction between the magnetic ions. However, when the angle is 90° the exchange interaction in ferromagnetic and is much weaker.
In this work Cu^{2+} magnetic ions in $BaCu_2V_2O_8$ interact with each other within copper-oxygen plaquettes via weak ferromagnetic exchange interaction because the partially occupied d-electronic orbitals of copper ions overlap with the oxygen p-orbitals under 90° within the square plaquettes.

2.5 Classification of the magnetic models

Although magnetic compounds have a three-dimensional crystal structure it is possible to realize the magnetic exchange interactions only along particular directions. This is because the magnetic exchanges interactions are strongly dependent on the overlap of the electronic orbitals of the magnetic ions which are not isotropic and are strongly affected by the symmetry of the crystal and electronic structure of the magnetic ions and their local environment. Therefore, depending on the dimensionality of the magnetic exchange interactions magnetic systems can be distinguished as 1D, 2D or 3D magnetic systems in sense of the dimensionality of their exchange interactions.
Apart of the dimensionality of the magnetic exchange interactions, the total spin of the magnetic ions can be characterized by a different degree of freedom which is reflected in the number of non-zero components of the corresponding spin vector.

2.5.1 Ising model

When the spin is rigidly fixed along one axis, it can be described by a spin vector with only one non-zero component. This model is known as the *Ising* model, and is named after Ernst Ising who introduced it for the first time, it is described by the Hamiltonian [7]:

$$\hat{\boldsymbol{H}} = -J \sum_{i,j} \boldsymbol{S}_i^z \cdot \boldsymbol{S}_j^z \tag{2.24}$$

Here J is the magnetic exchange interaction between the i and j magnetic ions and $\boldsymbol{S}_j^z$ is a non-zero spin component along a single axis.
The *1D Ising model* consists of 1D chain of the one-component spins and display long-range ordered state where the spins point strictly ferromagnetically or antiferromagnetically (depending on the ferromagnetic or antiferromagnetic exchange interaction J, respectively) only

at zero temperature. At any temperature, which is different from zero, the 1D Ising system with a single defect has infinite entropy in the thermodynamic limit while the energy cost for defect formation is finite. This makes the state with defects is more preferable than the ordered state according to the second law of the thermodynamic.
The *2D Ising model* consists of a 2D lattice of one-component spins each of which interacts with its four nearest neighbours (in the case of a square lattice) via exchange constant J. W. Onsager showed using the transfer matrix method that this system, in contrast to the 1D Ising model, displays a phase transition to the magnetically long-range ordered state at a finite transition temperature which is [11]:

$$k_B T = \frac{2J}{ln(1+\sqrt{(2)})} = 2.269...J \tag{2.25}$$

Note, that this transition does not contradict to the Mermin-Wagner theorem [12] which states that the Goldstone modes destroy the long-range magnetic order at finite temperatures in the magnetic systems where the dimensionality of the exchange interactions is less than two. Indeed, the number of the excited Goldstone modes equals d_s-1 where d_s is the dimensionality of the spin vector. Because for the Ising model d_s=1 there are no excited Goldstone modes due to the spontaneous symmetry breaking (long-range order)[13].

2.5.2 2D XY model

When the spin is free to rotate within the plane, it can be represented by a classical planar rotor which is described by a spin vector with two non-zero components and is known as the *XY model*. It is convenient to describe this model by the Hamiltonian in polar coordinates [13]:

$$\hat{\boldsymbol{H}} = -J \sum_{i,j} |\boldsymbol{S}|^2 cos(\phi_i - \phi_j) \tag{2.26}$$

Here J is a magnetic exchange interaction between the i and j magnetic ions and ϕ_i and ϕ_i are the angles of the ith and jth spins with an arbitrary axis. The Mermin-Wagner theorem prohibits conventional magnetic long-range order at finite temperature in the 2D XY model due to the Goldstone modes which are excited along with the spontaneous symmetry breaking to recover the initial symmetry of the system.
However, Berezinskii independently with Kosterlitz and Thouless suggested that the 2D XY magnetic system displays a topological phase transition from a disordered to a quasi-ordered state which is based on the spin-vortex anti-vortex pair formation [14; 15; 16; 17]. The paired vortices have an opposite circulation (Fig.2.3) and are topological defects in that sense that there is no continuous transformation which can transform a vortex to an anti-vortex [**?**]. Below the transition temperature T_{BKT} the vortices and anti-vortices are strongly bonded on

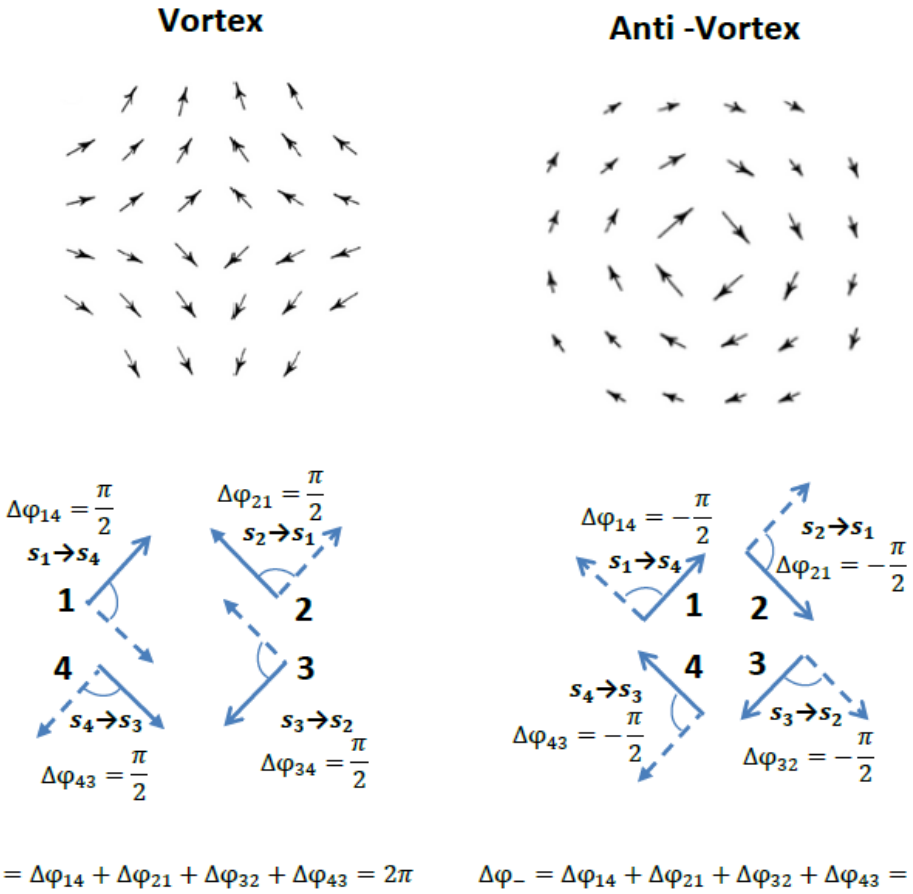

Figure 2.3: A sketch of the vortex and antivortex spin configuration (top). Calculation of the cumulative change in spin-angle in the enclosed clockwise path over vortex and anti-vortex spin-configurations (bottom).

pairs forming the quasi-ordered state, but above the transition temperature the pairs start to decompose creating a plasma (because they have opposite circulation) of vortices.

2.5.3 Heisenberg model

The *Heisenberg model* is the most common model for the description of the magnetic properties of a compound. In this model the spins are represented by the spin-vectors whose three components are all non-zero and, therefore, the spins freely fluctuate in three-dimensions. Neighbour magnetic ions interact with each other along the different crystallographic directions via the magnetic exchange constants $J_{i,j}$ which can have different values along different directions. The magnetic properties of this magnetic system are described by the Hamiltonian:

$$\hat{\boldsymbol{H}} = \sum_{i,j} J_{i,j} \boldsymbol{S_i} \cdot \boldsymbol{S_j} \tag{2.27}$$

Here $\vec{\boldsymbol{S}}_{\boldsymbol{i}}$ and $\vec{\boldsymbol{S}}_j$ are the total spins of the ith and jth magnetic ions and $J_{i,j}$ is a magnetic exchange interaction between them.
Usually, the magnetic exchange interactions are realized between the magnetic ions in along three dimensions within the crystal. This type of the magnetic system corresponds to the *"3D Heisenberg model"*. In the simplest case the magnetic exchange interactions are the same and are realized only between the nearest neighbour atoms. In the ground state the magnetic system displays long-range magnetic order where all spins are ferromagnetically or antiferromagnetically aligned with each other according to the magnetic exchange interactions between them. The phase transition to the magnetically long-range ordered state happens at a finite transition temperature called T_c or T_N for a ferromagnet or antiferromagnet respectively and depends on the strength of the magnetic exchange interactions. Below T_N or T_c the excitations can be viewed as the spins precessing in a collective manner around their equilibrium positions. The spin fluctuations from the equilibrium positions can be expanded on the basis of plane waves oscillating perpendicular to the spin direction. Such a representation of these collective spin oscillations is called *Spin-Wave excitations*. The physical meaning of the Spin-Waves can be illustrated by analogy to the normal mode of the phonon excitations. The *Spin-Waves* are quantized and can be described by the creation and annihilation of the S-1 *magnon* quasiparticle. The energy dispersion of the spin-wave excitations is different for the ferromagnetic (eq.2.28) and antiferromagnetic (eq.2.29) systems and is given by the relations [18]:

$$E(q) = 4SJ_{FM}((1 - cos(2\pi h)) + (1 - cos(2\pi k)) + (1 - cos(2\pi l))) \tag{2.28}$$

$$E(q) = 2SJ_{AFM}\Big[1 - (\frac{1}{3}\Big(cos(2\pi h) + cos(2\pi k) + cos(2\pi l)\Big))^2\Big]^{0.5} \tag{2.29}$$

Here J_{FM} and J_{AFM} are the ferromagnetic and antiferromagnetic exchange interactions, respectively, q is the wave vector which is defined in the reciprocal by the reciprocal lattice units h,k,l and a is the crystal lattice parameter.
For the isotropic Hamiltonian (eq.2.27) the spin-wave dispersion is gapless. However, the spin-wave magnetic excitation spectrum will be gapped in case of the anisotropy of the spins-fluctuations. The anisotropy of the spin fluctuations appears due to the crystal field effects and can be defined in the Hamiltonian either by single-ion anisotropy or exchange anisotropy. The single-ion anisotropy is given in the Hamiltonian by adding an anisotropy term $\mathrm{D}_{anis}\mathrm{S}_i^{z^2}$ where D_{anis} is a strength of the anisotropy. Easy axis anisotropy is achieved for $\mathrm{D}_{anis}<0$ while easy-plane anisotropy is achieved for $\mathrm{D}_{anis}>0$. The exchange anisotropy is defined by the anisotropic dot product $\boldsymbol{S_i} \cdot \boldsymbol{S_j}$:

$$J_{ij}\boldsymbol{S_i} \cdot \boldsymbol{S_j} = J_{ij}(\epsilon(S_i^x S_j^x + S_i^y S_j^y) + \Delta S_i^z S_j^z) \tag{2.30}$$

where J_ij is the exchange interaction.
In the isotropic case ϵ=Δ=1 and for Ising anisotropy $\Delta \gg \epsilon$ while for planar anisotropy $\Delta \ll \epsilon$. Note, that both Δ and ϵ have a dimensionless value in contrast to the single-ion D_{anis} which has the same units as the magnetic exchange interactions.
In this thesis, the explored compound $BaNi_2V_2O_8$ has a spin-wave magnetic excitation spectrum which consists of two gapped spin-wave modes implying that the magnetic structure of $BaNi_2V_2O_8$ is anisotropic. This anisotropy was described in the Hamiltonian of $BaNi_2V_2O_8$ in terms of the single-ion anisotropy. The analysis of directional dependence of the ratio of the intensities of the splitted spin-wave modes reveals that the lower energy mode is gapped by the easy-axis anisotropy while the higher energy mode is gapped by the easy-plane anisotropy. The details of the analysis of the magnetic excitations spectrum of $BaNi_2V_2O_8$ is given in Chapter 4.
The second compound explored in this thesis is $BaCu_2V_2O_8$. It is an example of another typical Heisenberg model which is a *"1D Heisenberg dimerized (alternating) chain"*. In *"1D Heisenberg alternating chain"* the $S = \frac{1}{2}$ magnetic ions are strongly coupled by the dominant antiferromagnetic exchange interaction J_{intra} into the pairs which are called *dimers*. These dimers interact with each other via the weak interdimer magnetic exchange interaction J_{inter} along one particular direction forming a 1D magnetic chain. The magnetic system is described by the Hamiltonian:

$$H = \sum_i J_{intra}\, \mathbf{S}_{i,1} \cdot \mathbf{S}_{i,2} + J_{inter}\, \mathbf{S}_{i,2} \cdot \mathbf{S}_{i+1,1}. \tag{2.31}$$

Here J_{intra} and J_{inter} are the intra- and interdimer exchange couplings respectively and the i denotes the dimer side. The magnetic properties are characterized by the non-magnetic single ground state and S=1 excited triplet state. The magnetic excitations are hard-core bosons where the hard-core constraint allows only one per dimer site. However the excitations can hop from one dimer to another via the weak interdimer exchange interaction J_{inter}. For a system of isolated dimers J_{inter}=0 the energy dispersion is flat and corresponds to the intradimer exchange interaction J_{intra}. When the dimers interact with each other via the interdimer magnetic exchange interaction $J_{inter} \neq 0$ the dispersion is centred at J_{intra} and characterized by a bandwidth equal to J_{inter} and dispersion given by the relation:

$$E(q) = J_{intra} - \frac{J_{inter}}{2} cos(qd) \tag{2.32}$$

Here d is the dimer periodicity. The J_{inter} is usually presented as $J_{inter}=\alpha J_{intra}$ where α is the strength of the dimerization and equals 1 and 0 for the limited cases of the uniform chain and isolated dimer system. In $BaCu_2V_2O_8$ α was extracted to be 0.2925 and the J_{inter} was found to be ferromagnetic making this a rare example of a dimer chain with ferromagnetic interdimer interactions.

2.6 Critical phenomena

The 3D Heisenberg and 2D Ising models are characterized by the second-order phase transition from the disordered to the magnetically ordered state. This transition occurs at a certain transition temperature T_c which is finite and is called the *critical temperature* or *ordering temperature* and was briefly mentioned in the previous section. Above this temperature the system does not display long-range spin-spin correlations so that the average magnetization equals zero. The spin-spin correlations are characterized by a finite *correlation length* which in general corresponds to the length scale over which the physical properties of the system are homogeneous. At and below the transition temperature the correlation length of the magnetic system becomes infinite which means that the spins of the magnetic ions are fully correlated which is experimentally observed as a positive spontaneous magnetization or staggered magnetisation in case of an antifferomagnet. Therefore, the phase transition to the long-range magnetically ordered state breaks the continuous symmetry by selecting the direction of the spontaneous magnetization. The Goldstone modes are the excitations of the symmetry broken states. They can recover the initial symmetry of the system and their success depends on the type and dimensionality of the magnetic system. In particular, Mermin and Wagner showed that Goldstone modes destroy long-range magnetic order at any finite temperature in the magnetic systems whose dimensionality is less or equal two (except the 2D Ising system) while in three-dimensional systems there is always a finite temperature where the magnitude of the Goldstone modes is small allowing long-range magnetic order to survive.

This type of transition from the disordered to the strongly correlated ordered state is not limited to the magnetic systems and is a general fundamental property of many-particle systems which can be treated by applying thermodynamics. Moreover, the *critical behaviour* of different systems in the vicinity of the critical point is found to be *universal* and independent of the type of phase that forms at the transition. Phase transitions can be categorized depending on the dimensionality and symmetry of the system. The *order parameter* is a directional dependent physical quantity whose properties are directly related to the type of symmetry breaking that occurs at the phase transition. For magnetic systems the *order parameter* is the magnetization whose behaviour depends on the spin degree of freedom and is different in the case of spins which are Ising (1 degree of freedom) and Heisenberg (3 degree of freedom). Thus, dimensionality and spin degrees of freedom can be used to categorized most systems into a few general classes. Each of these classes is characterized by a set of universal constants which are called *critical exponents*. There are three universal *critical exponents* for magnetic systems β,γ,δ which define the thermal behaviour of the magnetization and other quantities and are connected with each other by the Rushbrooke's identity: $2\beta+\gamma+\delta=2$.

The thermal behaviour of the *order parameter* is described by a Power Law where the power depends on the critical exponent β. Thus, the analysis of the temperature dependencies of

the magnetization and related quantities provide a general information about the dimensionality of the magnetic system.
In this work the critical behaviour of $BaNi_2V_2O_8$ were explored by the analysis of the temperature dependence of the integrated intensity of the magnetic Bragg Peak which is the square of the spontaneous magnetization and thus, related to the order parameter. The critical exponent is extracted and reveals that below the phase transition to the long-range magnetically ordered state, there is a crossover from one type of the magnetic model to another as is discussed in detail in Chapter 5.

3 Techniques

3.1 Introduction

This chapter describes the experimental techniques which were used during the research presented in this thesis.
Because all experiments were performed on the samples of $BaCu_2V_2O_2$ and $BaNi_2V_2O_2$ which were grown for this work, this chapter starts from the description of the *floating zone method* which was used for the first time for the crystal growth of the both compounds.
The magnetic properties of the compounds can be characterized using a variety of the techniques which are discussed in the main part of this Chapter. To get initial information about the magnetic properties of the investigated system usually measurements of the *constant-field susceptibility* are performed. These thermodynamic measurements are relatively simple, they can be performed in the lab, do not require a large amount of the sample but at the same time are very powerful methods for the initial characterization of the magnetic properties of the new system.
The main results of the presented research is based on the inelastic neutron scattering experiments. That is why the discussion of the inelastic neutron scattering techniques occupies most of this Chapter. This discussion starts from a brief introduction of the *neutron properties* and possible neutron sources which are generally used in research. After that, the basic principles of the neutron scattering process are described in the section *Theory of the neutron scattering process*. Finally the two types of the inelastic neutron scattering techniques, which were used in the presented work, are described in the sections *Triple-Axis Spectrometer* and *Time of flight Spectrometer* , respectively.

3.2 Floating zone technique

All single crystals of both compounds $BaCu_2V_2O_8$ and $BaNi_2V_2O_8$ were grown in the Crystal Laboratory at the Helmholtz Zentrum Berlin für Materialien und Energie (HZB), using the traveling-floating-zone method. A sketch of the typical floating-zone furnace is plotted in Fig. 3.1. Here, the two rods of the polycrystalline compound are placed on top of each other surrounded by the four tungsten halide lamps where the each lamp is focused on the point where the rods touch by the ellipsoidal mirror. The top rod is called a *Feed rod* while the bottom rod is the *Seed rod*. Under the heat from the lamps both rods start melting into the

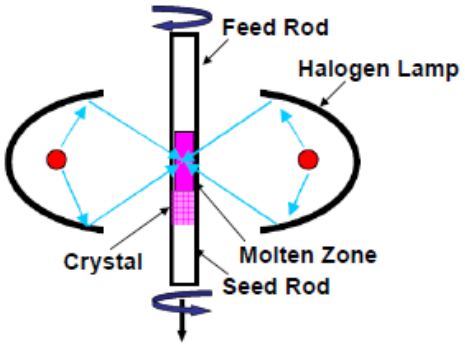

Figure 3.1: Sketch of the traveling-solvent-floating-zone furnace. This figure is taken from the work [19].

molten zone where the radiation emitted by the lamps is focused. In order to mix the molten zone both rods are rotated in opposite directions. The molten zone is slowly shifted upward along the *Feed rod* by raiseing the lamps and mirrors and the crystal grows on the *Seed rod* as the mixture below the molten zone solidifies.
The particular growth conditions such as atmosphere, pressure and growth rate during the single crystal growth of $BaCu_2V_2O_8$ and $BaNi_2V_2O_8$ monocrystalline samples are given in the Introduction section to Chapter 4 and Chaper 6, respectively.

3.3 DC susceptibility measurements

Measurements of the thermodynamic properties such as constant field (DC) magnetic susceptibility allows a lot of information to be extracted about the magnetic properties of the system. The magnetic susceptibility χ is defined as the magnetic moment $\boldsymbol{M}$ induced by an applied magnetic field $\boldsymbol{H}$ per unit volume of the system so that $\boldsymbol{M}=\chi\boldsymbol{H}$ and it is common to use the molar susceptibility $\chi_{mol}=\chi V_m$ where V_m is the molar volume.
Depending on the sign of the χ_{mol} magnetic systems are divided on *diamagnetic* ($\chi_{mol}<0$) where the magnetization opposes the applied field and *paramagnetic* ($\chi_{mol}>0$) where it is parallel to the field. Weak *diamagnetism* is present in all systems and has an order of magnitude of:

$$\chi_{diam} = -\frac{Ne^2\mu_0}{V6m_e}\sum_{i=1}^{Z}\langle r_i^2\rangle \tag{3.1}$$

Here, r_i is the ionic radius and Z is the number of electrons on the outer shell.
In the paramagnetic state the induced magnetization is aligned along the applied field. For isolated magnetic ions the averaged field-induced magnetic moment within the semiclassical

approach brings the *Curie Law*:

$$\chi_{par} = \frac{n\mu_0\mu_{eff}^2}{3k_BT} \tag{3.2}$$

Here, k_B is the Boltzman constant, μ_0 is a magnetic permeability of free space, n is the number of the magnetic ions and $\mu_{eff} = g_J\mu_B\sqrt{J(J+1)}$ is the effective moment of the magnetic ion where g_J is the Landé g-factor, μ_B is the Bohr magneton and J is an total angular momentum. Therefore, $M_s{=}n \cdot \mu_{eff}$ defines the *Saturation magnetization* -the magnetization which is achieved when all n magnetic moments are aligned.
At low temperatures the quantum magnetic exchange interactions between the magnetic ions start to play a role and can drive the phase transitions to the ferromagnetically or antiferromagnetically ordered state at a particular transition temperature T_c. The magnetic susceptibility of these systems in the paramagnetic state at temperatures, which are several times higher than any magnetic ordering temperatures, will follow to the *Curie-Weiss law*:

$$\chi_{par} = \frac{C}{T - \Theta_{CW}} \tag{3.3}$$

Where Θ_{CW} is the *Curie-Weiss temperature* which is proportional to the effective magnetic exchange interactions $J_{exchange}$ in the system :

$$\Theta_{CW} = \frac{z(g_J - 1)^2 J_{exchange} J(J+1)}{3k_B} \tag{3.4}$$

Here, z is a number of the nearest neighbouring magnetic ions which interact with a particulre magnetic ion via the magnetic exchange interaction $J_{exchange}$. The sign of the Curie-Weiss temperature Θ_{CW} characterizes the type of the interactions, whether ferromagnetic (positive Θ_{CW}) or antiferromagnetic (negative Θ_{CW}) [7]. C in the equation 3.3 is the Curie constant which is given by the relation:

$$C = \frac{N_A g_J^2 \mu_B^2 J(J+1)}{3k_B} \tag{3.5}$$

Here, N_A is the Avogadro number and μ_B is the Bohr magneton.
Thus, the analysis of the magnetic susceptibility data as a function of temperature allows the sign and magnitude of the magnetic exchange interactions to be estimated in the magnetic system. It also indicates the transition temperature to the ordered state, if present, because phase transitions are usually accompanied by sudden changes in the magnetic susceptibility. The application of a constant field in different directions with respect to the crystal axes

provides information about the magnetic anisotropy in the explored system.
In this work the magnetic susceptibility data as a function of temperature was measured for single crystalline samples of $BaCu_2V_2O_8$ and $BaNi_2V_2O_8$ in weak constant fields applied in different directions with respect to the crystal axes. The measurements were performed using a Superconducting QUantum Interference Device (SQUID) and Physical Property Measurement System (PPMS) with vibrational sample magnetometer (VSM) whose basic principles are described below. The particular experimental settings of these measurements and the results are given in the corresponding sections in Chapter 4 and Chapter 6.

3.3.1 VSM induced magnetometer

In the VSM magnetometer, the measurements of the average magnetic moment in the sample induced by the applied magnetic field is based on the Faraday's law of induction which connects the change of the enclosed magnetic flux $d\Phi$ with the induced voltage V_{ind} by the relation:

$$V_{ind} = -\frac{d\Phi}{dt} = -NS\frac{dB}{dt} \tag{3.6}$$

The magnetometer consists of a set of pick-up coils. During the measurements the magnetized sample is placed inside the coils and is moving through them so that the voltage is induced according to the Faraday's law and can be detected, allowing the magnetic susceptibility to be extracted.
The sample is mounted on a stick which is vibrating (moving sinusoidally) with fixed frequency during the measurements inside the pick-up coils and induces a sinusoidal voltage response which is amplified and lock-in detected in the VSM detection module:

$$V_{ind} = -\frac{d\Phi}{dt} = -\frac{d\Phi}{dz}\cdot\frac{dz}{dt} = 2\pi A\cdot\omega\cdot C\cdot \boldsymbol{M}\cdot sin(2\pi\omega t) \tag{3.7}$$

where ω is the vibration frequency, C is a coupling constant, $\boldsymbol{M}$ is the magnetization of the sample and A is the amplitude of oscillation.

3.3.2 SQUID magnetometer

The SQUID magnetometer is based on a Josephson junction and consists of the two superconductors which form a loop and are separated by thin isolation layers which are tunnelling barriers. Below the critcal temperature the electrons bound in Cooper pairs can tunnel the barrier creating a supercurrent $I = I_0 sin\delta$ where I_0 is a critical current, $\delta = \frac{2\pi V}{\Phi_0}$, and Φ_0 is the magnetic flux quantum [20]. (Fig.3.2 (a))
If the external magnetic flux path through the SQUID superconducting ring is biased by a constant current $I > 2I_0$, the voltage V across the ring will oscillate with the periodicity of Φ_0 when the magnetic flux is changed and one oscillation in voltage corresponds to an

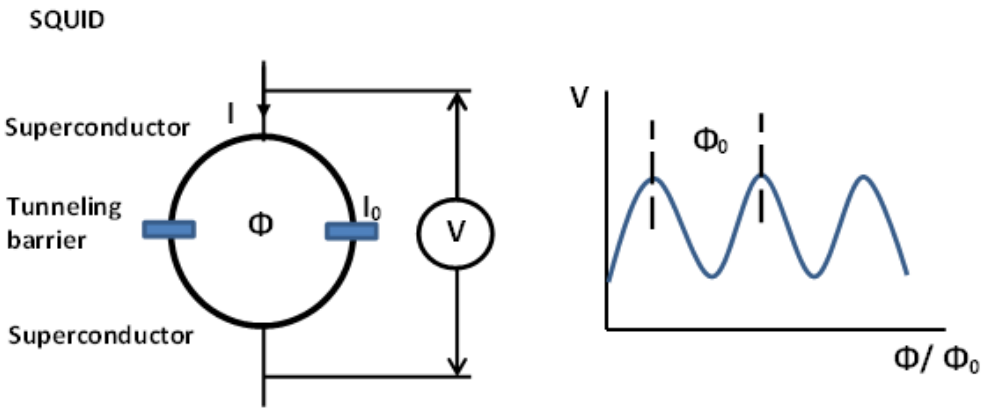

Figure 3.2: (a) Sketch of SQUID superconducting ring based on Josephson junction. (b) Voltage modulation as a function of external magnetic flux

increase of the external magnetic flux by one magnetic flux quantum-Φ_0 (Fig.3.2 (b)). This allows extremely weak changes of the external magnetic flux (Φ_0) to be detected which makes a SQUID one of the most sensitive magnetic devices at present.

3.4 Neutron scattering spectroscopy

Inelastic neutron scattering spectroscopy is a powerful experimental technique which allow the magnetic excitation spectrum of powder or single crystalline samples to be directly measured. The spectrum can be used to precisely determine the value and sign of the magnetic exchange interactions within the system via comparison to theoretical models. Depending on the energy of the neutron flux a wide range of magnetic excitations from a few tenths of meV to hundreds of meV can be explored.
This section starts from the description of the neutron properties and explains why they are particular useful for the investigation of the magnetic properties of the system. After getting acquainted with neutron properties, the basic principles of the neutron scattering process will be introduced to understand how neutrons interact and scatter from matter. Finally, two inelastic neutron scattering techniques which were used in this work are discussed.

3.4.1 Neutron properties and neutron sources

Neutrons are composite subatomic particles which have a mass which is similar to the proton. In contrast to protons and electrons, neutrons are electrically neutral, therefore, they do not interact with the Coulomb potential of the atoms. However, neutrons have non-zero magnetic moment due to its spin which equals to one-half. These properties allow neutrons to interact either with the nucleus via short-range nuclear forces or with the spins of the unpaired electrons of the magnetic ion via the dipole-dipole interaction. Because neutrons

interact with atomic nuclei via short-range nuclear forces they are sensitive to light particles (such as hydrogen) which are almost transparent to X-rays. These properties make neutron scattering a powerful technique to probe and explore the magnetic properties of solids in condensed matter physics.
For scientific purposes neutrons can be obtained from two types of the neutron sources which are a nuclear reactor and a spallation neutron source. In a research reactor the neutrons are produced continuously in time by spontaneous fission of ^{235}U. This is in contrast to the spallation source where the neutrons come as a pulsed flux which is created by punching high energy protons into a heavy metal target. Depending on their energies neutrons can be divided on the cold-neutrons (0.1 meV-10 meV), thermal-neutrons (5 meV-100 meV) and epithermal-neutrons (more than 100 meV). Reactor sources produce neutron beams which follow a Maxwellian distribution of neutrons velocities and the spectrum is dominated by the thermal neutrons with a small contribution of cold and epithermal-neutrons. The spectrum of the pulsed flux from the spallation neutron source is less intense with respect to a reactor source and is usually shifted to higher energies. In both neutron sources the flux of cold or thermal neutrons can be extracted from the high energy part of the spectrum by using a moderator which cools the neutrons to the required temperature [21].
In this work the inelastic neutron scattering experiments were performed using instruments located in both types of the neutron sources. Because $BaCu_2V_2O_8$ has an energy range for its magnetic excitations of 36 meV-46 meV, its magnetic excitation spectrum was explored using thermal neutrons. The magnetic excitation spectrum of $BaNi_2V_2O_8$ was found to range from 0 meV-25 meV and therefore was investigated using both cold and thermal-neutron instruments.

3.4.2 Theory of the neutron scattering process

The scattering process of the monochromatic neutron flux on a sample is described by the *partial differential cross section* (or, in some literature, just *differential cross section*) $\frac{d^2\sigma}{d\Omega dE_f}$ which characterises the number of the neutrons scattered per second in the particular solid angle dΩ with a final particular energy within the range E_f and $E_f + dE_f$. This is exactly the physical quantity which is measured in the neutron scattering experiment.
The neutron scattering cross section consists of coherent and incoherent parts [22]:

$$\frac{d^2\sigma}{d\Omega dE_f} = \left.\frac{d^2\sigma}{d\Omega dE_f}\right|_{coh} + \left.\frac{d^2\sigma}{d\Omega dE_f}\right|_{incoh} \tag{3.8}$$

The coherent scattering cross section describes the neutrons which are scattered by the collective behaviour in the scattering system such as Bragg peaks, phonons or spin-wave excitations. The incoherent scattering cross section represents the neutrons which are scattered

by individual, uncorrelated fluctuations in the scattering system and which do not produce an interference effects.

3.4.2.1 Fermi's Golden Rule

The neutrons have zero-charge and do not interact with the Coulomb electronic potential. Therefore, the neutron interaction with matter is very weak and it can be treated within the first Born approximation where the incident and scattered neutrons are considered as plane waves. The scattered wave in this approach is assumed to be weak and not to affect the incident beam.
The neutron scattering process is accompanied by the transition of the scattering system from the initial quantum state λ_i (before the interaction with neutrons) to the final quantum state λ_f. According to the Fermi's Golden Rule the *partial differential cross section* can be written in terms of the initial and final quantum states of the scattering system (sample) [22]:

$$\left.\frac{d^2\sigma}{d\Omega dE_f}\right|_{\lambda_i\to\lambda_f} = \frac{k_f}{k_i}\cdot\left(\frac{m_n}{2\pi\hbar^2}\right)^2\cdot|\langle\boldsymbol{k_f}\lambda_f|V_m|\boldsymbol{k_i}\lambda_i\rangle|^2\delta\big(\hbar\omega+E_i-E_f\big) \tag{3.9}$$

Here, $\hbar$ is the reduced Planck constant, m_n is a neutron mass, λ_i and λ_f are the initial and final quantum states of the scattering system, respectively. E_i and E_f are the energies of the states λ_i and λ_f, respectively. $\boldsymbol{k_i}$ and $\boldsymbol{k_f}$ are the wave vector of the incident and scattered neutrons, respectively. V_m is the interaction potential between the neutrons and the scattering system.

3.4.2.2 Nuclear scattering

Because neutrons are nuclear particles and have a magnetic moment, they interact with atomic nuclei. The interaction between the neutrons and nucleus has a short range which is usually much less than the wavelength of the incident neutrons and, therefore, can be described by the *Fermi pseudopotential*:

$$V(\boldsymbol{r}) = \frac{2\pi\hbar^2}{m_n}\cdot b\cdot\delta(\boldsymbol{r}) \tag{3.10}$$

Here, $\delta(\boldsymbol{r})$ is a Dirac-delta function and b is the scattering length of atomic nuclei which describes an interaction of the neutron with nuclear potential. The scattering length b is nuclear spin-dependent and it is different for different atoms and their isotopes. The sign of b is usually positive implying an repulsive interaction between neutrons and atomic nuclei. However, some elements are characterized by a negative scattering length (for example vanadium) which corresponds to an attractive potential of nucleus. Alloys of the elements with negative and positive scattering length allows a zero scattering length to be achieved for a specific ratio. For example, alloy of titanium and zirconium in the molar mass ratio 2:1 are

characterized by zero scattering length.
Using the *Fermi pseudopotential* (eq.3.10) and the plane-wave representation of the incident and scattered neutrons, Van Hove showed that the *partial differential cross section* (eq.3.8) can be presented in the form [21]:

$$\frac{d^2\sigma}{d\Omega dE_f} = \frac{d^2\sigma}{d\Omega dE_f}\bigg|_{coh} + \frac{d^2\sigma}{d\Omega dE_f}\bigg|_{incoh} = \frac{1}{2\pi\hbar}\cdot\frac{k_f}{k_i}\Big(S_{coh}(\boldsymbol{Q},\omega) + S_{incoh}(\boldsymbol{Q},\omega)\Big) \tag{3.11}$$

where $S_{coh}(\boldsymbol{Q},\omega)$ and $S_{incoh}(\boldsymbol{Q},\omega)$ are the coherent and incoherent scattering functions, respectively. These functions are called *dynamic correlation functions* and are given by the relations:

$$S_{coh}(\boldsymbol{Q},\omega) = (\bar{b})^2\sum_{j,j'}\int_{-\infty}^{+\infty}\langle e^{-i\boldsymbol{Q}\cdot\boldsymbol{R_{j'}(0)}}e^{-i\boldsymbol{Q}\cdot\boldsymbol{R_j(t)}}\rangle e^{-i\omega t}dt \tag{3.12}$$

$$S_{incoh}(\boldsymbol{Q},\omega) = (\bar{b^2} - (\bar{b})^2)\sum_{j}\int_{-\infty}^{+\infty}\langle e^{-i\boldsymbol{Q}\cdot\boldsymbol{R_j(0)}}e^{-i\boldsymbol{Q}\cdot\boldsymbol{R_j(t)}}\rangle e^{-i\omega t}dt \tag{3.13}$$

Here, $\boldsymbol{Q}$ is the *momentum transfer* which equals $\boldsymbol{Q} = \boldsymbol{k_i} - \boldsymbol{k_f}$. The frequency ω defines the energy transfer $E_t{=}h\omega$ where the *energy transfer* is the difference between the energies E_i and E_f which are the energies of the incident and scattered neutron, respectively. Finally $\boldsymbol{R_j(t)}$ is the position of the j^{th} atom at time t which can be written as $\boldsymbol{R_j(t)} = \boldsymbol{r_j} + \boldsymbol{u_j(t)}$ where $\boldsymbol{r_j}$ is the average position of the atom and $\boldsymbol{u_j(t)}$ is its displacement from its average position which is time-dependent.
The main advantage of the representation of the *partial differential cross section* via the *dynamic correlation functions* $S(\boldsymbol{Q},\omega)$ is that $S(\boldsymbol{Q},\omega)$ depends only on the momentum and energy transfers but not on the absolute values of $\boldsymbol{k_i}$ and $\boldsymbol{k_f}$.

3.4.2.3 Coherent elastic nuclear scattering

It is important to consider in particular the coherent elastic nuclear scattering when $|\boldsymbol{k_i}| = |\boldsymbol{k_f}|$ because it gives the information about the symmetry and periodicity of the crystal structure of the system. The expression inside the integrand of eq 3.12 can be simplified using the expression $\langle exp(U)exp(V)\rangle = exp\langle U\rangle^2 exp\langle UV\rangle$ where $U = -i\boldsymbol{Q}\cdot\boldsymbol{u_0}(0)$ and $V = -i\boldsymbol{Q}\cdot\boldsymbol{u_j}(t)$. After applying this relation and integration with respect to time the *partial coherent differential cross section* takes the form [21]:

$$\frac{d^2\sigma}{d\Omega dE_f}\bigg|_{coh} = \frac{N(2\pi)^3}{V_0}\sum_{G}|F_N(\boldsymbol{G})|^2\cdot\delta(\boldsymbol{Q}-\boldsymbol{G})\delta(h\omega) \tag{3.14}$$

Here, $\boldsymbol{G}$ is a vector of the reciprocal lattice. $|F_N(\boldsymbol{G})|$ is a *nuclear structure factor* which is

given by the formula:

$$F_N(\boldsymbol{G}) = \sum_j \bar{b}_j e^{i\boldsymbol{G}\cdot\boldsymbol{d_j}} e^{-W_j} \tag{3.15}$$

where $\boldsymbol{d_j}$ is the atomic positions within the unit cell and the Debye-Waller factor W characterises their small displacements.
When $|\boldsymbol{k_i}| = |\boldsymbol{k_f}|$ equation 3.14 can be integrated with respect to energy $\delta(h\omega)$ which gives the *coherent elastic differential cross section*:

$$\left.\frac{d\sigma}{d\Omega}\right|_{coh}^{el} = \frac{N(2\pi)^3}{V_0} \sum_G |F_N(\boldsymbol{G})|^2 \cdot \delta(\boldsymbol{Q} - \boldsymbol{G}) \tag{3.16}$$

The equation 3.16 gives the condition $\boldsymbol{Q}$=$\boldsymbol{G}$ for the elastic nuclear scattering which is, indeed, the same as Bragg's Law.

3.4.2.4 Coherent Magnetic scattering

As well as nuclear scattering, neutrons can be scattered by magnetic ions which have a magnetic moment due to unpaired electrons in their electron shell. The neutrons interact with the magnetic moment of the magnetic ions via the dipole-dipole interaction and the corresponding potential V_m in the equation 3.9 consists of both the spin (W_S) and orbital momentum (W_L) parts, respectively. The cross section (eq.3.9), therefore, will be written in the form [21; 22]:

$$\left.\frac{d^2\sigma}{d\Omega dE_f}\right|_{\sigma_i\lambda_i\to\sigma_f\lambda_f} = \frac{k_f}{k_i} \cdot \left(\frac{m_n}{2\pi\hbar^2}\right)^2 \cdot |\langle \boldsymbol{k_f}\sigma_f\lambda_f|W_S + W_L|\boldsymbol{k_i}\sigma_i\lambda_i\rangle|^2 \delta\big(\hbar\omega + E_i - E_f\big) \tag{3.17}$$

Here, σ_f and σ_i define the final and initial states of the neutron, respectively and should be taken into account because the magnetic potential $V_m = W_S + W_L$ contains the neutron spin operator $\boldsymbol{\sigma}$.
The matrix element $\langle \boldsymbol{k_f}|W_S + W_L|\boldsymbol{k_i}\rangle$ is given by the relation:

$$\langle \boldsymbol{k_f}|W_S + W_L|\boldsymbol{k_i}\rangle = 4\pi \sum_l exp(i\boldsymbol{k}\cdot\boldsymbol{r_i}) \Big\{ \{\hat{\boldsymbol{q}} \times (\boldsymbol{s_l} \times \hat{\boldsymbol{q}})\} + \frac{i}{\hbar q}(\hat{\boldsymbol{q}} \times \hat{\boldsymbol{p}}_{\boldsymbol{l}}) \Big\} \tag{3.18}$$

Here, the operators $\hat{\boldsymbol{s}}_{\boldsymbol{l}}$ and $\hat{\boldsymbol{p}}_{\boldsymbol{l}}$ are the spin and orbital momentum of the l^th electron and $\hat{\boldsymbol{q}}$ is the unit vector in the direction of the momentum transfer $\vec{\boldsymbol{Q}}$.
It is convenient to introduce a scattering operator $\boldsymbol{S}_\perp$ which is defined as [21; 22]:

$$\boldsymbol{S}_\perp = 4\pi \sum_l exp(i\boldsymbol{k}\cdot\boldsymbol{r_i}) \Big\{ \hat{\boldsymbol{q}} \times (\boldsymbol{s_l} \times \hat{\boldsymbol{q}})\} + \frac{i}{\hbar q}(\hat{\boldsymbol{q}} \times \hat{\boldsymbol{p}}_{\boldsymbol{l}}) \Big\} \tag{3.19}$$

Therefore, the scattering cross section can be rewriten in terms of the scattering operator $\boldsymbol{S}_\perp$:

$$\left.\frac{d^2\sigma}{d\Omega dE_f}\right|_{\sigma_i\lambda_i\to\sigma_f\lambda_f} = \frac{k_f}{k_i}\cdot\left(\frac{m_n}{2\pi\hbar^2}\right)^2\cdot|\langle\sigma_f\lambda_f|\hat{\boldsymbol{\sigma}}\cdot\boldsymbol{S}_\perp|\sigma_i\lambda_i\rangle|^2\delta\big(\hbar\omega+E_i-E_f\big) \tag{3.20}$$

The scattering operator $\boldsymbol{S}_\perp$ is related to the magnetization of the scattering system:

$$\boldsymbol{S}_\perp = \boldsymbol{S}_{\perp\boldsymbol{S}} + \boldsymbol{S}_{\perp\boldsymbol{L}} \tag{3.21}$$

where

$$\begin{aligned}
\boldsymbol{S}_{\perp\boldsymbol{S}} &= 4\pi\sum_l exp(i\boldsymbol{q}\cdot\boldsymbol{r_i})\{\hat{\boldsymbol{q}}\times(\boldsymbol{s_l}\times\hat{\boldsymbol{q}})\} = \hat{\boldsymbol{q}}\times(\boldsymbol{M_S}(\boldsymbol{Q})\times\hat{\boldsymbol{q}})\\
\boldsymbol{S}_{\perp\boldsymbol{L}} &= 4\pi\sum_l exp(i\boldsymbol{q}\cdot\boldsymbol{r_i})(\hat{\boldsymbol{q}}\times\hat{\boldsymbol{p}}_l) = \hat{\boldsymbol{q}}\times(\boldsymbol{M_L}(\boldsymbol{Q})\times\hat{\boldsymbol{q}})\\
\boldsymbol{M_S}(\boldsymbol{Q}) &= \int \boldsymbol{M_S}(\boldsymbol{r})\cdot exp(i\boldsymbol{q}\cdot\boldsymbol{r_i})\\
\boldsymbol{M_L}(\boldsymbol{Q}) &= \int \boldsymbol{M_L}(\boldsymbol{r})\cdot exp(i\boldsymbol{q}\cdot\boldsymbol{r_i})\\
\boldsymbol{M}(\boldsymbol{Q}) &= \boldsymbol{M_S}(\boldsymbol{Q}) + \boldsymbol{M_L}(\boldsymbol{Q})
\end{aligned} \tag{3.22}$$

Here, $\boldsymbol{M_S}(\boldsymbol{Q})$ and $\boldsymbol{M_L}(\boldsymbol{Q})$ are the Fourier transform of the spin and orbital magnetization operators $\boldsymbol{M_S}(\boldsymbol{r})$ and $\boldsymbol{M_L}(\boldsymbol{r})$, respectively, and $\boldsymbol{M}(\boldsymbol{Q})$ is the Fourier transform of the total magnetization $\boldsymbol{M}(\boldsymbol{r})$ of the scattering system.
The substitution of the equation 3.22 into the equation 3.21 brings very important relations:

$$\begin{aligned}
\boldsymbol{S}_\perp &= \boldsymbol{S}_{\perp\boldsymbol{S}} + \boldsymbol{S}_{\perp\boldsymbol{L}} = \hat{\boldsymbol{q}}\times(\boldsymbol{M}(\boldsymbol{Q})\times\hat{\boldsymbol{q}}) = \boldsymbol{M}(\boldsymbol{Q}) - (\hat{\boldsymbol{q}}\cdot\boldsymbol{M}(\boldsymbol{Q}))\cdot\hat{\boldsymbol{q}}\\
|\boldsymbol{S}_\perp|^2 &= \sum_{\alpha,\beta}(\delta_{\alpha,\beta} - \hat{\boldsymbol{q}}_\alpha\cdot\hat{\boldsymbol{q}}_\beta)S^*_\alpha\cdot S_\beta
\end{aligned} \tag{3.23}$$

The relations 3.23 shows that only the components of the magnetization $\boldsymbol{M}(\boldsymbol{Q})$ which are perpendicular to the direction of the wavevector transfer $\hat{\boldsymbol{q}}$ will contribute to the magnetic neutron scattering cross section.
In many cases it is sufficient to consider a *Heitler - London* model where the scattering system has a crystal structure which contains equivalent magnetic ions whose unpaired electron density is localised close to their equilibrium positions in the crystal lattice. The spin-orbit coupling is described by $\boldsymbol{LS}$-coupling.
When $\boldsymbol{L}$=0, the *partial differential cross section* within this model is given by the relation

[21]:

$$\left.\frac{d^2\sigma}{d\Omega dE_f}\right|_{coh.mag.} = (\gamma r_0)^2 \cdot \frac{k_f}{k_i}\Big(\frac{g}{2}\cdot F(\boldsymbol{Q})\Big)^2 exp^{-2W}\sum_{\alpha,\beta}(\delta_{\alpha,\beta} - \hat{\boldsymbol{q}}_\alpha \cdot \hat{\boldsymbol{q}}_\beta)S^{\alpha,\beta}(\boldsymbol{Q},\omega) \tag{3.24}$$

Here, γ is the neutron gyromagnetic ratio, r_0 is a classical electron radius and g is the *Landé g-factor* which equals g=2 if $\boldsymbol{L}$=0.
$F(\boldsymbol{Q})$ is the *Magnetic form factor* which is the Fourier transform of the normalized magnitization density of a magnetic ion which, in case of $\boldsymbol{L}$=0, is the spin density of the unpaired electrons $\rho_s(\boldsymbol{r})$:

$$F(\boldsymbol{Q}) = \int \rho_s(\boldsymbol{r}) e^{i\boldsymbol{Q}\cdot\boldsymbol{r}} d\boldsymbol{r} \tag{3.25}$$

$S^{\alpha,\beta}(\boldsymbol{Q},\omega)$ is the *Dynamic correlation function* which is the Fourier transform of the spin-spin correlation function $\langle S_0^\alpha(0) S_n^\beta(t)\rangle$:

$$S^{\alpha,\beta}(\boldsymbol{Q},\omega) = \frac{1}{2\pi\hbar}\int_{-\infty}^{+\infty} dt e^{-i\omega t}\sum_l e^{i\boldsymbol{Q}\boldsymbol{R_l}}\langle S_0^\alpha(0) S_l^\beta(t)\rangle \tag{3.26}$$

Here, $S_l^\beta(t)$ is the time-dependent angular momentum operator:

$$S_l^\beta(t) = exp(iHt/\hbar) S_l^\beta exp(-iHt/\hbar) \tag{3.27}$$

where H is the Hamiltonian, when $\boldsymbol{L}$=0 this angular momentum operator belongs to the spin only, however, when $\boldsymbol{L}\neq 0$ it belongs to the total angular momentum $\boldsymbol{J}$.
When $\boldsymbol{L}\neq 0$ the magnetic form factor F($\boldsymbol{Q}$) (eq. 3.25) also will be changed because the orbital momentum $\boldsymbol{L}$ will contribute to the magnetization density of the magnetic ion. In the general case the form factor will have a complicated form [23]:

$$F(\boldsymbol{Q}) = \int_0^\infty dr r^2 j_0(Qr)|\Phi(r)|^2 \tag{3.28}$$

where $j_0(Qr)$ is the first form of spherical Bessel function j_n and $|\Phi(r)|$ is the orbital wavefunction of the unpaired electrons.
However, the form factor (eq. 3.28) can be simplified assuming that $\boldsymbol{Q}$ is much smaller than the inverse of the mean radius of the $|\Phi(r)|$. In this case it can be represented as:

$$F(\boldsymbol{Q}) = \frac{g_S}{g} j_0 + \frac{g_L}{g}(j_0 + j_2) \tag{3.29}$$

Here, g_S, g_L and g are the spin-, orbit- and total *Landé* g-factors which are defined by the

relations:

$$g_S = 1 + \frac{S(S+1) - L(L+1)}{J(J+1)} \quad g_L = 1 + \frac{L(L+1) - S(S+1)}{2J(J+1)} \quad g = g_S + g_L \tag{3.30}$$

3.4.3 Scattering diagrams

It is very convenient to illustrate the neutron scattering process in neutron spectroscopy via scattering diagrams. Indeed, the *partial differential neutron cross section* depends on the wavevector $\boldsymbol{Q}$ and energy transfer $\hbar\omega$ which are connected by the relations:

$$\begin{aligned} &\boldsymbol{Q} = \boldsymbol{k_i} - \boldsymbol{k_f} \\ &|\boldsymbol{Q}|^2 = k_i^2 + k_f^2 - 2k_i k_f cos(2\theta) \\ &\hbar\omega = E_i - E_f = \frac{\hbar k_i^2}{2m} - \frac{\hbar k_f^2}{2m} \end{aligned} \tag{3.31}$$

Here, $\boldsymbol{k_i}$ and $\boldsymbol{k_f}$ are the wave vectors of the the incident and scattered neutron flux, respectively.
In the case of elastic scattering ($|k_i|$=$|K_f|$, $\hbar\omega$=0) the scattering diagram is an *Ewald sphere* (Fig.3.3 (a)) which illustrates the condition $\boldsymbol{Q}$=$\boldsymbol{G}$ of the Bragg reflection where $\boldsymbol{G}$ is a reciprocal lattice vector.
For inelastic scattering there are two possibilities for the scattering triangle (Fig. 3.3(b)), neutron energy loss or gain can occur during the scattering event at a scattering angle 2θ. The scattering triangles are widely used especially in Neutron Triple-Axis spectroscopy.

3.4.4 Triple-Axis Spectrometer

A Triple-Axis Spectrometer (TAS) is an inelastic neutron scattering instrument which was developed for the first time by a Canadian physicist Bertram Brockhouse for which he later won a Nobel Prize. Figure 3.4 shows a sketch of a typical Triple-Axis Spectrometer which consists of three major parts: *Monochromator*, *Sample* and *Analyzer*. The rotations of these parts around the corresponding axes define the region in energy and momentum space where the magnetic excitations are measured during the experiment.
The white neutron beam emitted from the neutron source hits the single crystal monochromator which diffracts only neutrons with a determined wavelength according to Bragg's Law. In order to remove the fast neutron background a sapphire filter is usually placed into the beam before the monochromator in such a way that the c-axis of the sapphire crystal is parallel to the beam direction. Sapphire has a wave length dependent cross section which is low for thermal neutrons but increases strongly for fast neutrons.
The monochromatic neutrons with an initially selected wavevector $\boldsymbol{k_i}$ are scattered by the sample in both elastically and inelastically. The analyzer behind the sample determines the

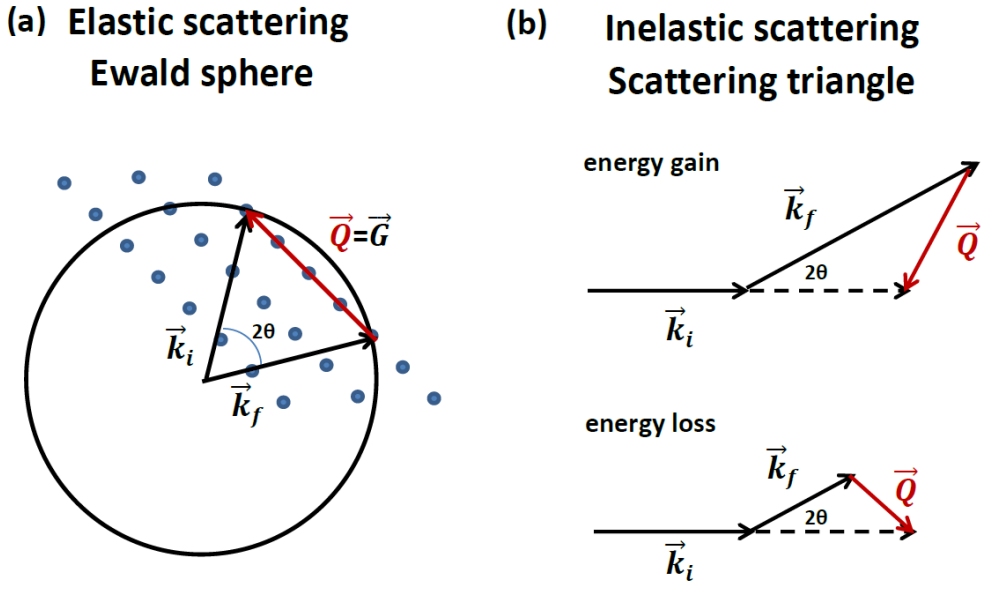

Figure 3.3: (a) Ewald sphere for the elestic neutron scattering. (b) Inelastic scattering triangles for case of the neutron energy gain (top) and neutron energy loss (bottom)

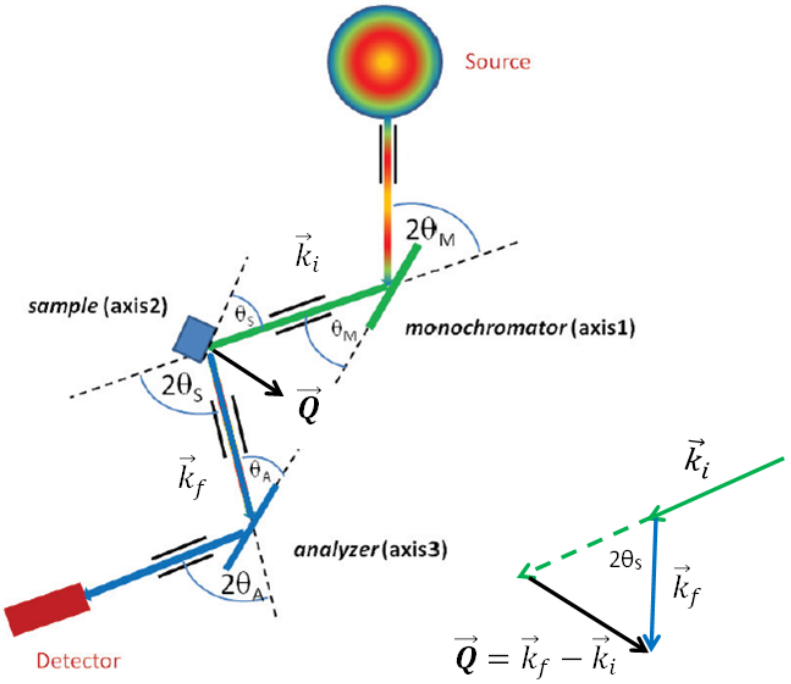

Figure 3.4: The principal schemes of the TAS-spectrometer and sketch of the scattering triangle [24].

final energy of the scattered neutrons due to its 2θ angle, thus, the energy transfer is measured. In order to prevent the selection of higher-order harmonics by the analyzer a filter such as a PG or Beryllium filter can be placed between the sample and the analyzer. To reduce the beam divergence and to improve the resolution several collimators can be placed along the beam. Finally, the selected neutrons with final wave vector $\boldsymbol{k_f}$ are detected by a ^{3}He detector. By varying the incident energy, final energy and scattering angle it is possible to reach a wide range of wavevector $\vec{Q}$ and energy transfers. It is normally the case that the final wave vector k_f of the neutrons is fixed by the analyzer, thus, the scans are usually made by varying either the momentum transfer (by varying the 2θ angle) or the energy transfer (by varying the $\boldsymbol{k_i}$ at the monochromator and the 2θ angle).
In the present work several TAS instruments were used depending on the experimental tasks and energy scale of the magnetic excitation spectrum of the explored compounds. The thermal TAS spectrometer PUMA at FRM2 (Munich, Germany) was used to collect single crystal inelastic neutron scattering data on $BaCu_2V_2O_8$ at base and finite temperatures and the particular experimental settings are given in Chapter 6 and Chapter 7. The magnetic excitation spectra in $BaNi_2V_2O_8$ were explored using both the cold neutron TAS PANDA (Munich, Germany) and the thermal neutron TAS PUMA (Munich, Germany) instruments. Indeed, the cold neutron TAS PANDA was necessary to accurately measure the lower energy part of the magnetic excitation spectrum of $BaNi_2V_2O_8$ because it gives a better resolution at low energy transfers and the full energy dispersion were collected on thermal neutron TAS PUMA. The critical phenomena in $BaNi_2V_2O_8$ were explored using the cold neutron TASP (PSI, Switzerland) for resolution reasons. The particular experimental settings are given in Chapter 4 and Chapter 5.

3.4.5 Time of Flight Spectrometer

A time of flight (TOF) neutron spectrometer is an efficient inelastic neutron scattering instrument which allows to measure a wide range of the momentum and energy transfers in ($\vec{Q}$,ω)-space simultaneously. This technique employs the basic relation between the neutrons wavelength and their velocity which allows to calculate the energy of the neutrons by measuring the time which they take to pass a known distance.
A TOF-spectrometer can have direct or inverted geometry: either final (E_f) or initial (E_i) energy of the neutrons is determined during the measurements. Figure 3.5 (left) shows a principal scheme and a space-time diagram of a typical TOF-spectrometer with direct geometry. For a spallation source the energy selection choppers rotate with particular frequency but different phases to select monochromatic neutron pulses from a white neutron beam. The monochromatic neutron pulse hits the sample after that the energy E_f of the scattered neutrons is determined using the time which they take to pass a known distance to the time-resolved detectors. The momentum transfer is calculated using the scattering angle (2θ) of

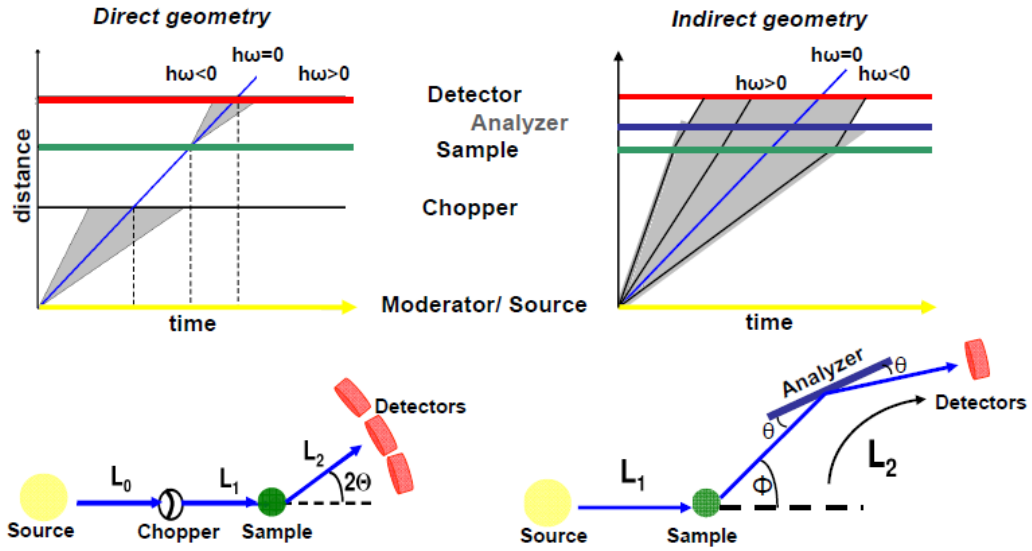

Figure 3.5: Space-time diagrams and the principal schemes of the TOF-spectromiters with direct (left) and inverted (right) geometry. This Figure is taken from the work [19].

the neutrons which is known from the position of the detectors.

A TOF-spectrometer with inverted geometry works the other way around. The principal scheme and the space-time diagram of the typical TOF-spectrometer with the inverted geometry is presented in Figure 3.5 (right). Here, the choppers select polychromatic neutron pulses which have a broad wavelength band. The polychromatic pulses hit the sample and scattered to the single crystal analyzer which selects from the scattered neutron beam only the neutrons which have a particular energy E_f according to the Bragg law. After that the time-resolved detectors measure the intensity of the selected neutrons as a function of time and scattering angle. Thus, the incident energy E_i and the corresponding energy and momentum transfers can be calculated. A TOF-spectrometer with inverted geometry usualy gives a stronger background signal compared to TOF-spectrometer with direct geometry because the sample is hit by the polychromatic pulses.

In the work presented here only time-of-flight neutron spectrometers with direct geometry were used. The thermal energy direct geometry chopper spectrometer Merlin at the Rutherford Appleton Laboratory in UK was used to collect the inelastic neutron scattering data on the powder samples of $BaNi_2V_2O_8$ and $BaCu_2V_2O_8$ at base and finite temperatures. The multi-chopper direct geometry cold neutron spectrometer LET was used to collect the inelastic neutron scattering data on the single crystalline sample of $BaNi_2V_2O_8$ at base temperature of 5K. The details of the experimental settings for these experiments are given in Chapter 4 and Chapter 6.

4 Magnetic properties of $BaNi_2V_2O_8$

4.1 Introduction

In the ideal case the two-dimensional (2D) quantum magnet is a planar magnetic system where the magnetic atoms are arranged and interact with each other within the plane.
In many cases this system can be described by the Heisenberg Hamiltonian:

$$H = \sum_{i,j} J_{i,j}\, \vec{S}_i \cdot \vec{S}_j \tag{4.1}$$

Here $J_{i,j}$ is a magnetic exchange interaction between the spins $\vec{S}_i$ and $\vec{S}_j$ of the magnetic ions at i and j sites which are counted twice and a positive sign defines antiferromagnetic exchange coupling. The Heisenberg interaction shown in this equation, where the interaction along all three spin components is equal, can be modified to act on just one (2D Ising) or two (2D XY) components. Alternatively, certain spin directions can be favoured by adding single ion anisotropy terms to the Hamiltonian. Depending on the magnetic model and spin-value the magnetic system is characterized by different magnetic properties. Search and investigation of compounds which are physical realizations of the ideal 2D quantum magnetic system leads to the observation of a wide range of the intriguing magnetic behaviour.
One of the most remarkable examples is high-T_c superconductivity which was discovered in some layered cuprates and does not belong to the conventional theory of superconductivity that is based on Cooper pairs where the pairing mechanism is phononic. High-T_c superconductivity was discovered for the first time in Ba-doped La_2CuO_4 at T_c=30K by A. Mueller and G. Bednorz [25] and later was detected in other cuprates such as $YBa_2Cu_3O_{6+x}$ [26] and $Ca_{2-x}Na_xCuO_2Cl_2$ [27]. All these compounds were formed from doped square lattices stacked on top of each other, where the layers of copper-oxygen CuO_4 plaquettes are only weakly coupled within the unit cell.
Apart from superconductivity, the layered magnetic systems have attracted considerable attention since exotic ground states such as spin-glasses [28] and spin-liquids [29] were predicted for 2D frustrated magnetic systems. Canonical spin glasses can occur in frustrated lattices which are partially diluted and have a combination of ferromagnetic and antiferromagnetic interactions. The spins are interacting with each other in a random way via the competing exchange interactions so that no long-range magnetic order can exist. Despite the absence of a periodic magnetic structure, there is a phase transition to a metastable *frozen state* at

a defined *freezing* temperature T_f when the spins develop static short range order without forming the conventional long-range ordered state [28]. Spin-glass ordering has been experimentally observed in doped layered copper oxides such as $La_{2-x}Sr_xCuO_4$[30] and La_2CuO_{4+y} [31] where the antiferromagnetic long-range order is destroyed and replaced by the short-range correlations for small hole-dopings x or y, while larger dopings lead to high-Tc superconductivity [32]. However, spin-glass behaviour is not limited to the layered copper oxides but also widely exists among 3D dilute alloys such as CuMn, AgMn, CuFe [7].

Another exotic phenomena which was proposed for 2D frustrated magnetic systems is spin-liquid behaviour [29]. In strongly frustrated magnetic systems the ground state is highly degenerated due to the presence of the competing magnetic exchange interactions. If the frustration is strong enough, the quantum fluctuations, caused by this frustration, can suppress or even destroy the Neel state. Thus, the magnetic system does not display long-range magnetic order even at zero temperature. That ground state, which is not characterized neither static order nor short-range order, is called a *spin-liquid* and was proposed for the first time by Anderson [29] who suggested that a 2D $S=\frac{1}{2}$ triangular antiferromagnet is likely to form such a ground state where the spins remain dynamic as for the 1D chain rather than in a Neel ordered state [29].

Real examples of spin-liquids are very rare, currently the best example is Herbertsmithite which is a good physical realization of a kagome antiferromagnet - a 2D network of corner-sharing triangles [33]. This triangular arrangement in combination with antiferromagnetic interactions is highly frustrated since it is impossible to satisfy all interactions simultaneously, as a result the spins continue to fluctuate between various possible configurations even in their ground state. $Ca_{10}Cr_7O_{28}$ is another example, it is formed from distorted kagome bilayers [34]. Both compounds show complete absence of static magnetism down to the lowest temperatures. Another 2D spin liquid candidate is α-$RuCl_3$ [35] which is a good example of a Kitaev spin-liquid where local Ising interactions on a honeycomb lattice lead to a high degree of competition. Although this compound does develop long-range magnetic order at low temperatures due to the interplane coupling, its excitations at the temperatures above the ordering temperature show indications of the predicted Majorana Fermions. Although frustrated magnetic systems are not limited by the 2D magnets and can also be realized in 3D magnetic systems, the planar triangle and kagome lattices are the most promising candidates for spin-liquids.

Conventional long-range magnetic order in 2D quantum magnets at finite temperatures can exist only in a 2D Ising magnetic system which was exactly solved theoretically by Onsager using the transfer-matrix method [11]. Indeed, long-range order breaks the continuous symmetry which results in excitations consisting of $n-1$ Goldstone modes which fluctuate transverse to the ground state spin orientation where n is the number of the spin components [13]. It was shown that for two and less dimensions the excited Goldstone modes destroy long-range magnetic order at any finite temperatures, while for systems with more than two

dimensions we can always find a temperature where the magnitude of the fluctuations is small. This concept is known as a Mermin - Wagner theorem [12] and forbids the long-range magnetic order in 2D quantum magnets at finite temperature except for the 2D Ising magnetic system.

Although the Mermin - Wagner theorem rules out conventional long-range for order in 2D magnetic systems with n>1, the possibility of a topological phase transition which is driven by the finite winding number of topological defects still exists. Kosterliz and Thouless [14; 15] independently from Berezinsky [16; 17] theoretically predicted for 2D XY magnets a topological phase transition from a disordered to a quasi- ordered phase which is associated with vortex-antivortex pair formation. The sketch of the spin-vortices and -antivortices arrangement was shown in Chapter 2 (Fig. 2.3).

For a long time the Kosterliz - Thouless -Berezinsky topological phase transition was observed only in an atomic gas in a trap [36], superfluids [37] and superconducting thin films [38] or under applied magnetic field [39]. However, recent theoretical Monte Carlo simulations performed by Cuccoli et. al. [40] proposed that this topological behaviour can also exist in 2D Heisenberg systems with weak XY anisotropy. This attracted strong attention for the search and investigation of such type of magnetic systems.

Crystal structure plays an important role for the magnetic properties. Thus, compounds, where the magnetic ions are arranged in planar layers which are well separated within the crystal lattice, are the best candidates for quasi-2D magnetic systems. Two well explored examples are the S=1 honeycomb antiferromagnets $BaNi_2(AsO_4)_2$ and $BaNi_2(PO_4)_2$ which have XY anisotropy [41; 42; 43; 44; 45]. Although these compounds have a layered honeycomb crystal structure of Ni^{2+} ions (spin-1), the thermodynamic measurements reveal a clear phase transition to a 3D long-range ordered state. Indeed, the heat capacity measurements of both $BaNi_2(AsO_4)_2$ and $BaNi_2(PO_4)_2$ reveal a strong sharp anomaly at the ordering temperature T_N which contradicts the expected behaviour of the heat capacity in 2D Heisenberg quantum magnets and indicates that $BaNi_2(AsO_4)_2$ and $BaNi_2(PO_4)_2$ are better regarded as quasi-2D Heisenberg magnetic systems [46].

This Chapter explores a new candidate for the 2D XY Heisenberg quantum magnetic system - the novel S-1 honeycomb quantum magnet $BaNi_2V_2O_8$. The investigation of this compound was performed using single crystal thermodynamic and inelastic neutron scattering techniques to determine its magnetic properties at base temperature and solve the magnetic Hamiltonian of this compound.

This Chapter starts from the description of the *Crystal structure* of the compound and then gives an *Overview of the proposed magnetic model* which was recently published in the literature along with the magnetic structure of $BaNi_2V_2O_8$ at base temperature. In particular, these two subsections show that $BaNi_2V_2O_8$ is a promising candidate for a 2D Honeycomb quantum magnetic system with strong planar XY anisotropy. After the *Introduction* section, the section *Crystal growth and sample characterization* gives details of the single crystal

growth of $BaNi_2V_2O_8$ where large high quality single crystal samples were grown for the first time. The investigation of the magnetic properties of $BaNi_2V_2O_8$ starts from the single crystal magnetic susceptibility measurements. The results are summarized in the section *Thermodynamic properties* and reveal the strong planar anisotropy of the magnetic system at low temperatures. The section *Magnetic excitations of $BaNi_2V_2O_8$* presents the results of both powder and single crystal inelastic neutron scattering measurements of $BaNi_2V_2O_8$ which reveal the gapped spin-wave magnetic excitations which disperse within the honeycomb plane. The excitations were found to be completely dispersionless in the out-of-plane direction confirming that $BaNi_2V_2O_8$ is a 2D XXZ Honeycomb antiferromagnet. Finally, the single crystal magnetic excitation spectra was well reproduced by linear spin-wave theory using the SpinW MatLab library to solve the Hamiltonian of the $BaNi_2V_2O_8$ and extract the values of the magnetic exchange interactions. The extracted results are presented in the section *Hamiltonian of $BaNi_2V_2O_8$* and reveal that $BaNi_2V_2O_8$ is an almost ideal 2D XXZ Honeycomb antiferromagnet with very weak interplane coupling and a small in-plane easy-axis anisotropy. Finally ,the results are summarized in the *Discussion and Conclusion Sections* where they are compared to the results previously published in the literature.

4.1.1 Crystal structure

$BaNi_2V_2O_8$ has a hexagonal crystal structure with a space group symmetry $R\bar{3}$ and lattice constants a=b=5.0575Å and c=22.33Å [47]. The magnetic S=1 Ni^{2+} ions are surrounded by O^{2-} ions forming edge-sharing NiO_6 octahedra. These octahedra are arranged into the honeycomb layers within the (ab)-plane which are separated along the *c*-axis by nonmagnetic $V^{5+}O_4$ tetrahedra and Ba^{2+} ions. All magnetic Ni^{2+} ions are equivalent and all distances between them are the same. Because the Ni^{2+} magnetic ions form an ideal honeycomb net, $BaNi_2V_2O_8$ is assumed to be an unfrustrated magnetic system except for the presence of second neighbour interactions. The interlayer distance is relatively large with respect to the intralayer Ni^{2+}-Ni^{2+} distance. Indeed, the ratio of the distance between the honeycomb layers d_L=7.75Å to the distance d_{nn}=2.90Å between the first nearest neighbouring Ni^{2+} magnetic ions equals 2.57 suggesting very weak interplane magnetic exchange coupling and implying that the dominant magnetic exchange interaction occurs via a Ni^{2+}-O-Ni^{2+} superexchange path within the honeycomb plane [47]. Thus, the crystal and magnetic structure of $BaNi_2V_2O_8$ suggests that this compound can be a good physical realization of the 2D magnetic system with XY planar anisotropy.

4.1.2 Overview of the proposed magnetic model

$BaNi_2V_2O_8$ is a novel quantum magnet but no comprehensive analysis of its magnetic properties has been done so far although a model of its magnetic structure was proposed in the literature [47]. In his work Rogado et al. used neutron powder diffraction measurements

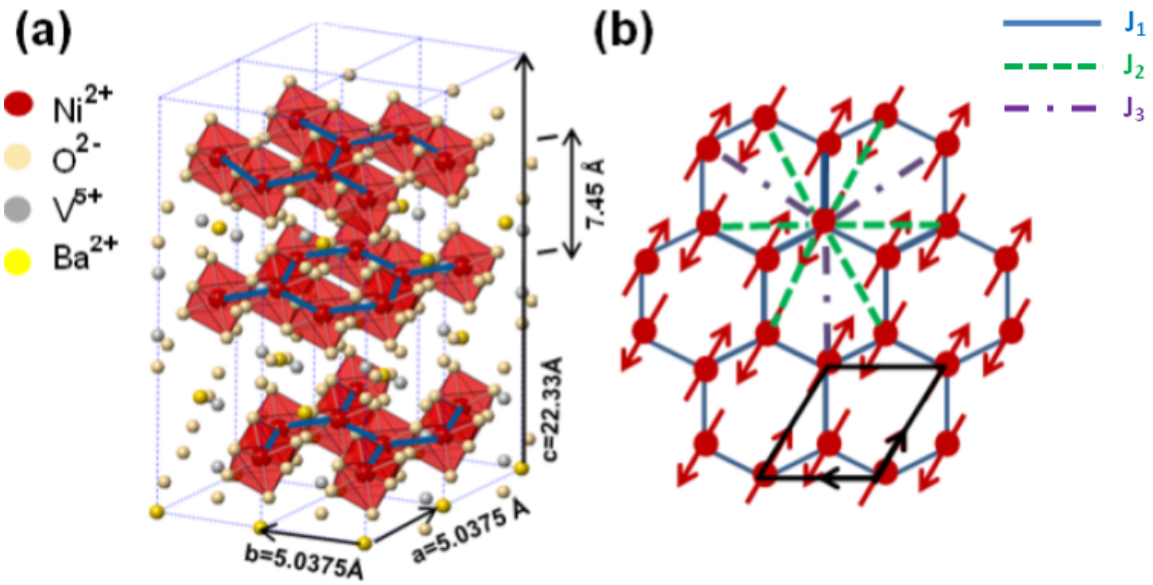

Figure 4.1: (a) Crystal structure of $BaNi_2V_2O_8$ (b) magnetic structure of $BaNi_2V_2O_8$ showing only the magnetic Ni^{2+} ions. The arrows represent the relative spin direction, only one of the three possible twins is presented

show that the magnetic structure of $BaNi_2V_2O_8$ develops long-range magnetic order with the propagation vector to $\mathbf{k}$=(1,0,$\frac{1}{2}$) below the transition temperature of T_N ≈50K. In their ground state the spins lie within the honeycomb plane and are collinear so that each points antiparallel to its 3 nearest neighbours. Although the presence of the long-range-magnetic order implies that $BaNi_2V_2O_8$ is 3D Heisenberg magnetic system with three-dimensional magnetic exchange interactions, the specific heat and single crystal susceptibility measurements reveal only very weak features of a phase transition in the vicinity of the transition temperature which can be attributed to the phase transition to the ordered state. This result suggests that the magnetic exchange interaction, which is responsible for the long-range order, is very weak. Moreover, the single crystal susceptibility measurements reveal strong XY anisotropy in $BaNi_2V_2O_8$. Rogado et al. analysed the powder high temperature susceptibility data of $BaNi_2V_2O_8$ using the high temperature series expansion for an S=1 2D honeycomb antiferromagnet [48]. The dominant AFM exchange integration was extracted to be ≈48K. However, the high temperature series expansion is valid only in the temperature region where the system is in paramagnetic state. Thus, the investigated temperature region of 160K -295K probably is not high enough to apply this approach.

4.2 Crystal growth and sample characterization

Powder and single crystalline samples of $BaNi_2V_2O_8$ were grown by Dr. A. T. M. N. Islam in the Crystal Laboratory at the Helmholtz Zentrum Berlin für Materialien und Energie (HZB)

in Berlin, Germany.
Crystal growth was carried out in an optical image furnace (FZ-T 10000-H-VI-VPO) equipped with four 150 W tungsten halide lamps focused by ellipsoidal mirrors. The starting material for crystal growth was prepared from high purity powder of BaCO3 (99.997%, Alfa Aesar, Puratronic®), NiO (99.998%, Alfa Aesar, Puratronic®) and V_2O_5 (99.99%, Alfa Aesar, Puratronic®) mixed thoroughly in the 1:2:1 molar ratio. After mixing, the powder of stoichiometric composition was calcined in an alumina crucible in air at 900°C twice for 12 hours each, with intermediate grinding. The powder was then pulverized and packed into a cylindrical rubber tube and pressed hydrostatically up to 2000 bars in a cold-isostatic-pressure (CIP) machine and sintered in air at 1000°C for 12 hours. A dense cylindrical rod with a diameter of about 6mm and length 7-8 cm was prepared in this process. Since the compound melts incongruently, we have planned the crystal growth by the traveling-solvent-floating-zone (TSFZ) technique using an off-stoichiometric solvent. For this, a solvent with an excess amount of $BaCu_2O_6$ over the stoichiometric composition was prepared in the same process as the feed rod. About 0.5 grams of solvent material was attached to the tip of the feed-rod by melting in the FZ furnace. The feed rod was then suspended from the upper shaft using nickel wire with the solvent composition in the lower end so, that the crystal growth can start from an off-stoichiometric composition. Another small feed rod was fixed to the lower shaft to support the melt. Crystal growth was performed in ambient air at a growth rate of 0.2 mm/h. Two single crystalline pieces about 8 mm in length and 5 mm in diameter and 11 mm in length and 5 mm in diameter were obtained in this process.
After growth a piece of the crystal was ground and checked for phase purity using the X-ray powder diffractomiter Brucker D8 in the sample Characterisation Laboratory at HZB. A piece of the single crystal was also polished and checked under a polarized optical microscope for grain boundaries or inclusions. The monocrystalline state of the crystals was verified by using the Orient express neutron Laue diffractometer at ILL, Grenoble, France and the X-ray Laue diffractometer in the the sample Characterisation Laboratory at HZB. Orientexpress software was used to analyse the diffraction images.

4.3 Thermodynamic properties

This section describes the investigation of the magnetic properties of $BaNi_2V_2O_8$ using the magnetic susceptibility measurements over a wide temperature range which were performed in the Laboratory for Magnetic Measurement at Helmholtz Zentrum Berlin fur Materialien und Energie. The section starts from the subsection *Experimental settings* which gives the description of the experimental setups such as the direction of the applied magnetic field, investigated temperature range and characteristics of the explored samples. Then, the subsection *Results of the DC susceptibility measurements* presents the analysis of the collected data. In the low-temperature regime the data do not display any clear signature of a phase

transition to long-range magnetic order but reveal the strong planar anisotropy of this magnetic system. To estimate the values of the total and dominant magnetic exchange interactions, the susceptibility data of $BaNi_2V_2O_8$ were collected at high-temperatures and analysed using the Curie-Weiss law and high temperature series expansion, respectively. Finally, the *Discussion* subsection summarizes the results and compares them to those published in the literature.

4.3.1 Experimental settings

The magnetic susceptibility measurements were carry out in the Laboratory for Magnetic Measurements at the Helmholtz Zentrum Berlin using the Physical Property Measurement System (PPMS) and Magnetic Property Measurement System with a Vibrating Sample Magnetometer (MPMS-VSM) by Quantum Design. The measurements were performed for both the low (2K-400K) and high (300K-800K) temperature regimes under an applied magnetic field of 1T.
Three samples with masses $m_1 = 8.48$mg, $m_2 = 19.38$mg, $m_3 = 4.85$mg were cut from the different single crystal growths of $BaNi_2V_2O_8$ and prepared for the magnetic susceptibility measurements. Each sample was oriented using the Laue X-ray diffraction instrument and then cut into retangular shapes with faces parallel and perpendicular to the crystallographic c-axis. The X-ray Laue diffractometer uses a Mo K_α X-ray source. For the low tempreture VSM measurements a glass sample holder and GE vanish glue was used while in the high temperature regime the sample was attached to an oven integrated zirconia stick with cement glue. The sample mass was determined before and after each measurement, thus, the mass loss due to the mounting was taken into account.

4.3.2 Results of the DC susceptibility measurements: Low-T regime

Figure 4.2(a) shows the background-subtracted magnetic susceptibility data of the single crystal sample of $BaNi_2V_2O_8$. The data were collected in the low temperature regime (2K - 400K) for a magnetic field of 1T applied parallel (solid black line) and perpendicular (solid blue line) to the c axis. Both susceptibilities display a broad maximum in the vicinity of T=150K which is usually attributed to low-dimensional quantum magnetic behaviour. Above this maximum both data sets behave isotropic and susceptibility smoothly decreases with temperature increase. The weak difference in the magnitude of the susceptibility data within the temperature region at 150K -400K for the two field directions can be attributed to the anisotropy of the Landé g-factor which was found to be of $g_{H\perp c}$=2.243 and $g_{H||c}$=2.225 [49]. Below this maximum the susceptibilities start to behave anisotropically. Indeed, below 80K the $\chi_{\perp c}$ starts to drop much faster than $\chi_{H||c}$ which shows a weak minimum at ≈52 K below which $\chi_{H||c}$ increases and then stays almost constant with further temperature decrease. However, both $\chi_{H\perp c}$ and $\chi_{H||c}$ reveal no clear signature for the phase transition to

the magnetically ordered state.
The analysis of the derivative of the data with respect to temperature reveals that $\chi_{H||c}$ has a minimum at T=52K and an inflection point at T=48.0K±0.5K. Indeed, Figure 4.2(b) shows that the first derivative of the $\chi_{H||c}$ equals zero at the temperature T=52K satisfying the condition $\frac{d\chi_{H||c}}{dT}$=0 for the extremum of the data. At T=48K ± 0.5K the first derivative of the $\chi_{H||c}$ has a sharp minimum while the second derivative is zero by that satisfying the condition $\frac{d^2\chi_{H||c}}{dT^2}$=0 for an inflection point. The inflection point in the $\chi_{H||c}$ data at T=48K ± 0.5K can be assigned to the phase transition to long-range magnetic order.
The analysis of the first derivative of the $\chi_{H\perp c}$ data with respect to temperature reveals only an inflection point at T=52K where the anisotropy becomes more pronounced and where the $\chi_{H||c}$ data has a minimum. Indeed, the first derivative of $\chi_{H\perp c}$ in Figure 4.2(b) shows a broad maximum in the vicinity of the temperature of T=52K satisfying the condition $\frac{d^2\chi_{H\perp c}}{dT^2}$=0 for an inflection point in the data at this temperature.
The observed behaviour of both $\chi_{H\perp c}$ and $\chi_{H||c}$ data is in good agreement with earlier published experimental results [47]. The inflection point in the $\chi_{H||c}$ data at T=48K ± 0.5K is consistent with a weak feature observed earlier in both $\chi_{H||c}$ and heat capacity data at the same temperature which were also attributed to the phase transition [47]. Moreover, both $\chi_{H\perp c}$ and $\chi_{H||c}$ data qualitatively agree well with the results of the quantum Monte Carlo simulations of the magnetic susceptibility of S=$\frac{1}{2}$ Heisenberg XXZ magnet [40]. The quantum Monte Carlo simulations (QMC) performed for the S=$\frac{1}{2}$ Heisenberg XXZ magnet predict that the out-of-plane susceptibility data has a minimum which is well above the T_{BKT} transition temperature [40]. This minimum was attributed by Coccoli et. al. to a crossover to the XY-anisotropy regime and is in good agreement with the minimum observed in the experimental $\chi_{H||c}$ data of $BaNi_2V_2O_8$ at T=52K (Fig. 4.2(a-b)).

4.3.3 Results of the DC susceptibility measurements: High-T regime

In order to extract the Curie-Weiss temperature and to estimate the value of the magnetic exchange coupling, the magnetic susceptibility data were measured and analysed over the high temperature range.
The solid green line in Figure 4.2(c) presents the high temperature susceptibility data of the single crystalline sample (sample S1) of $BaNi_2V_2O_8$ measured up to 900K with a magnetic field of 1T applied perpendicular to the *c*-axis. The high-temperature data were combined with the low-temperature data and the impurity Curie tail was subtracted. The results reveal that on cooling there is a huge jump in the susceptibility data at 600K-650K which was not present on heating. Further measurements of the same sample show that this feature is irreversible. Measurements of the samples from different crystal growths reproduced the same behaviour which is most likely caused by a decomposition or loss of oxygen from the sample, resulting in a permanent change of the chemical formula. However, the susceptibility

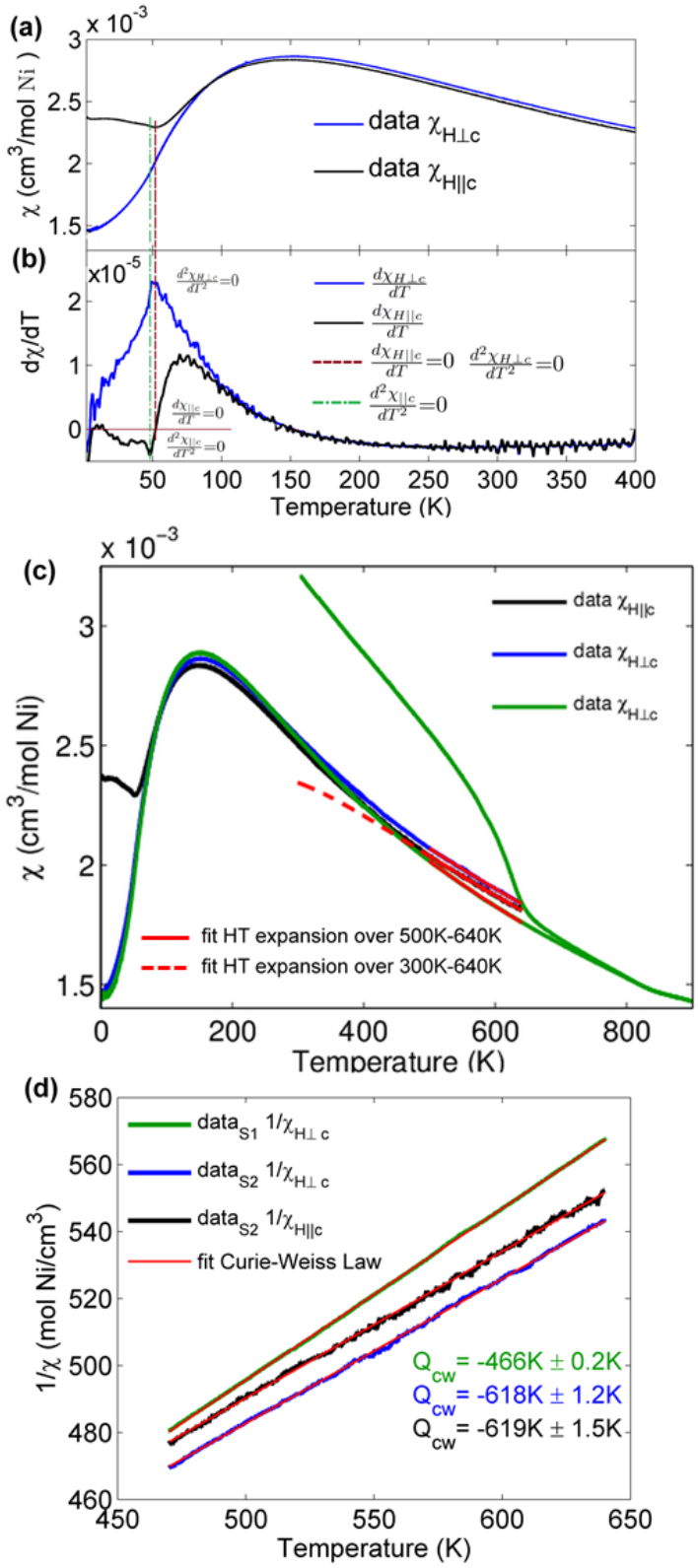

Figure 4.2: (a) The magnetic susceptibility data collected on a single crystal of $BaNi_2V_2O_8$ within the temperature range 2.8K-400K under applied magnetic field of 1T are plotted as a function of temperature. The magnetic field was applied parallel ($\chi_{H||c}$) and perpendicular ($\chi_{H\perp c}$) to the c-axis. (b) The first derivetive of the magnetic susceptibilty data with respect to temperature. (c)The combined low-temperature (2.8K-400K) and high temperature (2.8K-900K) magnetic susceptibility for various samples, field directions and temperature range. (d) The inverse magnetic susceptibility data plotted as a function of temperature and fitted to the Curie-Weiss Law.

measurements performed only up to a maximum temperature of T=650K do not display this unconventional behaviour and are identical on cooling and heating. The solid black and blue lines in Figure 4.2(c) show respectively $\chi_{H||c}$ and $\chi_{H\perp c}$ collected on an another sample (sample S2) up to a maximum temperature of T=640K and combined with low-temperature data. Neither $\chi_{H||c}$ nor $\chi_{H\perp c}$ displays unconventional behaviour either on cooling or heating within the temperature region of 300K-640K. However, measurements of this sample up higher temperatures reproduced the same unconventional magnetic behaviour with the behaviour observed in sample S1.
Thus, the magnetic susceptibility data were analysed over the temperature range 2K-640K.

4.3.3.1 Curie-Weiss law analysis

To extract the Curie-Weiss temperature all three sets of the high-temperature magnetic susceptibility data were analysed over the temperature range of 470K-640K where the system is supposed to be in a paramagnetic state and, therefore, Curie - Weiss Law can be applied :

$$\chi = \frac{2C}{T - \Theta_{CW}} \tag{4.2}$$

Here, C is the Curie-Weiss constant and factor of 2 takes into account that susceptibility was normalized per mole Ni, Θ_{CW} is the Curie - Weiss temperature.
Figure 4.2(d) shows the inverse magnetic susceptibility data plotted as a function of temperature within the temperature region from 470K-640K. This representation simplifies the analysis because the slope of the line is the inverse of the Curie-constant and the constant term of the line is the ratio of the Curie -Weiss temperature to the Curie constant. Indeed:

$$\frac{1}{\chi} = \frac{T}{2C} - \frac{\Theta_{CW}}{2C} \tag{4.3}$$

Here, the notations are the same with the previous formula.
Figure 4.2 (d) shows that all three inverse susceptibility datasets linearly depend on temperature in agreement with the equation 4.3. Therefore, each data set was fitted using a linear function and the Curie-Weiss temperature was extracted from the fit analysis (Fig.4.2 (d) red line). The Curie-Weiss temperatures $\theta_{H||c}$=-619K$\pm$1.5K and $\theta_{H\perp c}$=-618K$\pm$1.2K extracted respectively from the fit analysis of the inverse $\chi_{H||c}$ and $\chi_{H\perp c}$ data collected on the sample S2 are almost the same within the error. However, the Curie-Weiss temperature extracted from the $\chi_{H\perp c}$ data collected on the sample S1 is different and equals $\theta_{H\perp c}$=-466K$\pm$0.2K. This difference of the Curie-Weiss temperatures extracted from analysis of the data collected on different samples is attributed (i) to the accuracy of the SQUID and PPMS measurements which can be 20% when extrapolated over a large temperature range and (ii) to a presence of weak demagnetization whose anisotropic tensor results to shape dependence of a magnetic

suscepsubility of the sample.
The Curie-Weiss temperatures extracted from the $\theta_{H\perp c}$ collected on the samples S1 and S2 were averaged and found to be θ_{CW}=-542K±76K. The negative sign of the extracted values confirms that $BaNi_2V_2O_8$ is antiferromagnet.
The inverse value of the Curie constant was also extracted from the fit analysis of the inverse susceptibility data for all three data sets from the slope of the fitted line. Similar to Curie-Weiss temperature, the Curie constants extracted from the fit analysis of the inverse $\chi_{H||c}$ and $\chi_{H\perp c}$ data collected on the sample S2 are almost the same and equal $C_{H\perp c}$=1.158 cm^3K/mol ± 0.001 cm^3K/mol and $C_{H\perp c}$=1.141 cm^3K/mol ± 0.001 cm^3K/mol. These values are different from the Curie constant $C_{H\perp c}$=0.970 cm^3K/mol ± 0.001 cm^3K/mol extracted from the data collected on the sample S1. Thus, for further analysis the values were averaged and the Curie constant is found to be C=1.06 cm^3K/mol ±0.12cm^3K/mol.
To find out the effective magnetic moment μ_{eff} the definition of the Curie constant was used [7]:

$$C = \frac{N_A \cdot \mu_B^2 \cdot g^2 \cdot J(J+1)}{3k_B} = \frac{N_A \cdot \mu_B^2 \mu_{eff}^2}{3k_B} \tag{4.4}$$

Here, N_A is the Avogadro constant, μ_B is the Bohr magneton, g is Landé g-factor, J is a total angular momentum and μ_{eff} is an effective magnetic moment. Using this equation and the extracted average value of the Curie constant C=1.06 cm^3K/mol ±0.12cm^3K/mol the effective magnetic moment was found to be μ_{eff} =2.91 ± 0.16 μ_B/Ni^{2+}. Although this value is in good agreement with the value of the effective magnetic moment μ_{eff} =3.12 μ_B/Ni^{2+} of the Ni^{2+} magnetic ion which was measured in another compound with Ni^{2+} [7], it is remarkably different from the expected theoretical value μ_{eff} =5.59 μ_B/Ni^{2+} calculated for $3d^8$ electronic configuration with the values S=1, L=3 and J=4. This difference is commonly observed for the 3d ions in an octahedral crystal field [7] and is attributed to quenching of the orbital angular momentum due to the strong crystal field effects which were discussed in detail in Chapter 2. Indeed, the exctracted value μ_{eff} =2.91 ± 0.16 μ_B/Ni^{2+} is in much better agreement with the theoretical μ_{eff} =2.83 μ_B/Ni^{2+} calculated using the values L=0, J=S=1, g_J=2.
Using the Curie - Weiss temperature θ_{CW}=-542K±76K and the fact that the ground state is characterized by L=0, the total value of the magnetic exchange interactions in $BaNi_2V_2O_8$ can be estimated using the relation [7]:

$$\Theta_{CW} = -\frac{2S(S+1)(g-1)^2 \sum_{n=i}^{N} z_i J_i}{3k_B} \tag{4.5}$$

Here, S is the spin value, k_B is the Boltzmann constant, g is a Landé-factor which is $g_{H\perp c}$=2.243 for $BaNi_2V_2O_8$ [49], z_i is a number of neighbours connected to the magnetic ion by the magnetic exchange interactions J_i. In this case $\sum_{n=i}^{N} z_i J_i = 3J_1 + 6J_2 + 3J_3$

where J_1, J_2 and J_3 are the first- , second- and third-neighbour magnetic exchange interactions, respectively (Fig.4.1 (b)) assuming their double counting in the Hamiltonian (eq. 4.1). The negative sign is placed in front of equation in order to be consistent with the Hamiltonian (eq. 4.1) where the AFM interaction is defined to be positive. Using the relation 4.5 the total value of the magnetic exchange interaction J_{total} in $BaNi_2V_2O_8$ can be defined as $J_{total}=J_1+2J_2+J_3$ consistent with the definition of the Hamiltonian (eq. 4.1). The value of J_{total} was estimated to be: J_{total}=7.5 meV ± 1.0 meV.

4.3.3.2 High-temperature series expansion

To estimate the value of the first-nearest neighbour magnetic exchange coupling within the honeycomb plane, the high-temperature susceptibility data were analysed using the high-temperature series expansion proposed by Rushbrook et. al. for 2D magnetic systems [48]:

$$\chi = \frac{N_A \cdot \mu_{eff}^2}{3k_BT}\left(\sum_{m=0}^{6} b_m(|J_1|/kT)^m\right)^{-1} \tag{4.6}$$

Here, N_A is the Avogadro number, k_B is the Boltzmann constant and $\mu_{eff}=g\cdot\sqrt{S(S+1)}\mu_B$ is the effective magnetic moment in units of Bohr magneton μ_B. The b_n are the expansion coefficients which depend on the crystal structure and for the honeycomb lattice they were found to be b_1=4, b_2=7.333, b_3=7.111, b_4=-5.703, b_5=-22.281 and b_6=51.737 and J_1 is the first-neighbour magnetic exchange interaction which is consistent with the Hamiltonian (eq. 4.1). This expansion assumes only the first neighbour interaction and valid only within the temperate region where the system is in a paramagnetic state.

The three data sets of susceptibility data collected on the sample S1 and sample S2 were fitted over the temperature range of 500K-640K using the equation 4.6 varying the parameters μ_{eff} and J_1. In Figure 4.2 (c) the solid red lines over the experimental data give the best fit to the data $\chi_{H\perp c}$ and $\chi_{H||c}$ collected on sample S2 and of the data $\chi_{H\perp c}$ collected on sample S1. The extracted values of the first-neighbour magnetic exchange interaction J_1 were found to be J_1=5.80 meV ± 0.01 meV ($\chi_{H\perp c}$ collected on S1), J_1=6.82 meV ± 0.01 meV ($\chi_{H\perp c}$ collected on S2) and J_1=6.88 meV ± 0.01 meV ($\chi_{H||c}$ collected on S2). The values of the first-neighbour magnetic exchange interaction J_1 exctracted from the analysis of $\chi_{H\perp c}$ and $\chi_{H||c}$ collected on the same sample S2 were averaged. Thus, the first-neighbour magnetic exchange interaction J_1 lies within the range 5.80 meV<J_1<6.85 meV where the average value of J_1 equals J_1=6.32 meV ± 0.52 meV.

The dashed red line through the $\chi_{H||c}$ collected on Sample 2 shows the solution extracted from the analysis over the temperature range of 500K-640K and plotted over a wider temperature range of 300K-640K. The agreement with experimental data breaks down below the temperature of 450K confirming that below this temperature the system is not in paramagnetic state and, therefore, the high-temperature series expansion cannot be used below

T=450K.

4.3.4 Discussion

The single crystal magnetic susceptibility measurements were performed both in the low and high temperature regimes under an applied magnetic field of 1T applied parallel ($\chi_{H||c}$) and perpendicular ($\chi_{H\perp c}$) to the *c*-axis. Both the $\chi_{H||c}$ and $\chi_{H\perp c}$ susceptibility data reveal broad maxima at 150K-200K which is typical for low dimensional antiferromagnets. Below this maximum, at T=80K, the magnetic susceptibilities start to display anisotropic behaviour which becomes most pronounced at the temperature of T=52 K where the $\chi_{H||c}$ data have a minimum. The presence of this minimum in the $\chi_{H||c}$ data was predicted theoretically using QMC simulations for the S=1/2 Heisenberg XXZ model and is associated with the crossover to an XY anisotropy dominated regime (Fig. 4.3(a) which is Fig. 22 in the ref. [40]). Figure 4.3 (a) shows the results of the QMC simulations for the S=1/2 Heisenberg XXZ with a weak Ising easy-plane anisotropy Δ=0.02 thaken form the work [40]. Its comparison to the results of the susceptibility data of $BaNi_2V_2O_8$ reveals a perfect qualitative agreement for both directions of the applied magnetic field. Indeed, $\chi_{H\perp c}$ susceptibility data of $BaNi_2V_2O_8$ display a characteristic minimum at T=52K (Fig. 4.3(b)) which is predicted by QMC simulations at the reduced temperature of t=0.3 scaled on the counted once dominant magnetic exchange interaction in the system. Using the value of the total magnetic exchange interaction J_{total}=7.56 meV$\pm$1meV estimated from the analysis of the Curie-Weiss temperature and taking into account that it was counted twice in the Hamiltonian, the temperature of the observed minimum in the $\chi_{H\perp c}$ is scaled to be $T_{min}k_B/J_{total}$=0.298 which is in good agreement with the value of t=0.3 predicted by QMC simulations. Thus, below T=52K $BaNi_2V_2O_8$ clearly displays the behaviour of a 2D Heisenberg XXZ magnet with a strong planar anisotropy.

Neither $\chi_{H||c}$ nor $\chi_{H\perp c}$ display any significant signature for the phase transition to the long-range ordered state suggesting that an interplane magnetic exchange interaction, which is probably responsible for the long-range ordered, state is very weak. The analysis of the derivatives of the magnetic susceptibilities data reveals that both $\chi_{H||c}$ and $\chi_{H\perp c}$ have an inflection point at T=48K which can be attributed to the transition to long range magnetic order. This is in agreement with the weak feature which was previously observed in both $\chi_{H||c}$ and ΔC_p at T=48K$\pm$0.5K and was also attributed to the transition to the 3D ordered state [47].

The analysis of the magnetic susceptibility data within the high temperature region of 500K-640K reveal a Curie-Weiss temperature Q_{CW}=-542K$\pm$76K which was extracted for the first time. From this Curie-Weiss temperature the total value of the magnetic exchange interaction J_{total} was estimated to be $J_{total}=J_1 + 2J_2 + J_3$=7.56 meV $\pm$ 1 meV where J_1, J_2 and J_3 are the first- , second- and third-neighbour magnetic exchange interactions, respectively

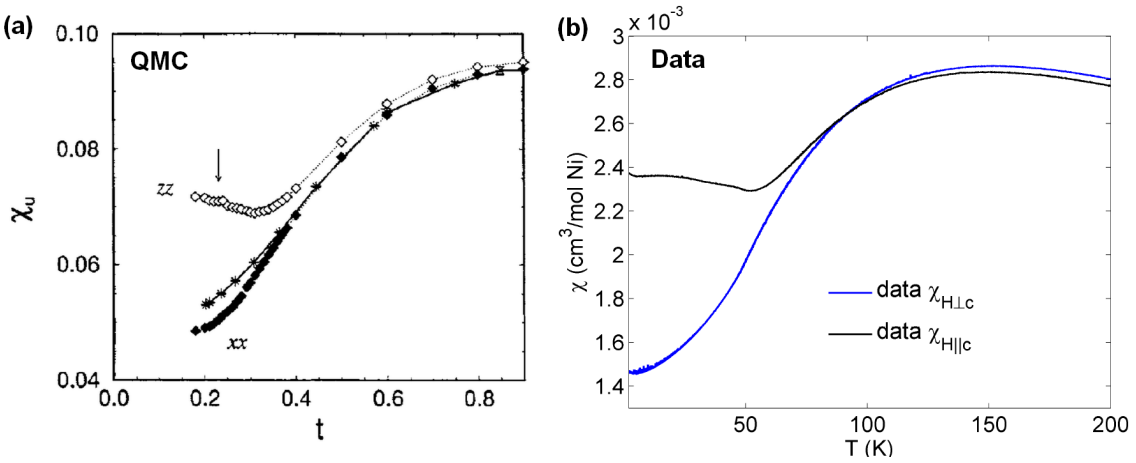

Figure 4.3: (a) The magnetic susceptibility data computed using QMC simulations for 2D Heisenberg XXZ square lattice model with weak Ising in-plane anisotropy Δ=0.02 plotted in the reduced temperature scale Tk_B/J_1 where J_1 is the dominant magnetic exchange interaction. The figure is taken from [40] with author permission. (b) The $\chi_{H||c}$ and $\chi_{H\perp c}$ susceptibility data collected on single crystal of $BaNi_2V_2O_8$

which are consistent with the Hamiltonian (eq. 4.1).

The analysis of the high temperature magnetic susceptibility data using the high temperature series expansion (eq. 4.6) estimates the value of the first-nearest neighbour magnetic exchange interaction to be of J_1=6.325 meV $\pm$ 0.0525 meV. This value is higher than the value J_1=48K (4.138 meV) proposed earlier in the literature [47] which was based on the analysis of the powder susceptibility data using the same high temperature series expansion. However, this discrepancy can be explained by the fact that the powder susceptibility data have been analysed within the temperature region $\approx$160K-295K which is not high enough. Indeed, the high temperature series expansion is only valid above the Curie- Weiss temperature which is extracted here for the first time and found to be Q_{CW}=-542K$\pm$76K.

4.4 Magnetic excitations of $BaNi_2V_2O_8$

This section presents the results of the powder and single crystal inelastic neutron scattering measurements of $BaNi_2V_2O_8$ which were performed at several neutron facilities in order to explore the magnetic excitation spectrum of this compound and to solve its Hamiltonian. The section starts from the description of the experimental settings which are given in the subsection *Experimental settings of the inelastic neutron scattering experiments*. The analysis of the results of the inelastic neutron scattering experiments starts from the analysis of the *Powder spectrum* which gives an overview of the powder magnetic excitation spectrum of $BaNi_2V_2O_8$ revealing spin-wave type excitations extending up to 26 meV. To properly explore the magnetic interactions of $BaNi_2V_2O_8$ *The Single crystal Spectrum* was analysed. The results reveal that the single crystal magnetic excitation spectrum of $BaNi_2V_2O_8$ consists

of two spin-wave modes which are dispersing within the honeycomb plane and are completely dispersionless in the out-of-plane direction suggesting negligible interplane coupling. Both modes are gapped which is attributed to the presence of both strong XY and weak in-plane anisotropy in the magnetic system. Finally, the powder and single crystal magnetic excitation spectra of $BaNi_2V_2O_8$ were simulated within linear spin-wave theory using the Spin-W MatLab Library to solve the Hamiltonian of this compound. *Comparison of the INS data with the SpinW simulations* shows that the simulations well reproduce the experimental data. They reveal that $BaNi_2V_2O_8$ is a quasi 2D Heisenberg quantum magnet with strong XY anisotropy where a dominant antiferromagnetic coupling is realized between the nearest neighbour magnetic ions in the honeycomb plane while weaker antiferromagnetic second neighbour coupling is also present. The results of this section are summarized and discussed in the *Discussion subsection.*

4.4.1 Experimental settings of the inelastic neutron scattering experiments

The magnetic properties of $BaNi_2V_2O_8$ were investigated using inelastic neutron scattering techniques and the measurements were performed using different instruments depending on the experiental needs.

First, a powder sample of $BaNi_2V_2O_8$ with total mass of 19.03 g was measured using the high intensity, medium resolution time-of-flight spectrometer MERLIN at the Rutherford Appleton Laboratory, United Kingdom in order to get an overview of the magnetic excitation spectrum. The sample was placed inside a closed cycle cryostat and cooled down to a temperature of 5K which was the base temperature (BT). The Fermi chopper was operated in four different modes which are characterized by the frequencies of 400Hz, 300Hz, 250Hz and 200Hz and were phased to select the neutrons with incident energies of E_i=80 meV, E_i=50 meV, E_i=35 meV and E_i=20 meV, respectively. The corresponding resolution at the elastic line was found to be of E_i=5.1 meV$\pm$0.1 meV, E_i=3.2 meV$\pm$0.06 meV, E_i=2.26 meV$\pm$0.06 meV and E_i=1.24 meV$\pm$0.02 meV, respectively. This can be found by fitting the elastic signal at a place without a Bragg peak.

To explore the magnetic excitation spectrum of $BaNi_2V_2O_8$, the single crystal inelastic neutron scattering measurements were performed at the thermal neutron triple-axis spectrometer PUMA at the Forschungs Neutronenquelle Heinz-Maier-Leibniz (FRM2), Munich, Germany. The single crystal sample of $BaNi_2V_2O_8$ with mass of m=340mg was preoriented in advance with the (H,K,0) plane as the horizontal instrumental scattering plane using the X-ray Laue difractometer at HZB. The sample holder with the preoriented sample was put into the closed-cycle cryostat that allowed cooling down to a base temperature of 3.5K. To explore the energy dispersion within the honeycomb (*ab*)-plane, the constant energy scans were performed along the H or K directions at fixed energy transfers within the energy range of E=2 meV-29 meV with a step in energy of 1 meV. For these measurements a double-focused

pyrolytic graphite monochromator (PG (002)) was used together with a doubly-focused PG (002) analyser which provides a calculated resolution of 2 meV at fixed final wave-vector of k_f =2.662Å^{-1}. A sapphire filter was located in the main beam in front of the monochromator to reduce the fast neutron background while two PG (002) filters in series were placed between the sample and analyser to eliminate high-order neutrons from the scattered beam.

To precisely investigate the low-energy part of the magnetic excitation spectrum, the same sample of $BaNi_2V_2O_8$ was measured at the cold neutron triple-axis spectrometer PANDA at FRM2, Munich, Germany. The orientation of the sample was kept the same and the measurements were performed in the (H,K,0) scattering plane by taking constant energy scans along (h,1-h,0) direction at fixed energy transfers within the energy range of E=0.5 meV-13 meV with a step in energy of 0.5 meV.

In order to explore the energy dispersion of the magnetic excitation in the out-of-plane direction, the sample orientation was changed by rotation of the sample holder by 90 degree so that measurements were performed in (H,0,L) scattering plane. The constant-wave vector scans were performed along (1,0,L) directions for different fixed values of L over the energy range up to 5 meV. All data were collected at the base temperature of 4.3K, which was achieved by using a closed-cycle cryostat. The final wave vector k_f= 1.57 Å^{-1} was kept fixed giving an energy resolution value of 0.138 meV which was obtained by measuring of the full width at half maxima (FWHM) of the incoherent scattering. A Beryllium filter was used in front of the analyzer in order to remove the high-order wavelengths.

To extract accurate values of the energy gaps and to verify the dispersionless of magnetic excitation spectrum along the c-direction, the high resolution inelastic neutron scattering measurements were performed using the Cold Neutron Triple-Axis spectrometer TASP, at Paul Scherrer Institute (PSI), Switzerland. This instrument was equipped with a vertically focused PG (002) monochromator and a horizontally focused PG (002) analyzer. The final wave vector was fixed at k_f =1.23Å^{-1} giving the energy resolutions of 0.065 meV and 0.074 meV for focused and flat analyzers modes, respectively. For these inelastic neutron scattering measurements the analyser was kept focused due to its higher intensity and better resolution. The resolution was determined by the FWHM of the incoherent scattering. A new sample from a different crystal growth with mass of m=500mg was preoriented in advance with the (H,K,0) plane as the instrumental scattering plane using the X-ray Laue instrument at HZB. The sample holder with the preoriented sample was mounted inside an orange cryostat that allowed it to be cooled down to a base temperature of 1.47K. Constant wave vector scans were performed at (1,0,0) and (1,0,1/2) over the energy range of 0 meV-5.5 meV at the base temeprature.

To further explore the magnetic excitation spectrum of $BaNi_2V_2O_8$ in different directions and to test their equivalence, the single crystal inelastic neutron scattering measurements were performed at the high-resolution cold neutron multi-chopper spectrometer LET, at the Rutherford Appleton Laboratory, United Kingdom. The measurements were carried out us-

ing the time-of-flight inelastic neutron scattering technique which was discussed in Chapter 3. The main advantage of this technique is that it can measure a large area of the reciprocal lattice simultaneously over a range of several energy transfers. The orientation of the sample with mass of m=500mg was kept the same and was aligned with the (H,K,0) plane as the instrumental scattering plane. The sample was placed in an orange cryostat with a base temperature of 1.5K. The inelastic neutron scattering measurements were performed at base and finite temperatures but in this Chapter only the INS data collected at the base temperature will be discussed. The data were collected for four different incident energies of E_{i1}=2.97 meV, E_{i2}=5 meV, E_{i3}=10.2 meV and E_{i4}=30.6 meV simultaneously which are characterized by a calculated energy resolution of ΔE_{i1}=0.05 meV, ΔE_{i2}=0.1 meV, ΔE_{i3}=0.31 meV and ΔE_{i4}=1.2 meV, respectively.

4.4.2 Powder Spectrum

The powder inelastic neutron scattering data of $BaNi_2V_2O_8$ collected in the long-range magnetically ordered phase at 5K at MERLIN time-of-flight instrument is presented in Figure 4.4(a). The data show an intense inelastic signal over the energy scale of 0 meV-26 meV which displays clear V-shaped dispersion which is typical for spin-wave excitations. These spin-wave type excitations have their first minimum at $|Q|$=1.45Å^{-1} which corresponds to the proposed $(1,0,\frac{1}{2})$ magnetic Bragg peak position. A Van Hove singularity is observed at 26 meV indicating the top of the excitation band. The intensity of the excitations is strong at low wavevectors and decreases with increasing wavevector confirming its magnetic nature.

4.4.3 Single crystal Spectrum

In order to learn more about the magnetic excitations in $BaNi_2V_2O_8$, to find out the values of the magnetic exchange interactions and to determine the type and dimensionality of this quantum magnet single crystal inelastic neutron scattering measurements were performed both in the honeycomb plane ((a^*, b^*)-plane) and along the out-of-plane directions (c^*-axis).

4.4.3.1 Energy dispersion within the honeycomb plane

To get an overview of the single crystal magnetic excitation spectrum over the full energy scale and to investigate the magnetic exchange interactions within the honeycomb plane, single crystal inelastic neutron scattering measurements were performed within the (H,K,0) scattering plane using the PUMA thermal triple-axis spectrometer.
Figure 4.4((c)-(e)) shows the single crystal inelastic neutron scattering data collected at the base temperature of 5K along different directions within the (H,K,0) plane (red arrows in Figure 4.4(b)). Figure 4.4(c) shows constant energy scans performed along the (0,k,0) direction

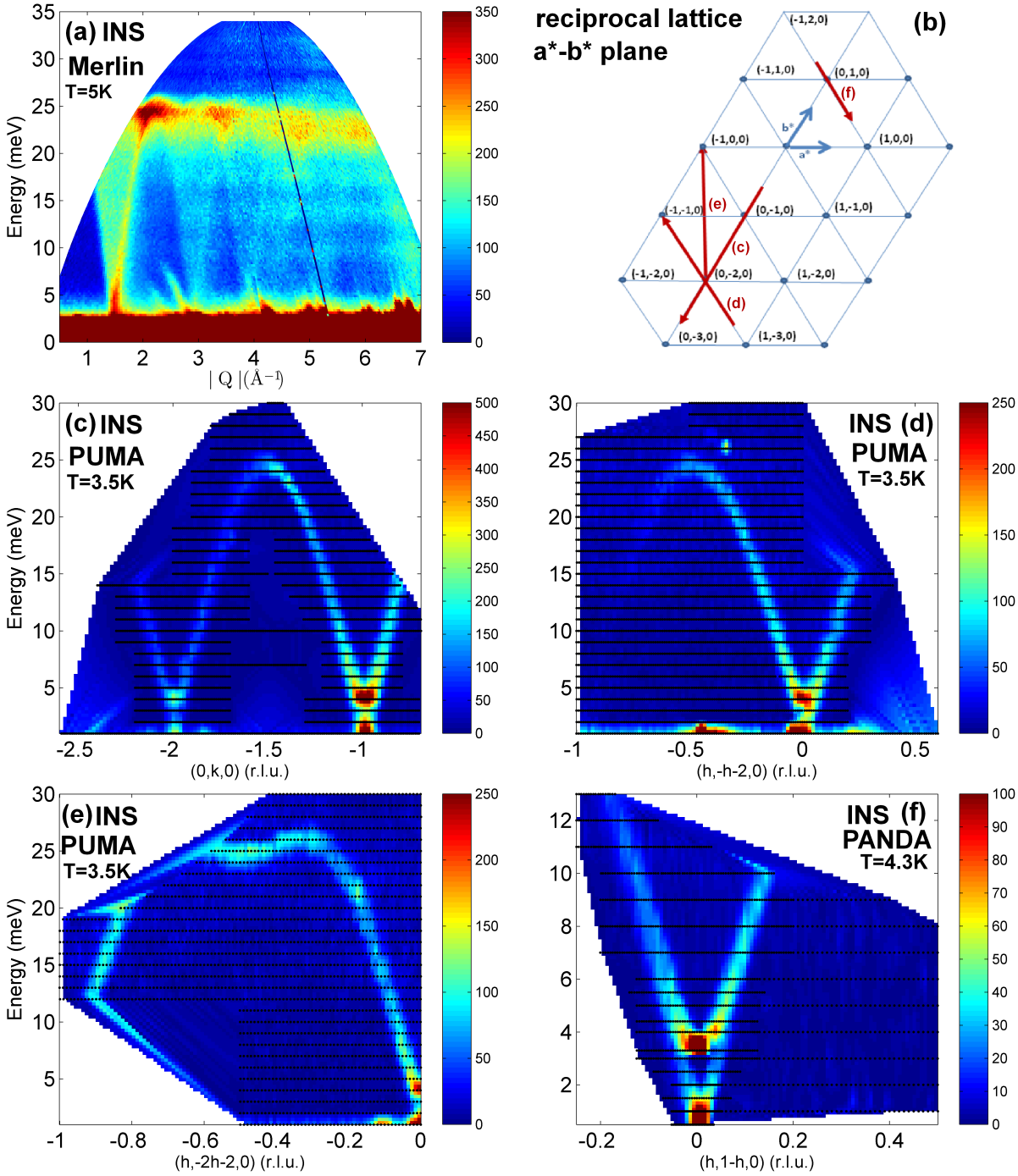

Figure 4.4: (a) INS data measured on a powder sample of $BaNi_2V_2O_8$ at 5K using an incident neutron energy of 35 meV and a Fermi chopper speed of 250 Hz. (b) Reciprocal space map of the honeycomb plane showing the measured scan directions. (c)-(e) Single crystal INS data of $BaNi_2V_2O_8$ measured on PUMA at T=3.5K along the directions (c) (0,k,0), (d) (h,-h-2,0) and (e) (h,-2h-2,0). (f) Single crystal INS data measured on PANDA at T=4.3K along the direction (h,1-h,0). All single crystal INS data were collected over (Q,ω) space whose area is notified on the figures by the black dotted lines. The features which appear out of this area (e.g.panel (e) the feature below E=12meV from h=-1 to h=-0.5) are artifact of the smoothing and should be ignored.

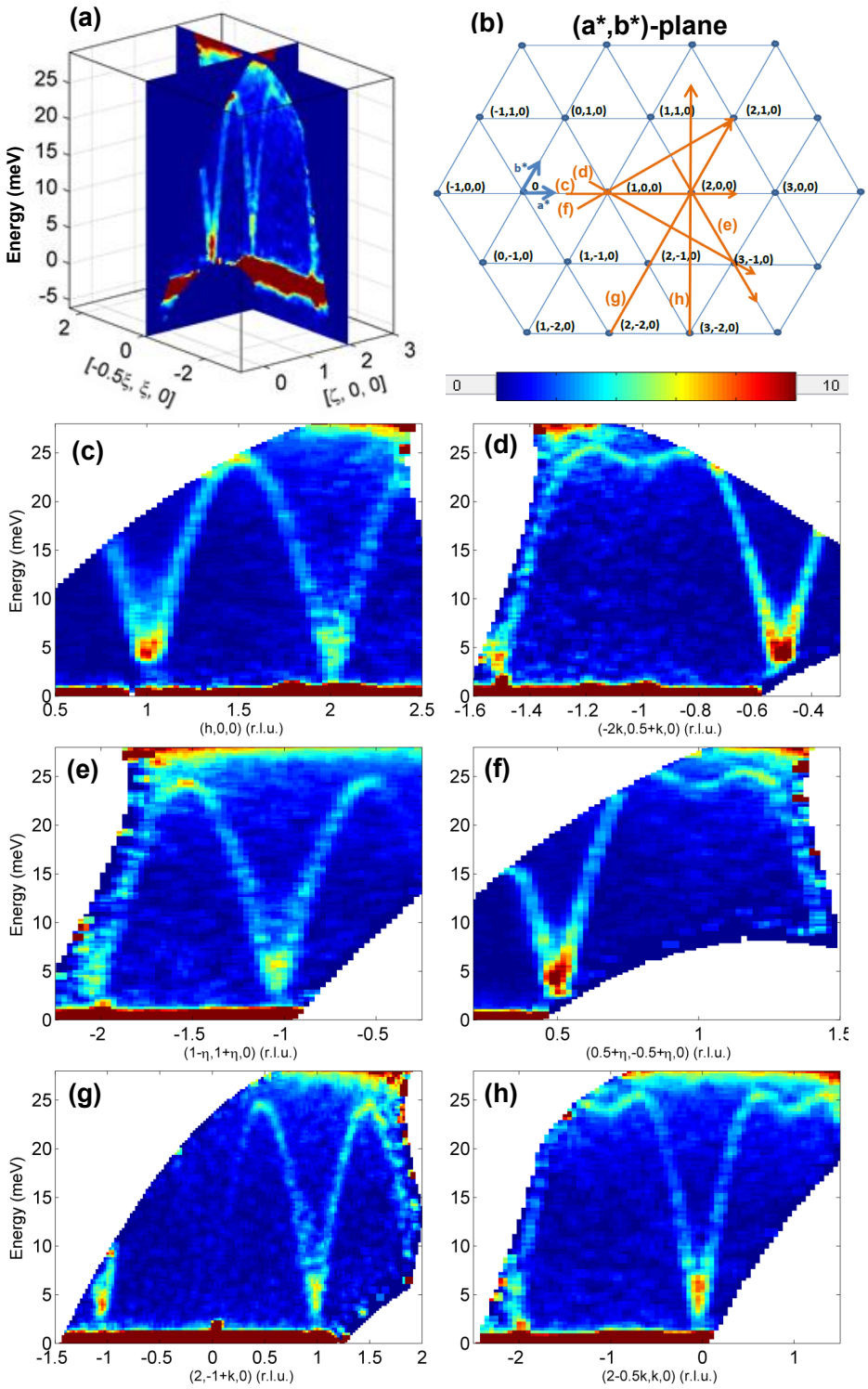

Figure 4.5: (a) The INS data set collected at the cold neutron multi-chopper spectrometer LET at T=5K and showing the dispersion as a function of energy and wavevector in the honeycomb plane and integrated along c*-axis (b) Reciprocal space map of the honeycomb plane displaying the directions of the slices through the LET data. (c)-(h) Slices through the LET data plotted as a function of energy transfer and wavevector along the directions (c) (h,0,0) (d) (-2k,0.5+k,0), (e) (1-η,1+η,0), (f) (0.5+η,0.5-η,0), (g) (2,-1+k,0), (h) (2-0.5k,k,0) in the (a*,b*)-plane and integrated over c*.

which reveal that the magnetic excitation spectrum of $BaNi_2V_2O_8$ consists of the two split spin-wave type modes. Both modes disperse out from the magnetic Bragg peak positions and are consistent with a honeycomb lattice. Figure 4.4(d) shows the INS data measured along the (h,-2-h,0) direction. The comparison of the INS data in Figure 4.4(c) and Figure 4.4(d) demonstrates that both modes disperse along the (0,k,0) and (h,-2-h,0) directions in the same way which suggests that the exchange interactions between the nearest neighbouring atoms are equivalent. Figure 4.4(e) shows that the dispersion along the (h,-2h-2,0) direction has a modulation in the high energy region.

To precisely explore the low-energy part of the magnetic excitation spectrum of $BaNi_2V_2O_8$, single crystal inelastic neutron scattering measurements were also carried out within the (H,K,0) scattering plane using the cold neutron PANDA spectrometer. High resolution constant energy scans were measured at 3.5K along the (h,1-h,0) direction over the energy range of 0 meV-13 meV with energy steps of 0.5 meV. The results are plotted in Fig. 4.4(f) and confirm that the modes are split by an energy gap of 3.5 meV which, as will be shown later, can be attributed to the XY anisotropy of the magnetic system.

To further verify the equivalence of the magnetic exchange interactions between the nearest neighbour atoms single crystal inelastic neutron scattering measurements were performed on the high-resolution cold neutrons multi-chopper spectrometer LET using the time-of-flight neutron scattering technique which allows to cover a large region of the reciprocal space. The principles of this technique were explained in Chapter 3.

Figure 4.5 (a) shows the data which are visualized using the Horace software package and plotted as a function of energy and wavevector transfer in the hexagonal plane. The data were integrated along the c*-axis over the scale from -3.5 (r.l.u.) to 3.5 (r.l.u.) assuming that there is no energy dispersion in this direction. Figure 4.5(b) illustrates the directions of the slices through the data in the reciprocal space. The slices through the LET data are presented in Fig. 4.5(c)-(h) and show the dispersion as a function of energy and wavevector along the (h,0,0), (1-η,1+η,0), (2,-1+k,0), (-2k,0.5+k,0),(0.5+η,-0.5+η,0) and (2-0.5k,k,0) directions, respectively (orange arows in Fig. 4.5(b)).

The comparison of the data collected at LET (Fig. 4.5(c)-(h)) with the data collected at PUMA (Fig.4.4(c)-(e)) and PANDA (Fig.4.4(f)) reveals that the magnetic excitation spectrum of $BaNi_2V_2O_8$ consists of spin-waves type modes which disperse along the crystallographically equivalent directions in the reciprocal lattice in the same way, implying the equivalence of the first-neighbour magnetic exchange coupling in all directions. The presence of the weak modulation on top of the dispersion along the (h,-2h-2,0), (-2k,0.5+k,0), (0.5+η,-0.5+η,0) and (2-0.5k,k,0) directions is a signature of a weak second-neighbour interaction which is also equivalent for the crystallographically equivalent directions.

4.4.3.2 Energy dispersion in the out-of-plane direction

To investigate the magnetic exchange interactions between the honeycombs layers, inelastic neutron scattering measurements were performed along the out-of-plane L direction using the high resolution cold neutron spectrometer PANDA.
Figure 4.6(a) shows the constant wave vector scans at (1,0,L) over the energy range of 0 meV-5 meV where L was fixed at values from 0 to 1 in step of 0.1. A strong elastic signal at $(1,0,\frac{1}{2})$ corresponds to the magnetic Bragg peak while the elastic signal at (1,0,1) is a nuclear one. The almost flat inelastic signals at $\approx$0.5 meV and $\approx$3.5 meV correspond to the two in plane spin-wave modes. It clearly reveals that the upper energy mode is dispersionless in the out-of-plane direction within experimental resolution. Although the low-energy mode also looks almost flat, it is difficult to judge unambiguously whether it is dispersionlessness or not because of the strong contamination from the elastic channel.
It is difficult to distinguish from the scans in Fig. 4.6(a) whether the low-energy mode is really gapped because of the strong contribution from the elastic signal. However, the individual constant wave vector scan at the (1,0,0) dispersion minimum reveals that both modes are gapped. Indeed, Figure 4.6(b)(black filled dots) presents a high resolution constant wavevector scan at the (1,0,0) dispersion minimum measured at a temperature of 1.5 K using the cold neutron TASP instrument, PSI, Zurich, Switzerland. The result clearly reveals that there are two modes with an energy gap of E_1=0.41 meV$\pm$0.03 meV and E_2=3.25$\pm$0.03 meV, respectively.
These accurate values of the energy gaps were extracted from the fit analysis using the RESCAL software which convolves the dispersion relation with the instrumental resolution function calculated for the instrument settings in this experiment (solid red line in Fig. 4.6(b)). Because the excitations in $BaNi_2V_2O_8$ disperse within the (H,K,0) plane and appear to be spin-waves, the energy dispersion based on the spin-wave calculations for the energy spectrum of the Heisenberg honeycomb-lattice antiferromagnet [50] was used with two energy gaps introduced artificially. The result of the fit analysis of the (1,0,0) energy scan is given by the solid red line in Figure 4.6(b) and provides a good agreement with the experimental INS data. The low-energy mode is found to be substantially broader than the instrumental resolution due to the presence of the several split modes as will be shown later in this Chapter. The higher energy mode is resolution limited. The fact that both modes are gapped suggests that the magnetic system has both in-plane and planar (XY) anisotropies.
To examine the dispersionlessness of the low excitation mode along the *c*-axis, a constant-wavevector scan at $(1,0,\frac{1}{2})$ was measured in order to compare it with the constant wavevector scan at (1,0,0). Indeed, if the low excitation mode dispersed along the *c*-axis, the position of the maximum in the constant-wavevector scans measured at different fixed wavevector transfers would be different. Figure 4.6(b)(black empty squares) shows the constant wavevector scan at (1,0,1/2) where the elastic contribution from the (1,0,1/2) magnetic Bragg

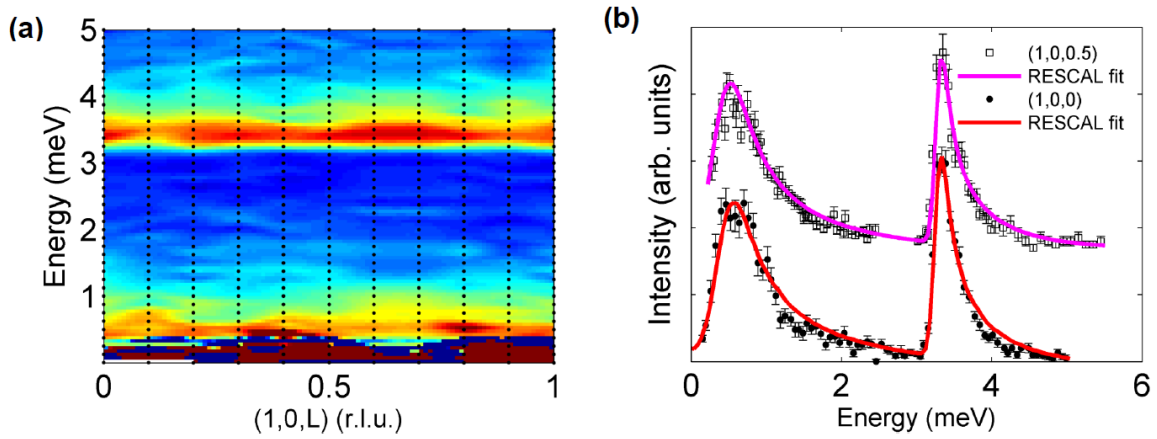

Figure 4.6: a) Single crystal INS data measured at T=3.5K using the PANDA spectrometer as a function of wavevector along the (1,0,L) direction and energy. b) The background- subtracted constant wavevector scans at the (1,0,0) and at Q(1,0,0.5) measured at T=1.5K using the TASP spectrometer, the two scans are shifted vertically with respect to each other for clarity, the colours lines give the fit analysis using the RESCAL software.

peak and the flat background were subtracted. The magenta line in Fig. 4.6(b) presents the fit analysis of the constant wave vector scan at (1,0,1/2). The peak positions were extracted to be E_1=0.38 meV$\pm$0.03 meV and E_2=3.25 meV$\pm$0.03 meV and are almost the same within the error as the peak postions of E_1=0.41 meV$\pm$0.03 meV and E_2=3.25 meV$\pm$0.03 meV observed in the energy scan at (1,0,0). The tiny energy shift of 0.03 meV in the position of the low-energy mode can be attributed either to resolution effects or to weak modulations due to the presence of an extremely small interplane coupling.
These results prove the dispersionlessness of both modes in the out-of-plane direction implying that the magnetic exchange interaction between the honeycomb layers is extremely weak despite the presence of the long-range magnetic order.

4.4.3.3 Anisotropy of the spin fluctuations

The presence of two modes at the in-plane antiferromagnetic zone centre which are gapped for all out-of-plane wavevectors implies the presence of an anisotropy in the magnetic interactions. Rogado et. al. [47] found that in the ordered states the spins order in the honeycomb plane suggesting that there is XY anisotropy in this magnetic system. Therefore, the two observed spin-wave excitation branches are expected to be caused by the spin fluctuations within the honeycomb plane perpendicular to the ordering direction and due to the fluctuations in the out-of-plane (c-axis) direction.
The intensities of the two modes at their gap energies can be used to verify the type of fluctuations and, therefore, the nature of the anisotropies in $BaNi_2V_2O_8$. Indeed, the magnetic neutron scattering cross-section strongly depends on the direction of the wavevector transfer

$\vec{Q}$ with respect to the spin $\vec{S}$ direction as was discussed in Chapter 2. Only the components of the $\vec{S}$ which are perpendicular to the $\vec{Q}$ will contribute to the scattering cross section. When the spins are in their ordered state, the neutron scattering cross section should be proportional to the relation [22]:

$$I \propto (1-\hat{q}_{\tilde{x}}^2)\cdot S^{\tilde{x}\tilde{x}}(Q,w) + (1-\hat{q}_{\tilde{y}\tilde{y}}^2)\cdot S^{\tilde{y}}(Q,w) + (1-\hat{q}_{\tilde{z}}^2)\cdot S^{\tilde{z}\tilde{z}}(Q,w) \tag{4.7}$$

Here, $\hat{q}$ is a unit vector in the direction of $\vec{Q}$ and $\hat{q}_{\tilde{x}}$, $\hat{q}_{\tilde{y}}$, $\hat{q}_{\tilde{z}}$ are its components within the local coordinate system $\tilde{x}$,$\tilde{y}$,$\tilde{z}$. The local axis are chosen so that $\tilde{x}||\hat{s}$, $\tilde{y} \perp \hat{s}$ and $\tilde{z}=\tilde{x}\times\tilde{y}$ where $\hat{s}$ is a unit vector along the ordering direction of the spins. The first term in equation 4.7 is responsible for the elastic magnetic signal, while the second and third terms give the intensity of the inelastic neutron scattering for the spin-fluctuations along the $\tilde{y}$ and $\tilde{z}$ directions which are perpendicular to the ordering direction of the spins. Therefore, the ratio of the scattering intensities of the modes due to the spin fluctuations along the $\tilde{y}$ and $\tilde{z}$ directions is proportional to the relation :

$$\frac{I_{\tilde{z}}}{I_{\tilde{y}}} \propto \frac{(1-\hat{q}_{\tilde{z}}^2)}{(1-\hat{q}_{\tilde{y}}^2)} \tag{4.8}$$

Here, $I_{\tilde{z}}$ and $I_{\tilde{y}}$ are the scattering intensities of the modes due to the spin-fluctuations along the $\tilde{y}$ and $\tilde{z}$ directions, respectively. If there are domains, the terms $\hat{q}_{\tilde{z}}^2$ and $\hat{q}_{\tilde{y}}^2$ should be averaged over the domains and replaced in eq. 4.8 by the terms $\langle\hat{q}_{\tilde{z}}^2\rangle$ and $\langle\hat{q}_{\tilde{y}}^2\rangle$ [51].
The equation 4.8 shows that the ratio of the intensities of the two modes should change as a function of the wavevector transfer when the components of the wavevector transfer perpendicular to their fluctuation directions change.
In $BaNi_2V_2O_8$ the spins in their ordered state lie within the honeycomb plane. There are three twins where the spins are rotated within the plane by 120 ° to each other. Therefore, for all twins the corresponding $\tilde{x},\tilde{y}$ axis lie within the honeycomb plane and the $\tilde{z}$-axis is parallel to the c-axis. The spin-wave fluctuations are caused by the displacements of the spins within the honeycomb plane along the $\tilde{y}$-axis perpendicular to the ordering direction ($\tilde{x}$-axis) and in out-of-plane direction along the c-axis ($\tilde{z}$-axis). Thus, the ratio of the scattering intensities of the modes due to the in-plane and out-of-plane spin fluctuations is proportional to the relation:

$$\frac{I_c}{I_{(a,b)}} \propto = \frac{(1-\langle\hat{q}_c^2\rangle)}{(1-\langle\hat{q}_{\tilde{y}}^2\rangle)} \tag{4.9}$$

Here, I_c and $I_{(a,b)}$ are the scattering intensity of the modes due to the spin-fluctuations along the c-axis and within the honeycomb plane, respectively. $\langle\hat{q}_{\tilde{c}}^2\rangle$ and $\langle\hat{q}_{\tilde{y}}^2\rangle$ are the squares of the component of the $\vec{q}$ along the c- and $\tilde{y}$-axes, respectively, averaged over all three twins.
Figure 4.7(a) shows the constant wavavector scans measured at (1,0,L) for the different values of L at 5K using the PANDA spectrometer. The intensity of the high-energy mode is found to

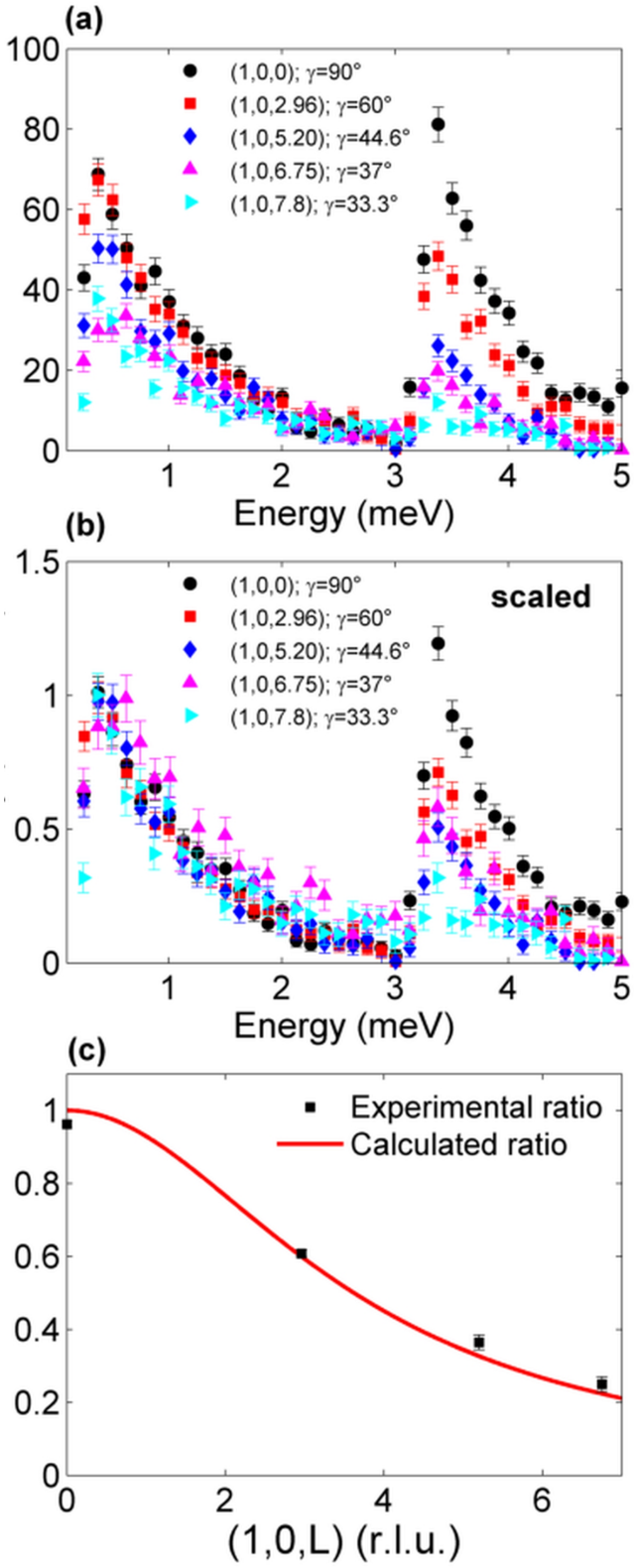

Figure 4.7: (a) Constant wavevector scans at (1,0,L) with values of L fixed at 0, 2.96 , 5.20, 6.75 and 7.8 measured at T=3.5K using the PANDA spectrometer and (b) normalized to the intensity of the first mode. (c) The ratio of the intensities of the higher energy mode to the lower energy mode plotted as a function of L. The solid red line gives the calculated ratio of the intensities using the equation 4.13.

depend strongly on the component of the wavevector transfer along the c-axis while the low-energy mode does not. Indeed, in the energy scan at (1,0,0), when the wavevector transfer lies entirely within honeycomb plane, both modes have approximately the same intensities. In contrast, in the energy scan at (1,0,7.8) when the wavevector transfer is mostly along the L direction, the high energy mode almost disappears.

To simplify the comparison of the intensity ratio of the higher to lower energy modes for different values L, the intensity of each individual energy scan was scaled to the amplitude of the corresponding lower energy mode (Fig. 4.7(b)). It is clear that this ratio is constantly decreasing as L increases from L=0 to L=7.8. The fact that the neutron scattering cross-section of the higher energy mode decreases as the wavevector transfer becomes increasingly parallel to the c-axis suggests that this mode is due to the fluctuation parallel to the c-axis. The lower energy mode has only a weak dependence on the component of wavevector transfer along the c-axis and, therefore, must be due to an in-plane fluctuation.

For the quantitative analysis of the observed directional dependence, the ratios of the intensities of the higher energy mode (I_{HM}) to the lower energy mode (I_{LM}) were extracted from the constant wavevector scans at (1,0,0), (1,0,2.96), (1,0,5.2) and (1,0,6.75) and plotted as a function of L (solid black squares in Figure 4.7(c)). The constant wave vector scan at (1,0,7.8) was not analysed because of the extremely weak intensity of the higher energy mode. Because in the constant wavevector scans with L=0, 2.96, 5.2 the two modes are well separated from each other and their intensities do not overlap, the integrated intensities of these modes were found as an area under the background-subtracted data. However, in the constant wavevector scan at (1,0,6.75) the low-energy mode is broad and clearly overlaps with the higher energy mode. To accurately distinguish the contribution of each mode, the constant wavevector scan at (1,0,6.75) was fitted using an asymmetric Gaussian function (see Chapter 7 for detailed description of this function) and the integrated intensities were extracted from the fit parameters.

The extracted directional dependence can be compared with the theory predictions using the relations (4.7)-(4.9). The magnetic structure of $BaNi_2V_2O_8$ suggests the presence of three twins with spins rotated in the plane by 120° with respect to each other. Figure 4.8(a) shows the honeycomb plane of $BaNi_2V_2O_8$ where all three twins are plotted together with the corresponding local coordinate systems $\tilde{x}_n, \tilde{y}_n, \tilde{z}_n$. Each local coordinate system $\tilde{x}_n, \tilde{y}_n, \tilde{z}_n$ was constructed for every twin where $\tilde{x}_n || \vec{s_n}$, $\tilde{y}_n \perp \vec{s_n}$, $\tilde{z}_n || c$-axis corresponds to the twin.

Because for all twins $\tilde{z}_n$ is parallel to the c-axis, $\hat{q}_{\tilde{z}_1}=\hat{q}_{\tilde{z}_2}=\hat{q}_{\tilde{z}_3}=\hat{q}_c$ where $\hat{q}_c$ is the projection of the unit wavevector $\hat{q}$ on the c-axis (see Fig. 4.8(b)):

$$\begin{aligned} \hat{q}_c &= cos(\gamma) \\ \langle \hat{q}_c^2 \rangle &= cos^2(\gamma) \end{aligned} \tag{4.10}$$

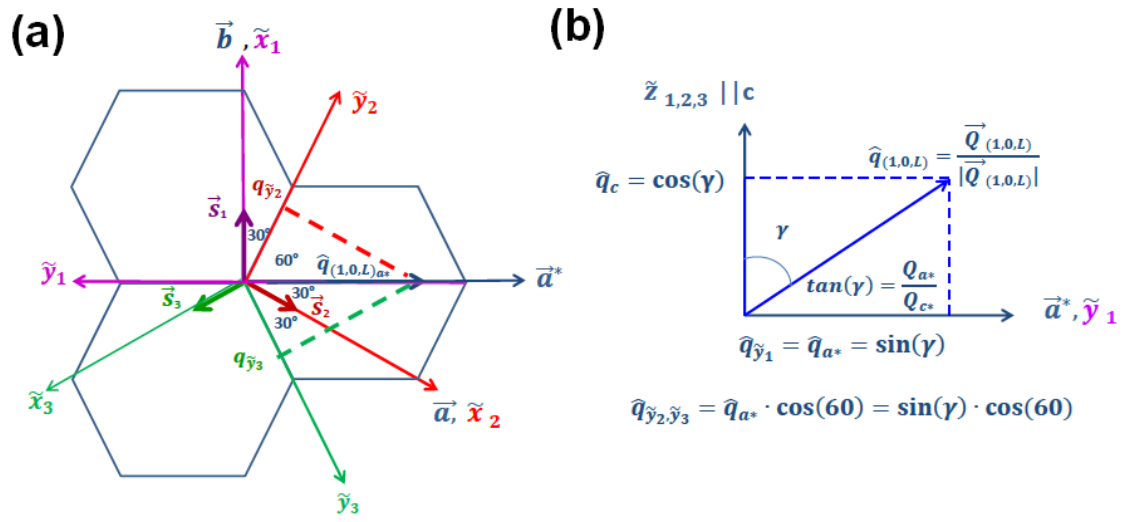

.

Figure 4.8: a) A sketch of the magnetic structure of $BaNi_2V_2O_8$ within the honeycomb plane with the projection of the wavevector transfer on the (a*b*)-plane. b)A sketch of the scattering (a*c*)-plane with the wavevector transfer $\vec{Q}$

Here, γ is the angle between the wavector transfer $\vec{Q}$ and the c-axis which is $\gamma = atan(\frac{Q_{a^*}}{Q_{c^*}})$ where $Q_{a^*}=\frac{2\pi \cdot h}{a \cdot cos(30)}$ and $Q_{c^*}=\frac{2\pi \cdot l}{c}$.
The projection of $\hat{q}$ on the $\tilde{y}_n$-axis can be found for each twin using the relation:

$$\hat{q}_{\tilde{y}_n} = \hat{q}_{a^*} \cdot cos(\beta) = sin(\gamma) \cdot cos(\beta_n) \tag{4.11}$$

Here, β_n is the angle between the a^*-axis and $\tilde{y}_n$-axis for twin N. As shown in Fig. 4.8(a) β_1=180°, β_2=β_3=60° in the first, second and third twins, respectively. Therefore:

$$\begin{aligned} \hat{q}_{\tilde{y}_1} &= -sin(\gamma) \\ \hat{q}_{\tilde{y}_2} &= \hat{q}_{\tilde{y}_3} = sin(\gamma) \cdot cos(60) \\ \langle \hat{q}^2_{\tilde{y}} \rangle &= \frac{1}{3} \cdot sin^2(\gamma) + \frac{2}{3} \cdot sin^2(\gamma) \cdot cos^2(60) \end{aligned} \tag{4.12}$$

The ratio of the intensity of the mode due to the out-of-plane spin fluctuations to the intensity of the mode due to in-plane spin fluctuations averaged over all twins can be obtained by the substitution of the equations (4.10) and (4.12) to (4.9):

$$\frac{I_c}{I_{(a,b)}} \propto \frac{(1 - cos^2(\gamma))}{(1 - (\frac{1}{3} \cdot sin^2(\gamma) + \frac{2}{3} \cdot sin^2(\gamma) \cdot cos^2(60)))} \tag{4.13}$$

The solid red line in Fig. 4.7(c) shows the ratios of the intensities calculated using the equation 4.13 and the relation tanγ=$\frac{Q_a^*}{Q_c^*}$ where $Q_{a^*} = \frac{2\pi h}{a \cdot cos(30)}$ and $Q_{a^*} = \frac{2\pi l}{c}$ and plotted as a

function of L where L varies from 0 to 7. The calculated results were scaled to the data to simplify the comparison with the experimental results. The calculated ratios decrease as L increases from L=0 to L=7 as the angle γ between the wavevector transfer and c-direction decreases from 90° to 37° which is in perfect agreement with the directional dependence observed experimentally.
These results confirm that the higher energy mode is caused by spin fluctuations along the c-axis while the lower energy mode is due to the fluctuations within the honeycomb plane.
The excitations fluctuating along the *c*-axis are gapped because the XY anisotropy makes it energetically unfavourable for spins to have a component along the *c* direction. The excitations fluctuating in the (ab)-plane, however, are expected to be gapless because all directions in this plane are equally favourable. The presence of a gap for the in-plane excitations suggests the presence of an additional in-plane anisotropy. This would be a weak Ising anisotropy which establishes the spin ordering direction and creates an energy cost for fluctuations within the plane but perpendicular to this direction giving rise to a gap in this excitation branch.

4.4.3.4 Hamiltonian of $BaNi_2V_2O_8$

To determine the values of the magnetic exchange interactions and estimate the anisotropy in $BaNi_2V_2O_8$, the spin-wave spectrum of the compound was simulated using the SpinW Matlab Library [52] which is based on linear spin-wave theory and can perform numerical calculations of the spin wave energies and intensities for complex magnetic lattices with commensurate or incommensurate magnetic order. The simulations were performed for the Hamiltonian of $BaNi_2V_2O_8$:

$$H = \sum_{i>j} J_n \cdot \boldsymbol{S_i} \cdot \boldsymbol{S_j} + \sum_{i>j} J_{nn} \cdot \boldsymbol{S_i} \cdot \boldsymbol{S_j} + \sum_{i>j} J_{nnn} \cdot \boldsymbol{S_i} \cdot \boldsymbol{S_j} + \sum_{i>j} J_{out} \cdot \boldsymbol{S_i} \cdot \boldsymbol{S_j} + \\ + \sum_{i>j} D_{XY} \cdot S_i^{c^2} + \sum_{i>j} D_{inplane} \cdot S_i^{x^2} \tag{4.14}$$

Here, J_n, J_{nn} and J_{nnn} are the nearest, next-nearest and third-neighbour isotropic Heisenberg intraplane magnetic exchange interactions, respectively. J_{out} is the Heisenberg interplane magnetic exchange coupling. The two last terms D_{XY} and $D_{inplane}$ describe the hard-axis (easy-plane) and easy-axis single ion anisotropies of the Ni^{2+} magnetic ions, respectively. In this Hamiltonian a positive sign of the magnetic exchange interaction corresponds to antiferromagnetic coupling. A hard-axis (easy-plane) single-ion anisotropy is defined by a positive value while an easy-axis single-ion anisotropy is negative. The easy-plane anisotropy D_{XY}, is assumed to be perpendicular to the c-axis, while the easy-axis anisotropy $D_{inplane}$ is within the honeycomb plane. The magnetic exchange interactions in the Hamiltonian (eq. 4.14) are counted once in contrast to the Hamiltonian (eq. 4.1). Therefore, J_n=2·J_1 if J_1 is the nearest

neighbour magnetic exchange interaction in the Hamiltonian (4.1).
The ordering wave vector, spin directions and magnetic structure of $BaNi_2V_2O_8$ are known from previous powder neutron diffraction measurements [47] and were input into the SpinW calculation as fixed parameters. Particularly, the directions of the spins were fixed to point antiferromagnetically along the directions $\vec{S}_1$(1,0,0), $\vec{S}_2$(0,1,0), and $\vec{S}_3$(-1,1,0) for the first, second and third twins, respectively.
Figure 4.9(a) shows a sketch of the magnetic structure of $BaNi_2V_2O_8$ (twin 1) within the honeycomb plane where the solid violet, green and brown lines represent the J_n, J_{nn} and J_{nnn} magnetic exchange paths, respectively. This magnetic structure suggests that the first- and third-neighbour magnetic exchange interactions are antiferromagnetic while the second-neighbour interaction is ferromagnetic. However, this is not always the case because if an interaction is weak, its sign can be reversed without changing the magnetic structure. Therefore, if J_n is the strongest interaction, a weakly antiferromagnetic J_{nn} and/or a weakly ferromagnetic J_{nnn} are possible. Thus, the signs of the exchange parameters proposed by the magnetic structure of $BaNi_2V_2O_8$ were set as initial values which then were varied during the fit analysis.
The magnetic long-range order observed in $BaNi_2V_2O_8$ at temperatures below T_N implies that the Hamiltonian of this system has an interplane magnetic exchange coupling J_{out}. Figure 4.9(b) shows the sketch of the magnetic structure of $BaNi_2V_2O_8$ (twin 1) within a single unit cell. There are several magnetic exchange paths J_{out1} (solid orange line), J_{out2} (solid cyan line) and J_{out3} (solid blue line) which alone or in combination can be responsible for the interplane magnetic coupling. According to the magnetic structure of $BaNi_2V_2O_8$, the magnetic exchange path J_{out1} is realized between the magnetic ions whose spins are pointing in the same direction while J_{out2} and J_{out3} are between the magnetic ions whose spins are ordered antiferromagnetically.
The red flattened ellipsoids centred at the magnetic ions in Figure 4.9 (a)-(b) represent the planar anisotropy of the system. The semi-principal axis of these ellipsoids is along the spin ordering direction representing a weak easy-axis anisotropy.
The spin-wave magnetic excitation spectra within the plane and the out-of-plane directions were then simulated iteratively for various values of J_n, J_{nn}, J_{nnn} ,J_{out}, D_{XY}, $D_{inplane}$. The simulations were performed for every twin and the results were averaged over the twins assuming that these twins have equal weight. The parameters J_n, J_{nn}, J_{nnn} were found to be strongly coupled which means that the range of the solutions of each of these parameters depends strongly on the values of the other two parameters.
To extract the whole range of the possible solutions, the parameters J_n, J_{nn}, J_{nnn} were varied manually taking into account their strong coupling. In particular, the first neighbor interaction J_n was changed within the range from 5.8 meV to 13.3 meV with a step of 0.3 meV and for each fixed value of J_n the ranges of the solutions for J_{nn} and J_{nnn} where extracted. The agreement of all exctracted solutions with the experimental data was checked

by a comparison of the spin-wave modes calculated using the spin-wave theory (solid red line over the data on Fig. 4.10 (b)-(c)) with the dispersion within the honeycomb plane observed experimentally.

Although a good agreement of the simulated energy dispersions within the honeycomb plane with the experimental data was achieved for a wide range of parameters J_n, J_{nn}, J_{nnn}, the constraint for the total value of the in-plane magnetic exchange coupling J_{total} extracted from the analysis of the Curie-Weiss temperature (section 4.4.3.4) restricts the continuum of the solutions as discussed below. The constraint J_{total}=J_1+ 2J_2+J_3=7.5meV±1.0meV extracted in section 4.4.3.4 assumes a double counting of the magnetic exchange constants in the Hamiltonian and, therefore, should be multiplied by factor of 2 for the Hamiltonian where the magnetic exchange interactions are counted once. Thus, the constraint for the total value of the nearest neighbours magnetic exchange interactions J_n, J_{nn} and J_{nnn} in the Hamiltonian (eq. 4.14) is:

$$J_n + 2J_{nn} + J_{nnn} = 2 \cdot (J_1 + 2J_2 + J_3) \approx 15meV \pm 2meV \tag{4.15}$$

The extracted solutions reveal that the nearest-neighbour magnetic exchange interaction J_n is the dominant one and takes values in the range of 11.3 meV$\leqslant J_n \leqslant$13.35 meV. The positive sign of J_n suggests that J_n is antiferromagnetic which is in agreement with the spin correlations proposed by the magnetic structure.

The second-neighbour magnetic exchange interaction J_{nn} is found to be the second strongest interaction and lies in the range of 0.85 meV$\leqslant J_{nn} \leqslant$1.5 meV which is approximately ten times weaker than the dominant J_n magnetic exchange interaction. The presence of J_{nn} in the Hamiltonian is obligatory to reproduce the weak modulation on top of the energy dispersion along the (h,-2h-2,0) direction which was observed experimentally (Fig. 4.4(e)). Although the magnetic structure of $BaNi_2V_2O_8$ suggests that the spins of the second neighbouring magnetic ions are pointing in the same direction (Fig.4.9(a)), the second neighbour interaction is found to be antiferromagnetic implying a weak frustration of the magnetic system.

A third-neighbour interaction J_{nnn} is not found to be necessary to reproduce the experimental data. However, J_{nnn} was introduced to the Hamiltonian (eq. 4.14) to estimate the order of magnitude of possible longer-range interactions and their effect on the solutions of the first and second neighbour interactions J_n and J_{nn}, respectively. It was found that the third-neighbour interaction can be either ferromagnetic or antiferromagnetic. Antiferromagnetic J_{nnn} cannot exceed 0.4 meV. It slightly improves the agreement of the simulations with the experimental data but it is not necessary to reproduce the experimental data. AFM J_{nnn} increases the range of the solutions of J_n and J_{nn}. In particularly, in the presence of J_{nnn}, J_n varies within the range 10.9meV$\leqslant J_n \leqslant$13.35meV and J_{nn} lies within the range of 0.85 meV$\leqslant$

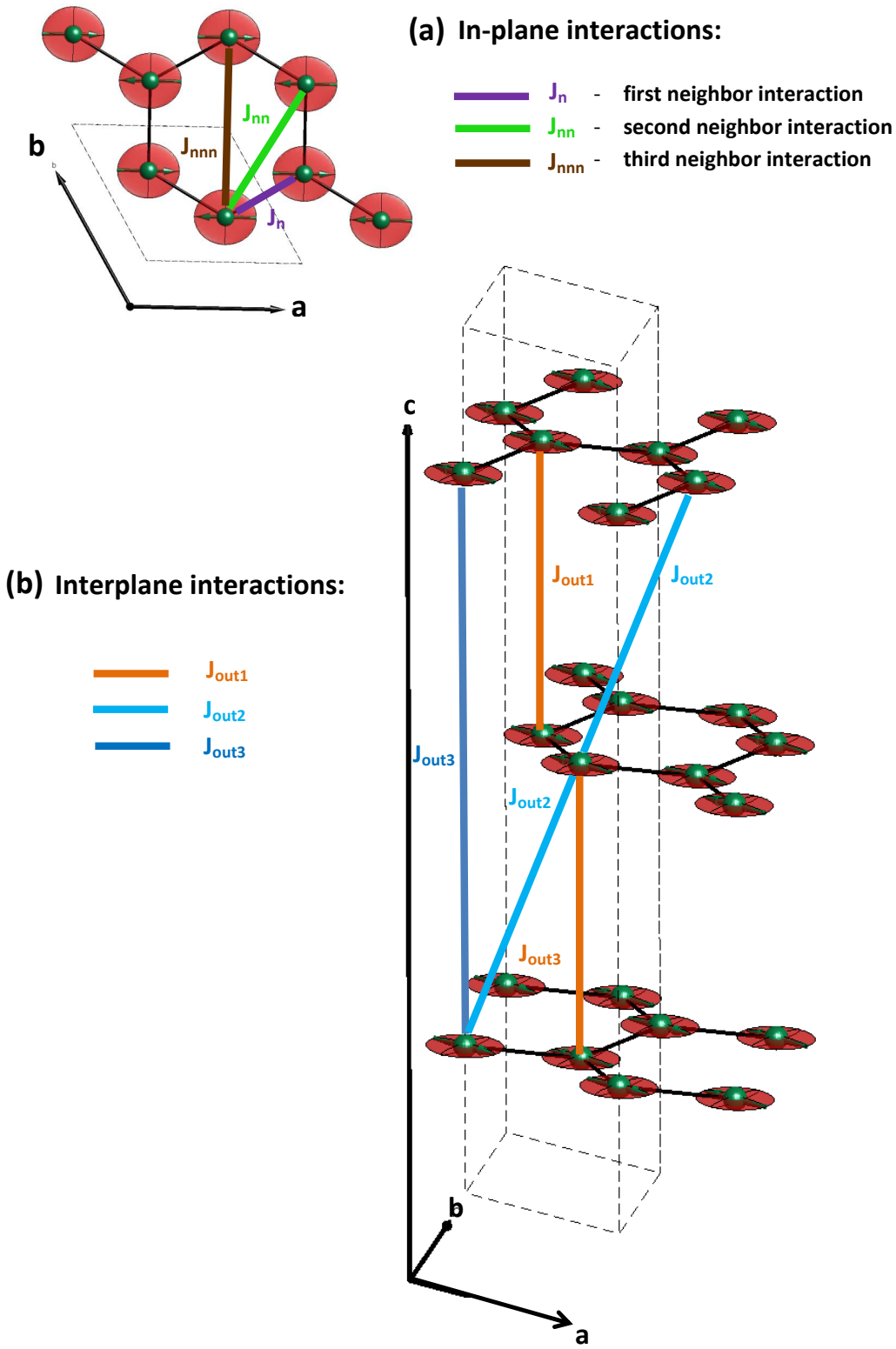

Figure 4.9: (a) Sketch of the magnetic structure of $BaNi_2V_2O_8$ within the honeycomb plane showing only the magnetic Ni^{2+} ions and inequivalent magnetic exchange paths between them. The Ni^{2+} ions are represented by green spheres while the green arrows indicate the spin directions in the ordered state. The red disks represent the easy-plane anisotropy D_{XY}. The solid violet, green and brown lines represent the first-, second- and third-neighbour magnetic exchange coupling. (b) Single unit cell of $BaNi_2V_2O_8$ where the possible interplane magnetic exchange paths are presented. Only inequivalent magnetic exchange paths are plotted to simplify a plot.

J_{nn} $\leqslant$1.65 meV. The absolute value of a FM $|J_{nnn}|$ cannot exceed 0.1 meV otherwise it reduces the agreement of the simulation with the experimental data. Indeed, the modulation on top of the dispersion along the (h,-2h-2,0) direction becomes too sharp for FM $|J_{nnn}|\geqslant$0.1 meV.

The parameters $D_{inplane}$ and D_{XY} which are responsible for the easy-axis and easy-plane anisotropies, respectively, are required in the Hamiltonian (eq. 4.14) to reproduce the energy gaps at E_1=0.41 meV$\pm$0.03 meV and E_2=3.25 meV$\pm$0.03 meV observed experimentally in the high resolution constant-wavevector scans at the dispersion minima (1,0,0) (Fig. 4.6(b)). The value of the D_{XY} parameter is found to be D_{XY}=0.0695 meV$\pm$0.0015 meV. This value was extracted from the size of the high-energy gap at E_2=3.25 meV$\pm$0.03 meV using the fact that the higher energy mode is due to out-of-plane spin fluctuations.

The value of the $D_{inplane}$ parameter equals $D_{inplane}$=-0.00090 meV$\pm$0.00015 meV. It was found from the size of the lower energy gap at E_1=0.41 meV$\pm$0.03 meV because lower energy mode was found to be caused by the in-plane spin fluctuations.

An upper limit for the interplane coupling J_{out} was extracted from the conditions (i) the upper mode is dispersionless in the out-of-plane direction (within the resolution error) and (ii) the energy shift of the lower mode at (1 0 0) with respect to $(1, 0, \frac{1}{2})$ does not exceed the experimentally observed value of 0.03 meV.

The magnetic exchange path J_{out1} corresponds to the shortest distance between the two honeycomb layers and is realized between the magnetic ions whose spins are pointing in the same direction (Fig. 4.9(b) orange line). The simulations of the magnetic excitation spectrum reveal that J_{out1} is ferromagnetic and give a dispersion in the out-of-plane direction which has a minimum at (1,0,0) and maximum at (1,0,1). The absolute value of J_{out1} should not exceed $|J_{out1}|\leqslant$0.00045 meV in order to satisfy the conditions (i)-(ii).

The magnetic exchange path J_{out2} corresponds to the second shortest distance between the honeycomb planes and is realized between the two magnetic ions whose spins are pointing in the opposite directions (Fig. 4.9(b) cyan line). J_{out2} is found to be antiferromagnetic in agreement with the magnetic structure of $BaNi_2V_2O_8$. The simulations of the magnetic excitation spectrum reveal that AFM J_{out2} produces a dispersion in the out-of-plane direction which has a minimum at (1,0,0) and maximum at (1,0,1), similar to the FM J_{out1}. However, the dispersion caused by the AFM J_{out2} is found to have a wider bandwidth than the dispersion caused by the FM J_{out1}. This is because there are six J_{out2} magnetic exchange paths per Ni^{2+} magnetic ion in contrast to a single J_{out1} path. As result, the AFM J_{out2} should be much weaker in absolute value than FM J_{out1} to satisfy the conditions (i)-(ii). Indeed, the absolute value of AFM J_{out2} which satisfies the conditions (i)-(ii) is found to be less than J_{out2} $\leqslant$0.00005 meV which is nine times weaker than the estimated value of J_{out1}. Although a single J_{out2} is weak and unlikely to be sufficient to induce long-range order in $BaNi_2V_2O_8$ observed at 50K [47], the six J_{out2} magnetic exchange paths provide an effective magnetic exchange interaction of $6J_{out2}$=0.0003 meV per magnetic ion which is comparable to the J_{out1}

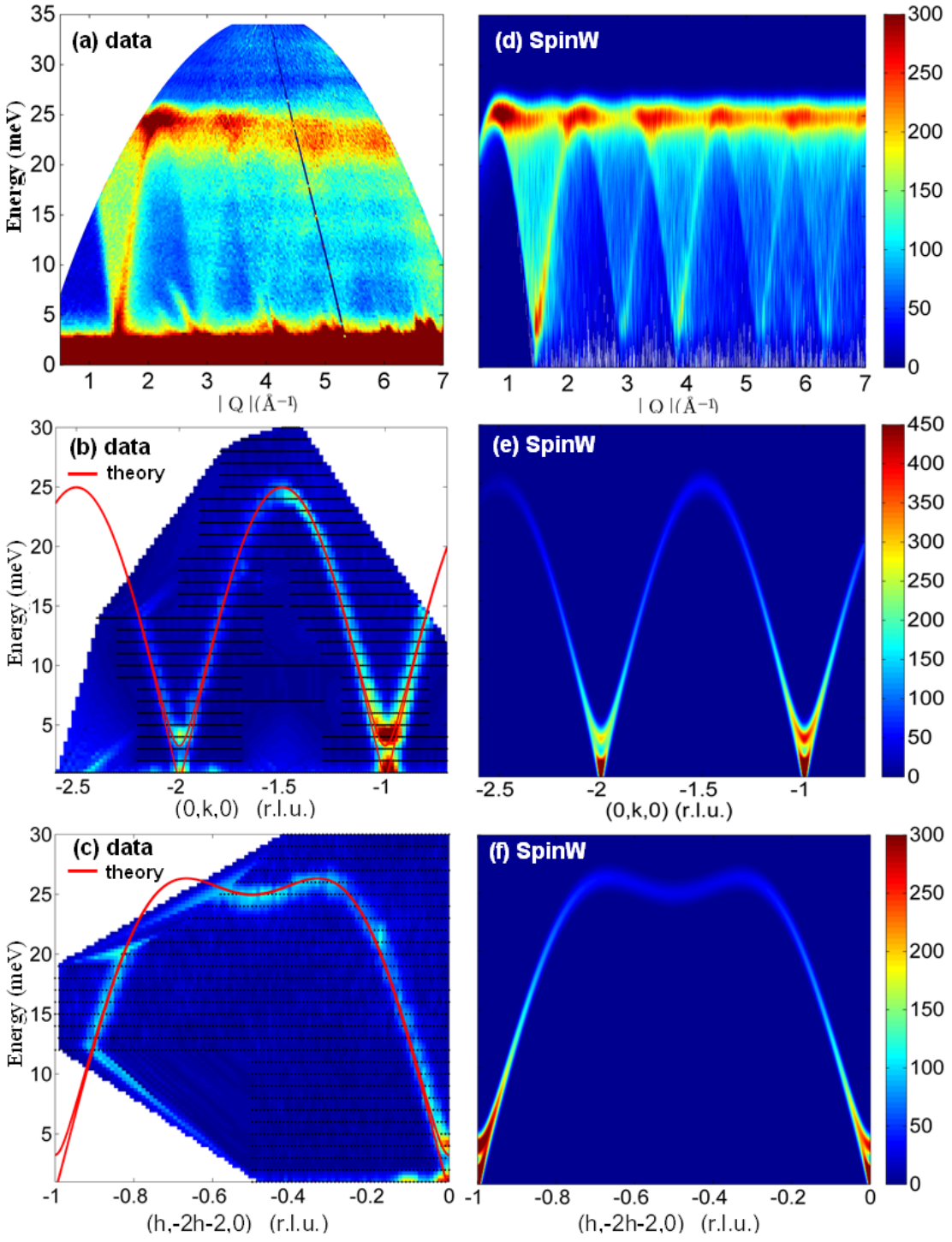

Figure 4.10: (a) INS data measured on a powder sample of $BaNi_2V_2O_8$ at 5K on the Merlin spectrometer using an incident neutron energy of 35 meV and a Fermi chopper speed of 250 Hz. (b)-(c) Single crystal INS data of $BaNi_2V_2O_8$ measured on the PUMA spectrometer at T=3.5K along the directions (b) (0,k,0) and (c) (h,-2h-2,0). All single crystal INS data were collected over (Q,ω) space whose area is notified on the figures by the black dotted lines. The features which appear out of this area are artifact of the smoothing and should be ignored. (d) Spin-Wave simulations of the powder magnetic excitation spectrum of $BaNi_2V_2O_8$. (e)-(f) Spin-Wave simulations of the single crystal magnetic excitation spectrum of $BaNi_2V_2O_8$ along the directions (e) (0,k,0) and (f) (h,-2h-2,0). The calculated spin-wave modes are represented by the solid red lines through the data on (b)-(c). All simulations were performed for the Hamiltonian (eq. 4.14) with the parameters of J_n=12.3 meV ,J_{nn}=1.25 meV, J_{nnn}=0.2 meV, J_{out}=-0.00045 meV D_{XY}=0.0695 meV, $D_{inplane}$=-0.0009 meV.

magnetic exchange path. Therefore, each of these paths can contribute to develop long-range order. However, simulations based on the J_{out2} path provide an energy dispersion whose bandwidth is wider than was experimentally observed. Thus, J_{out1} is more likely realized in $BaNi_2V_2O_8$ rather than J_{out1}.

Because nearest neighbour honeycomb layers are shifted with respect to each other, the first and third planes can interact via the exchange path J_{out3} (Fig. 4.9(b) blue line). This path corresponds to the shortest distance between the first and third honeycomb planes in the unit cell of $BaNi_2V_2O_8$ and is realized between the magnetic ions whose spins are aligned antiferromagnetically with respect to each other. The SpinW simulations confirm that J_{out3} is AFM and reveal that J_{out3} produces a dispersion along the c-axis which has a maximum at (1,0,0) and a minimum at (1,0,1) in contrast to the J_{out1} and J_{out2}. It was also found that this dispersion has the same energy values at (1,0,0) and (1,0,0.5) for any values of J_{out3} and a lower energy mode is almost flat if J_{out3} does not exceed the value $J_{out3} \leqslant 0.0012$ meV. Although J_{out3} is found to be the strongest interaction which can satisfy the conditions (i)-(ii), the large distance d=14.8Å between the corresponding magnetic ions reduces the probability of the presence of J_{out3}.

Figure 4.10((a),(b),(c)) shows the powder and single crystal inelastic neutron scattering data of $BaNi_2V_2O_8$. The solid red lines over the data on panels (b) and (c) represent the spin-wave modes calculated for the Hamiltonian (eq. 4.14) using the medium solutions of the fitted parameters J_n=12.3 meV ,J_{nn}=1.25 meV, J_{nnn}=0.2 meV, J_{out1}=-0.00045 meV D_{XY}=0.0695 meV, $D_{inplane}$=-0.0009 meV and reproduce the energy dispersion observed experimentally well. Fig.4.10((d),(e),(f)) shows the simulations of the convoluted magnetic excitation spectra which correspond to the calculated spin-wave modes. The simulations show a perfect agreement with the experimental data. Indeed, the magnetic excitations in the simulated powder spectra (Fig. 4.10(d)) extend up to 26 meV and display the typical V-shaped cones of the magnon dispersions with the first minimum at $|Q|=1.45Å^{-1} \pm 0.05Å^{-1}$ completely matching the experimental data (Fig. 4.10(a)). The simulated dispersions within the (H,K,0) scattering plane (Fig. 4.10(e),(f)) are also consistent with the data (Fig.4.10(b),(c)), respectively. In particular, the intensity modulations of the simulated modes are in excellent agreement with the modulation due to the magnetic structure factor observed in the experimental spectra.

Figure 4.11(a,b,c) shows the single crystal INS data of $BaNi_2V_2O_8$ measured along the (1,0,L) direction together with the theoretical neutron scattering cross section and the spin-wave energy dispersion calculated using the linear spin wave theory where J_{out} equals to J_{out1}=-0.00045 meV. The simulated magnetic excitation spectrum is in good agreement with the experimental data confirming the relevance of the Hamiltonian (eq. 4.14). The calculated spin-wave dispersion reveals that the lower energy band consists of several spin-wave modes in contrast to the higher energy band which has only one mode. This result explains why the lower energy peak in the constant energy scan at (1,0,0) was found to be substantially broader than the instrumental resolution while the higher energy peak was resolution limited.

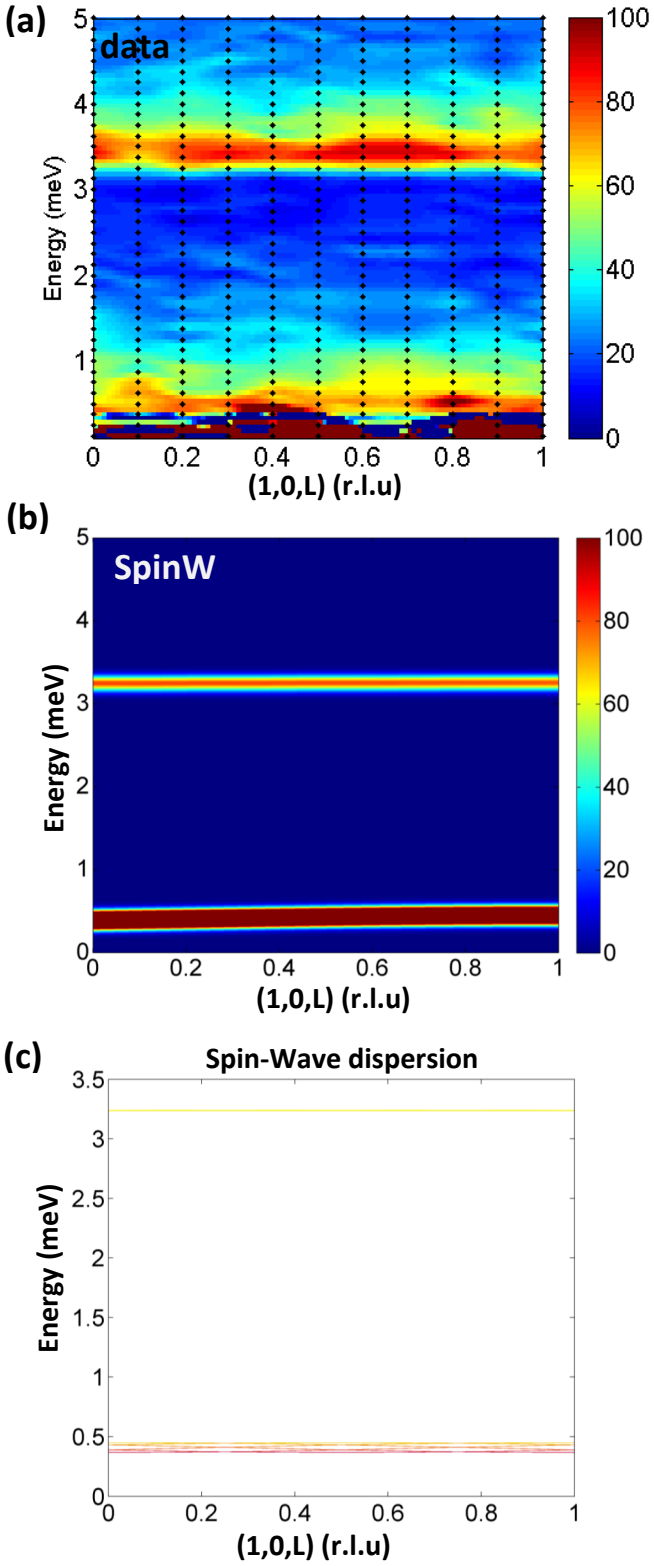

Figure 4.11: (a) Single crystal INS data of $BaNi_2V_2O_8$ measured at T=4.3K at the PANDA spectrometer along the (1,0,L) direction. (b) Theoretical inelastic neutron scattering cross section and (c) the spin wave dispersion simulated along the (1,0,L) direction using the SpinW library for the Hamiltonian (eq. 4.14) with the parameters of J_n=12.3 meV ,J_{nn}=1.25 meV, J_{nnn}=0.2 meV, J_{out}=-0.00045 meV D_{XY}=0.0695 meV, $D_{inplane}$=-0.0009 meV

4.4.4 Discussion

The magnetic excitation spectra of powder and signal crystal samples of $BaNi_2V_2O_8$ were investigated using inelastic neutron scattering techniques. The results reveal that the magnetic excitation spectrum consists of the two spin-wave excitation branches with different gap sizes which are dispersing out of the magnetic Bragg peak position within the honeycomb plane and are almost dispersionless (within the resolution) along the out-of-plane direction suggesting that the interplane magnetic exchange interaction is very small.
The presence of the two excitation branches implies the presence of anisotropy in the magnetic system which is in agreement with the magnetic structure of $BaNi_2V_2O_8$ proposed in the literature [47]. Indeed, powder neutron diffraction measurements of $BaNi_2V_2O_8$ reveal that the spins lie almost within the honeycomb plane suggesting the presence of an XY anisotropy in $BaNi_2V_2O_8$.
The high resolution energy scans at the dispersion minimum at (1,0,0) reveal that both modes are gapped and have a gap energy of E_1=0.41 meV$\pm$0.03 meV and E_2=3.25 meV$\pm$0.03 meV, respectively. These values are in qualitative agreement with the values E_1=0.2 meV and E_2=3 meV which were briefly mentioned in the paper by Knafo et. al. [53]. However, in this paper the data is not shown and there are no details of the related experiments and analysis, thus, it is difficult to compare their results.
The analysis of the relative intensities of these modes as a function of the component of the wavevector transfer along the c*-axis reveals that the lower energy mode is caused by spin fluctuations within the honeycomb plane while the higher energy mode is due to spin-fluctuations along the c-axis. The fact that the higher energy mode is due to the spin-fluctuations in the out-of-plane direction confirms the presence of sizeable XY anisotropy which makes these fluctuations energetically more costly to excite.
Although all directions within the (ab)-plane seem to be equivalent, the energy gap of the lower mode caused by the in-plane spin fluctuations implies the presence of a weak in-plane Ising-like anisotropy. The presence of this Ising-type anisotropy is in agreement with the proposed magnetic structure of $BaNi_2V_2O_8$ which suggests that the spins are pointing along one of the three equivalent hexagonal axis within the honeycomb plane [47].
The values of the magnetic exchange interactions and anisotropies were extracted by performing simulations of the powder and single crystal magnetic excitation spectra of $BaNi_2V_2O_8$ within the linear spin-wave theory approach which allows the Hamiltonian of the magnetic system to be solved. Both powder and single crystal inelastic neutron scattering data were reproduced well using the Heisenberg Hamiltonian with in-plane and planar single-ion anisotropies (eq. 4.14). The best agreement of the simulations with the experimental data was achieved when the parameters of the magnetic exchange interactions J_n, J_{nn}, J_{nnn} and the parameters of the in-plane $D_{inplane}$ and planar D_{XY} single-ion anisotropies lie within the range: 10.9 meV$\leqslant J_n \leqslant$13.35 meV, 0.85 meV$\leqslant J_{nn} \leqslant$1.65 meV, -0.1 meV$\leqslant J_{nnn} \leqslant$0.4 meV

D_{XY}=0.0695meV±0.0015 meV, $D_{inplane}$= -0.00090 meV ±0.00015 meV.
The extracted value of the first neighbour magnetic exchange interaction J_n agrees well with the value of the first-neighbour magnetic exchange interaction J_1=6.325 meV±0.525 meV estimated from the fit analysis of the single crystal magnetic susceptibility data of $BaNi_2V_2O_8$ using the high-temperature series expansion for the honeycomb crystal lattice. Indeed, taking into account the relation J_n=2·J_1 due to the difference of the definitions of the Hamiltonians (eq. 4.1) and (eq. 4.14), the scaled value $2J_1$=12.65 meV±1 meV is almost in the middle of the suggested range for J_n :10.9 meV⩽ J_n ⩽13.35 meV. However, both values of J_1 and J_n extracted here are considerably higher than the value of J_1=48K (4.138 meV) proposed earlier in the literature and extracted from the analysis of the high-temperature susceptibility data of $BaNi_2V_2O_8$ [47]. This difference is, probably, because *Rogado et al.* in their work [47] analysed the temperature region which is not hight enogth so that the system is not in paramagnetic state and, therefore, the high-temperature series expansion is not accurate enough.
The interplane magnetic exchange coupling was found to be extremely small and most likely is realized via the shortest interplane magnetic exchange path J_{out1} (Fig. 4.9(b) orange line) which is ferromagnetic and does not exceed in an absolute value $|J_{out1}|$⩽0.00045 meV. There were another possible magnetic exchange paths J_{out2} and J_{out3} found, which are both antiferromagnetic and can also contribute to interplane coupling. However, J_{out2} is found to produce an energy dispersion with bandwidth wider than it was observed experimentally while J_{out3} is realized between the first and third honeycomb plane within the unit cell and, therefore, seems to responsible for the interplane coupling due to the long distance. Thus, although a weak contribution of J_{out2} and J_{out3} to interplane coupling cannot be excluded, J_{out1} seems to be more likely to be the dominant one. The weak values of the possible interplane coupling explain the absence of any clear signature for the long-range order phase transition in the susceptibility data.
The extracted upper limits of the possible interplane couplings J_{out1}, J_{out2} and J_{out3} are found to be surprisingly small for a system which displays a long-range magnetically ordered state. The presence of the long-range order with such weak interplane coupling can be explained by the presence of the weak easy-axis anisotropy. Indeed, *Knafo et. al.* in their work [53] demonstrated the importance of the easy-axis anisotropy for inducing of the long-range magnetically ordered state in $BaNi_2V_2O_8$ by exploring the effects of the field- and pressure-induced anisotropies on the ordering temperature T_N. Thus, the combination of a very weak interplane coupling and very weak in-plane easy-axis anisotropy in $BaNi_2V_2O_8$ may be sufficient to induce long-range magnetic order at a finite temperature in this magnet.

4.5 Conclusions

In this chapter the magnetic properties of $BaNi_2V_2O_8$ were explored using the single crystal magnetic susceptibility measurements and powder and single crystal inelastic neutron scattering measurements.

The magnetic susceptibility data collected on a single crystal of $BaNi_2V_2O_8$ reveal that at low temperatures $BaNi_2V_2O_8$ behaves as a 2D Heisenberg antiferromagnet with XY anisotropy. In particular, the magnetic susceptibility data reveal that $BaNi_2V_2O_8$ starts to behave anisotropically already below T≈80K and below T=52K clearly displays the behaviour of 2D Heisenberg XXZ magnet with a strong planar anisotropy as revealed by a minimum in the susceptibility for H||c. Moreover, data reveal no clear signature of the transition to the long range magnetically ordered state and have only an inflection point at T_N=48K±0.5K suggesting very weak interplane coupling.

The analysis of the magnetic excitation spectrum confirms that at base temperature $BaNi_2V_2O_8$ is described well by a 2D XXZ Heisenberg model. In particular, the inelastic neutron scattering measurements reveal that $BaNi_2V_2O_8$ has a spin-wave excitation spectrum which disperses within the honeycomb plane and is almost dispersionless (within the resolution error) in the out-of-plane direction. This magnetic excitation spectrum consists of two spin-wave modes caused by the in-plane and out-of-plane spin-wave fluctuations, respectively. Both modes are gapped implying the presence of both a dominant XY anisotropy and a weak easy-axis anisotropy.

The fit analysis of the magnetic spectrum of $BaNi_2V_2O_8$ was performed by applying linear spin-wave theory and using the Hamiltonian (eq. 4.14). The results reveal that the dominant term is the first neighbour in-plane magnetic exchange coupling J_n which is antiferromagnetic and lies within the range 10.9 meV$\leqslant J_n \leqslant$13.35 meV. The second J_{nn} and third J_{nnn} neighbour in-plane interactions are found to be much smaller and to vary within the ranges 0.85 meV$\leqslant J_{nn} \leqslant$1.65 meV and -0.1 meV$\leqslant J_{nnn} \leqslant$0.4 meV, respectively. Although the system displays long range order, the interplane coupling J_{out} is found to be extremely small and lies within the energy range -0.00045 meV$\leqslant J_{out} \leqslant$0.0012 meV. The values of the XY and easy-axis anisotropies are found to be D_{XY}=0.0695 meV±0.0015 meV, $D_{inplane}$=-0.00090 meV±0.00015 meV confirming the planar character of the magnetism in this compound.

In order to compare the magnetic properties observed in $BaNi_2V_2O_8$ with the magnetic properties of the related nickel-based S=1 honeycomb magnets $BaNi_2(PO_4)_2$ and $BaNi_2(AsO_4)_2$, an effective in-plane magnetic exchange interaction J_{eff} is introduced by the formula:

$$J_{eff} = \frac{\sum_n^3 (z_n^+ |J_n| - z_n^- |J_n|)}{N_{nearest}} \tag{4.16}$$

Here, J_n is the absolute value of the exchange interaction between a magnetic ion and its

n^{th}-nearest neighbour, z_n^+ and z_n^- are the numbers of the bonds between a magnetic ion and its n^{th}-nearest neighbour which reinforce and contradict the magnetic structure, respectively. $N_{nearest}$ is the number of the first-nearest neighbouring magnetic ions which is $N_{nearest}$=3 for a honeycomb lattice. The exchange interactions are introduced up to third neighbours and are assuming to be counted twice for each bond in the Hamiltonian. Thus, J_{eff} characterizes the magnitude of the in-plane magnetic exchange interaction per magnetic ion. For example, in $BaNi_2V_2O_8$ the antiferromagnetic first neighbour interaction reinforce the magnetic structure which has antiferromagnetic order between first neighbour while the antiferromagnetic second neighbour interaction contradicts to the magnetic structure.

The effective in-plane magnetic exchange interaction per Ni^{2+} magnetic ion in $BaNi_2V_2O_8$ is estimated to be J_{eff} ≈5 meV (J_{eff}/k_B = 58K) using the averaged solutions of the exchange interactions. The single counting of the extracted exchange interactions was taken into account.

The estimated value of J_{eff} ≈5 meV (J_{eff}/k_B = 58K) in $BaNi_2V_2O_8$ is found to be much larger than the values J_{eff} = 0.896 meV (J_{eff}/k_B = 10.4K) and J_{eff} = 0.948 meV (J_{eff}/k_B = 11K) calculated for the related nickel-based S=1 honeycomb magnets $BaNi_2P_2O_8$ and $BaNi_2As_2O_8$, respectively, using the magnetic exchange interactions and the magnetic structures which are given in the literature [43; 46; 54].

The most likely interplane magnetic exchange coupling J_{out1} in $BaNi_2V_2O_8$ scaled by J_{eff} is found to be J_{inter}=0.000045J_{eff} which is twice weaker than the scaled interplane coupling J_{inter}=0.00009J_{eff} estimated for $BaNi_2P_2O_8$ [46] and confirms the strong 2D character of the magnetic interactions in $BaNi_2V_2O_8$.

Because of the weak interplane magnetic coupling the magnetic ordering temperature T_N = 0.82J_{eff}/k_B in $BaNi_2V_2O_8$ is suppressed with respect to the ordering temperatures observed in $BaNi_2(PO_4)_2$ and $BaNi_2(AsO_4)_2$ which are T_N=2.35J_{eff}/k_B and T_N=1.77J_{eff}/k_B, respectively [46].

The extracted value of the planar anisotropy in $BaNi_2V_2O_8$ scaled on J_{eff} is found to be D_{XY}≈0.014J_{eff} which is much smaller than the scaled planar anisotropies D_{XY} ≈ 0.673J_{eff} and D_{XY} ≈ 0.636J_{eff} observed in $BaNi_2(PO_4)_2$ and $BaNi_2(AsO_4)_2$, respectively [46; 54].

Because the scaled planar anisotropy is weak, anisotropic behaviour appears in $BaNi_2V_2O_8$ at lower temperatures than in $BaNi_2(PO_4)_2$ and $BaNi_2(AsO_4)_2$ when scaled by the effective in-plane exchange interaction. Indeed, the anisotropic behaviour in $BaNi_2V_2O_8$ appears in the susceptibility at temperatures below T=1.8J_{eff}/k_B (T=80K) while for $BaNi_2(PO_4)_2$ and $BaNi_2(AsO_4)_2$ the anisotropy already is ivedent below T_{ani}≈ 3J_{eff}/k_B (T=32K) and T_{ani}≈ 2.9J_{eff}/k_B (T=32K), respectively [46].

Thus, the 2D planar anisotropic magnetic behaviour in $BaNi_2V_2O_8$ appears over the temperature range from T_N = 0.82J_{eff}/k_B to T_{ani}=1.8J_{eff}/k_B which is narrower and lower when scaled by of the effective in-plane exchange interaction than in $BaNi_2(PO_4)_2$ and $BaNi_2(AsO_4)_2$ where it appears over the ranges from T_N=2.35J_{eff}/k_B to T_{ani}=3J_{eff}/k_B

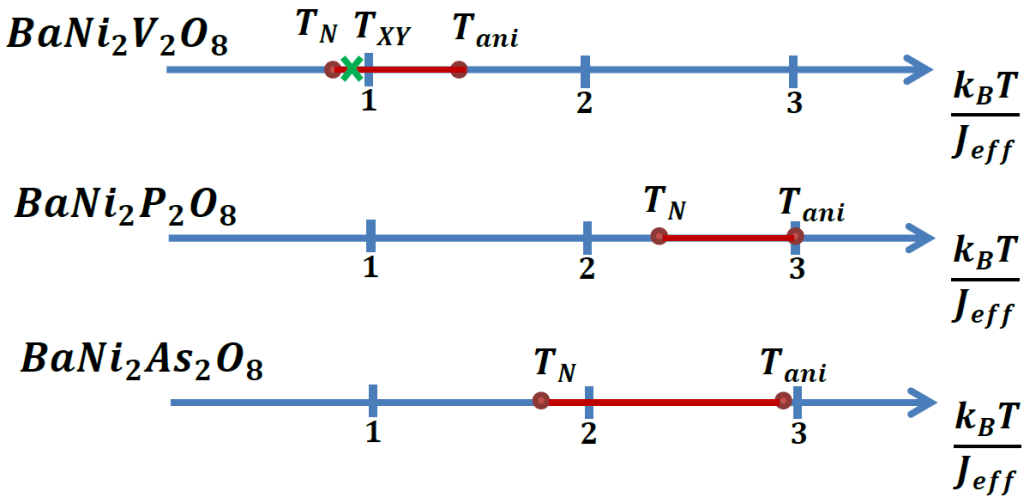

Figure 4.12: Comparison of the onset temperatures for anisotropic behaviour (T_{ani}) and magnetically ordered (T_N) phases in $BaNi_2V_2O_8$, $BaNi_2(PO_4)_2$ and $BaNi_2(AsO_4)_2$ plotted in the scale of the effective in-plane exchange interaction J_{eff}. The green cross represents the T_{XY} temperature scaled on J_{eff} where the characteristic mimnimum predicted by the QMC [40] appears in the suscepsubility data of $BaNi_2V_2O_8$.

and from T_N=1.77J_{eff}/k_B to T_{ani}=2.9J_{eff}/k_B, respectively (Fig. 4.12). However, only in $BaNi_2V_2O_8$ is the characteristic feature of the transition to the dominant XY regime accessible which appears as a minimum in the susceptibility data for H||c at T_{XY}=0.896 J_{eff}/k_B (T_{XY} = 52K) and which was predicted by Quantum Monte Carlo Simulation (QMC) for 2D XXZ model [40]. To compare the T_{XY} observed in $BaNi_2V_2O_8$ with the results of QMC simulations, J_{eff} should be multiplied by factor of 2 due to the double counting in the Hamiltonian. The transition temperature to the dominant XY regime in $BaNi_2V_2O_8$ in this scale is T'_{XY} = 0.448J'_{eff}/k_B where J'_{eff}=2J_{eff} which is in an agreement with the temperature T≈0.3 J/k_B predicted for the 2D XXZ model with Ising easy-plane anisotropy of Δ = 0.02 by QMC [40].

These results prove that $BaNi_2V_2O_8$ behaves as a strongly 2D magnetic system with planar anisotropy which makes this compound a promising candidate for the search of the BKT behaviour, especially at low relative temperature.

5 Critical phenomena in $BaNi_2V_2O_8$

5.1 Introduction

In the previous Chapter it was shown that $BaNi_2V_2O_8$ is an almost 2D Heisenberg magnetic system with a planar anisotropy. It was found that the magnetic excitation spectrum of this compound is described well by the Heisenberg Hamiltonian:

$$H = \sum_{i>j} J_n \cdot \boldsymbol{S_i} \cdot \boldsymbol{S_j} + \sum_{i>j} J_{nn} \cdot \boldsymbol{S_i} \cdot \boldsymbol{S_j} + \sum_{i>j} J_{nnn} \cdot \boldsymbol{S_i} \cdot \boldsymbol{S_j} + \sum_{i>j} J_{out} \cdot \boldsymbol{S_i} \cdot \boldsymbol{S_j} + \sum_{i>j} D_{XY} \cdot S_i^{c^2} + \sum_{i>j} D_{inplane} \cdot S_i^{x^2} \tag{5.1}$$

Here, J_n, J_{nn}, J_{nnn} are the first-, second- and third-neighbours isotropic Heisenberg magnetic exchange interactions within the honeycomb plane, J_{out} is the out-of-plane coupling, and D_{XY} and $D_{inplane}$ are the single ion easy-plane and easy-axis anisotropies of the Ni^{2+} magnetic ions, respectively. The Hamiltonian of $BaNi_2V_2O_8$ consists of both in-plane and out-of-plane magnetic exchange interactions, but the first-neighbour interaction was found to be $10.9meV \leqslant J_n \leqslant 13.35meV$ which is the dominant one and is ten times bigger than the second-neighbour interaction $0.85meV \leqslant J_{nn} \leqslant 1.65meV$. The out-of-plane magnetic exchange interaction is negligibly small and equals to 10^{-5} order of J_n. Although the extracted value of the easy-plane anisotropy D_{XY}=0.0695meV$\pm$0.0015meV is small, it is, however, much stronger then the found value of the easy-axis anisotropy $D_{inplane}$=-0.0009meV$\pm$0.00015meV. Thus, $BaNi_2V_2O_8$ is a good physical realization of the quasi-2D Heisenberg quantum magnet with a dominant planar anisotropy that makes this compound a potential candidate for the search and investigation of the Berezinskii-Kosterlitz-Thouless (BKT) critical behaviour [14; 15; 16; 17].

Berezinsky-Kosterliz-Thouless critical behaviour is a topological phase transition from disordered to the quasi-long-range magnetically ordered state proposed for 2D XY magnets where conventional long-range magnetic order is prohibited by the Mermin-Wagner theorem [12]. Indeed, according to the Mermin-Wagner theorem there is no phase transition with the spontaneous symmetry breaking in the magnetic systems whose dimensionality is less than or equals to two due to the excitations of the Goldstone modes. Kaplan and Stanley were the first who showed that the zero-field magnetic susceptibility in two-dimensional magnets to diverges according to a power-law at finite temperature giving evidence for the phase tran-

sition [55]. Later, Kosterlitz and Thouless, independently with Berezinskii, further explored this behaviour and revealed the evidence for a transition in the XY (spins confined to a plane) model [14]. They were drawing an analogy to the dislocation theory of melting where the liquid in the vicinity of the freezing point has a concentration of the free dislocations in equilibrium state which can move to the surface producing viscous flow [56]. They suggested that in XY model, similar to the dislocation theory of melting, this phase transition is caused by the topological defects which, in case of XY model, are spin-vortices [14]. At low-temperatures the strongly-bound pairs of the spin vortices with opposite circulations occur forming the quasi-long-range ordered state and coexist with the Goldstone modes which destroy the conventional long-range magnetic order. There are no free vortices in this quasi-long-range magnetically ordered state below the transition temperature T_{BKT}, however, with temperature increase the pairs are spatialy extent and their density population are increasing. As result, the pairs become unstable and start to decompose forming the flux of free vortices above the transition temperature T_{BKT}. Thus, the transition temperature T_{BKT} separates the quais-long-range magnetically ordered low-temperature phase of the strongly-bound spin vortex-antivortex pairs with the disordered high-temperature phase of a plasma of free unbound vortices [13; 57]. Above the T_{BKT} transition temperature the experimentally observable temperature dependence of the correlation length follows to the exponential law, in contrast to the conventional power law, given the key for the experimental observation of the BKT behaviour:

$$\xi_{BKT} = A \cdot \exp\left(b \cdot \left(\frac{T - T_{BKT}}{T_{BKT}}\right)^{-0.5}\right) \tag{5.2}$$

Here A and b are non-universal constants where b depends on the crystal lattice and was found to be b=1.5 for the square crystal lattice [15].

The Berezinsky-Kosterliz-Thouless phase transition was experimentally observed for the first time in the two-dimensional ^{4}He films [58] and was later confirmed also in the two-dimensional superconducting thin films [59; 60] and in two-dimensional atomic gas [61; 62].

Although the Berezinsky-Kosterliz-Thouless phase transition was originally predicted for the 2D XY model, recent theoretical investigations show that it can also exists in the 2D Heisenberg magnetic system with very weak planar anisotropy. Indeed, Cuccoli et. al. [40] performed the Quantum Monte Carlo simulations (QMC) on L×L square lattice with S=$\frac{1}{2}$ XXZ Hamiltonian:

$$H = \frac{J_n}{2} \sum_{i,j} \left[\left(1 - \Delta_\mu\right) \left(\hat{S}_i^x \cdot \hat{S}_j^x + \hat{S}_i^y \cdot \hat{S}_j^y\right) + \left(1 - \Delta_\lambda\right) \left(\hat{S}_i^z \cdot \hat{S}_j^z\right) \right] \tag{5.3}$$

Here $\hat{S}_i^x$,$\hat{S}_i^y$,$\hat{S}_i^z$ are the spin operators, J_n is the nearest neighbour magnetic exchange interaction, Δ_μ and Δ_λ are the easy-axis and easy-plane anisotropies, respectively. They prove that even weak value of in-plane anisotropy of Δ_λ=0.02 is enough to run the Berezinsky-Kosterliz-

Thouless scenario with the transition temperature $T_{BKT}=\frac{4\pi\rho_s}{ln(c/\Delta_\lambda)}$ where c is constant and ρ_s is the spin stiffness. The temperature dependence of the ξ^{xx}_{fit} extracted from the fit analysis of the spin-spin correlation function simulated for the Hamiltonian (eq. 5.3) using QMC is perfectly consistent with the exponential decay proposed for the BKT behaviour (eq. 5.2). Thus, Cuccoli et. al. introduced the reason for search of the Berezinsky-Kosterliz-Thouless behaviour in the solid compounds which magnetic properties are described by the 2D Heisenberg XXZ model where the planar anisotropy can be very weak. Although these compounds usually have the conventional long-range magnetically ordered phase below the finite ordered temperature T_N, just above this transition temperature they can display 2D XXZ behaviour which is, according to Cuccoli et. al, sufficient for the BKT scenario.

This Chapter presents the investigation of the critical phenomena in S=1 honeycomb antiferromagnet $BaNi_2V_2O_8$ which is potential candidate to display the BKT behaviour because it is found to be a good physical realization of 2D XXZ Heisenberg model (see Chapter 4). The critical phenomena in $BaNi_2V_2O_8$ was earlier explored using the electron spin resonance (ESR) technique [49]. Heinrich et. al. extracted the value of the BKT transition temperature T_{BKT} = 43.3K from the fit analysis of the temperature dependence of the ESR line width within the temperature range of 50K-300K. They used the fact that the ESR line width is proportional to the cube of the correlation length in XY model along with the relation for the thermal decay of the correlation length proposed by the BKT theory. However, they also showed that the temperature dependence of the ESR linewidth can be also fitted well by the conventional power law with the critical exponent p=2.3 which is similar to the values empirically observed in several 2D Heisenberg magnets with finite interplane coupling [46]. A close result was recently observed in the measurements of $BaNi_2V_2O_8$ using the electronic paramagnetic resonance (EPR) and ^{51}V nuclear magnetic resonance (NMR) techniques [63]. Waibel et al. show that the temperature dependence of the longitudinal NMR relaxation rate of the ^{51}V nuclie can be fitted well by the square function of the correlation length over the temperature range up 300K where the correlation length exponentially decays with temperature increase according to the Berezinsky-Kosterliz-Thouless theory [63]. The BKT transition temperature was extracted to be T_{BKT}=40.2K$\pm$0.5K and was found to be the same for both parallel and perpendicular directions of the applied magnetic field of B=1.6T to the *c*-axis and for the higher field of B=7T applied parallel to *c*-axis. However, the temperature dependence of the relaxation time was found to deviate from BKT behaviour and follows to the power-law decay with critical exponent of p=1.13 $\pm$0.09 for the higher magnetic field of B=7T applied perpendicular to the *c*-axis. The deviation from BKT behaviour was explained by the tendency of the spins to point out in perpendicular direction to the applied magnetic field which suppresses the vortices formation if the strong magnetic field is applied within the plane [63].

In this Chapter the critical behaviour in $BaNi_2V_2O_8$ is explored using the elastic and inelastic neutron scattering techniques. This Chapter starts from the section *Experimental settings*

which gives the description of the experimental conditions for all performed experiments along with the description of the instrumental resolution function. The next section *Results of the single crystal neutron diffraction measurements* presents the analysis of the collected data. First, an accurate value for the ordered temperature T_N was extracted from the analysis of temperature dependence of the inverse width of the $(1,0,\frac{1}{2})$ magnetic Bragg peak. Then, the critical exponent was extracted from the analysis of the temperature dependence of the integrated intensity of the $(1,0,\frac{1}{2})$ magnetic Bragg peak using the Power Law. It was shown that $BaNi_2V_2O_8$ behaves as the 2D XXZ magnetic system just below the ordered temperature T_N but displays the crossover to the 2D Ising-like system with temperature decreases. Above the ordering temperature T_N, in the temperature region where $BaNi_2V_2O_8$ behaves as 2D XXZ Heisenberg antiferromagnet, the temperature dependence of the critical exponent was measured over a wide temperature range. The observed results are analysed in the section *Correlation length* and reveal that the temperature dependence of the correlation length in $BaNi_2V_2O_8$ does not follow any conventional power law but is described well using the BKT relation. In the *Discussion* section the extracted value of the BKT transition temperature was compared to the values reported earlier and the reason for the Neel order is discussed. Finally, a crossover phase diagram is presented showing that $BaNi_2V_2O_8$ evolves from 2D Heisenberg behaviour at high temperature through to 2D XXZ behaviour and then to Ising behaviour at the lowest temperatures.

5.2 Experimental settings of the single crystal neutron diffraction experiment

In order to detect the $(1,0,\frac{1}{2})$ magnetic Bragg peak in single crystal diffraction data of $BaNi_2V_2O_8$, single crystal elastic neutron scattering measurements of $BaNi_2V_2O_8$ were performed using the cold neutron triple-axis spectrometer PANDA at FRM2, Munich, Germany. The instrument was equipped with a doubled-focused pyrolytic graphite (PG002) monochromator and analyser. A single crystal sample with a mass of m=340 mg was aligned with the (h,0,l) plane as the instrumental scattering plane. The sample was mounted on a sample holder and then was placed into a closed-cycle cryostat and cooled down to base temperature of 4.3K. A final wave vector k_f=1.57Å^{-1} of the analyser was kept fixed giving the energy resolution of 0.138 meV. The measurements were performed along (1,0,L) direction at both base temperature and finite temperature of T=60K.

To explore the critical phenomena in $BaNi_2V_2O_8$, single crystal elastic neutron scattering measurements were performed on the cold neutron triple-axis spectrometer TASP at the Paul Scherrer Institute (PSI), Switzerland. This instrument was equipped with an vertically focused PG(002) monochromator and a horizontally focused PG (002) analyser. A single crystal sample with a mass of m=550 mg from a different crystal growth was mounted on

a sample holder and preoriented with the (h,k,0) plane using the X-ray Laue diffractometer in the Sample characterization laboratory at HZB. The sample holder with the preoriented sample was mounted inside a small Orange Cryostat that allowed it to be cooled down to base temperature of T=1.47K. The Orange Cryostat was placed on a goniometer table which allows an initial orientation of the sample to be corrected up to 10 degree. For this experiment the initial (h,k,0) scattering plane of the sample was tilted by 5 degree with respect to the horizontal axis perpendicular to the (1,0,0) direction. Thus, the measurement were carried out in the (h-k/2,k,h/2) scattering plane which allowed the $(1,0,\frac{1}{2})$ magnetic Bragg peak to be reached. The analyser was set flat because this settings provided higher resolution and the final wave vector was fixed at k_f=1.23Å^{-1} giving the energy resolution of 0.074 meV. An energy resolution was determined by measuring the FWHM of the elastic line at the incoherent scattering at base temperature. During the experiment both A3 and Q elastic scans were performed through the $(1,0,\frac{1}{2})$ magnetic Bragg peak at base and finite temperatures within the temperature range of 1.47K-56 K. The directions of these measurments are shown in Figure 5.1 by the violet and green lines, respectively. Particularly, the Q_h scans were perfomed along the $(h,0,\frac{1}{2})$ direction. The temperatures were set with accuracy of 0.03K. The Q and A3 resolution were found to be ΔQ_h=0.010(r.u.l) and ΔA3=0.468 °, respectively, by extracting of FWHM from the fit analysis of these scans through the $(1,0,\frac{1}{2})$ magnetic Bragg peak at the base temperature using the Pearson VII function (Fig. 5.2(a-b) red dashed dot lines). This function was found to be the best description of the instrumental resolution function and is described in detail in the next subsection *Resolution function*.

In the second part of the same experiment the temperature dependence of the correlation length was explored. The analyser was removed so that the TASP spectrometer was used in the diffraction mode and both elastic and inelastic signals were detected. An incident wavevector of k_i=2.662 Å^{-1} was used along with a PG filter between a monochromator and sample. A 40' collimator was placed between the monochromator and sample to improve the A3 angle resolution from ΔA3=0.484° to ΔA3=0.387°. The resolution value was determined as a FWHM of the A3 scan through the $(1,0,\frac{1}{2})$ magnetic Bragg peak at base temperature which was extracted from the fit analysis using the Pearson VII function. The A3 scans through the $(1,0,\frac{1}{2})$ magnetic Bragg peak were measured at base temperature of 1.47K and over the temperature range from 48K to 68K in steps of 0.25K and 1K (violet arrows in Fig.5.1).

To improve the statistics of the results, the temperature dependence of the correlation length was explored second time using the TASP instrument in two-axis mode keeping the instrument settings the same as for the previous experiment. For this experiment the same sample was used, and measurements were again performed in the (h-k/2, k, h/2) scattering plane. To check the reproducibility of the results, the correlation length was investigated by measuring the Q scans in the (1-k/2,k,1/2) direction through the (1,0,0.5) magnetic Bragg peak (orange arrows in Fig. 5.1). The measurments were performed over the temperature range 48K -

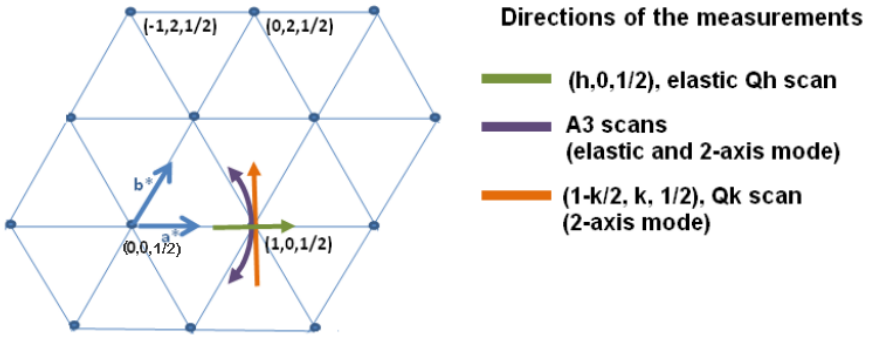

Figure 5.1: The sketch of the (h,k,1/2) plane in the reciprocal lattice of $BaNi_2V_2O_8$. The green and violet arrows show the directions of the elastic Qh and A3 scans, respectively, through the $(1,0,\frac{1}{2})$ magnetic Bragg peak. The orange and violet arrows show the directions of the Q and A3 scans, respectively, which were performed in 2-axis mode of the TASP spectrometer.

140K with steps of 0.25K, 0.5K, 1K, 2K, 5K, 10K and 40K depending on the temperature region. To take into account the resolution effects, a Q_k scan was measured at base temperature and then was fitted using the Pearson VII function. The Q resolution was determined as a FWHM extracted from the fit analysis and was found to be ΔQ=0.0102.

5.2.1 Resolution function

The line shape of the magnetic Bragg peak is described only by the instrumental resolution function which is supposed to be a Gaussian in the ideal case. However, it was found in this experiment that the Pearson VII function [64] fits the collected experimental data much better than the Gaussian, possibly due to the complexity of the resolution function in a real experiment. Pearson VII function is generally used to fit the X-ray diffraction data and is given by the equation:

$$F_{PearsonVII} = \frac{A \cdot 2\Gamma(m)\sqrt{2^{\frac{1}{m}}-1}}{\sqrt{\pi}\Gamma(m-1/2)W_p}\left(1+4\cdot\frac{\left(2^{\frac{1}{m}}-1\right)}{W_p^2}(x-x_0)^2\right)^{-m} \tag{5.4}$$

Here x_0 is the peak position, W_P is the full width of half maximum (FWHM) and A is the area under the peak. Γ is the factorial function and m is a parameter that determines the peak shape. In the limiting cases of the of the profile-shape parameter m=1 and m $\rightarrow \infty$ the Pearson VII function has Lorentzian and Gaussian line shape profiles, respectively. Indeed, when the profile-shape parameter m=1 then Γ(m)=1 and $\Gamma(0.5)=\sqrt{\pi}$ and the Pearson VII function gets the form of Lorentzian function :

$$F_{PearsonVII} \underset{m=1}{=} \frac{2\cdot A}{\sqrt{\pi}\sqrt{\pi}W_p}\left(1+4\cdot\frac{1}{W_p^2}(x-x_0)^2\right)^{-1} = \frac{A}{\pi}\cdot\frac{\frac{W_p}{2}}{\left(\left(\frac{W_p}{2}\right)^2+(x-x_0)^2\right)} \tag{5.5}$$

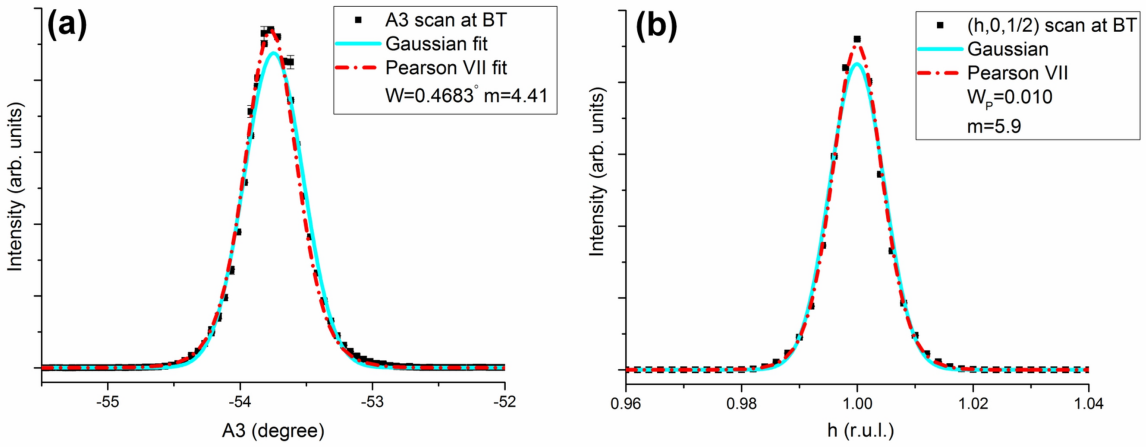

Figure 5.2: (a) The A3 scan through the $(1,0,\frac{1}{2})$ magnetic Bragg peak at the base temperature (b) The Q scan through the $(1,0,\frac{1}{2})$ magnetic Bragg peak at the base temperature. This data was collected on TASP instrument.

when the profile-shape parameter goes to infinity m $\rightarrow \infty$, one can replace the term $2^{\frac{1}{m}}$ by the two first terms of the Taylor expansion $2^{\frac{1}{m}} \approx 1+\frac{1}{m}\ln(2)$ whereupon, taking into account the relation $\lim_{m\rightarrow\infty} \frac{\Gamma(m+a)}{m^a\Gamma(m)}=1$ and the definition of the exponential function $e^x = \lim_{n\rightarrow\infty}(1+\frac{x}{n})^n$, the Pearson VII function yields a Gaussian function :

$$\begin{aligned}\lim_{m\rightarrow\infty} F_{PearsonVII} &= \frac{A\cdot 2\Gamma(m)\sqrt{ln(2)}}{\sqrt{\pi}\sqrt{m}\Gamma(m-1/2)W_p}\left(1+\frac{1}{m}\left(\frac{2\sqrt{2ln(2)}}{W_p}(x-x_0)\right)^2\right)^{-m} = \\ &= \frac{A\cdot 2\sqrt{2ln(2)}\cdot\exp\left(-\left(\frac{2\sqrt{2ln(2)}}{W_p}\right)^2(x-x_0)^2\right)}{\sqrt{2\pi}\cdot W_p}\end{aligned} \tag{5.6}$$

Figures 5.2(a) and 5.2(b) show elastic scattering A3 and Q scans through the $(1,0,\frac{1}{2})$ magnetic Bragg peak at base temperature, respectively. Both scans were fitted by the Gaussian and Pearson VII functions using the Origin 9 software, and the results are plotted over the data in Figure 5.2(a-b). The results clearly reveal that the Pearson VII function reproduces the line shape of the $(1,0,\frac{1}{2})$ magnetic Bragg peak better than the Gaussian function which does not accuratelly fit the maximum of the peak.

5.3 Results of the single crystal neutron diffraction

To illuminate the magnetic structure in $BaNi_2V_2O_8$, the single crystal elastic neutron scattering measurements within the (h,0,l) scattering plane were performed along the (1,0,L) direction at the base temperature at the PANDA instrument. The results are plotted in Figure 5.3(a) and show that there are two intense elastic signals at $(1,0,\frac{1}{2})$ and (1,0,1). The

peak at (1,0,1) is consistent with the position of a nuclear Bragg peak calculated for the crystal structure of $BaNi_2V_2O_8$ using CrystalDiffract software. The $(1,0,\frac{1}{2})$ peak is consistent with the magnetic Bragg peak with the propagation vector $(1,0,\frac{1}{2})$ proposed in the literature [47]. In order to test the magnetic nature of the peak at $(1,0,\frac{1}{2})$, the elastic scan along the (1,0,L) direction was repeated at finite temperature T=60K which is higher than the ordered temperature T_N=50K proposed in the literature [47]. Indeed, the nuclear Bragg peaks are temperature independent while the magnetic Bragg peak should disappear above the T_N. The data collected at the finite temperature (Fig.5.3(b) blue filled circles) are plotted over the data collected at the base temperature (Fig.5.3(b) green squares) revealing that there is no signal at $(1,0,\frac{1}{2})$ at T=60K. This results confirms that the strong elastic signal at $(1,0,\frac{1}{2})$ at the base temperature is the $(1,0,\frac{1}{2})$ magnetic Bragg peak.

5.3.1 Ordered temperature

To further investigate the magnetic structure of $BaNi_2V_2O_8$ and to clarify the ordering temperature T_N, elastic A3 scans were performed through the $(1,0,\frac{1}{2})$ magnetic Bragg peak within the (h-k/2,k,h/2) scattering plane at different temperatures within a temperature range of BT-56K using the TASP instrument. Figure 5.3(b) shows the A3 scans through the $(1,0,\frac{1}{2})$ magnetic Bragg peak at the selected finite temperatures of T=47K, T=47.25K, T=47.5K, T=47.75K, T=48K. Their comparison with the A3 scans through the $(1,0,\frac{1}{2})$ magnetic Bragg peak at base temperature reveals that the line shape of the $(1,0,\frac{1}{2})$ magnetic Bragg peak is temperature independent below 47.5 K and then starts to broaden rapidly above T=47.75 K. This result is confirmed by the analysis of the temperature dependence of inverse FWHM of the $(1,0,\frac{1}{2})$ magnetic Bragg peak which is plotted in Fig. 5.3(c). The FWHM was extracted from the fit analysis of the $(1,0,\frac{1}{2})$ magnetic Bragg peak at each temperature within the explored temperature range of T=BT-56K using the PearsonVII function whose all parameters were varied. The PearsonVII function was used because, as was shown above, it reproduces the line shape of the $(1,0,\frac{1}{2})$ magnetic Bragg better than the conventional Gaussian function and, therefore, gives more accurate value of the FWHM. The extracted temperature dependence of the inverse FWHM immediately reveals that inverse FWHM of the $(1,0,\frac{1}{2})$ magnetic Bragg peaks at finite temperatures below T $\leqslant$47.5K are the same, within the fitting error, with the value at base temperature, while above T=47.75K it sharply deacreases. This behaviour can be associated with loss of the long-range magnetic order and indicates that T_N lies within the temperature range of 47.5K-47.75K. The ordering temperature was fixed at T_N=47.75K for further analysis because the inverse FWHM at T=47.75K is smaller then the inverse FWHM at all lower temperatures by the values which exceed the fitting errors while the inverse FWHM at T=45.5K is almost the same with the inverse FWHM at T=25K within the fitting error.

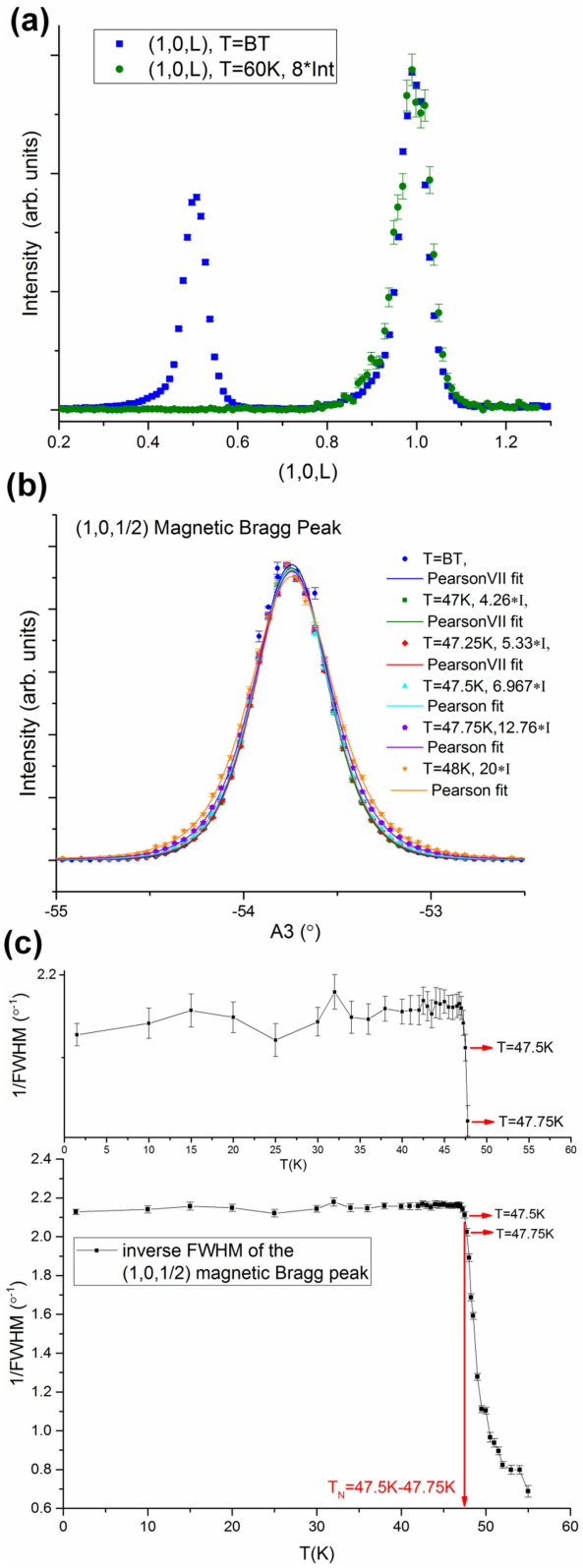

Figure 5.3: (a) Elastic neutron scattering data collected on single crystal of $BaNi_2V_2O_8$ along the (1,0,L) direction within the (h,0,l) scattering plane at the base (green squares) temperature and at temperature of T=60K using the PANDA instrument (filled blue circles). (b) The A3 scans through the $(1,0,\frac{1}{2})$ magnetic Bragg peak at base temperature (blue circles) and finite temperatures of T=47K (green squares), T=47.25K (red rhombus), T=47.5K (cyan triangles), T=47.75K (violet pentagons), T=48K (orange stars) measured in the TASP instrument (c) The inverse FWHM width of the A3 scans through the $(1,0,\frac{1}{2})$ plotted as a function of temperature.

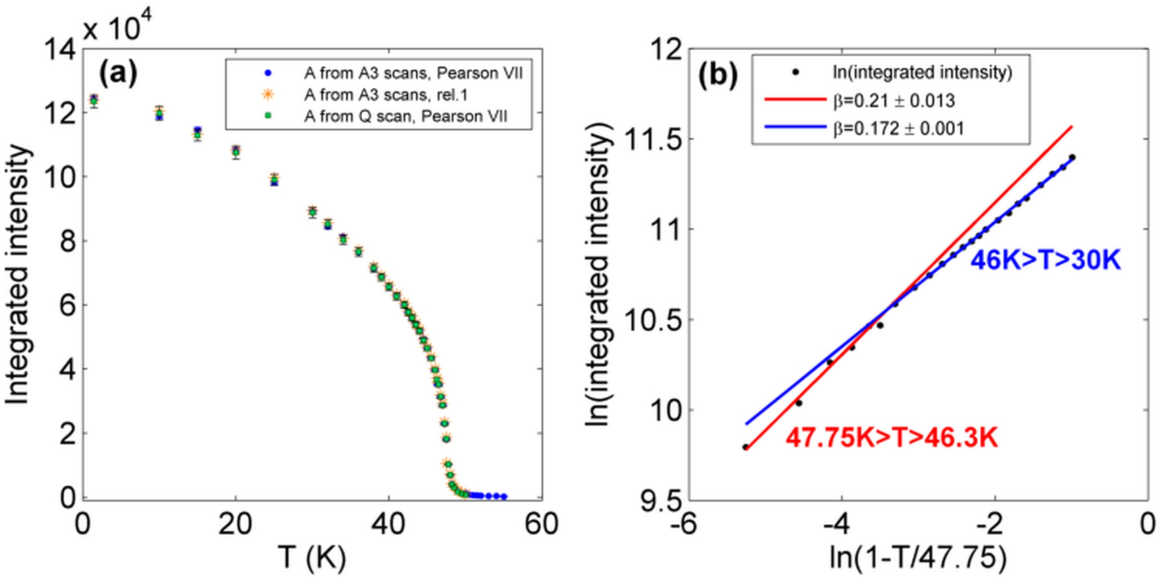

Figure 5.4: (a) Temperature dependence of the integrated intensity of the $(1,0,\frac{1}{2})$ magnetic Bragg peak extracted from A3 scans (filled blue circles) and from the Q scans (filled green squares). (b) Integrated intensity of the $(1,0,\frac{1}{2})$ magnetic Bragg peak extracted from A3 scans plotted as a function of the reduced temperature in logarithmic scale and fitted using the power law over the temperature regions of 46.3K-47.5K (solid red line) and 30K-46K (solid blue line).

5.3.2 Below T_N: critical exponent of $BaNi_2V_2O_8$

In order to determine the critical exponent of $BaNi_2V_2O_8$ which will indicate the type and dimensionality of this magnetic system, the temperature dependence of the integrated intensity of the $(1,0,\frac{1}{2})$ magnetic Bragg peak was explored. For this purpose, the A3 elastic scans through the $(1,0,\frac{1}{2})$ magnetic Bragg peak at different finite temperatures within the temperature range of BT-56K were fitted using the PearsonVII function, and the extracted values of the area (parameter A) were plotted as a function of temperature (Fig.5.4 (a) (blue filled circles)). To verify the values of the area (parameter A) extracted from the fit analysis using the Pearson VII function, the integrated intensity of the magnetic Bragg peak at fixed temperatures, in addition, was calculated using the relation: $A=0.5\cdot\sum_i(x_{i+1}-x_i)\cdot(I(x_{i+1})+I(x_i))$ (rel. 1). Here, x_i and I_i are the degree and intensity of the data points in elastic A3 scan at the particular temperature, respectively. The areas A extracted using this relation (Fig. 5.4(a) (orange stars)) were plotted over the values A extracted from the fit analysis using the Pearson VII function (Fig. 5.4(a)(blue filled circles)) as a function of temperature. The comparison of two data sets reveals that they are almost identical which validates the fit analysis performed using the Pearson VII function.

The extracted values of the integrated intensity A smoothly decrease as temperature increase but start to drop down steeply above 47K and asymptotically tend to zero above the inflection point at 48.25K - 48.5K. To test the reproducibility of the extracted values, Q elastic scans

were performed in the (h,0,$\frac{h}{2}$) direction through the (1,0,$\frac{1}{2}$) magnetic Bragg peak over the temperature range of T=BT-50K. The temperature dependence of the integrated intensity of the magnetic Bragg peak extracted from the fit analysis of the Q scans was renormalized to compare it with the results extracted from the A3 scans and plotted in Fig. 5.4.(a) (green filled squares). The comparison of the temperature dependence of the integrated intensity of the (1,0,$\frac{1}{2}$) magnetic Bragg peak extracted from the A3 and Q scans after renormalization reveals that they are identical within the error. However, the values extracted from the A3 scans are more preferred for the further analysis because they were measured within a wider temperature range.

5.3.2.1 Power law analysis

To find out the value of the critical exponent in $BaNi_2V_2O_8$, the temperature dependence of the integrated intensity of the (1,0,$\frac{1}{2}$) magnetic Bragg peak extracted from the fitting of the A3 scans was analysed using the power law relation:

$$I \sim M^2 \sim \left(\frac{T_N - T}{T_N}\right)^{2\beta} \tag{5.7}$$

Here I is the integrated intensity of the magnetic Bragg peak, M is the magnetisation of the magnetic system below the ordering temperature T_N, β is the critical exponent and T is a variable temperature. This equation can be rewriten in the form:

$$ln(I) \sim ln\left(\frac{T_N - T}{T_N}\right)^{2\beta} = 2\beta ln(\varepsilon) \tag{5.8}$$

Here ε is the reduced temperature $\varepsilon = \frac{T_N - T}{T_N}$. Thus, the integrated intensity of the magnetic Bragg peak in the vicinity of the transition temperature should linearly depend on the reduced temperature ε in a logarithmic scale and the slope of the line equals 2β.
Figure 5.4 (b) shows the integrated intensity of the (1,0,$\frac{1}{2}$) magnetic Bragg peak versus the reduced temperature $\varepsilon = \frac{T_N - T}{T_N}$ in a logarithmic scale over the 30K<T<47.5K ($0.005<\varepsilon<0.37$) temperature range. The Neel temperature was fixed to the temperature T_N=47.75K above which the Bragg peaks becomes broader. Although the linear dependence is expected, the experimental curve does not follow a straight line. Indeed, there is a clearly observed crossover at 46K-46.3K which breaks the curve on the two temperature regions $0.005<\varepsilon_I<0.03$ (46.3K<T<47.5K) and $0.036<\varepsilon_{II}<0.37$ (30K<T<46K). Each of these temperature regions is fitted well independently using the power law with the critical exponents of β_I=0.21±0.013 and β_{II}=0.172±0.001, respectively. The critical exponent β_I, which characterizes the temperature region just below the transition temperature T_N, is close to the value predicted for the 2D Heisenberg XY magnetic system (β=0.23) where the finite magnetization can exists

Compaund	Spin	β	T range ε	Type of system	Ref.
K_2CuF_4	Ferromagnet S=$\frac{1}{2}$	0.33±0.03	0.001<ε<0.02	3D Heisenberg (β=0.35 [46]) or 3D XY model (β=0.33 [46])	[66]
		0.22	0.03<ε<0.3	2D XY model (β=0.23 [65])	
MnF2D	Antiferromagnet S=$\frac{5}{2}$	0.31±0.02	0.003<ε<0.02	3D XY or 3D Ising (β=0.31 [46])	[67]
		0.22±0.02	0.02<ε<0.5	2D XY model	
MnF2H	Antiferromagnet S=$\frac{5}{2}$	0.31±0.02	0.005<ε<0.02	3D XY or 3D Ising	[68]
		0.23±0.01	0.04<ε<0.44	2D XY model	[69]
CuF4D	Antiferromagnet S=$\frac{1}{2}$	0.3±0.01	ε<0.05	3D XY or 3D Ising	[70]
		0.22±0.02	0.05<ε	2D XY model	
$MnPS_3$	Antiferromagnet S=$\frac{5}{2}$	0.32±0.01	ε<0.03	3D XY or 3D XY or 3D Ising	[71] [72]
		0.25±0.01	0.03<ε	2D XY model	[73]
$BaNi_2P_2O_8$	Antiferromagnet S=1	0.33	ε<0.02	3D XY	[46]
		0.23	0.02<ε	2D XY model	[74]
$BaNi_2As_2O_8$	Antiferromagnet S=1	0.33	ε<0.01	3D XY or 3D Ising	[46]
		0.135	0.01<ε	2D Ising model	

Table 5.1: Critical exponents of the different layered magnets over the varied reduced temperature ranges. The notations are following: $\varepsilon=\frac{T_N-T}{T_N}$ is the reduced temperature where T_N is the ordering temperature, MnF2D ≡ $Mn(HCOO)_2{\cdot}2D_2O$, MnF2H ≡ $Mn(HCOO)_2{\cdot}2H_2O$, CuF4D≡$Cu(HCOO)_2{\cdot}4D_2O$.

as a finite size effect [65]. At lower temperature region the critical exponent β_{II} is smaller and lies between the values for the 2D Heisenberg XY magnetic system [65] and 2D Ising model (β=0.125) which can be attributed to the presence of the weak in-plane easy-axis anisotropy in $BaNi_2V_2O_8$.

5.3.2.2 Discussions

The investigation of the critical behaviour in $BaNi_2V_2O_8$ reveals that there is a crossover between two temperature regions. In the vicinity of the ordering temperature T_N (46.3K<T<47.5K) the magnetic system is characterised by the critical exponent β_I=0.21±0.013 which is close to the predicted value for the 2D Heisenberg XXZ magnetic system[65] while at lower temperatures (30K<T<46K) the critical exponent β_{II}=0.172±0.001 is smaller and tends to the value β=0.125 for the 2D Ising model.

This crossover can be explained by the complexity of the Hamiltonian of $BaNi_2V_2O_8$ which was discovered in previous Chapter. Indeed, when the Hamiltonian of a system is composed of the several interaction terms, which specify different dimensionality or symmetries, the

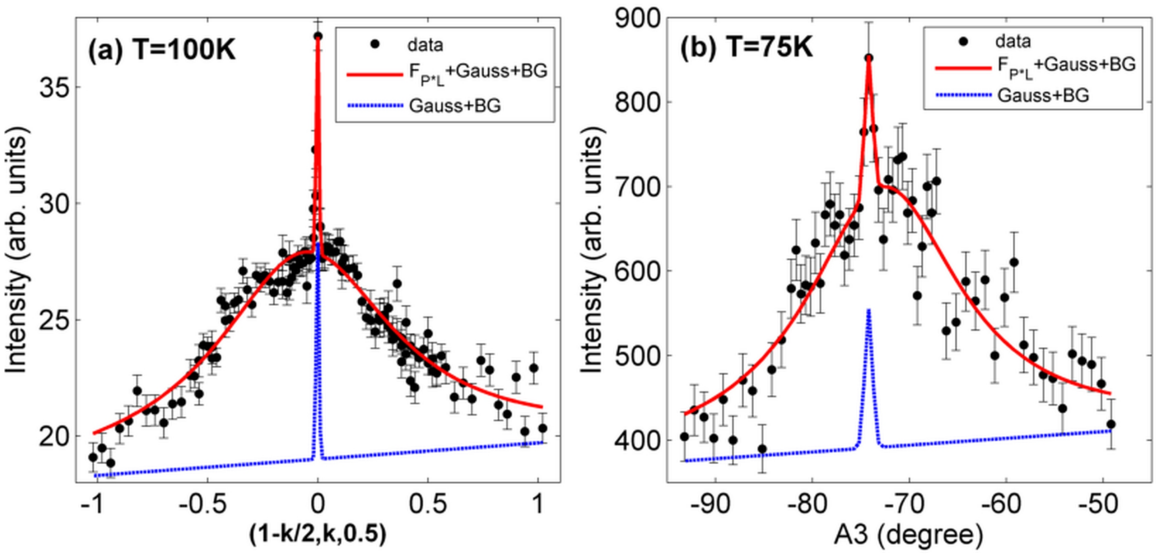

Figure 5.5: (a) Q scan through the $(1,0,\frac{1}{2})$ magnetic Bragg peak at T=100 K simultaneously fitted by the sum of F_{L*P} function with fixed Wp =3.7433 m=3.7433 and Gaussian function taking into account flat background contribution. The area (A), FWHM (W_G) and peak position (x_n) of the Gaussian function were found to be of A=0.140±0.0143, W_G=0.0136±0.0015 and x_n=-0.0015±0.0008, respectively. (b) A3 scan through the $(1,0,\frac{1}{2})$ magnetic Bragg peak at T=75 K simultaneously fitted using the sum of $F_{(L*P)}$ function with fixed Wp =3.7433 m=3.7433 and Gaussian function taking into account flat background contribution. The area (A), FWHM (W_G) and peak position (x_n) of the Gaussian function were found to be of A=160±62, W_G=0.9164±0.3432 and x_n=-74.19±0.16, respectively.

magnetic properties of the system, such as the critical exponent, would be characterized by the dominant property. On decreasing temperature the weaker terms start to play a role which would be reflected in the observed magnetic behaviours [66].

The Hamiltonian of $BaNi_2V_2O_8$ consists of the six terms where the dominant terms are the first- and second-neighbour in-plane magnetic exchange interactions along with XY planar anisotropy. These dominant terms mean that to first approximation $BaNi_2V_2O_8$ is described by the 2D XXZ Heisenberg model which is, indeed, confirmed by the value of the critical exponent extracted over the 46.3K-47.5K temperature range. However, with temperature decrease the minor terms, such as the weak in-plane easy-axis Ising anisotropy, starts to play a role which is experimentally observed by a reduction in the value of the critical exponent extracted within the lower temperature region of 30K-46K. This is in agreement with the conclusion of Cuccoli et. al. [40] who showed that the magnetic properties of 2D XXZ Heisenberg antiferromagnets are strongly affected by the easy-axis anisotropy even if it is much smaller than the dominant magnetic exchange coupling.

The similar crossover of the critical behaviour from higher to lower dimensionality and/or to different spin degrees of freedom were also observed in different 3D quantum magnets (Table 5.1), where the value of the critical exponent became smaller with temperature deacrease.

Series of S=$\frac{1}{2}$ and S=$\frac{5}{2}$ layered magnets such as K_2CuF_4, $MnPS_3$ and $BaNi_2P_2O_8$ follow to the exponential law with critical exponents of the 3D magnetic systems with different spin degrees of freedom just below the T_N, but at slightly lower temperatures display the crossover to the 2D XY magnetic system (Table 5.1).

5.3.3 Above T_N: Correlation length of $BaNi_2V_2O_8$

To investigate the thermal decay of the spin-spin correlation function in $BaNi_2V_2O_8$, the temperature dependence of the correlation length was measured and analysed using different approaches. For this reason, both energy-integrated A3 and Q scans were measured through the (1,0,$\frac{1}{2}$) magnetic Bragg peak at different temperatures above T_N=47.75meV using the TASP spectrometer which was operated in two-axis mode. The collected data then were analysed using a conventional Lorentzian function convolved with a resolution function and the correlation length was extracted from the inverse full width at half maximum as is discussed below. The Lorentzian function was used because it is a Fourier transform of the exponential function which typically describes the spatial decay of the spin-spin correlation function in direct space.

All measurements were performed in the (h-k/2,k,h/2) scattering plane, and the Q scans were measured along (1-$\frac{k}{2}$,k, $\frac{1}{2}$) direction (see example scans in Figure 5.5(a-b)). Because the (-2,0,1) nuclear Bragg peak has half the d-spacing of the (1,0,$\frac{1}{2}$) magnetic Bragg peak, the collected energy-integrated magnetic signal contains a $\frac{\lambda}{2}$ contamination. This contamination is clearly observed at high temperatures, where the magnetic signal becomes weaker and its intensity becomes comparable with the 2nd order of nuclear Bragg peak whose intensity is temperature independent. Indeed, Fig.5.5 shows the A3 and Q scans through the (1 0 $\frac{1}{2}$) magnetic Bragg peak at 75K and 100K, respectively, where the sharp features in the vicinity of -74.16°in A3 scan and k=0 in Q scan corresponds to the (-2,0,1) nuclear Bragg peak contamination.

To analyse the collected data and to extract the temperature dependence of the FWHM of the A3 and Q scans, the fitting function was introduced:

$$F_{L*P}(x) = A \cdot \int_{-\infty}^{\infty} F_P(t) * L(x-t)dt \tag{5.9}$$

$$L(x) = \frac{\frac{W_L}{2}}{\left(\frac{W_L}{2}\right)^2 + (x-x_0)^2} \tag{5.10}$$

Here F_P is the Pearson VII function (eq.5.4), which takes into account the instrumental resolution effects, and L(x) is a conventional Lorentzian function (eq. 5.10) where W_L is the Lorentzian width, x_0 is a peak position and A is the area under the peak. To take into account

the resolution effects is necessary in order to distinguish the contribution of the resolution broadening into the total width which is experimentally measured. The parameters of the resolution function were fixed at the values Wp=0.3855°, m=4.65 and Wp= 0.0102 m=3.7433 for the analysis of the A3 and Q scans at finite temperatures, respectively. These resolution parameters were extracted from the analysis of the A3 and Q scans at base temperature using the F_{L*P} (x) function with fixed the parameter WL which tends to zero. The infinite integral in the convolution was replaced by the definite integral over a region, which greatly exceeds the region of the fitted peak. During the analysis of the A3 scans the integration was done over the range [-200°,200°] while the FWHM of the peaks vary (depending on the temperature) within the range 1°-20°. During the analysis of the Q scans the integration range was [-15:15] while the FWHM of the peak varies approximately from 0.02 to 1.1.
In order to remove the nuclear contamination from the collected data, the (-1,2,0) nuclear Bragg peak in the A3 scan at 75K and in the Q scan at 100K were fitted using the sum of the Gaussian function with the background contribution and, simultaneously, with the function F_{L*P} which describes the magnetic signal taking into account the resolution effects. The results are plotted in Fig. 5.5(a-b) (solid red line), and the extracted parameters of the nuclear peak were kept fixed for the fit analysis at the lower temperatures using the fact that the intensity of the nuclear Bragg peak is temperature independent.
Keeping fixed the extracted parameters of the nuclear peak and the parameters of the resolution function, the A3 and Q scans at different temperatures were fitted by the function F_{L*P} with varying parameters of the peak position (x_0), Lorentzian width (W_L) and the integrated area (A). Although the nuclear Bragg peak contamination was taken into account, the line shapes of both A3 and Q scans just above the ordering temperature T_N=47.75meV and below the temperature of T=53K cannot be reproduced by F_{L*P}. Indeed, Figure 5.6(a-b) shows the Q and A3 scans measured through the $(1,0,\frac{1}{2})$ magnetic Bragg peak at 49K which were fitted using the F_{L*P} function (dashed blue line on Fig.5.6(a-b)). The fitted line obviously does not correctly reproduce the experimental data in both scans. Since there is no reason to assume that the parameters of the resolution function are different from the one extracted at base temperature, this result implies that the integrated intensity of the magnetic signal does not follow to the conventional Lorentzian behaviour. However, at higher temperatures ($T \geqslant 53K$) the line shape of the peaks in both A3 and Q scans is described well by the function F_{L*P} (Fig. 5.6(c-d)).
The values of the FWHM extracted from the fit analysis using the F_{L*P} with varied parameters within the temperature region from 48K to 53K are incorrect because the maximum of the fitted line is much lower than the intensity of the experimental data. In order to extract the correct values of the Lorentzian width, the Q and A3 scans were fitted manually within the temperature region from 48K to 53K using the same function F_{L*P} so that the width and maximum of the fitted line match the experimental data even though the fit is poor further from the maximum (solid red line on Fig.5.6(a-b)). To get the error of the parameters ex-

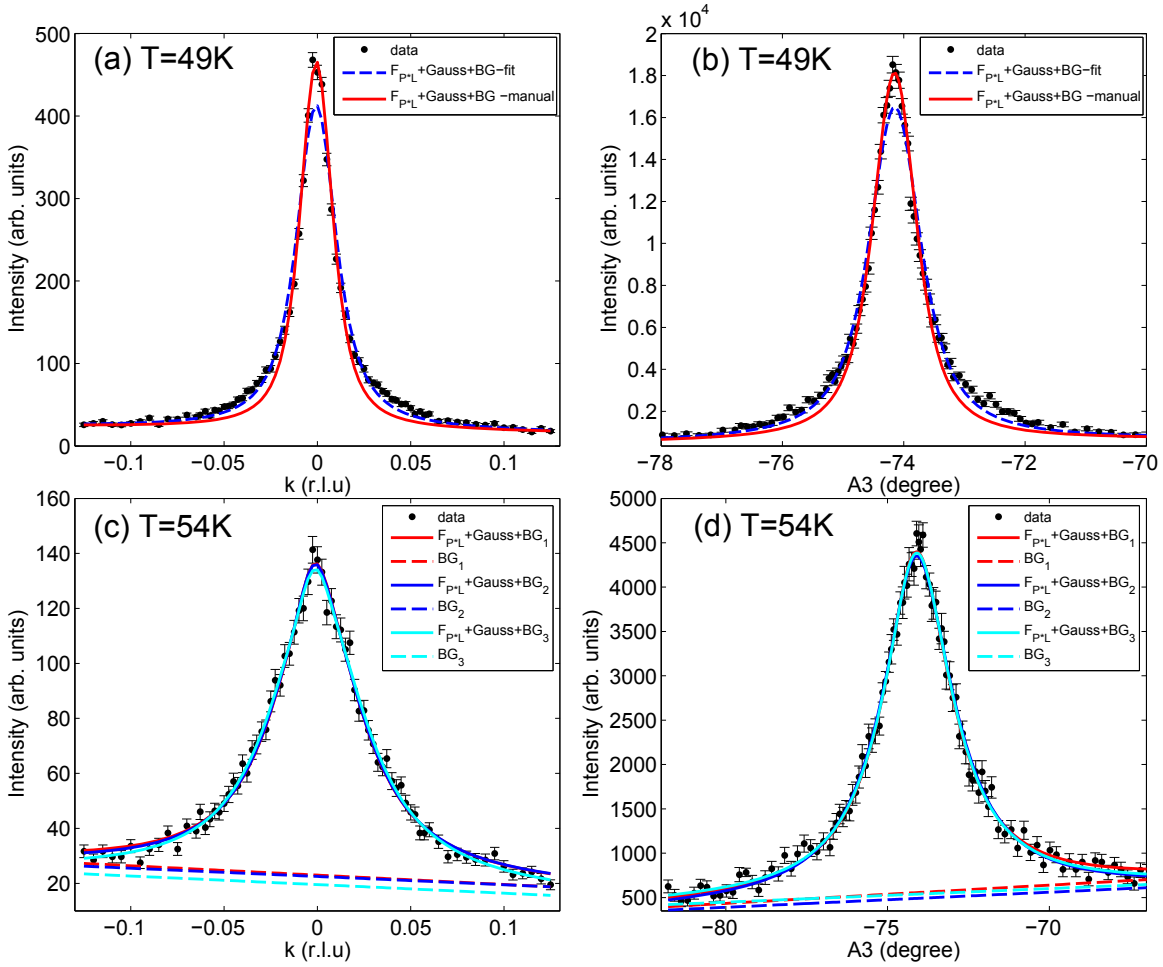

Figure 5.6: (a) A3 and (b)Q scan through the (1,0,0.5) magnetic Bragg peak at T=49 K fitted by the F_{L*P} function taking into account a flat background and nuclear Bragg peak contribution manually (solid red line) and automatically (solid blue line), respectively (c)Q scan through the $(1,0,\frac{1}{2})$ magnetic Bragg peak at T=54K fitted automatically by F_{L*P} at different fixed backgrounds. The varied W_L for the three backgrounds were found to be of $W_{L_{BG1}}$=0.0533±0.1099 ($\xi_{Q_{BG1}}$=15.026Å^{-1}±0.292Å^{-1}), $W_{L_{BG2}}$=0.054±0.106 ($\xi_{Q_{BG2}}$=14.827Å^{-1}±0.274Å^{-1}), $W_{Q_{BG3}}$=0.0586±0.1014 ($\xi_{Q_{BG3}}$=13.681Å^{-1}±0.332Å^{-1}). The averaged correlation length over the values $\xi_{Q_{BG}}$ with different background was found to be $\bar{\xi_Q}$=14.51Å^{-1}±0.66Å^{-1} (d) A3 scan through the $(1,0,\frac{1}{2})$ magnetic Bragg peak at T=54K fitted automatically by F_{L*P} with different fixed backgrounds. The varied W_L were found to be of $W_{L_{BG1}}$=2.56±0.04 ($\xi_{A3_{BG1}}$=15.47Å^{-1}±0.24Å^{-1}), $W_{L_{BG2}}$=2.71±0.04 ($\xi_{A3_{BG2}}$=14.61Å^{-1}±0.22Å^{-1}), $W_{L_{BG3}}$=2.59±0.05 ($\xi_{A3_{BG3}}$=15.24Å^{-1}±0.31Å^{-1}). The averaged correlation length over the values $\xi_{A3_{BG}}$ with different background was found to be $\bar{\xi_{A3}}$=15.1Å^{-1}±0.4Å^{-1}

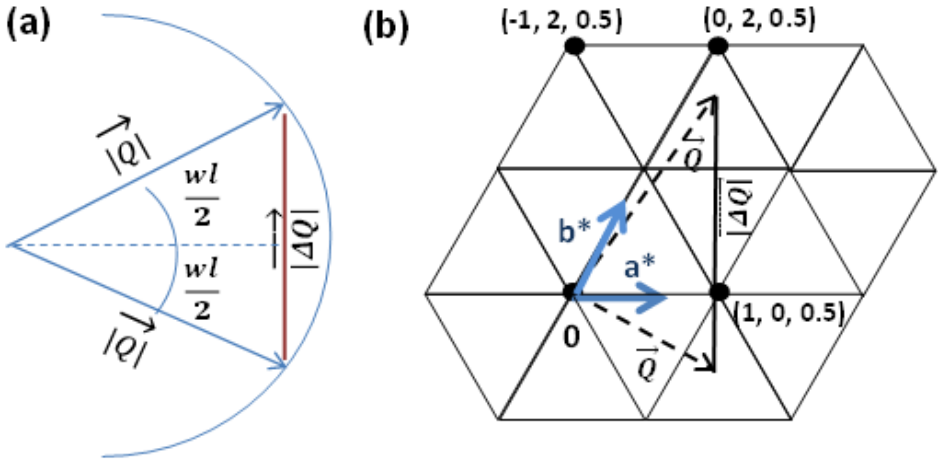

Figure 5.7: Sketch of the relation between the change of the wave vector trasfer $\Delta\bar{Q}$ and the (a) A3 angle in the A3 scan (b) k component in the Q scan.

tracted from this manual fit, the parameters of the Lorentzian width W_L and the integrated area A were manually varied for each scan and the maximum, minimum and optimum values of the parameters were extracted.

At higher temperatures the background is increasing and becomes comparable with the magnetic signal. Therefore, its contribution might influence on the results of the fit analysis. In order to take into account the error due to the ambiguous background subtraction at higher temperatures, the several backgrounds subtractions were applied for each temperature above 53K. The examples are presented in Fig. 5.6(c-d), and the extracted values of the $W_{L_{BG}}$ (and corresponding values of the correlation length) are given in the figure caption in order to give a feeling for how the background subtraction influences the results.

The correlation length was calculated from the inverse Lorentzian width, which was extracted from the fit analysis of the A3 and Q scans. The Lorentzian widths, which were extracted from the analysis of A3 scans, have degree units which can be converted to the inverse angstrom units using the following relation which is illustrated in Fig. 5.7(a):

$$|\Delta\vec{Q}_{(1,0,\frac{1}{2})}| = 2|\vec{Q}_{(1,0,\frac{1}{2})}| \cdot sin\left(\frac{W_{L_{deg}}}{2} \cdot \frac{\pi}{180}\right) \tag{5.11}$$

This relation connects the width in term of the A3 angle with the width in term of the wave vector transfer $\Delta\vec{Q}$ (Fig.5.7 (a)). Here $W_{L_{deg}}$ is the Lorentzian width extracted from the analysis of A3 scans in degree units. $|\vec{Q}_{(1,0,\frac{1}{2})}|$ is the absolute value of the $(1,0,\frac{1}{2})$ wave vector transfer .

Thus, the correlation length in the angstrom units is connected with the Lorentzian width

extracted from the analysis of the A3 scan in the degree units by the following relation:

$$\xi(\text{Å}) = \frac{1}{|\Delta\vec{Q}_{(1,0,\frac{1}{2})}|} = \frac{1}{2|\vec{Q}_{(1,0,\frac{1}{2})}| \cdot sin\left(\frac{W_{L_{deg}}}{2} \cdot \frac{\pi}{180}\right)} \tag{5.12}$$

In order to get the error of the correlation length, the equation eq. 5.12 should be differentiated:

$$\frac{d\xi}{dW_{L_{deg}}} = \frac{\pi}{180 \cdot 2 \cdot 2 \cdot |\Delta\vec{Q}_{(1,0,\frac{1}{2})}|} \cdot cot\left(\frac{W_{L_{deg}}}{2} \cdot \frac{\pi}{180}\right) \tag{5.13}$$

$$\Delta\xi(\text{Å}) = \frac{\Delta W_{L_{deg}} \cdot \pi}{180 \cdot 2 \cdot 2 \cdot |\Delta\vec{Q}_{(1,0,\frac{1}{2})}|} \cdot cot\left(\frac{W_{L_{deg}}}{2} \cdot \frac{\pi}{180}\right) \tag{5.14}$$

The last equation 5.14 connects the error of the correlation length $\Delta\xi$ in the angstrom units with the fitting error $\Delta W_{L_{deg}}$ of the Lorentzian width $W_{L_{deg}}$ in the degree units.
In the Q scans the wave vector transfer $\vec{Q}_{(1,0,\frac{1}{2})}$ does not lie in the (a*b*) plane, however, its change $|\Delta\vec{Q}_{(1,0,\frac{1}{2})}|$ lies within the plane along the (-1,2,0) direction and is proportional to the change of the k coordinate (Fig. 5.7(b)). That means that the extracted Lorentzian width $W_{L_{Q_k}}$ of the Q scan in terms of k can be converted to the inverse angstrom units using the following transformations:

$$W_{L_{Q_{\text{Å}^{-1}}}} = W_{L_{Q_k}} \cdot sin(60) \cdot a^* = W_{L_{Q_k}} \cdot sin(60) \cdot \frac{2\pi}{a \cdot sin(120)} \tag{5.15}$$

Here $W_{L_{Q_{\text{Å}^{-1}}}}$ is Lorentzian width in the inverse angstrom units, and a^* and a are the lattice constant in the reciprocal and crystal lattice, respectively. Thus, the correlation length ξ and its error $\Delta\xi$ in the angstrom units can be found using the following equations:

$$\xi(\text{Å}) = \frac{a}{2\pi \cdot W_{L_{Q_k}}} \tag{5.16}$$

$$\Delta\xi(\text{Å}) = \frac{a \cdot \Delta W_{L_{Q_k}}}{2\pi \cdot (W_{L_{Q_k}})^2} \tag{5.17}$$

Here the notations are the same as the notations in the previous equations.
The average $\bar{\xi_{A3}}(\text{Å})$ and $\bar{\xi_Q}(\text{Å})$ of the correlation length over the values $\xi_{T,BG}(\text{Å})$ were extracted separately from A3 and Q scans at each particular temperature T for the different background subtractions (see example in the caption of Fig. 5.6). The errors $\Delta\bar{\xi_T}(\text{Å})$ were calculated according to the formula $\Delta\bar{\xi_T}(\text{Å}) = \sqrt{\sigma^2_{\xi_T} + \Delta\bar{\xi}^2_{T,BG}}$ where $\sigma^2_{\xi_T}$ is the standard deviation of the correlation length $\bar{\xi}_{T,BG}$ calculated at particular background BG from the average value $\bar{\xi}_T$ at the particular temperature T. $\bar{\Delta\xi}_{T,BG}$ is the average value of the errors

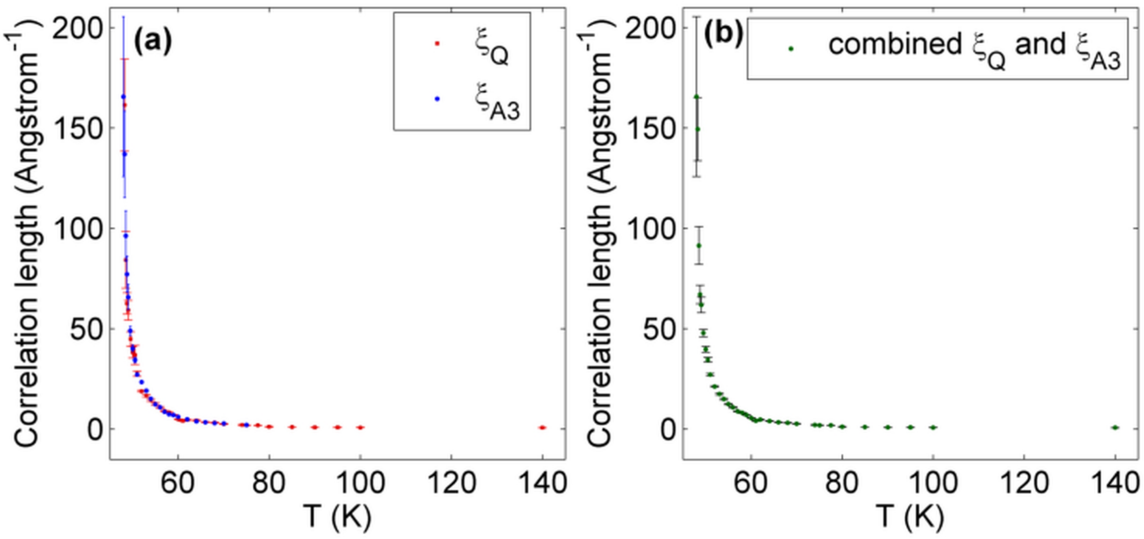

Figure 5.8: (a) Correlation length extracted from the analysis of the A3 (filled blue circles) and Q (filled red squares). (b) The correlation lengths ξ_{A3} and ξ_Q extracted from the analysis of the A3 and Q scans, respectively and combined with the tolerance 0.1K.

$\Delta\xi_{T,BG}$ for different backgrounds at the particular temperature T. For the manually fitted scans at temperatures below 53K the average values of the correlation length $\bar{\xi}_T$ were found by averaging of the correlation lengths calculated from the maximum, minimum and optimum values of the Lorentzian width at particular temperature T. The error $\Delta\bar{\xi}_T$ was calculated as a standard deviation.

Figure 5.8(a) shows the correlation lengths $\bar{\xi_{A3}}$(Å) and $\bar{\xi_Q}$(Å) extracted from the analysis of the A3 and Q scans, respectively, and plotted as a function of temperature. Their comparison reveals that they agree well with each other within the error. For further analysis the correlation lengths $\bar{\xi_{A3}}$(Å) and $\bar{\xi_Q}$(Å) were combined with the tolerance less than the temperature step. Thus, the values at the same temperatures were algebraically averaged (Fig. 5.8(b)).

5.3.3.1 Power Law analysis

In order to explore the magnetic properties of $BaNi_2V_2O_8$ above the transition temperature T_N, the temperature dependence of the correlation length $\bar{\xi}$(Å) extracted in the previous subsection was analysed using the conventional power law [46; 75]:

$$\xi_T = A \cdot \left(\frac{T - T_N}{T_N} \right)^{-\nu} \tag{5.18}$$

Here A is a scaling factor, T_N is the ordering temperature and ν is the universal constant which characterises the class of the magnetic correlations in the magnetic system and can

take values of ν=0.64 (3D Ising - space dimensionality d=3, spin components n=1), ν=0.66 (3D XY - d=3, n=2) , v=0.7 (3D Heisenberg system - d=3, n=3) or ν=1 (2D Ising system - d=2, n=1) [46; 75]. Assuming the ordering temperature of T_N=47.75K, the temperature dependence of the correlation length $\bar{\xi}$(Å) was fitted using the power law (eq. 5.18) over the whole temperature range 48K-140K. The scaling factor A was varied depending on these different fixed values of power ν in the assumption that the behaviour is consistent over explored temperature range and there are no magnetic crossovers.

The results of the fit analysis are plotted over the data and reveal that the data do not exactly correspond to any of the magnetic structures which were listed above, although the power law for 2D Ising system (ν=1) provides a better fit than the others. Fig. 5.9(a)(solid red line with red dots) presents the power law fit when the power ν and the scaling factor A were simultaneously varied. The value ν=1, which corresponds to 2D Ising system, is the closest to the extracted value of the power ν=1.15 and indicates the 2D Ising-like behaviour of the critical exponent.

These results are valid only in the assumption of the absence of crossovers in the magnetic behaviour within the fitted temperature region 48K-140K. In order to check this, the inverse correlation length was plotted in logarithmic scale as a function of the natural logarithm of the reduced temperature $\varepsilon = \left(\frac{T}{T_N} - 1\right)$ where T_N=47.75K is the ordering temperature (Fig. 5.9 (b)). The inverse correlation length plotted as a function of reduced temperature in logarithmic scale should follow a straight line, whose slope corresponds to the value of the power ν:

$$\ln(\xi_T) = +\ln A - \nu \ln\left(\frac{T}{T_N} - 1\right) \tag{5.19}$$

The results plotted in Figure 5.9(b) and reveal that the data cannot be fitted by the single straight line over the whole temperature range. Indeed, the observed temperature dependence of the correlation length plotted in logarithmic scale noticeably deviates from the straight line: just above T=48K and at high temperatures above 80K. The analysis of the intermediate temperature region of 48.25K-77.5K reveals that the data within this temperature region also cannot be fitted using the single straight line, and, at least, two different linear regions exists. First region is T=48.25K-54K and characterized by the power law with the value of ν=0.9 which is close to the value ν=1 for the 2D Ising model. The second region is over the temperature range T=54K-77.5K and is characterized by the power law with the power of ν=1.37 which does not correspond to any known values which were listed above. It is interesting to note that this crossover temperature of T=54K is just above that where a change of peak shape was observed, as discussed in section 5.3.3.

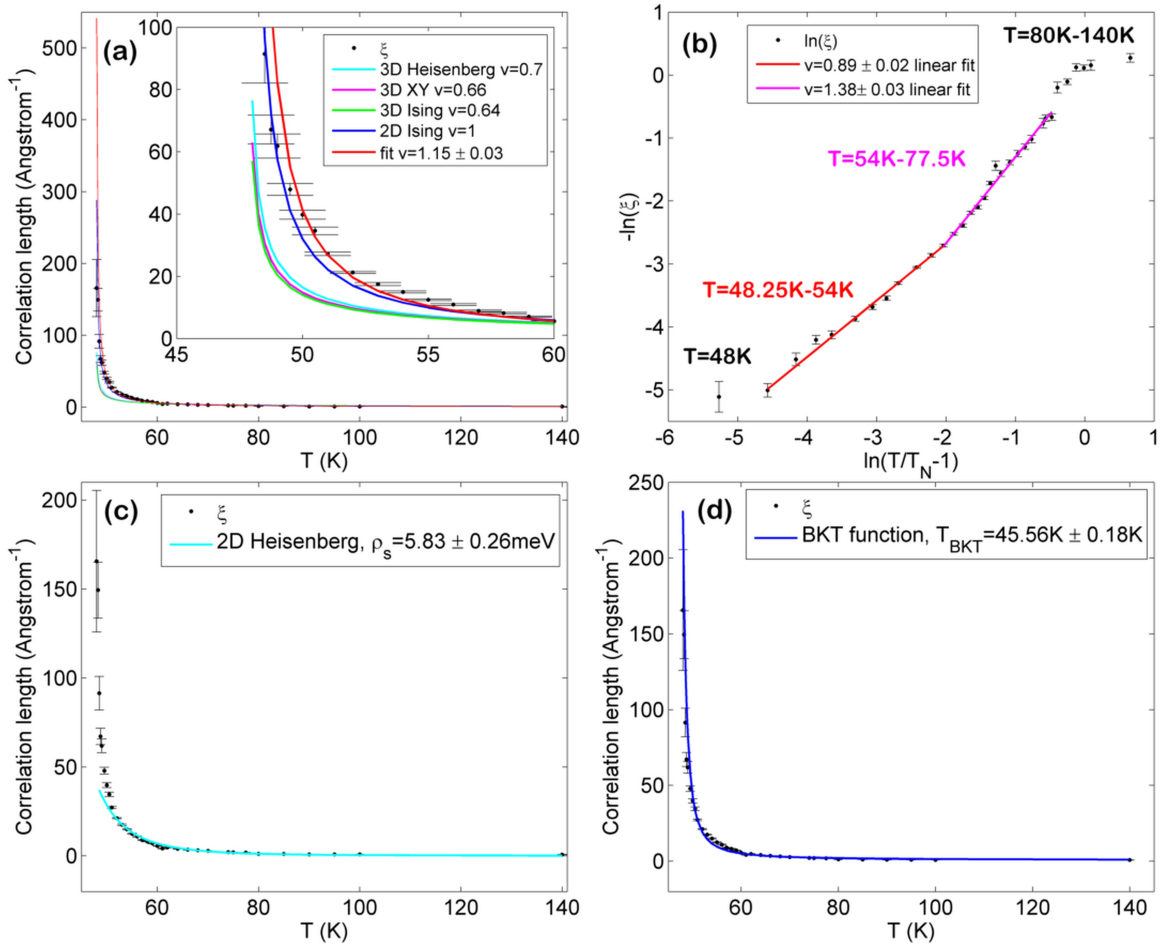

Figure 5.9: (a) Temperature dependence of the correlation length fitted using the power law with the different fixed values of the power. (b) Temperature dependence of the correlation length plotted in the logarithmic scale and fitted using the linear function. (c) Temperature dependence of the correlation length fitted using the equation for the 2D Heisenberg model. (d) Temperature dependence of the correlation length fitted using the Berezinskii-Kosterlitz-Thouless approach.

5.3.3.2 2D Heisenberg approach

Because the thermal decay of the correlation length $\bar{\xi}$(Å) in $BaNi_2V_2O_8$ was found to be different from the conventional power law [46; 75], the data were analysed using the results of the renormalization group calculations for 2D Heisenberg system [76]. This model does, of course, not include Ising anisotropy or interplane coupling, and therefore long-range magnetic order is expected only at T=0K.

Using the low temperature renormalization group calculations Chakravarty, Halperin and Nelson (CHN) predict that the temperature dependence of the correlation length $\xi(T)$ in the 2D Heisenberg system in the vicinity of the ordered state at T=0K is described by the relation [76]:

$$\xi(T) = C_\xi \cdot a \cdot \exp\left(\frac{2\pi\rho_s}{k_B T}\right) \tag{5.20}$$

Here a is a lattice constant, the C_ξ is non-universal constant which depends on the system and ρ_s is the non-universal spin-stiffness constant at T=0. This relation claims to be universal, and, therefore, the equation 5.20 can be applied for the analysis of the temperature dependence of the correlation length extracted from $BaNi_2V_2O_8$ if the non-universal parameters of C_ξ and ρ_s are set as variables.

Figure 5.9(c) presents the results of the fit analysis of the temperature dependence of the correlation length in $BaNi_2V_2O_8$ using the 2D Heisenberg approach (eq. 5.20). The results reveal a perfect agreement with the experimental data above the temperature T=52K. However, at lower temperatures (below T=52K) the 2D Heisenberg model does not reproduce the data. To extract the accurate value of the spin stiffness, the data were fitted using 2D Heisenberg approach (eq. 5.20) over the temperature range of T=52K-140K. The extracted value of the spin stiffness was found to be ρ_s=5.34meV$\pm$0.22meV. Although there is no exact calculations of the spin stiffness for the honeycomb lattice, the relation for the spin stiffness constant ρ_s with nearest neighbour exchange coupling J was derived for the S=1 square lattice system within the spin-wave approximation [77; 78]:

$$\rho_s = Z_{\rho_s}(S) J_{2D} S^2 \tag{5.21}$$

where

$$Z_\rho(S) = 1 - \frac{0.235}{2S} - \frac{0.041}{(2S)^2} + O\Big(\frac{1}{2S}\Big)$$

Here S is a spin value and J_{2D} is the first-nearest neighbour magnetic exchange interaction. This equation was derived for the Hamiltonian where the magnetic exchange interaction were counted twice. Therefore, $J_{2D}=\frac{J_n}{2}$, and J_n is the first-nearest neighbour magnetic exchange interaction in the Hamiltonian (eq. 4.6).

Assuming that the relation for Z_ρ(S) for the S-1 system with a honeycomb lattice is similar to

the S-1 system with a square lattice, the first-nearest neighbour magnetic exchange interaction J was estimated and was found to be J_{2D}=6.12 meV ± 0.25meV. Taking into account the difference in the definition of the Hamiltonians which was discussed above, the value $2J_{2D}$ =12.24±0.5 meV is found to be in good agreement with the value J_n=12.3 meV which was extracted from the spin-wave analysis (see Chapter 4). In conclusion, the 2D Heisenberg model goes an adequate and consistent description of the correlation length at temperature above 52K.

5.3.3.3 Berezinskii-Kosterlitz-Thouless approach

To complete an investigation of the spin correlations in $BaNi_2V_2O_8$ at finite temperatures, the Berezinskii-Kosterlitz-Thouless approach (BKT) [14; 15; 16; 17] was applied for the analysis of the experimental data.
According to the Berezinskii-Kosterlitz-Thouless theory the 2D XY magnetic system has a topologically quasi-ordered state which is characterized by the strongly bound vortex - antivortex pair formation below the transition temperature T_{BKT}. Above the transition temperature T_{BKT} the vortex - antivortex pairs decompose forming the plasma of moving vortices which can be experimentally observed as an exponential thermal decay of the correlation length:

$$\xi_{BKT} = A \cdot \exp\left(b \cdot \left(\frac{T}{T_{BKT}} - 1\right)^{-0.5}\right) \tag{5.22}$$

Here b is non-universal constant which was found to be b=1.5 for the square crystal lattice, A is a scaling factor and T_{BKT} is the Berezinskii-Kosterlitz-Thouless transition temperature. Initially, the BKT topological phase transition was proposed only for the 2D XY classical model where long range order is prohibited by the Mermin-Wagner theorem [12]. Later, S. Hikami and T. Tsuneto showed for the 3D planar layered magnetic systems with a weak interplane coupling that if the intraplane correlation length is less than the order of the effective scale $L_{eff} = \sqrt{\frac{J_n}{J_{out}}} \cdot d$, this magnetic system behaves as a true two-dimensional (2D XY) magnet [79]. Here J_n and J_{out} are the in-plane first-neighbour and out-of-plane magnetic exchange interactions, respectively, and d is an interlayer distance. This concept /(criteria) was widely applied for the search of the Berezinskii-Kosterlitz-Thouless phenomena in the superconducting thin films which are good physical realization of the quasi-2D XY models [80; 81; 82]. Recent Quantum Monte Carlo simulations reveal that BKT phenomena can also exist in 2D XXZ Heisenberg magnets with weak in-plane anisotropy [40]. These results together have suggested the possibility to search for BKT phenomena in 3D solid-state magnetic compounds with layered magnetic structures and magnetic ions with XXZ anisotropy. A number of honeycomb antiferromagnets were found to be good candidates [46; 72; 73].
These criteria make $BaNi_2V_2O_8$ a relevant magnetic system for an analysis within the Berezinskii-

Kosterlitz-Thouless approach. Indeed, $BaNi_2V_2O_8$ has a layered crystal structure and the neutron diffraction data reveal that the magnetic properties of $BaNi_2V_2O_8$ are described well by the 2D XXZ Heisenberg model just below the transition temperature T_N=47.75K. Moreover, using the values of the first-nearest neighbor magnetic exchange interaction J_n = 12.3meV and the largest possible interplane coupling J_{out3} = 0.0012meV of $BaNi_2V_2O_8$ extracted in Chapter 4 and the interlayer distance d=7.45Å [47], the effective length L_{eff}, where the three-dimensional ordering starts to play a role, is estimated to be L_{eff}≈754Å. This estimated value of the effective length is much larger than the largest value of the correlation length ξ_{48K}=163Å observed at T=48K. This implies, according to the S. Hikami and T. Tsuneto criteria [79], that at the temperature of T=48K and higher, $BaNi_2V_2O_8$ behaves as a 2D magnet. Thus, the Berezinskii-Kosterlitz-Thouless approach, which was originally proposed for the 2D XY model and later extended for 2D XXZ Heisenberg magnets, can be applied for the analysis of the temperature dependence of the correlation length of $BaNi_2V_2O_8$ over the whole temperature range from 48K to 140K.

Figure 5.9 (d) shows the temperature dependence of the correlation length in $BaNi_2V_2O_8$ fitted using the Berezinskii-Kosterlitz-Thouless equation (solid blue line) with b fixed to 1.5. The results reveal good agreement with the experimental data over the whole temperature range 48K-140K which is the best fit from the all applied models. The transition temperature is extracted to be T_{BKT}=45.56K±0.18K, and the scaling factor is A=0.352Å.

The ratio of the first-neighbour magnetic exchange interaction J_n to the interplane magnetic exchange coupling J_{out} in $BaNi_2V_2O_8$, which would correspond to this transition temperature within 2D XY isotropic model, can be estimated. Indeed, as was discussed above, S. Hikami and T. Tsuneto [79] suggested that the layered magnets behave as a 2D XY system if the correlation length ξ_{2D} is less than $L_{eff}=\sqrt{\frac{Jn}{J_{out}}}\cdot d$, and the three-dimensional ordering exists only when the correlation length is of the same order as L_{eff}. Within the 2D regime the correlation length ξ_{2D} should follow to the Berezinskii-Kosterlitz-Thouless equation (eq. 5.22). This gives to the boundary condition for the effective correlation length L_{eff} which should be satisfied at the $T=T_N$, since at $T=T_N$ the system starts to display the three-dimensional ordering.

$$L_{eff} = A \cdot \exp\left(b \cdot \left(\frac{T_N}{T_{BKT}} - 1\right)^{-0.5}\right) \tag{5.23}$$

where

$$L_{eff} = \sqrt{\frac{Jn}{J_{out}}} \cdot d \tag{5.24}$$

Here T_N=47.75K is the ordering temperature extracted from the neutron diffraction data. Using the values T_{BKT}=45.56, A=0.352Å extracted from the fit analysis of the experimental

data the ratio $J_n J_{out}$ is found to be:

$$\frac{Jn}{J_{out}} = 1986 \tag{5.25}$$

The extracted value $\frac{Jn}{J_{out}} = 1986$ within quasi-2D XY model is remarkably different from the ratio $\frac{Jn_{sw}}{J_{out_{sw}}} = 10250$ extracted from the analysis of the single crystal neutron scattering data using the spin-wave theory with the anisotropic Heisenberg Hamiltonian (eq. 4.1). This result implies that the magnetic interplane coupling should be ≈ 5 times larger than the interplane coupling extracted from the analysis within 2D XXZ Heisenberg model with weak easy-axis anisotropy in order to achieve long-range order at T_N=47.75K. It stresses the importance of the weak easy-axis anisotropy in the Hamiltonian of $BaNi_2V_2O_8$ for the formation of the long-range order. The value of the interplane magnetic exchange coupling extracted from the spin-wave theory is cleary not strong enough to create the long-range ordered state in $BaNi_2V_2O_8$ alone at the transition temperature T_N=47.75K. Indeed, the substitution of the ratio $\frac{Jn_{sw}}{J_{out_{sw}}} = 10250$ extracted from the spin-wave theory to equation 5.23 allows the ordering temperature within quasi-2D XY model for these in-plane and out-of-plane magnetic exchange couplings to be estimated. Solving the equation 5.23 with respect to T_N gives the solution for the ordering temperature T_N=47.25K within 2D XY model which is lower than the experimentally observed ordering temperature T_N.

5.3.3.4 Discussion

The thermal decay of the correlation length in $BaNi_2V_2O_8$ was analysed using the different approaches. It was found that the temperature dependence of the correlation length does not exactly correspond to any of the conventional known power laws. However, the power law for 2D Ising model (ν=1) [46; 75] was found to provide a better fit just above T_N (48K-53K) than the other models in this temperature region, indicating the 2D Ising-like critical behaviour of the magnetic system. This result is in agreement with the observations for the critical exponent and is consistent with the presence of the weak easy-axis anisotropy in the derived Hamiltonian of $BaNi_2V_2O_8$.

Since the power law does not unambiguously characterize the type of magnetic structure of $BaNi_2V_2O_8$, the temperature dependence of the correlation length was analysed within the 2D Heisenberg approach which is based on the renormalization group calculations [76]. Although this approach does not take into account the Ising-anisotropy and the interplane coupling, it reproduces the experimental data well for temperatures T>52K. The value of the first-neighbour magnetic exchange interaction J_{2D}=6.12meV$\pm$0.25meV estimated from the fit analysis within 2D Heisenberg approach [76; 77; 78] agrees well with the value J_n=12.3meV extracted from the simulations of the magnetic excitation spectrum based on the linear spin-

wave theory. Indeed, taking into account the relation $J_{2D}=\frac{J_n}{2}$ due to the difference of the definitions of the Hamiltonians, the scaled value $2J_{2D}$=12.24meV ±0.5 meV is almost the same with the value J_n=12.3meV extracted from the analysis of the energy dispersion using linear spin-wave theory.

Within the temperature region below T=52K the 2D Heisenberg approach [76] does not fit the data. Moreover, the line shape of the integrated magnetic signal over this temperature range was found to be different from the convolution of the instrumental resolution function with the conventional Lorentzian function. The unconventional behaviour of the line shape of the collected data at the temperatures T=48K-52K suggests the unconventional spin-spin correlations within this temperature range. Thus, it was shown that neither power law [46; 75] nor 2D Heisenberg approach[76] reproduce the temperature dependence of the correlation length of $BaNi_2V_2O_8$ within whole temperature region 48K-140K.

The comparison of the highest experimental value of the correlation length ξ_{48K}=163Å at T=48K with the criteria suggested by S. Hikami and T. Tsuneto [79] implies that above the temperatures T⩾48K $BaNi_2V_2O_8$ behaves as a 2D magnet. This observation is in agreement with the results of the diffraction neutron scattering data which reveal that $BaNi_2V_2O_8$ is described well by 2D XXZ Heisenberg model just below the transition temperature.

Since $BaNi_2V_2O_8$ is more likely in 2D regime rather than in 3D at the temperature of T⩾48K, the data were analysed within the Berezinskii-Kosterlitz-Thouless approach [14; 15; 16; 17] over the whole temperature range 48K-140K. This approach fits the experimental data well over whole temperature region and the transition temperature is found to be T_{BKT}=45.56K±0.18K. This value is consistent with, although slightly larger, than the transition temperatures T_{BKT}=43.3K [49] and T_{BKT}=40.2K±0.5K [63] published in the literature and which were based on the analysis of the temperature dependences of the ESR linewidth and longitudinal ^{51}V relaxation time measured in $BaNi_2V_2O_8$, respectively. This difference could be attributed to the difference between the temperature regions which were analysed. Indeed, the ESR measurements were performed by M. Heinrich and et. al. [49] over the temperature range above the temperature T=50K which was believed to be the ordering temperature based on the powder neutron diffraction data [47]. Later, Waibel et. al.[63] specified the ordering temperature to be T_N=48.1K as a temperature where the transition from the paramagnetic phase to the spin-flop phase was experimentally observed in the NMR measurements of $BaNi_2V_2O_8$. However, the precise single crystal elastic neutron scattering measurements described in the present work (see subsection *Ordering temperature*) reveal that the ordering temperature lies within the temperate region 47.5K-47.75K, and therefore the temperature dependence of the correlation length of $BaNi_2V_2O_8$ in the presented work was explored within the temperature region T=48K-140K with particularly tiny step of 0.25K within the temperature region of T=48K-49K.

The comparison of the different aproaches reveals that the Berezinskii-Kosterlitz-Thouless theory is the only one which reproduces well the temperature dependence of the correla-

tion length in $BaNi_2V_2O_8$ over the whole temperature range (T=48K-140K) including the temperature range of T=48K-53K where the line shape was found to be different from the convolution of the instrumental resolution function with the conventional Lorentzian function.

5.4 Conclusions

In this chapter the comprehensive analysis of the critical behaviour in $BaNi_2V_2O_8$ have been done using diffraction neutron scattering measurements. The ordering temperature was found to lay within the temperature range 47.5K-47.75K and was set to be T_N=47.75K for the data analysis.

Two temperature regions below and above the ordering temperature were explored. Both a critical exponent and a thermal decay of the correlation length were measured and analysed using the several approaches. This analysis provides the complete phase diagram of the magnetic structure of $BaNi_2V_2O_8$ which is presented in Fig. 5.10.

The investigation of the temperature dependence of the correlation length reveals that $BaNi_2V_2O_8$ is described well by the isotropic 2D Heisenberg model [76] at high temperatures T$\geqslant$52K. This result agrees well with the proposed Hamiltonian (eq.4.6). Indeed, at high temperatures only the dominant term of this Hamiltonian, which is the first-neighbour Heisenberg isotropic magnetic exchange interactions within the plane, plays role and only isotropic nearest neighbour correlations exist in the system at the temperatures above T=52K.

When the temperature is decreasing, weaker terms of the Hamiltonian such as XY anisotropy start to contribute to the magnetic properties of $BaNi_2V_2O_8$. Although the temperature dependence of the correlation length does not follow to the isotropic 2D Heisenberg model below T=52K, it satisfies the S. Hikami and T. Tsuneto's criteria for 2D XY model [79]. This implies that $BaNi_2V_2O_8$ is in 2D XXZ regime within the temperature region 48K-52K. This results is in agreement with the magnetic susceptibility measurements which reveal that below T=52K $BaNi_2V_2O_8$ clearly displays a behaviour of 2D Heisenberg XXZ magnet with a strong planar anisotropy. Indeed, both $\chi_{||}$ and $\chi_{\perp}$ data have an inflection point or even minimum at the temperature T=52K and below this temperature an anisotropic behaviour of magnetic susceptibility becomes the most pronounced (see Chapter 4.4 for details). Moreover the analysis of the temperature dependence of the spontaneous magnetization just below of the ordering temperature T_N reveals that the magnetic structure of $BaNi_2V_2O_8$ is described well by the 2D XXZ Heisenberg model within the temperature range 46.3K$\leqslant$T$\leqslant$47.5K. The critical exponent was extracted to be β=0.21 within the temperature region 46.3K$\leqslant$T$\leqslant$47.5K which is very close to the theoretical value of β=0.23 proposed for the 2D XXZ magnetic system [65]. These results suggest that when temperature is decreasing below 52K the magnetic excitations evolve from 2D isotropic nearest-neighbour correlations to planar correlations where the free vortex excitations should exist according to the Berezinskii-Kosterlitz-Thouless theory [14; 15; 16; 17] and Quantum Monte-Carlo simulations [40] until long-range order occurs

destroying the vortices.

The presence of the BKT vortex excitations in $BaNi_2V_2O_8$ just above the ordering temperature T_N=47.75K was probed by the analysis of the thermal decay of the correlation length. It was shown that BKT theory provides a good fit for the experimental data at all temperatures above T_N=47.75K , particularly within the temperature region 48K-52K where no other theory can provide an explanation. The transition temperature was extracted to be T_{BKT}=45.56K$\pm$0.18K and corresponds to the temperature where the free vortex excitations would start to occur in the absence of the conventional long-range order. This result implies the presence of the free vortex excitations in $BaNi_2V_2O_8$ above the ordering temperature T_N. The free vortex excitations are especially pronounced within the temperature range 48K-52K where $BaNi_2V_2O_8$ described by the 2D XXZ Heisenberg model but does not have a long-range order.

At the ordering temperature T_N=47.75K the long-range order (LRO) occurs destroying the vortex excitations and the spin-ordered state prevent the spin-vortex formation, although $BaNi_2V_2O_8$ is described by 2D XXZ Heisenberg model just below the ordering temperature T_N (46.3K$\leqslant$T$\leqslant$47.5K).

The transition to the ordered state in $BaNi_2V_2O_8$ is most likely driven by both interplane coupling and Ising in-plane anisotropy. Indeed, using the S. Hikami and T. Tsuneto's criteria[79] it was shown that the interplane coupling J_{out}<0.001 extracted from the analysis of the INS data (see Chapter 4.4 for details) is not strong enough to run the LRO-state at T_N=47.75K alone within the 3D XY model (assuming T_{BKT}=45.56K$\pm$0.18K).

The presence of the Ising in-plane anisotropy was confirmed and experimentally observed in a reduction of the critical exponent when temperature is decreasing. Indeed, the analysis of temperature dependence of the spontaneous magnetization reveals the crossover of the critical exponent from β=0.21 to β=0.172 at the temperature T=46.3K-46.K. The value β=0.172 extracted within the temperature region 30K<T<46K is close to the value β=0.125 for 2D Ising model [75]. The 2D Ising-like behaviour of the $BaNi_2V_2O_8$ at lower temperatures is in agreement with the proposed Hamiltonian of $BaNi_2V_2O_8$ which contains a weak easy-axis anisotropy within the plane. This weak term starts to effects on the magnetic properties of $BaNi_2V_2O_8$ only at low temperatures.

It is remarkable that $BaNi_2V_2O_8$ displays critical properties of 2D magnetic systems both below and above the ordering temperature T_N. This is in contrast to the other layered honeycomb antiferromagnets such as $MnPS_3$ (S=$\frac{5}{2}$) [71; 73] , $BaNi_2P_2O_8$ (S=1) [74] and $BaNi_2As_2O_8$ (S=1) [46] where the crossover of critical exponent from 3D to 2D appeares below the ordering temperature T_N. Indeed, the analysis of the temperature dependence of the spontanious magnetization in these magnetic systems reveals that $MnPS_3$ (S=$\frac{5}{2}$), $BaNi_2P_2O_8$ (S=1) and $BaNi_2As_2O_8$ (S=1) behave as a 3D Heisenberg magnets above and just below T_N and display a behaviour of 2D XXZ magnetic system only below T<0.97T_N.

The transition temperature T_{BKT}=45.56K, extracted from the analysis of the temperature

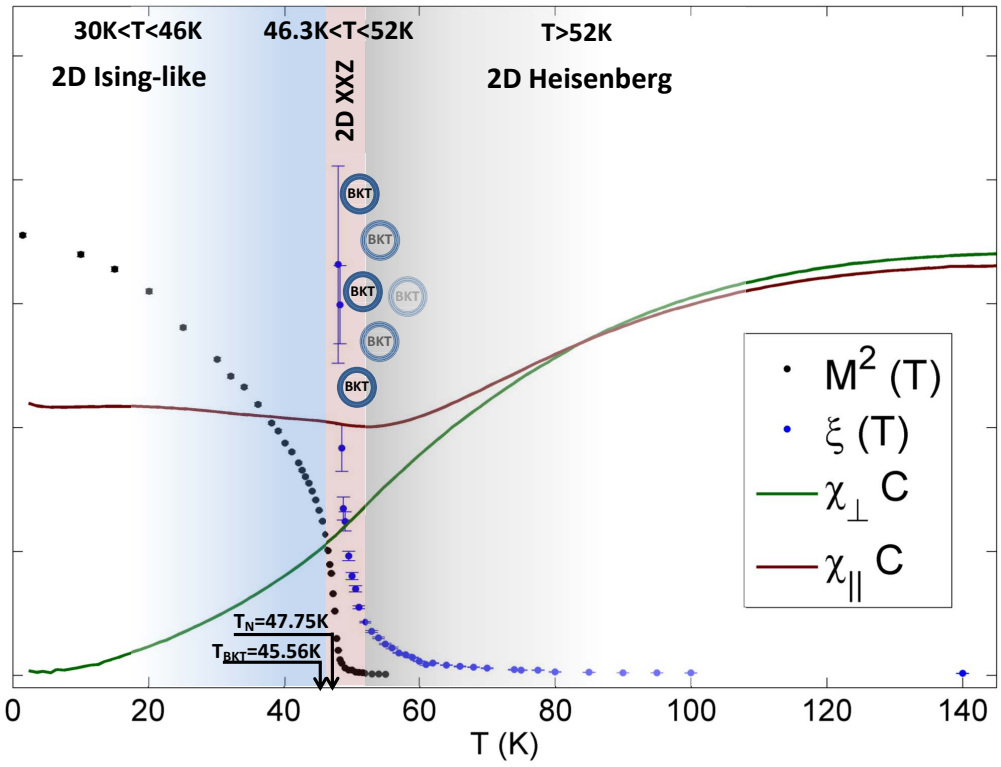

Figure 5.10: Phase diagram of $BaNi_2V_2O_8$. The filled black circles is the temperature dependence of the integrated intensity of the $(1,0,\frac{1}{2})$ magnetic Bragg peak. The filled blue circles is the temperature dependence of the correlation length. The solid dark red and green lines represent the magnetic susceptibility data in perpendicular and parallel direction of the field to the c-axis, respectively. The round empty circles indicate the temperature region where the free vortex excitations are expected.

dependence of the correlation length in $BaNi_2V_2O_8$, lies within the temperature range where $BaNi_2V_2O_8$ is described by the 2D XXZ Heisenberg model but below the T_N=47.75K. This is similar to the relation of the transition temperatures T_{BKT} proposed for $MnPS_3$ (S=$\frac{5}{2}$) [72], $BaNi_2P_2O_8$ (S=1) [46] and $BaNi_2As_2O_8$(S=1) [46] with respect to the corresponding T_N in these compounds. Indeed, in all these compounds the transition temperature T_{BKT} was found to be lower than the ordering temperature T_N and corresponded to the temperature range where the system assigned to 2D XXZ model. However, in contrast to $BaNi_2V_2O_8$, the critical exponents in these compounds follow to the 2D XXZ model only below T_N where the LRO exists and supposed to prevent the free vortex formation.

Thus, $BaNi_2V_2O_8$ is proved to be an unique quasi-two-dimensional antiferromagnet which behaves as a 2D Heisenberg, 2D XXZ or even 2D-Ising-like magnetic system depending on the explored temperature region and where the BKT free-vortex excitations are expected within the temperature region of T=48K-52K, where $BaNi_2V_2O_8$ follows to the 2D XXZ Heisenberg model but does not have the long-range-order jet.

6 Magnetic properties of $BaCu_2V_2O_8$

6.1 Introduction

Dimerized magnets are system where spin-half magnetic ions are strongly coupled into the pairs via antiferromagnetic (AFM) exchange interactions as was discussed in Chapter 2. One pair is called *a dimer* and is characterized by a spin-singlet nonmagnetic ground state and a degenerated S-1 triplet state (s_z=±1,0) which is separated from the ground state by an energy gap Δ (Fig. 6.1(a)). The excitations are called *triplons* and are restricted by the hard - core constraint which allows only one excitation per dimer site [83]. The Hamiltonian of the total system where the dimers do not interact with each other is the sum of the Hamiltonians of all the individual dimers (Fig. 6.1b). However, in real compounds isolated dimers rarely exist and the dimers usually interact with each other via weak (with respect to the dominant intradimer coupling) interdimer magnetic exchange interactions (Fig. 6.1c). In this case the triplon excitations are mobile and can hop from one dimer to another. They can interact strongly with each other via the interdimer magnetic exchange coupling and the hard - core repulsion [84].
The interdimer magnetic exchange coupling can be one-, two- or three-dimensional.
In one-dimension dimerized magnetic systems can form alternating chains as was discussed in Chapter 2. Here, the dimers are coupled one-dimensionally along a particular direction within the crystal lattice forming chains where the strong intradimer magnetic exchange interaction alternates with the weaker interdimer magnetic exchange coupling. The magnetic properties in the absence of the magnetic field are well described by the Hamiltonian [45]:

$$H = \sum_{i=1}^{L/2} J_{\text{intra}}\, \vec{S}_{2i-1} \cdot \vec{S}_{2i} + J_{\text{inter}}\, \vec{S}_{2i} \cdot \vec{S}_{2i+1}. \tag{6.1}$$

here, the J_{intra} is a dominant intradimer magnetic exchange interaction, J_{inter} is a weaker interdimer magnetic exchange coupling, $\vec{S}_{2i}$ is a spin of the magnetic ion at the $2i$ crystal site and L is the total number of the magnetic ions in the system.
Alternating chains are particularly interesting because they can develop strongly correlated behaviour at finite temperatures which was recently observed in the AFM-AFM alternating chain compound copper nitrate [84; 85]. The persistence of correlation effects in this compound was experimentally observed as an asymmetric Lorentzian thermal line shape

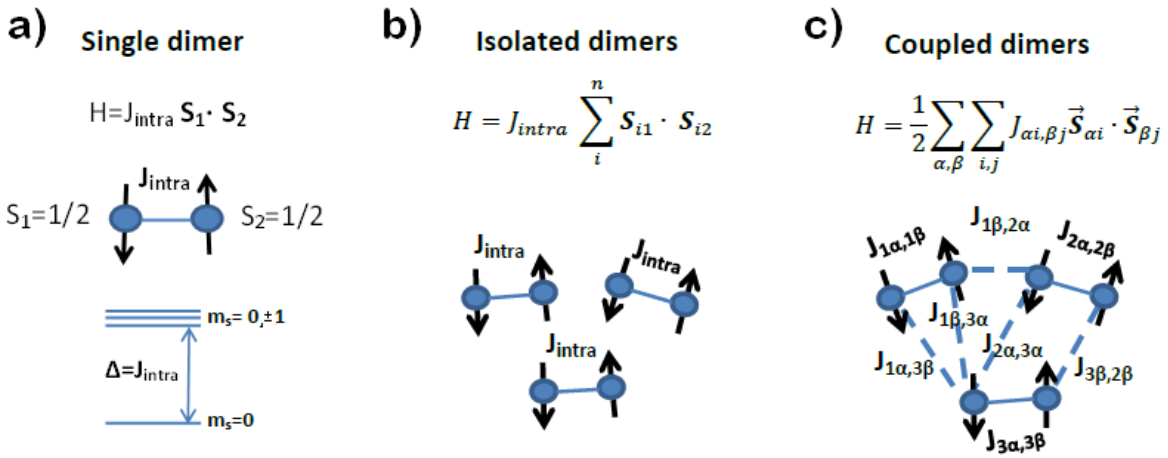

Figure 6.1: (a) Hamiltonian and the sketch of the energy levels of the single dimer. Here, S_1 and S_2 are spins within the dimer, J_{intra} - intradimer magnetic exchange coupling, Δ - energy gap, m_s -component of the spin along a particular axis. (b) Hamiltonian and the sketch of the isolated dimers. Here, S_{1i} and S_{2i} are spins within the i^{th} dimer, J_{intra} - intradimer magnetic exchange coupling, n- the total number of the dimers within the system (c) Hamiltonian and the sketch of coupled dimers. Here, $S_{\alpha i}$ denotes the spin of the α magnetic ion within the i^{th} dimer in a system, $J_{\alpha i,\beta j}$ - denotes the magnetic exchange coupling between the α magnetic ion of the i^{th} dimer with the β magnetic ion of the j^{th} dimer $J_{intra} = J_{\alpha,i,\beta,i}$

broadening of its magnetic excitations which contradicts the conventional picture of temperature effects in magnetism [86]. In the conventional picture the temperature rise induces uncorrelated collisions between the magnetic excitations which are experimentally observed as an symmetric Lorentzian broadening of their line shapes [87; 88; 89]. Because of these collisions, the excitations lose their coherence that results in their damping. The unconventional asymmetric lineshape broadening at finite temperatures observed in copper nitrate was attributed to strongly correlated behaviour which is assumed to be caused by strong interactions between the excitations via the interdimer exchange coupling and the hard-core repulsion [84]. This phenomena is not limited to the one-dimensional case and later was observed in the three-dimensional dimerized antiferromagnet $Sr_3Cr_2O_8$ where the magnetic excitations were found to broaden asymmetrically with increasing temperature similar to the observed thermal behaviour of the magnetic excitations in copper nitrate [84; 85]. Strongly correlated behaviour over a wide temperature range has potential application for quantum devices which are based on quantum coherence and need to be able to work at finite temperatures making the search and investigation of compounds which display this phenomenon an important scientific task.

For the two- and three-dimensional dimerized magnetic systems the Hamiltonian becomes more complicated and can be written as:

$$H = \frac{1}{2}\sum_i J_{\text{intra}}\,\vec{S}_{i\alpha}\cdot\vec{S}_{i\beta} + \frac{1}{2}\sum_{\alpha,\beta}\sum_{i\neq j} J^{inter}_{\text{i}\alpha,\text{j}\beta,}\,\vec{S}_{i\alpha}\cdot\vec{S}_{j\beta} \tag{6.2}$$

Here, the J_{intra} is the intradimer magnetic exchange coupling, $J^{inter}_{i\alpha,j\beta}$ is the interdimer magnetic exchange coupling, i and j denote the dimer sites while the α and β distinguish the two magnetic ions within the dimer.

A typical example of a 2D dimerized magnetic system is the layered antiferromagnet $BaCuSi_2O_6$ where spin-half copper magnetic ions are coupled into the dimerized CuO_4 plaquettes which are arranged within the crystal lattice into tetragonal bilayers [90]. This compound is famous for displaying the Bose-Einstein condensation (BEC) of triplet excitations at the critical magnetic field of H_c=23.5 T applied along the c-axis [91; 92]. The application of the external magnetic field H_c adds the additional term $-g\mu_B \sum_{i\alpha} H_0 s^z_{i\alpha}$ to the Hamiltonian where the g is the g-factor, μ_B is Bohr magneton and z- is the direction of the applied magnetic field. Under the applied magnetic field the triplet states are split losing their degeneracy due to the Zeeman effect. Because of the Zeeman splitting, the energy of the lowest triplet state $|1,1\rangle$ decreases and, if the applied magnetic field H_0 achieves the critical value of $H_c = \frac{\Delta}{g\mu_B}$, the energy gap Δ closes and the triplons start to condense into the ground state forming long-range magnetic order in the system.

The Bose-Einstein condensation of the triplet excitations was first discovered in 3D dimerized AFM $TlCuCl_3$ where the edge-sharing $CuCl_6$ octahedra are interacting with each other in all three spatial dimensions [93; 94]. BEC behaviour was also experimentally observed in the 3D dimerized AFM $Sr_3Cr_2O_8$ [95]. In one-dimension, condensation of magnons does not give rise to long-range magnetic order, but rather to a Luttinger liquid state with spinon excitations as observed in copper nitrate [96].

Although a wide range of extraordinary quantum phenomena were recently explored in the dimerized quantum antiferromagnets, dimerized magnetic systems with *ferromagnetic* interdimer exchange coupling have not to be explored so far. This is partially explained by the extremely rare physical realizations of the AFM-FM dimerized magnetic systems.

This Chapter explores the magnetic properties of the novel quantum magnet $BaCu_2V_2O_8$ and proves that $BaCu_2V_2O_8$ is a dimerized alternating chain where the antiferromagnetic dimers are coupled by weak ferromagnetic interactions contradicting to all previous models which assumed that $BaCu_2V_2O_8$ is an AFM-AFM alternating chain or isolated dimer system [41; 42; 43; 97; 98].

It starts from the section *Introduction* where the subsections *Crystal structure* and *Overview of the suggested models* give a brief overview of the crystal structure and magnetic properties of $BaCu_2V_2O_8$ which were recently proposed in the literature. Then the section *Crystal growth* gives the details of the powder and single crystal synthesis of samples of $BaCu_2V_2O_8$ in particular high quality large single crystal of $BaCu_2V_2O_8$ were grown and investigated here for the first time. The results of the bulk properties of $BaCu_2V_2O_8$ are reported in the section *Thermodynamic measurements* revealing the low dimensional dimerized behaviour

in $BaCu_2V_2O_8$ with a weak ferromagnetic exchange coupling and estimate the values of the energy gap, intra- and interdimer magnetic exchange interactions. Finally, the section *Magnetic excitations of $BaCu_2V_2O_8$* describes the results of the inelastic neutron scattering experiments which were used to solve the magnetic Hamiltonian of $BaCu_2V_2O_8$ and provide accurate values of the magnetic exchange interactions in this compound. In addition the comparison of the experimental results with the results of density matrix renormalization group calculations proves that $BaCu_2V_2O_8$ is an 1D alternating AFM-FM chain. The *Discussion* section summarizes the results of this Chapter and compares them to the recently proposed magnetic models of $BaCu_2V_2O_8$ in the literature.

6.1.1 Crystal structure

$BaCu_2V_2O_8$ has a tetragonal crystal structure which is characterized by space group $I\bar{4}2d$ with the lattice parameters $a = b = 12.744$ Å, $c = 8.148$ Å[99]. The magnetic $S = 1/2$ Cu^{2+} ions are coordinated by O^{2-} ions in square-planar geometry where the CuO_4 plaquettes form the edge-sharing Cu_2O_6 pairs which are connected to each other via VO_4 tetrahedra where the non-magnetic V^{5+} atoms have two non-equivalent crystallographic sites $V(I)^{5+}$ and $V(II)^{5+}$. The *c*-axis always lies within the Cu_2O_6 double plaquettes which rotate about this axis by 180° to form twofold screw chains (Figure 6.2(a)). There are both left- and right-handed screw chains. Figure 6.2(b) shows the crystal structure projected onto the (ab)-plane. Within each unit cell there are 4 screw chains where the two left-handed screw chains (LH) are rotated by 90° with respect to the two right-handed (RH) screw chains. Thus, the plaquettes of the RH and LH screw chains always contain {100} and {010} crystal planes, respectively. Although $BaCu_2V_2O_8$ contains a 3D arrangement of copper oxygen plaquettes, its crystal structure suggests that $BaCu_2V_2O_8$ is rather a 1D chain or a ladder magnetic system then a 2D or 3D quantum magnet because of the rotations of these plaquettes around the *c*-axis.

6.1.2 Overview of the suggested models

The magnetic properties of $BaCu_2V_2O_8$ have been recently investigated since the crystal structure and crystal growth of this compound were published for the first time [99; 100]. However, there is no unambiguous model of the magnetic properties for this compound so far. Indeed, the models of $BaCu_2V_2O_8$ proposed in the literature range from the AFM-AFM alternating chains models [97; 98] to isolated AFM dimer model [101]. First, *He et al.* [97] proposed that $BaCu_2V_2O_8$ consists of non-interacting pairs of linear alternating AFM chains (Fig. 6.2c Model I). They suggest that these alternating dimerized chains arise along the *c*-axis via the dominant antiferromagnetic superexchange path Cu-O-V(I)-O-Cu (J_1^* in Fig. 6.2c) and a weaker antiferromagnetic superexchange path Cu-O-Cu between the Cu^{2+} ions within the edge-sharing double plaquettes (J_2 in Fig. 6.2c). They also estimat the values of the energy gap Δ=230K and the magnetic exchange couplings J_1^*=260K and J_2=52K from

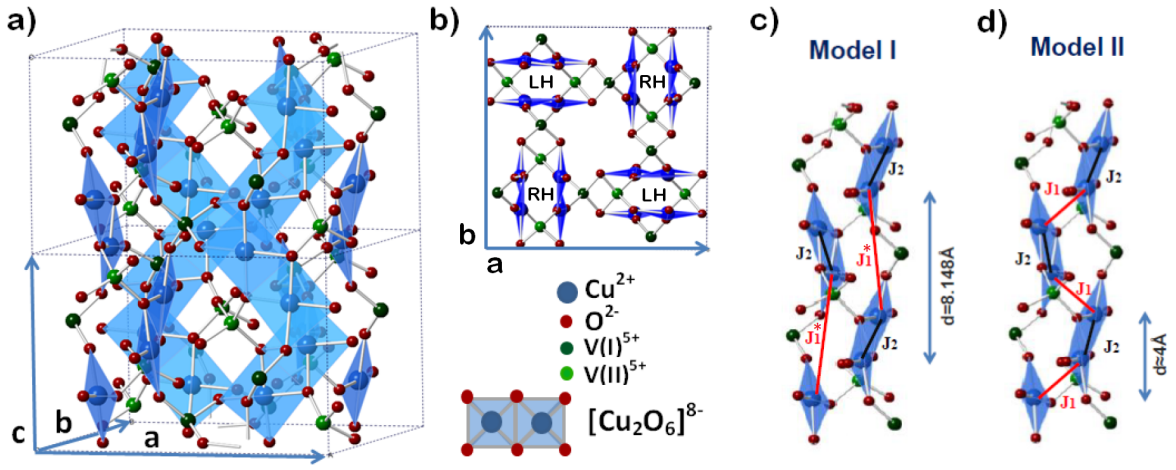

Figure 6.2: (a)crystal structure of $BaCu_2V_2O_8$ where the Ba^{2+} ions are omitted for clarity. (b) Projection of crystal structure of $BaCu_2V_2O_8$ on the *ab*-plane, the Ba^{2+} ions are omitted (c) the proposed model of the non-interacting individual linear chains arrangement within the crystal lattice [97] (d) the proposed model of the screw chain arrangement within the crystal lattice [98]

the analysis of the powder susceptibility data.

However, this model is based only on a speculation about the magnetic exchang paths recently proposed for the similar compounds and is not supported by direct measurements or calculations of $BaCu_2V_2O_8$ to verify these particular magnetic exchange paths. Moreover, later analysis of the ^{51}V nuclear magnetic resonance measurements[43; 101] revealed that $BaCu_2V_2O_8$ is a dimerized antiferromagnet where the energy gap lies within the energy range of 450K-470K contradicting the value Δ=230K suggested by *He et al.* [97].

In contrast to the linear AFM alternating chains model [97], the AFM alternating screw chain model (Fig. 6.2d Model II), which was proposed by *Koo et al.* [98], is derived from the results of extended Hückel tight-binding calculations. This model suggested that the AFM alternating chain consists of a dominant AFM super exchange path Cu-O-V(II)-O-Cu (J_1 in Fig. 6.2d) and a weaker AFM exchange path Cu-O-Cu (J_2 in Fig. 6.2d) within the copper oxygen plaquettes with an alternation ratio of $\approx$0.164. Although this chain is also running along the *c*-axis, it is not straight, but forms a screw around the *c*-axis. Note that the antiferromagnetic nature of the magnetic exchange paths in these calculations was assumed *a priori*.

The AFM screw alternating chain model is consistent with first principles electronic structure calculations[101] which also suggest that J_1 (Fig. 6.2d) is the dominant AFM superexchange path while the path J_2 (Fig. 6.2d) is responsible for the interdimer exchange coupling. However, the alteration ratio is proposed to be J_2/J_1=0.05 by these electronic structure calculations suggesting that the isolated dimer model is more appropriate for the description of the magnetic properties of $BaCu_2V_2O_8$ [101].

6.2 Crystal growth

This section describes the process of the powder synthesis and powder and single crystal growth of $BaCu_2V_2O_8$ which were performed in the Crystal Laboratory at the HZB by Dr. A.T.M.N. Islam.
Crystal growth of $BaCu_2V_2O_8$ was carried out in an optical image furnace (Crystal Systems Corp., Japan) equipped with four 300 W tungsten halide lamps focused by four ellipsoidal mirrors. The starting material for crystal growth was prepared by a standard solid-state reaction [100]:

$$BaCO_3 + 2CuO + V_2O_5 = BaCu_2V_2O_8 + CO_2 \uparrow \tag{6.3}$$

using high purity powder of $BaCO_3$ (99.997%, Alfa Aesar) CuO (99.995%, Alfa Aesar) and V_2O_5 (99.99%, Alfa Aesar) which were mixed with the 1:2:1 molar ratio. After mixing thoroughly in ethanol, a powder of stoichiometric composition was calcinated in a platinum crucible in air at 650°C twice for 12 hours each time with intermediate grindings. The powder was then pulverized, packed into a cylindrical rubber tube and pressed hydrostatically up to 3000 bars in a cold-isostatic-pressure (CIP) machine. A cylindrical rod with diameter of about 6mm and length 7-8 cm prepared in this process was then sintered in Air at 750°C for 12 hours. A dense and crack-free feed could be obtained in this process.
The crystal growth of the single crystal sample of $BaCu_2V_2O_8$ was performed using the travelling-solvent-floating-zone technique (TSFZ) using an off-stoichiometric composition for the solvent to decrease the melting temperature because $BaCu_2V_2O_8$ is known to decompose around 770°C, close to its melting temperature [100]. The basic overview of this technique was given in the Chapter 3. A solvent with the composition of 5mol% excess V_2O_5 was prepared in the same process as the feed rod and about 0.5 grams of it was attached to the tip of the feed-rod to start the growth. The feed rod of stoichiometric composition was suspended from the upper shaft a using nickel wire, while another small feed rod was fixed to the lower shaft to support the melt. Crystal growth was performed in ambient air atmosphere at a growth speed of 0.2 mm/hour. A single crystalline piece of about 4.5 cm in length and 5.5 mm in diameter was obtained in this process.
After growth a small piece of the single crystal was ground and checked with X-ray powder diffraction (Brucker D8) for phase purity. A cross-section of the single crystal was polished and checked under a polarized optical microscope to confirm there is no residual phase, grain boundaries or inclusions in the crystal. The single crystallinity of the sample was confirmed by systematically taking several X-ray Laue patterns from different parts of the crystal.

6.3 Thermodynamic properties

This section presents the results of the bulk properties measurements of $BaCu_2V_2O_8$ which have been performed at the Laboratory for Magnetic Measurement in Helmholtz Zentrum Berlin fur Materialien und Energie in order to characterize the magnetic properties of $BaCu_2V_2O_8$. The subsection *Experiment settings* provides the experimental details for the constant field (DC) susceptibility measurements which were performed on the single crystal of $BaCu_2V_2O_8$ for the different field directions with respect to the crystal c-axis. To estimate the size of the energy gap and the values of the intra- and interdimer magnetic exchange coupling, the data were analysed using two different approaches assuming that $BaCu_2V_2O_8$ is a dimerized magnetic system and the results are presented in the subsection *Results of the DC susceptibility measurements*. Finally, in the *Discussion* subsection the results are discussed and compared to the results published in the literature.

6.3.1 Experiment settings

Two samples with a mass of m_1=19.9 mg and m_2=19.2 mg were cut along the $c-$crystal axis from small pieces of the different single crystals growths of $BaCu_2V_2O_8$ and were prepared for the magnetic susceptibility measurements: the quality and the alignment of each sample was checked using the X-ray Laue diffraction instrument equipped with an Cu K_α X-ray tube at the Sample characterization laboratory at HZB. For the analysis of the Laue diffraction patterns the Orient express software was used [102].
The magnetic susceptibility measurements were performed using a Quantum Design PPMS magnetometer in the low (2 K-400 K) and high (300 K-900 K) temperature regimes under an applied magnetic field of 1T in both parallel and perpendicular field directions (with respect to the c-axis). The basic principles of the instrument and the measurements were given in the Chapter 3. In the low temperature regime a glass sample holder and GE varnish glue were used while in the high temperature regime the sample was mounted on the oven integrated zirconia stick by cement glue. The background of the each sample holder was determined from the fitting analysis of the raw susceptibility data of the empty sample holder with a small amount of glue and then was subtracted from the raw data. After this subtraction the data were normalized in order to get the susceptibility per mole of magnetic ion. For further analysis the data collected in the low- and high-temperature regimes were combined.

6.3.2 Results of the DC susceptibility measurements

Figure 6.3(a) shows the best set of the background-subtracted normalized susceptibility data of the single crystals of $BaCu_2V_2O_8$ for parallel ($\chi_{H||c}$, blue filled circles) and perpendicular ($\chi_{H\perp c}$, green filled triangles) magnetic field direction to the c-axis. They are plotted as a function of temperature. The data reveal isotropic behaviour of the magnetic susceptibility

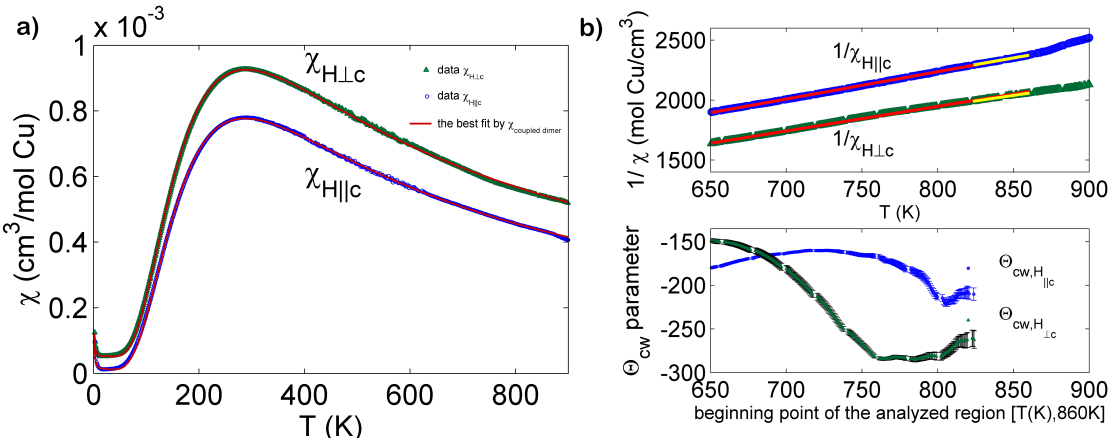

Figure 6.3: (a) The temperature dependence of the magnetic susceptibility data collected on a single crystal of $BaCu_2V_2O_8$, measured at a constant magnetic field of H=1T applied in parallel (green triangles) and perpendicular (blue circles) direction to the *c*-axis. The solid red and magenta lines give the best fit analysis by the coupled dimer model (eq. 6.5) taking account of the contribution of the impurities and temperature independent terms (eq. 6.3). (b) top figure: temperature dependence of the inverse $\chi_{H||c}$ and $\chi_{H\perp c}$ magnetic susceptibilities, the impurity and temperature independent therms are subtracted. The solid red and magenta lines give the fit by the inverse Curie-Weiss Law (eq. 6.4) within the temperature range of [650K,860K], the solid yellow lines give the fit by the inverse Curie-Weiss Law (eq. 6.4) within the temperature range from 820K to 860K. bottom figure: extracted values of the Curie-Weiss temperature plotted as a function of the starting point T_{start} of the fitted temperature region (T_{start},860K), where T_{start} varies within the range (650K,820K).

with respect to the *c*-axis within the whole temperature range. Indeed, both $\chi_{H||c}$ and $\chi_{H\perp c}$ look identical except for the difference in their amplitudes which can be attributed to the anisotropy of the *g*-factor [103]. A broad maximum appears in the both data sets in the vicinity of the temperature of T=280K as is commonly observed in low-dimensional quantum magnets. Below this maximum both $\chi_{H||c}$ and $\chi_{\perp}$ smoothly drop down with temperature decrease and do not display any signatures of the phase transitions. At very low temperature T<15K, both $\chi_{H||c}$ and $\chi_{\perp c}$ turn up and start slightly increasing as temperature is tending to zero. This behaviour at T<15K is associated with the paramagnetic contribution from the impurities which starts to play a role only in the vicinity of a zero temperature because of the small amount of the impurities. To take into account this contribution from the impurities as well as the contribution of the diamagnetic core susceptibility and van Vleck paramagnetism the data at low temperature T<15K were fitted by a Curie-Weiss law including the temperature independent terms and which were kept fixed for further analysis:

$$\chi_{(T<15K)} = \chi_{imp} + \chi_{T-indep}; \chi_{T-indep} = \chi_0 + \chi_{vv} \tag{6.4}$$

Here, T is a variable temperature, C_{imp} is a Curie impurity's constant, Θ_{imp} is a Curie impurity's temperature, χ_0 is a diamagnetic core susceptibility and χ_{VV} describes a van

Vleck paramagnetism.
Apart from this low temperature impurity tail, both the $\chi_{||c}$ and $\chi_{\perp c}$ susceptibilities tend towards zero at zero temperature which is a signature for a non-magnetic ground state and gapped magnetic excitations. This is in agreement with the assumption that $BaCu_2V_2O_8$ is a dimerized magnetic system which is characterized by a singlet ground state and gapped excitations.

6.3.2.1 Curie-Weiss law

To learn more about the dominant magnetic exchange interaction the data were analyzed using the Curei-Weiss law. The top part of the Figure 6.3(b) presents the inverse magnetic susceptibility data plotted as a function of temperature at high temperatures above T=650 K. According to the Curie-Weiss law at sufficiently high temperatures, where the compound is in its paramagnetic phase, the inverse magnetic susceptibility linearly depends on the temperature:

$$\chi = \frac{2C}{T - \Theta_{CW}} \Rightarrow \frac{1}{\chi} = \frac{T}{2C} - \frac{\Theta_{CW}}{2C} \tag{6.5}$$

Indeed, an equation 6.4 shows that the slope of this line corresponds to the inverse Curie constant where the factor of two takes into account that the susceptibility was normalized per mole Cu. The constant term equals to the ratio of the Curie-Weiss temperature (Θ_{CW}) to the Curie constant (C). AFMs are characterized by a negative Curie-Weiss temperature while ferromagnets (FM) have a positive Curie-weiss temperature
To extract the Curie-Weiss temperature of $BaCu_2V_2O$, the inverse magnetic susceptibility data were fitted by a straight line over the temperature range of (T_{start},860K), where the starting point lies within range of $T_{start} \in$[650,820]. The starting point of the fitted temperature region was varied because the temperature above which $BaCu_2V_2O_8$ is in paramagnetic phase is unknown, above this temperature the extracted Curie-Weiss temperature is independent of the fitted temperature region. The temperature of T=860K was chosen as a maximum temperature because of the clearly observed non-linear behaviour of the inverse $\chi_{||c}$ data above this temperature which may be due to a structural phase transiton or other changes in the sample. The solid yellow and red lines in the Figure 6.3(b) shows the results of the fit analysis within the temperature ranges of (650K,860K) and (820K,860K) while the Figure 6.3(c) shows the values of the Curie-Weiss temperature extracted within the different temperature regions (T_{start}(K),860K) and plotted as a function of the starting point T_{start}. The results unambiguously reveal that $BaCu_2V_2O$ has a dominant antiferromagnetic interaction. Indeed, the extracted Curie-Weiss temperature has a negative value independent of the fitted temperature region. However, the value of the Curie-Weiss temperature cannot be accurately determined because it strongly depends on the temperature region which means that the paramagnetic phase is not achieved. Because $BaCu_2V_2O$ decomposes at the temperature of 1043K [100], there is no possibility to measure this compound at higher temperatures.

6.3.2.2 The coupled-dimer model

In order to learn more about the magnetic properties of $BaCu_2V_2O_8$, the magnetic susceptibility data collected in both directions of the applied magnetic field with respect to the c-axis were fitted by the coupled dimer model assuming that $BaCu_2V_2O_8$ is a dimerized quantum magnet with weak interdimer exchange coupling [104; 105]. This model is based on mean field theory and allows the value of the dominant intradimer magnetic exchange coupling J_{intra} and weaker interdimer magnetic exchange coupling J_{inter} to be estimated. It does not, however, assume any particular dimensionality of the dimerized magnetic system.

$$\chi_{fit1} = \chi_{imp} + \chi_{coupled-dimers} + \chi_{T-indep} \tag{6.6}$$

where

$$\chi_{coupled-dimers} = \frac{3C/T}{3 + exp(J_{intra}/k_BT) + J_{inter}/k_BT} = \frac{N_A g^2 \mu_B^2 S(S+1)/k_BT}{3 + exp(J_{intra}/k_BT) + J_{inter}/k_BT}$$

Here, T is the temperature and k_B is the Boltzmann constant. In the middle part of equation 6.6 the Curie Constant C, the dominant intradimer magnetic exchange coupling J_{intra}, and the weaker (with respect to the dominant) interdimer magnetic exchange coupling J_{inter} are variables which can be fitted. In the right hand part of the equation the Curie constant is replaced by its definition and the g-factor becomes a variable to be fitted.
The solid red lines through the data in Figure 6.3 present the best fit of the experimental data by the coupled dimer model (eq. 6.6) which were achieved with the values of J_{intra} = 39.67 J_{inter} = -12.59 for the data $\chi_{||c}$ and J_{intra} = 39.94 J_{inter} = -7.23 for the data $\chi_{\perp c}$. The extracted values of the J_{intra} and J_{inter} from the $\chi_{\perp c}$ and $\chi_{||c}$ data sets are in good agreement with each other and can be averaged J_{intra} = 39.80 $\pm$ 0.13 J_{inter} = -9.87 $\pm$ 2.64. These results imply that the antiferromagnetic dimers are weakly coupled ferromagnetically with the dimerization ratio of J_2/J_1= -0.248 ,however, they do not provide the dimensionality of the inter-dimer magnetic exchange coupling.
Additionally, the fit analysis of the $\chi_{\perp c}$ and $\chi_{||c}$ data sets using the coupled-dimer model allows the anisotropic g-factor to be extracted which is found to be of $g_{||c}$=2.09 and $_{\perp c}$=2.27. In compounds with copper oxide plaquettes the anisotropic g-factor is related to the plaquette geometry. Because in $BaCu_2V_2O_8$ the plaquettes contain the c-axis and rotate about it, $g_{||plaquettes}$=$g_{||c}$=2.09 $\pm$ 0.03 while $g_{\perp plaquettes}$=2$g_{\perp c}$-$g_{||c}$=2.45 $\pm$ 0.03.

6.3.2.3 Low-T limit analysis

The $\chi_{\perp c}$ and the $\chi_{||c}$ magnetic susceptibility data of $BaCu_2V_2O_8$ were fitted using the Low-T limit approach for the S=1/2 1D gapped spin-system [106; 107] to estimate the energy

gap. This approach found to be appropriate for the analysis of the magnetic susceptibility of $BaCu_2V_2O_8$, because both models of $BaCu_2V_2O$ proposed in the literature suggest that $BaCu_2V_2O$ is a 1D alternating chain (see Fig. 6.2(c) and 6.2(d)).

$$\chi_{fit2} = \chi_{imp} + \chi_{Low-tlimit} + \chi_{T-indep} \quad \text{where} \quad \chi_{Low-tlimit} = \frac{A}{\sqrt{T}} exp\left(\frac{-\Delta}{k_B T}\right) \tag{6.7}$$

Here, χ_{imp} and $\chi_{T-indep}$ takes into account the contribution from the impurities and from the temperature independent terms respectively, A is a variable non-universal scaling constant, T is temperature, Δ is the gap size, k_B is the Boltzmann constant. This approach is valid within the temperature limit of $\frac{k_B T}{J_{max}} \rightarrow 0$

Figure 6.4(a) shows the $\chi_{\perp c}$ and $\chi_{||c}$ magnetic susceptibility data fitted by the Low-T limit approach (solid red line) in the temperature range from 2K up to 150K. The ratio of the upper temperature of T_{final}=150K to the value of the J_{intra} estimated by using the coupled-dimer model equals to $\frac{k_B T}{J_{intra}} \approx 0.3$. The extracted value of the energy gap equals Δ=32.54meV $\pm$0.01 meV. Although the fitting error is very small, the real error of the fit analysis is larger because the result is sensitive to the fitted temperature region. To show how the temperature range influences the results of the fit analysis, both the $\chi_{\perp}$ and $\chi_{||}$ susceptibility data were fitted over different temperature ranges from 2K up to T_{final} where the T_{final} varies within the range from 80K to 150K. The values of the energy gap extracted from the different temperature regions are plotted as a function of T_{final} in Fig. 6.5(b). This figure shows that the extracted values are almost the same and have an error which is less then 1% where the temperature T_{final} is in the range (100K, 150K). Below T_{final}=100 K the value of the energy gap extracted from the fit analysis is rapidly changing and their errors are continuously increasing indicating that the results extracted from the fit analysis within this temperature range are less reliable. The values of the energy gap extracted within the temperature region (2K,T_{final}) where T_{final} varies from 100K to 150K were averaged within each data set of $\chi_{\perp c}$ and $\chi_{||c}$. They were found to be Δ=32.64meV $\pm$ 0.65meV and Δ=32.18meV $\pm$ 0.67meV, respectively. So, the size of the energy gap in $BaCu_2V_2O_8$ extracted by using the Low-T approach can be estimated to Δ=32.4meV $\pm$ 0.7meV.

6.3.3 Discussion

Constant field magnetic susceptibility measurements were performed on a single crystal of $BaCu_2V_2O_8$ using parallel and perpendicular directions of the applied magnetic field of 1T with respect to the c-axis within a wide temperature range from 2K to 900K and the results of these measurements were presented and discussed. The results reveal that $BaCu_2V_2O_8$ behaves as an isotropic gapped low-dimensional quantum magnet with dominant AFM interactions which is in an agreement with the results of the constant field magnetic susceptibility

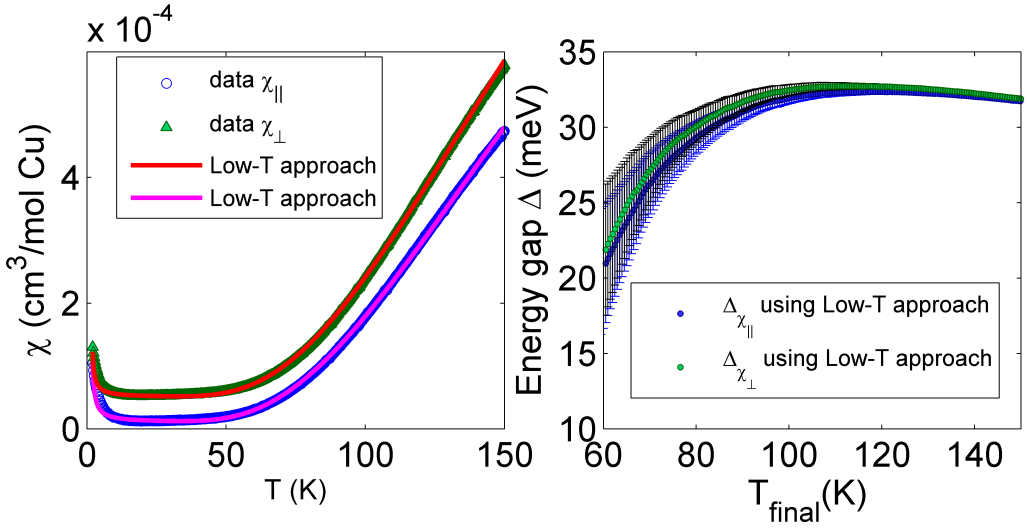

Figure 6.4: a) The temperature dependence of the magnetic susceptibility data collected on the single crystal of $BaCu_2V_2O_8$ at a constant magnetic field of H=1T applied in parallel (green triangles) and perpendicular (blue circles) direction with respect to the c-axis. Solid red and magenta lines give the best fit analysis by the Low-T approach, b) extracted values of the energy gap Δ plotted as a function of the final temperature T_{final} of the fitted temperature region (2K,T_{final}), where T_{final} varies within the range of (60K,150K)

measurements previously performed on the powder sample of $BaCu_2V_2O_8$ [97].

The clearly observed difference in the amplitudes of $\chi_{\perp c}$ and $\chi_{H||c}$ magnetic susceptibility data was attributed to the strong anisotropy of the g-factor because $BaCu_2V_2O_8$ contains the copper oxygen plaquettes [103]. The fitted values of the Landé-g factors extracted from the fit analysis of the coupled dimer model are $g_{||c}$=2.09 and $g_{\perp c}$=2.27, from which $g_{||plaquettes}$=2.09 $\pm$ 0.03 and $g_{\perp plaquettes}$=2.44 $\pm$ 0.03 were extracted. These values contradict the reported values of $g_{||c}$=2.44 and $g_{\perp c}$=2.13 where the crystal axes appear to have been accidentally swapped [41]. However, the extracted values $g_{||plaquettes}$=2.09 $\pm$ 0.03 and $g_{\perp plaquettes}$=2.44 $\pm$ 0.03 are in an good agreement with other cuprates with a square, planar coordination e.g. $BaCuSi_2O_6$ [108] and $Cu(NO_3)_2{\cdot}2.5H_2O$ [109] where $g_{||plaquettes}$ is also smaller then $g_{\perp plaquettes}$. Moreover, these values are in good agreement with the values $g_{||plaquettes}$=2.14 $\pm$ 0.03 and $g_{\perp plaquettes}$=2.44 $\pm$ 0.03 extracted from fitting the DMRG simulations of the magnetic susceptibility to the $BaCu_2V_2O_8$ data[110].

The low temperature region of both $\chi_{H\perp c}$ and $\chi_{H||c}$ data sets were fitted well by using the Low-T approach and the extracted value of the energy gap Δ=32.4meV $\pm$ 0.7meV is in good agreement with the values Δ=450K(38.8meV)-470K(40.5meV) which was observed in the ^{51}V nuclear magnetic resonance measurements [43; 101]. Although the Low-T approach was originally proposed for the spin-1/2 two-leg ladder Heisenber systems [106] and then was expanded for any gapped 1D spin-1/2 Heisenberg system [107], the good agreement of the fit results with the experimental data does not necessary imply one-dimensionality of the ex-

plored magnetic system. Indeed, the Low-T approach also fitted well the susceptibility data of 3D AFM $KCuCl_3$ [111] and the extracted value of the energy gap Δ=35K ($\approx$ 3meV) was in good agreement with the value Δ=2.7meV ($\approx 31.32K$) extracted from the INS measurements [112].
Both sets of the magnetic susceptibility data $\chi_{H\perp c}$ and $\chi_{H||c}$ magnetic susceptibility data were fitted well over the whole temperature range within the coupled-dimer model confirming that $BaCu_2V_2O_8$ is a dimerized magnetic system. The extracted values of the J_{intra} = 39.80meV $\pm$ 0.13meV and J_{inter} = -9.87meV $\pm$ 2.64meV for the magnetic exchange interactions suggest that the AFM dimers are ferromagnetically coupled, contradicting all models previously proposed in the literature where, the both intra- and interdimer magnetic exchange interactions are AFM [41; 42; 43; 97; 98]. The extracted dimerization ratio of $\frac{J_2}{J_1} = 0.248$ from the fit analysis using the coupled dimer model implies that $BaCu_2V_2O_8$ is an alternating chain rather than isolated dimer system.

6.4 Magnetic excitations of $BaCu_2V_2O_8$

This section presents the results of the inelastic neutron scattering measurements which were performed to explore the magnetic properties of quantum magnet $BaCu_2V_2O_8$. The experimental details of the powder and single crystal inelastic neutron scattering experiments performed on $BaCu_2V_2O_8$ are given in the subsection *Experimental settings of the inelastic neutron scattering experiments*. The subsection *Powder spectrum* gives an overview of the magnetic excitation spectrum of $BaCu_2V_2O_8$ from a powder inelastic neutron scattering experiment and shows that the magnetic system has highly gapped excitations and a small band width. To explore the magnetic properties of $BaCu_2V_2O_8$ in detail and to solve the Hamiltonian of this quantum magnet the results of inelastic neutron scattering experiments on a single crystal of $BaCu_2V_2O_8$ are analysed in the subsection *Single crystal spectrum*. The system is found to be an alternating chain with a strong antiferromagnetic intradimer interaction coupled by a weaker interdimer interaction that can be either ferromagnetic or antiferromagnet. To distinguish between these two possible magnetic models for $BaCu_2V_2O_8$ the subsection *Comparison with the DMRG computations* compares the inelastic neutron scattering data collected on the single crystal of $BaCu_2V_2O_8$ to the results of the theoretical approach based on the density matrix renormalization group theory which were computed by Alexander Tiegel from the theory department of Goettingen university under supervision of Dr. S.R. Manmana, Prof. Dr. A. Honecker and Prof. Dr. T. Pruschke. This comparison proves that the interdimer coupling is ferromagnetic. Finally the results of this section are summarized and discussed in the *Discussion* subsection.

6.4.1 Experimental settings of the inelastic neutron scattering experiments

To explore the magnetic excitation spectrum of $BaCu_2V_2O_8$ both powder and single crystal inelastic neutron scattering experiments have been done. In order to get an overview of the magnetic excitation spectrum and to determine its energy scale, powder inelastic neutron scattering measurements were performed using the high intensity, medium resolution time-of-light spectrometer MERLIN at the ISIS facility, Rutherford Appleton Laboratory, United Kingdom. The data were collected for a polycrystalline sample with a total mass of 21g which was cooled to a temperature of 5 K using a closed cycle cryostat. The Fermi chopper was operated in two different modes which are characterized by frequencies of 250Hz and 300Hz and were phased to select the neutrons with incident energies of E_i=36meV and E_i=50meV, respectively. The corresponding resolution at the elastic line was found to be of 2.2 meV and 3.8 meV, respectively. To distinguish the contribution from the phonons the measurements were repeated at a temperature of T=300K. Indeed, the intensity of the phonons increases while the intensity of the magnetic excitations decreases with increasing temperature.
To explore the magnetic excitation spectra of $BaCu_2V_2O_8$ in detail the INS measurements were performed on a single crystal using the high resolution thermal neutron Triple-Axis spectrometer PUMA at the Forschungs- Neutronenquelle Heinz-Maier-Leibniz (FRM2), Munich, Germany. For the mapping of the magnetic excitation spectrum along the principal axes a sample with a mass of 2.16g was preoriented in advance with the (H,0,L) plane in the instrumental scattering plane using the X-ray Laue difractometer in the Laboratory for the X-ray experiments at HZB.
The preoriented sample was mounted into a closed-cycle cryostat and the data were collected at a base temperature of 4K. The energy dispersion within the *ab*-plane and along the *c*-axis was explored by measuring constant energy scans either along the H or L directions at fixed energy transfers within the energy range of E=33meV-45meV with energy step of 1meV. For these measurements a double-focused pyrolytic graphite monochromator (PG (002)) with *d*-spacing of d_{002} = 3.355Å was used together with a doubly-focused PG (002) analyser which provides a calculated resolution of 2 meV at fixed final wave-vector of k_f =2.662Å^{-1}.
In order to accurately measure the size of the gap and the band width, high resolution constant wave-vectors scans were carried out at the dispersion minima (8,0,0) and (6,0,1) and the dispersion maximum (6,0,2) over the energy range from 33 to 45 meV. To precisely determine the energy peak position the energy resolution was improved by changing the PG (002) monochromator to the double-focused single crystal Cu monochromator (Cu(220)). The Cu(220) monochromator has a d-spacing of d_{220} = 1.28Å which is characterised by a calculated energy resolution value of 0.74meV at fixed final wave vector of k_f =1.97Å^{-1} and 0.992meV at fixed final wave vector of k_f =2.662 Å^{-1}.
In order to precisely investigate the intensity distribution of the energy dispersion, INS measurements were also performed on the IN8 high-flux thermal neutron three-axis spectrometer

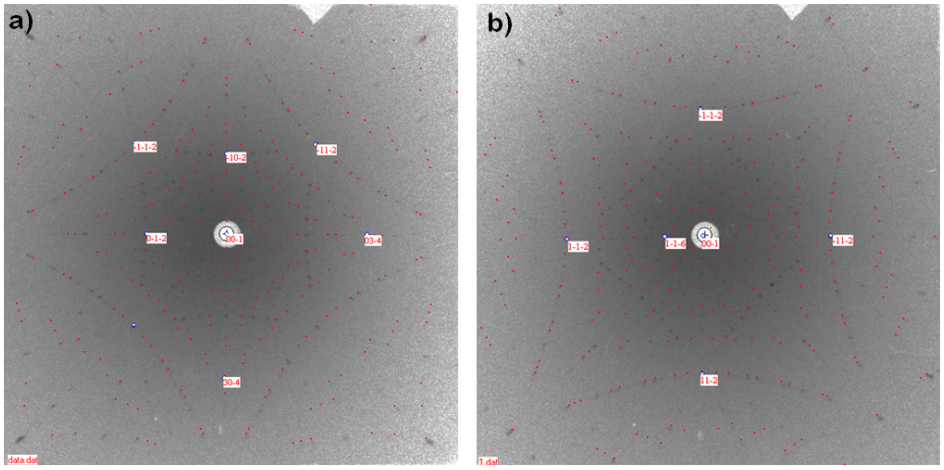

Figure 6.5: Laue diffraction pattern of $BaCu_2V_2O_8$. Incident X-ray beam is parallel to the *c*-axis.

at ILL in Grenoble, France. The principal scheme of the IN8 instrument corresponds to Fig.3.4 and was discussed in Chapter 3. In this experiment a Si (111) bent perfect crystal monochromator and analyser were used. The main advantage of the silicon analyser is that it has no second order Bragg peaks which reduces the background contribution. In this experiment two different samples with masses S_1=2.16g and S_2=1.38g were prepared and used. The first sample S_1 was the same used for the INS measurements at PUMA and it was aligned with the (H,0,L) plane in the instrumental scattering plane. The second sample S_2 was preoriented with the (H,H,L) plane in the instrumental scattering plane. Both samples were cut from the same single crystal of $BaCu_2V_2O_8$.

6.4.2 Powder spectrum

In order to get an overview of the magnetic excitation spectrum of $BaCu_2V_2O_8$, powder inelastic neutron scattering measurements were performed at base temperature of T=5K. The results are plotted in Fig. 6.6(a) and reveal that the magnetic excitation spectrum consists of a magnetic excitation band which extends over the energy range of ≈35-46meV whose intensity is strong at low wavevectors and decreases with increasing wavevector indicating its magnetic nature. The strong signal at low energies from 0-5meV is incoherent scattering while the intense excitations over the energies of 5meV - 36meV, whose intensities are weaker at low wavevectors and increase with increasing wavevector, are assosiated with the phonons. In order to verify the magnetic origin of the signal observed at base temperature, the measurments were repeated at a high temperature of T=300K. The results are plotted in Fig. 6.6(b) and show that the intensity of the excitations over the energy scale from 35meV-46meV decreases with increasing temperature, proving their magnetic nature. The signal below 30meV, in contrast, becomes more intense with temperature confirming that these are phonons.
Thus, the powder INS data reveal that $BaCu_2V_2O_8$ has a gapped magnetic excitations spec-

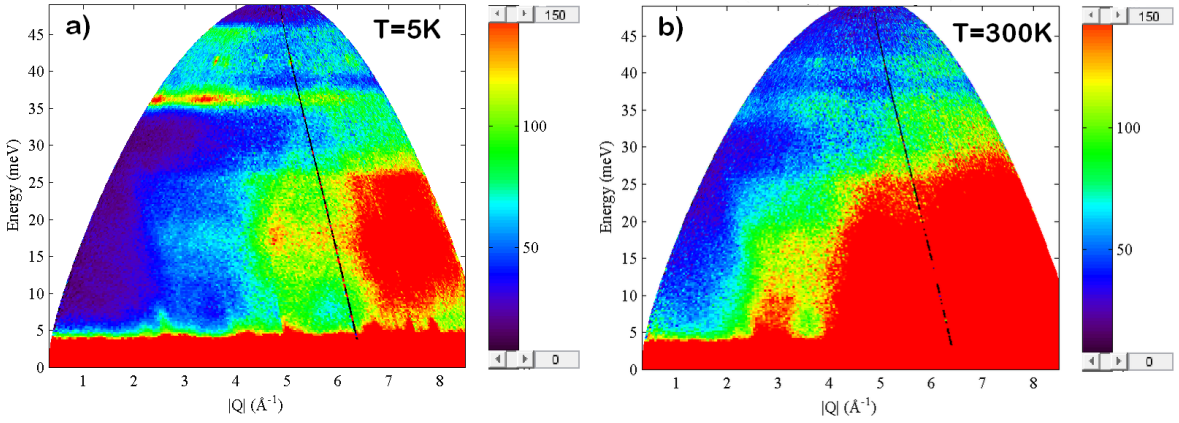

Figure 6.6: Inelastic neutron data collected on a powder sample of $BaCu_2V_2O_8$ at (a) base temperature of T=5K (b) A temperature of T=300K. The data were collected using an incident neutron energy of 50meV and a Fermi chopper speed of 300 Hz.

trum where the high ratio of the band width to the energy gap of ≈ 3.6. indicates the strong dimerization of the magnetic system.

6.4.3 Single crystal spectrum

To explore the magnetic properties of $BaCu_2V_2O_8$ in the detail and to determine the sign and the exact values of the magnetic exchange interactions, single crystal inelastic neutron scattering measurements were performed on $BaCu_2V_2O_8$. The measurements were carried out along both H and L directions within the (H,0,L) scattering plane in order to explore the magnetic exchange couplings along the *c*-axis and within the ab-plane.
Figure 6.7 (a)-(d) shows the INS data collected at base temperature along the (6,0,L), (2,0,L), (H,0,4), (H,0,5) directions at the PUMA triple-axis spectrometer at FRM2, Munich, Germany.
The results reveal that the magnetic excitation spectrum consists of two gapped excitations branches which both disperse along the L direction over the energy range of $\sim$ 36meV-46meV and are completely dispersionless along the H and K directions. Along the L direction both modes have the same periodicity and bandwidth, but are shifted with respect to each other by half a period along the L direction. Both modes modulate in intensity along both directions. Indeed, Fig. 6.7(e) shows the constant energies scans measured over the dispersion energy range either along the H or L directions at different fixed L or H values respectively. These mapping scans are plotted over the coordinates of the (H,0,L) scattering plane and reveal that both modes alternate in intensity along both the L direction and H direction. Indeed, the mode which has a maximum at even-L (mode B, indicated by the red dashed line in Fig. 6.7(e)) has its strongest intensity along (0,0,L), (5,0,L) and (6,0,L) directions and has much less intense along the (2,0,L) and (3,0,L) directions while the mode which has a minimum

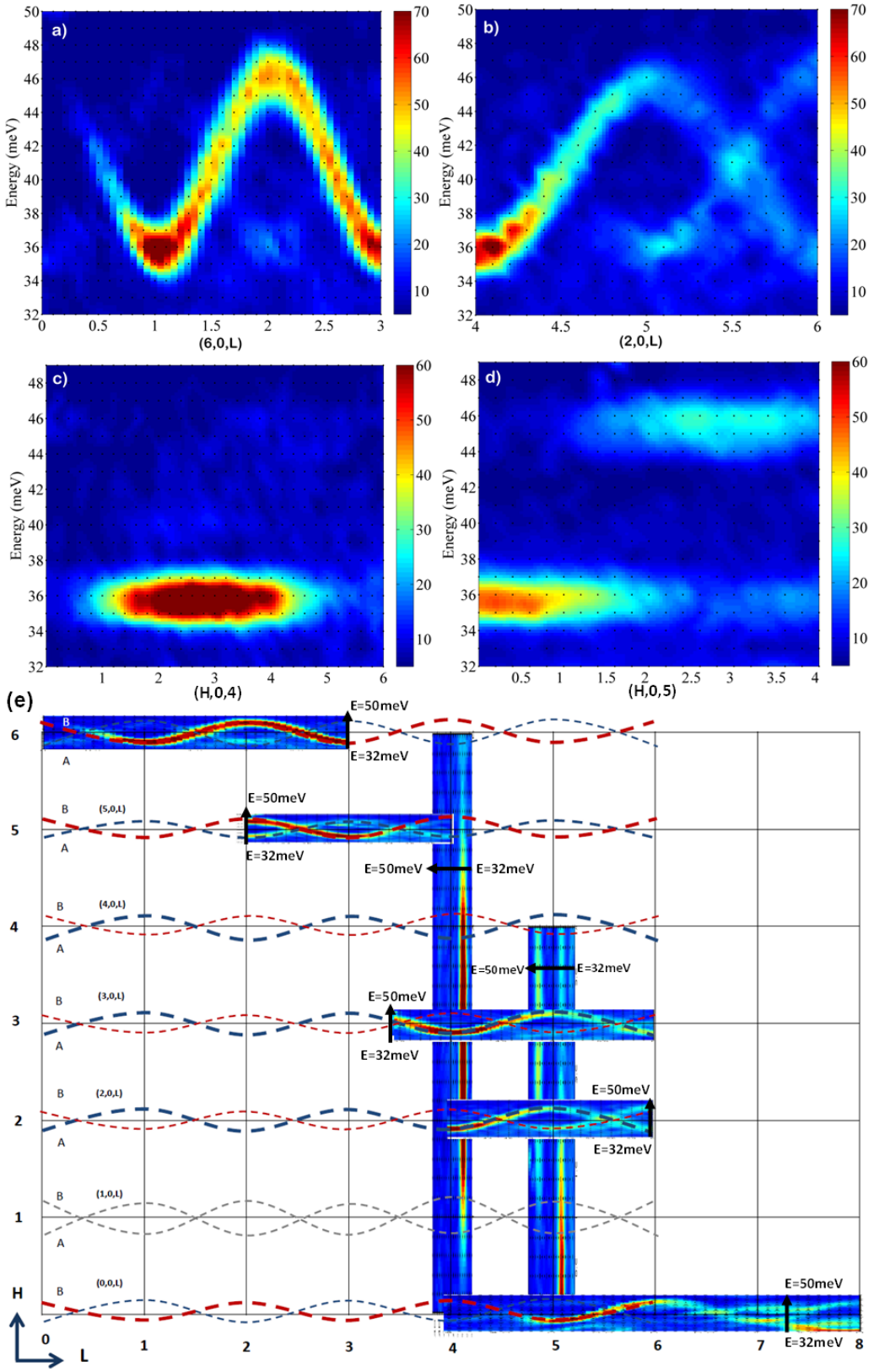

Figure 6.7: Single crystal INS data of $BaCu_2V_2O_8$ measured along the (a) (6,0,L) (b) (2,0,L) (c) (H,0,4) (d) (H,0,5) directions at base temperature of T=5K. (e) INS data collected along the (0,0,L), (2,0,L), (3,0,L), (5,0,L), (6,0,L), (H,0,4), and (H,0,5) directions as a function of energy at base temperature of T=5K and plotted over the coordinates of the (H,0,L) scattering plane. The solid black arrows indicate the energy scale of the mapping plots. The dashed blue line corresponds to mode B, which has a maximum at odd values of L such as (2,0,5) while the dashed red line corresponds to the mode A, which has a minimum at odd values of L such as (2,0,5). The linewidth indicates which mode has more intense signal in the particular direction.

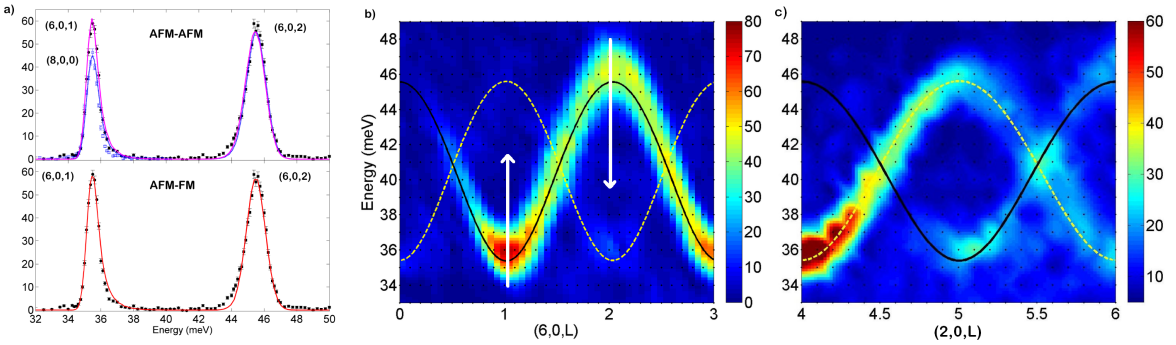

Figure 6.8: (a) On both panels: constant wave-vector scans at (6,0,1) (black filled dots), (8,0,0) (blue squares), (6,0,2) (black filled squares), top panel corresponds to the AFM-AFM solutions; solid magenta line gives fit with J_{intra}=40.75meV and α=0.225; dotted blue line gives fit with J_{intra}=40.74meV and α=0.227; bottom panel corresponds to the AFM-FM solution; The solid red line gives fit with J_{intra}=40.92meV and α=0.2925; All fits are done using one-magnon dispersion relation (eq. 6.8)[45] convolved with the instrumental resolution function by RESCAL software. (b) The one-magnon dispersion relations with the AFM-AFM (dashed yellow line) and AFM-FM (solid black line) solutions plotted over the INS data along the (6,0,L) direction. The white arrows indicate the directions of the constant Q scans at (6,0,1) and (6,0,2) which data are presented on panel (a). (c) The one-magnon dispersion relations with the AFM-AFM (dashed yellow line) and AFM-FM (solid black line) solutions plotted over the INS data along the (2,0,L) direction.

at odd-L (mode A, indicated by the blue dashed line in Fig. 6.7(e)) behaves the other way around.

These results imply that $BaCu_2V_2O_8$ is a strongly dimerized 1D magnetic chain (hence referred as an *alternating chain*) compound where the dimers are coupled along the c-axis while the coupling within the ab-plane is negligible. The presence of the two modes in the dispersion can be attributed to the complex structure factor and suggests that this alternating chain is not straight resulting in more than one dimer per magnetic unit cell.

6.4.3.1 Magnetic model of $BaCu_2V_2O_8$

Since the results of the INS single crystal experiment reveal the dimerized 1D behaviour of $BaCu_2V_2O_8$, a Heisenberg Hamiltonian for the alternating chain was chosen as an appropriate model to describe the magnetic properties of this compound [45].

$$H = \sum_i J_{\text{intra}}\, \mathbf{S}_{i,1} \cdot \mathbf{S}_{i,2} + J_{\text{inter}}\, \mathbf{S}_{i,2} \cdot \mathbf{S}_{i+1,1}. \tag{6.8}$$

Here, J_{intra} and J_{inter} are intra- and interdimer magnetic exchange couplings and i - denotes the sites of the magnetic copper ions. In this notation the negative sign corresponds to a ferromagnetic interaction while the positive sign corresponds to an antiferromagnetic interaction.

In order to solve this Hamiltonian and to determine the dimer periodicity in $BaCu_2V_2O_8$,

the one-magnon dispersion relation of an alternating chain calculated to 5^{th} order was used for the analysis of the energy dispersion along the L direction [45]:

$$\frac{\omega(k)}{J_{intra}} = \sum_{n=0}^{5} a_{\mathrm{n}}(\alpha) \cdot \cos(n \cdot Q \cdot d) \tag{6.9}$$

Here, J_{intra} is the dominant intradimer magnetic exchange interaction and α is the dimerization ratio of the interdimer to the intradimer magnetic exchange coupling $\alpha = \frac{J_{inter}}{J_{intra}}$. $Q = \frac{2\pi L}{c}$ is the wave vector transfer along the chain direction where L is a Miller index; d is the dimer periodicity within the crystal structure; n is an integer of the expansion and the coefficients a_n are :

$$\begin{aligned}
\mathrm{a}_0 &= 1 - \tfrac{1}{16} \cdot \alpha^2 + \tfrac{3}{64} \cdot \alpha^3 + \tfrac{23}{1024} \cdot \alpha^4 + \tfrac{3}{256} \cdot \alpha^5 \\
\mathrm{a}_1 &= -\tfrac{1}{2} \cdot \alpha - \tfrac{1}{4} \cdot \alpha^2 + \tfrac{1}{32} \cdot \alpha^3 + \tfrac{5}{256} \cdot \alpha^4 - \tfrac{35}{2048} \cdot \alpha^5 \\
\mathrm{a}_2 &= -\tfrac{1}{16} \cdot \alpha^2 - \tfrac{1}{32} \cdot \alpha^3 - \tfrac{15}{512} \cdot \alpha^4 - \tfrac{283}{18432} \cdot \alpha^5 \\
\mathrm{a}_3 &= -\tfrac{1}{64} \cdot \alpha^3 - \tfrac{1}{48} \cdot \alpha^4 - \tfrac{9}{1024} \cdot \alpha^5 \\
\mathrm{a}_4 &= -\tfrac{5}{1024} \cdot \alpha^4 - \tfrac{67}{9216} \cdot \alpha^5 \\
\mathrm{a}_5 &= -\tfrac{7}{4096} \cdot \alpha^5
\end{aligned}$$

The comparison of the first non-constant term $a_1(\alpha) \cdot \cos\left(\frac{2\pi L}{c} \cdot d\right)$ in relation 6.9, which is responsible for the periodicity of the dispersion relation, with the experimental dispersions along the L direction immediately reveals that the dimer periodicity d equals half of the c lattice parameter. Indeed, the experimental data reveal that the period (P) of the energy dispersion equals $P = 2$ (r. l. u.) and at the same time it equals to $P = \frac{2 \cdot \pi \cdot c \cdot}{2 \cdot \pi \cdot d}$. The extracted value of the dimer periodicity $d = \frac{c}{2}$ corresponds to the alternating screw chain model (Fig. 6.2(d)) while the linear chain model (Fig. 6.2(c)) can be excluded because it would have the periodicity of $d = c$.

The 1D alternating screw chain model supports the presence of two identical modes in the magnetic excitation spectra. Indeed, the J_{intra} and J_{inter} magnetic exchange couplings alternate twice within an one crystallographic unit cell along the c-axis. As a consequence, there are two inequivalent dimers per unit cell which leads to the observation of the shadow mode in the magnetic excitations spectrum [113; 114] due to the reduction of the Brillouin zone by a factor of 2 along the L direction.

6.4.3.2 The Hamiltonian of $BaCu_2V_2O_8$

To extract accurate values of the magnetic exchange interactions J_{intra} and J_{inter}, the energies of the peak at the dispersion minima (6,0,1), (8,0,0) and the dispersion maximum (6,0,2) were

analysed using the one-magnon dispersion relation of an alternating chain calculated to 5^{th} order (eq. 6.9) taking into account resolution effects. Although there are two modes in the experimentally observed magnetic excitation spectrum, the one magnon dispersion relation reproduces only one of them depending on the sign of the J_{inter} magnetic exchange interaction while the second one is a shadow mode due to the srew chain structure. Thus, two possible solutions can be extracted depending on which mode is analysed using the one-magnon dispersion relation as a main one. Indeed, the first non-constant term $a_1(\alpha) \cdot \cos\left(\frac{2\pi L}{c} \cdot d\right)$ in the relation 6.9 has minima at even-L and maxima at odd-L for a positive (AFM) J_{inter} and vice versa for a negative (FM) J_{inter}.

Since there is no preference regarding the sign of the J_{inter}, each mode should be analysed separately to get both solutions. Figure 6.8(a)(black filled dots) shows the combined high resolution constant wave-vector scans collected at base temperature at the intense dispersion minimum at (6,0,1) and at the intense dispersion maximum at (6,0,2) which correspond to the same mode "B". Since this mode has minima at odd-L and maximum at even-L it should follow to the one-magnon dispersion relation with AFM J_{inter}. Both energy scans were fitted by the one-magnon dispersion relation (eq. 6.9) convolved with the instrumental resolution function. The instrumental resolution function was calculated by the RESCAL software for the experimental settings which were used for these particular measurements [115]. Although the lifetime of the magnetic excitations at base temperature is supposed to be infinite corresponding to a delta function of the magnetic excitations in the magnetic excitation spectrum, the experimental observations are limited by the finite instrumental resolution function. The convolution of the energy dispersion with the experimental resolution function results in a finite width of the observed lineshapes of the magnetic excitations and also a tiny energy shift of the peak positions.

The solid red line on the bottom panel of Fig. 6.8(a) gives the best fit of the experimental data using this one-magnon dispersion relation convolved with the instrumental resolution function. The fitted curve reproduces the experimental data well revealing that the instrumental resolution function is asymmetric when convolved with the dispersion. The values of the dominant intradimer magnetic exchange coupling and the alternation parameter α extracted from the fit analysis are J_{intra}=40.92meV and α=-0.2925 and, indeed, imply that the AFM dimers are coupled ferromagnetically.

The substitution of the extracted values of J_{intra} and α to the eq. 6.9 yields the dispersion minimum of E_{601}=35.37 $\pm$ 0.05 meV and the dispersion maximum E_{602}=45.56 $\pm$ 0.05 meV which are shifted with respect to the experimentally observed peaks by less than 0.15meV illustrating the effect of resolution on the experimentally observed peak position.

In order to get an solution where both magnetic exchange interactions are antiferromagnetic, the other mode, which has minima at even-L and maxima at odd-L, should be analyzed in a similar way as it was done for the first mode "B". Alternatively, the first mode "B" (e.g dispersion minimum (6,0,1) and the dispersion maximum (6,0,2)) can be reanalysed by the

modified one-magnon dispersion relation calculated to 5^{th} where the cosines are replaced by the cosines with the phase shift of π e.g. $\cos\left(\frac{n\cdot 2\pi L}{c}\cdot d\right) \rightarrow \cos\left(\frac{n\cdot 2\pi L}{c}\cdot d+\pi\right)$. Indeed, the one-magnon dispersion relation modified by the phase shift of π has minima at odd-L and maxima at even-L for the solution where both magnetic exchange interactions are antiferromagnetic.

Although (8,0,0) is the dispersion minimum of the mode "A", this mode does not have a sufficiently intense dispersion maximum. Thus, in order to get the second solution, the dispersion minimum (6,0,1) and the dispersion maximum (6,0,2) were fitted by the modified one-magnon dispersion relation (eq. 6.9) where the cosines in the expansion are replaced by $\cos\left(\frac{n\cdot 2\pi L}{c}\cdot d+\pi\right)$. The values of the intradimer exchange coupling and the alternation parameter α were extracted to be J_{intra}=40.75meV and α=0.225 (solid magenta line on the top panel of Fig. 6.8(a)).

In order to verify this solution, the constant wave-vector scans at the dispersion minimum (8,0,0) (mode "A") and the constant wave-vector scan at the dispersion maximum (6,0,2) (mode "B") were fitted simultaneously by the one-magnon dispersion relation (eq. 6.9) where the cosines in the expansion were equal to $\cos\left(\frac{n\cdot 2\pi L}{c}\cdot d\right)$ and $\cos\left(\frac{n\cdot 2\pi L}{c}\cdot d+\pi\right)$, respectively, taking into account the instrument resolution function. The best fit is achieved with the solution of J_{intra}=40.74 and α=0.227 (dashed blue line on the top panel of Fig. 6.8(a)). These values are the same within error as the values which were extracted from the analysis of (6,0,1) and (6,0,2) using the modified one-magnon dispersion relation.

Figure 6.8(b,c) shows the one-magnon dispersion relation (eq. 6.9) plotted over the experimental dispersion along the (6,0,L) and (2,0,L) directions for both extracted AFM-FM (solid line) and AFM-AFM (dashed line) solutions of the alternating chain Heisenberg Hamiltonian (eq. 6.8). The plot confirms that both AFM-AFM and AFM-FM solutions provide an equally good agreement with the experimental data and cannot be distinguished only by the analysis of the energy peak positions.

6.4.3.3 Comparison with the DMRG computations

In order to unambiguously distinguish the solution of the Hamiltonian of $BaCu_2V_2O_8$, the results of the INS measurements were compared with the results of the DMRG computations which were performed by Alexander Tiegel from the theory department of Goettingen university under supervision of Dr. S.R. Manmana, Prof. Dr. A. Honecker and Prof. Dr. T. Pruschke [110]. The magnetic excitation spectra of $BaCu_2V_2O_8$ were computed directly in the frequency domain for a one-dimensional systems of finite size of 80 atoms and open boundary conditions using DMRG-based Chebyshev expansions at zero temperature. The computations were performed for the Hamiltonian of the alternating-chain (eq. 6.8) using both the AFM-AFM and AFM-FM solutions and taking into account the positions of the Cu^{2+} magnetic ions [110]. The relative weights of the magnetic exchange paths were chosen according

to the weights proposed for the screw-chain model[98], thus, J_{intra}=J_1 and J_{inter}=J_2. Because there are two screw chains with opposite sense of rotation in each $BaCu_2V_2O_8$ unit cell, the results were obtained as a superposition of both screw chains.
Figure 6.9 presents the results of the DMRG structure factor for the (6,0,L) and (H,0,5) directions at zero temperature for the AFM-AFM and AFM-FM models. For boths models the computations reveal that there are two gapped modes which match the experimental data in terms of the energy scale and periodicity. However, only the magnetic excitation spectrum computed for the AFM-FM screw alternating chain model matches the intensity distribution of the experimental data while the intensity distribution of the simulated spectrum for the AFM-AFM case displays the opposite intensity distribution with respect to the experimental data.
In order to get the weights of the magnetic exchange paths and to distinguish which one is responsible for the dominant AFM J_{intra} and which for the weaker FM J_{inter}, the DMRG computations were performed for the AFM-FM screw alternating chain model with the opposite assignment of the interactions, thus, J_{intra}=J_2 and J_{inter}=J_1. However, the results reveal no difference in the intensity distributions with respect to the model where J_{intra}=J_1 and J_{inter}=J_2.
The results of the DMRG computations distinguish the correct solution of the Hamiltonian of $BaCu_2V_2O_8$ and implie that $BaCu_2V_2O_8$ is a 1D alternating chain where the AFM dimers are coupled ferromagnetically along the *c*-axis. These computations prove that both dispersion modes arise from the screw-chain geometry of the compound where the magnetic exchange interactions are realized via the magnetic exchange paths Cu-O-V(II)-O-Cu and Cu-O-Cu which form the screw chain along the *c*-axis. However, the DMRG calculations cannot determine which of the two exchange paths J_1 and J_2 is the intradimer interaction and which is the interdimer interaction.

6.4.3.4 First moment sum rule

To distinguish which path is responsible for the weak FM interdimer exchange interaction J_{inter} and which gives rise to the dominant intradimer AFM exchange coupling J_{intra}, the single crystal INS data were analysed using the first moment sum rule [116; 117]:

$$\hbar\langle\omega\rangle_Q \equiv \hbar^2 \int_{-\infty}^{+\infty} \omega S(Q,\omega) d\omega \propto -\sum_m |F_{anis}(Q)|^2 \cdot J_m \langle \mathbf{S_0} \cdot \mathbf{S_{d_m}} \rangle (1 - cos(\mathbf{Q} \cdot \mathbf{d_m})) \qquad (6.10)$$

Here, in the middle part of equation 6.10, S(Q,ω) is the dynamic structure factor, **Q** is the wavevector transfer, ω is the frequency. In the right part of equation 6.10 $\langle \mathbf{S_0} \cdot \mathbf{S_{d_{J_m}}} \rangle$ is a spin-spin correlation function, J_m is the magnetic exchange constant which couples two spins separated by the distance $\mathbf{d_m}$. $F_{anis}(Q)$ is an anisotropic magnetic form factor for Cu^{2+} magnetic ions which takes into account the anisotropy of the $3d_{x^2-y^2}$ electronic orbital

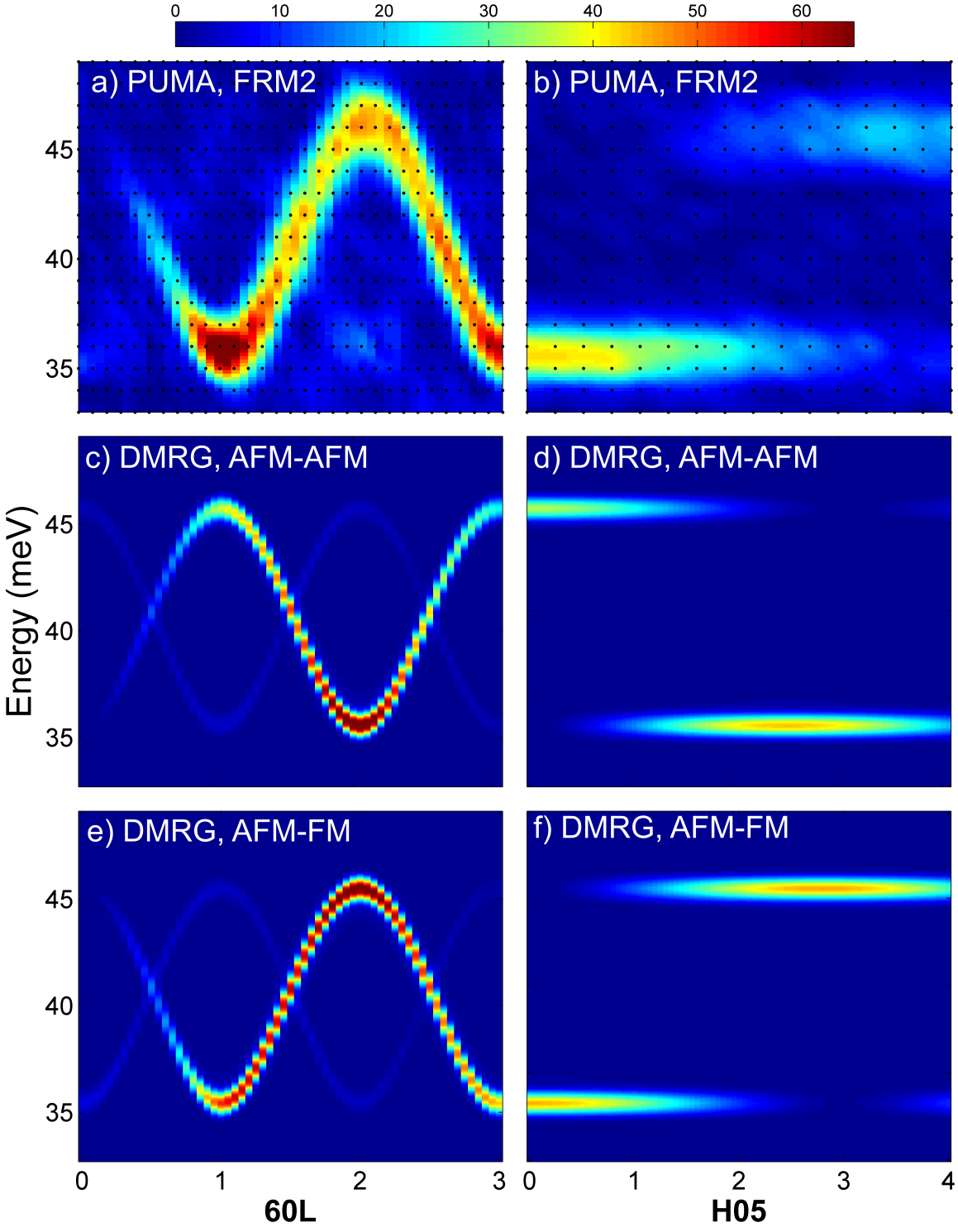

Figure 6.9: (a) INS data along (6,0,L) direction, (b) INS data along (H,0,5) direction, (c-d) DMRG computations for the AFM-AFM Hamiltonian of the magnetic excitation spectrum along (6,0,L) and (H,0,5) directions, (e-f)DMRG computations for the AFM-FM Hamiltonian of the magnetic excitation spectrum along (6,0,L) and (H,0,5) directions.

d_m	RH screw Chain			LH screw Chain		
	$d_{mRH.a}$	$d_{mRH.b}$	$d_{mRH.c}$	$d_{mLH.a}$	$d_{mLH.b}$	$d_{mLH.c}$
d_1=3.007Å	2.2939Å	0	1.944Å	0	2.2939Å	1.944Å
d_1^*=6.314Å	0	1.9116Å	6.04256Å	1.9116Å	0	6.04256Å
d_2=2.86Å	0	1. 9115Å	2.1298Å	1.9115Å	0	2.1298Å

Table 6.1: The distances $\mathbf{d}_m$ between the Cu-Cu magnetic ions and their projections on crystal axis for the CuO_4 plaquettes which contain *b-c* (Type I) or *a-c* (Type II) crystal axes.

and depends on the polar angle θ between the wavevector transfer Q and z-axis which is perpendicular to the plane of the orbital. [103; 117]:

$$F_{anis}(Q) = \langle j_0 \rangle - \frac{5}{7}(1 - 3cos^2\theta)\langle j_2 \rangle + \frac{9}{56}(1 - 10cos^2\theta + \frac{35}{4}cos^4\theta)\langle j_4 \rangle \tag{6.11}$$

Here, $\langle j_0 \rangle$,$\langle j_2 \rangle$ and $\langle j_4 \rangle$ are spherical Bessel functions. For CuO_4 copper-oxygen plaquettes, the $3d_{x^2-y^2}$ electronic orbitals lie within the plaquettes forming the strong covalent *d-p* bonds with the O 2p orbitals and the z-axis is perpendicular to the plaquettes [118]. Thus, the anisotropic magnetic form factor for Cu^{2+} magnetic ion within the copper-oxygen plaquettes is determined by equation 6.11 where the polar angle θ is the angle between the wavevector transfer and the normal to the plaquettes [103]. Because there are two types of the screw chains in $BaCu_2V_2O_8$ which contain either *b-c* or *a-c* crystal axes due to the two counter-rotation screw chains in each units cell (see Fig. 6.2(b)), two form factors with $\cos\theta_a = \frac{Q_a}{|Q|}$ and $\cos\theta_b = \frac{Q_b}{|Q|}$ should be taken into account in the general case. However, for the particular cases of Q with h=k both form factors are the same.

The first moment sum rule (eq. 6.10) connects the first moment of the dynamical structure factor with the expectation value of the spin-spin correlation function at base temperature for a Heisenberg Hamiltonian [117]. Each contribution $J_m\langle \mathbf{S_0} \cdot \mathbf{S_{d_m}} \rangle$ modulates with its own periodicity $(1 - cos(\mathbf{Q} \cdot \mathbf{d_m}))$, thus, the dominant one can be distinguished, however, the absolute value of the exchange interaction J_m cannot be extracted by this method. In the general case the two types of screw chains in $BaCu_2V_2O_8$ produce different modulations for the same d_m distance because their projections on the wavevector transfer are different and are connected by relations $d_{mRH.a}$=$d_{mLH.b}$ and $d_{mRH.b}$=$d_{mLH.a}$. Thus, for each coupling J_m between two Cu magnetic ions which are separated by the distance d_m two contributions $J_m\langle \mathbf{S_0} \cdot \mathbf{S_{d_m}} \rangle(1 - cos(Q_{a^*}d_{mRH.a} + Q_{b^*}d_{mRH.b} + Q_{c^*}d_{mRH.c}))$ and $J_m\langle \mathbf{S_0} \cdot \mathbf{S_{d_m}} \rangle(1 - cos(Q_{a^*}d_{mLH.a} + Q_{b^*}d_{mLH.b} + Q_{c^*}d_{mLH.c}))$ due to the two chains should be counted. However, for the particular case of Q with h=k both chains give the same modulation.

Because $BaCu_2V_2O_8$ has the space-group $I\bar{4}2d$ and Laue class 4/mmm, there are 16 symmetry-equivalent reflections which give four equally weighted, nonequivalent modulations which should be taken into account.

Figure 6.10(a-b) shows the raw INS data measured along (0,0,L) and (1,1,L) directions at 5K using the IN8 triple-axis spectrometer at ILL, Grenoble, France. These particular directions were chosen because of the clear background and simplified maths arising for the particular case of the wavevector Q with h=k. Figure 6.10(c-d) shows the background subtracted data within the area which is indicated in Fig. 6.10(a-b) by the white squares. These background subtracted data were used to calculate the first moment of the dynamic structure factor according to the left part of the equation 6.10 over the energy range of 34meV<E<46meV where the magnetic excitations exist. Figure 6.10(e-f) show the result plotted as a function of the projection of the wavevector transfer on the c^* axis along the (0,0,L) and (1,1,L) reciprocal lattice directions, respectively. The first moment of the dynamic structure factor was fitted using the right hand part of equation 6.10 with d_m fixed at the values for the proposed models (Table 6.1) [97; 98].

To identify the dominant interaction the data were fitted first only with a single contribution to $J_{d_m}\langle \mathbf{S_0} \cdot \mathbf{S_{d_m}} \rangle (1 - cos(\mathbf{Q} \cdot \mathbf{d_m}))$ where d_m was fixed at values d_1=3.007Å(solid blue line), d_2=2.86Å(solid magenta line) or d_1^*=6.314Å(solid green line). The results are plotted in Fig. 6.10(e-f). Here, d_2 corresponds to the distance between the copper ions within CuO_4 plaquettes and corresponds to the J_2 exchange interaction, d_1 is the distance which connects the copper-oxygen plaquettes in the screw chains along the c-axis corresponding to the J_1 interaction and d_1^* is the distance which connects the copper-oxygen plaquettes into the linear chains along the c-axis corresponding to the J_1^* interaction. For both the (0,0,L) and (1,1,L) directions the distance d_1^* gives a modulation with the clearly wrong periodicity while the both distances d_1 and d_2 provide the correct periodicity and d_1 gives a slightly better agreement with the data than the d_2. In order to distinguish which interaction J_1 or J_2 is the strongest, the first moment of the dynamic structure factor was fitted by the first moment sum rule relation with two contributions $J_1\langle \mathbf{S_0} \cdot \mathbf{S_{d_1}} \rangle (1 - cos(\mathbf{Q} \cdot \mathbf{d_1}))$ and $J_2\langle \mathbf{S_0} \cdot \mathbf{S_{d_2}} \rangle (1 - cos(\mathbf{Q} \cdot \mathbf{d_2}))$. The red lines in Fig. 6.10(e-f) give the best fit which is achieved for the values of $J_{d_1}\langle \mathbf{S_0} \cdot \mathbf{S_{d_1}} \rangle$= -984 ± 192, $J_{d_2}\langle \mathbf{S_0} \cdot \mathbf{S_{d_2}} \rangle$= -255 ± 122 for (0,0,L) direction and $J_1\langle \mathbf{S_0} \cdot \mathbf{S_{d_1}} \rangle$= -769 ± 177, $J_2\langle \mathbf{S_0} \cdot \mathbf{S_{d_2}} \rangle$= -500 ± 163 for (0,0,L) direction. The results extracted from the fit analysis of (0,0,L) and (1,1,L) directions agree well with each other within the error bar and suggest that the strongest interaction is realized between the copper ions which are separated by the distance d_1=3.007Å. This implies that J1 is the intradimer exchange interaction while J2 is the interdimer exchange interaction. The negative sign indicates that the spin correlations agree with the exchange constants i.e. they are not frustrated. Indeed, for the isolated singlets the spin-spin correlation is expected to be $\langle \mathbf{S_0} \cdot \mathbf{S_d} \rangle$= -3/4 [119].

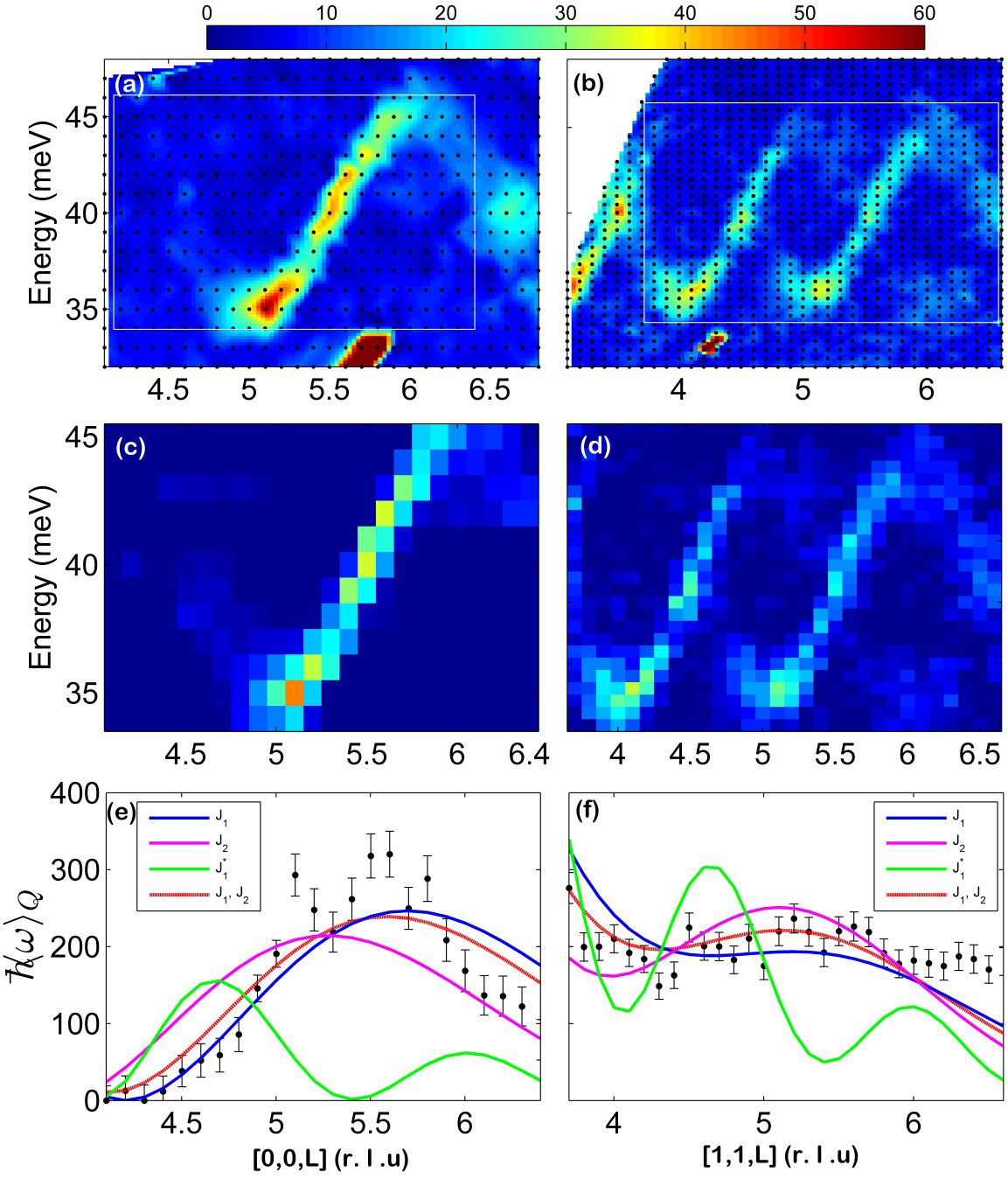

Figure 6.10: (a) Raw INS data along (0,0,L) direction, (b) raw INS data along (1,1,L) direction, (c) background subtracted INS data along (0,0,L) direction, (d) background subtracted INS data along (1,1,L) direction, (e-f) First moment of the dynamic structure factor calculated for the (0,0,L) and (1,1,L) directions, respectively, and fitted using the first moment sum rule relation (eq. 6.10) with single modulation contribution $J_m\langle \mathbf{S_0} \cdot \mathbf{S_{d_m}}\rangle(1 - cos(\mathbf{Q} \cdot \mathbf{d_m}))$ where d_m is fixed to the values d_1=3.007Å(solid blue line), d_2=2.86Å(solid magenta line) or d_1^*=6.314Å(solid green line) and with two contributions of d_1=3.007Åand d_2=2.86Å(solid red line)

6.4.3.5 Discussion

The powder and single crystal INS measurements of $BaCu_2V_2O_8$ were performed and analysed and the results were presented in this section.
The INS powder measurements reveal that $BaCu_2V_2O_8$ is a highly dimerized magnetic system where the magnetic excitations extend over the energy scale of 35meV-46meV. This result is in agreement with the analysis of the magnetic susceptibility data of $BaCu_2V_2O_8$ which predicts that the energy gap is $\Delta = 32.4$meV. The ratio of the energy gap to the band width equals 3.6 confirming that $BaCu_2V_2O_8$ is a highly dimerized magnetic system while the significant width of the band of the magnetic excitations suggests the presence of interdimer magnetic exchange coupling and contradicts the model of the isolated dimers which was suggested earlier in the literature [43; 101].
The single crystal INS measurements of $BaCu_2V_2O_8$ provide accurate values of the energy gap $\Delta = 35.37\text{meV} \pm 0.05\text{meV}$ and the band width $BW = 10.19\text{meV} \pm 0.05\text{meV}$. The results also reveal that the magnetic excitation spectrum consists of two gapped excitation modes which both disperse along the L direction and are completely dispersionless within the (a^*b^*) plane in agreement with one-dimensional dimerized chain models proposed in the literature [97; 98]. However, the analysis of the dispersion periodicity reveals that only the screw chain model [98] corresponds to the periodicity of the experimental dispersion. The screw chain model is also consistent with the presence of the doubled-modes observed in the excitation spectrum in a similar way to the zig-zag chain which causes a doubled-mode dispersion in the 1D ferromagnet $CoNb_2O_6$ [114] due to the fact that there are two dimers per unit cell along the c-axis.
The precise fit analysis of the energy dispersion of the single crystal magnetic excitation spectrum of $BaCu_2V_2O_8$ using the one-magnon dispersion relation calculated up to 5^{th} order reveals that there are two possible solutions of the Hamiltonian of $BaCu_2V_2O_8$. One solution suggests that both intra- and interdimer magnetic exchange couplings are AFM while the second solution proposes that the AFM dimers are coupled ferromagnetically.
Although the AFM-FM solution contradicts all models proposed in the literature [41; 42; 43; 97; 98; 101], it is in good quantitative agreement with the results of the analysis of the susceptibility data of $BaCu_2V_2O_8$ using the coupled-dimer model which also found that the interdimer interaction is ferromagnetic. Moreover, the comparison of the experimental magnetic excitation spectrum with the results of the theoretical DMRG computations which were performed by A. Tiegel for both the AFM-FM and AFM-AFM alternating screw chain models reveals that only AFM-FM solution provides the correct intensity distribution of excitation spectrum of $BaCu_2V_2O_8$.
In order to distinguish which path is responsible for the dominant AFM exchange interaction and which for the weak FM interdimer coupling, the first moment of the dynamic structure factor was calculated along the directions (0,0,L) and (1,1,L) and was fitted to the first mo-

ment of the data using the first moment sum rule relation. The results extracted from the analysis of both directions suggest that the dominant AFM magnetic exchange interaction J_{intra} is realized via the Cu-O-V(II)-O-Cu super-super exchange path J_1 while the weak FM interaction J_{inter} is realized via the Cu-O-Cu super-exchange path within the copper-oxygen plaquettes corresponding to J_2. This result is in qualitative agreement with the first principle electronic structure calculations [101] and with the relative weights proposed by Koo *et.al.* [98] for the screw chain model, however, both these theories predicted that J_2 was antiferromagnetic and/or very weak. The result found here that the interdimer interaction J_2 is in fact ferromagnetic is ,however, consistent with the Goodenougth - Kanamori - Anderson rule. Indeed, the bridge angle of the Cu-O-Cu path J_2 is 94° which according to the Goodenough - Kanamori - Anderson rule is close to the crossover from AFM to FM interaction [10; 9; 120], thus, a ferromagnetic interaction is possible.
Together these results show that $BaCu_2V_2O_8$ is an AFM-FM alternating screw chain which is running along the *c*-axis and where the dominant AFM exchange interaction J_{intra}=40.92meV is realized via the super-super exchange path Cu-O-V(II)-O-Cu while Cu-O-Cu magnetic exchange path within the edge-sharing plaquettes is responsible for the weak FM J_{inter}=-11.97meV exchange coupling.

6.4.4 Conclusions

In this Chapter the magnetic properties of $BaCu_2V_2O_8$ were explored by using a wide variety of experimental techniques such as single crystal magnetic susceptibility measurements as well as powder and single crystal inelastic neutron scattering measurements. The observed experimental data were analysed employing different theoretical approaches in order to distinguish between magnetic models and to solve the Hamiltonian of $BaCu_2V_2O_8$. In addition, the experimental magnetic excitation spectrum of single crystal $BaCu_2V_2O_8$ was compared to the results of the theoretical DMRG computations which were performed by A. Tiegel .
The analysis which was performed in this Chapter proves that $BaCu_2V_2O_8$ is a AFM-FM alternating screw chain where the AFM dimers are weakly coupled ferromagnetically along the *c*-axis. The magnetic properties of this compound were described well by the Heisenberg Hamiltonian for the 1D alternating chain [45] with magnetic exchange interactions of J_{intra}=40.92meV and J_{inter}=-11.97meV. The weak FM J_{inter} was found to be realized via the Cu-O-Cu super-exchange path within the double copper-oxygen plaquettes while the strong AFM J_{intra} which couples the spins into dimers occurs via the Cu-O-V(II)-O-Cu super-super exchange path. Together these interactions give rise to 1D AFM-FM alternating screw chains along the *c*-axis (Fig. 6.2(d)).
Because $BaCu_2V_2O_8$ is a rare example of 1D AFM-FM chain, it is a potential candidate to investigate various unconventional behaviours in a new type of unexplored magnetic system. Particularly the high ratio of the dimerization in $BaCu_2V_2O_8$ of 3.6 is similar to that of the

1D AFM-AFM alternating chain copper nitrate where strongly correlated behaviour at finite temperatures was recently observed for the first time [84]. This makes $BaCu_2V_2O_8$ a potential candidate for the search and investigation of coherent behaviour at finite temperatures in order to explore how this phenomenon is affected by the ferromagnetic interdimer exchange coupling.

7 Magnetic properties of $BaCu_2V_2O_8$ at finite temperatures

7.1 Introduction

In previous Chapter the magnetic Hamiltonian of $BaCu_2V_2O_8$ was extensively explored at base temperature using a combination of the experimental and theoretical techniques. $BaCu_2V_2O_8$ was found to be a spin-half highly dimerized 1D antiferromagnetic − ferromagnetic (AFM-FM) alternating screw chain where the antiferromagnetic dimers are weakly coupled ferromagnetically contradicting to all previous models suggested in the literature [41; 43; 97; 98; 101]. The magnetic excitation spectrum of this compound is gapped and extends within the energy range from 35.5 meV to 45.5 meV where the high ratio of the energy gap (Δ) to the band width ($\mathbf{B}$) of $\frac{\Delta}{\mathbf{B}} = 3.6$ is attributed to strong dimerization of the magnetic system. The magnetic interactions of this compound were described well in the previous Chapter by the spin$-1/2$ Heisenberg Hamiltonian for the 1D chain:

$$H = \sum_i J_1 \, \mathbf{S}_{i,1} \cdot \mathbf{S}_{i,2} + J_2 \, \mathbf{S}_{i,2} \cdot \mathbf{S}_{i+1,1}. \tag{7.1}$$

where J_1 and J_2 are the intra- and interdimer exchange couplings, respectively, and were deduced to be of $J_1 = 40.92meV \pm 0.01$ meV and $J_2 = -11.97meV \pm 0.1$ meV at base temperature with corresponding alternation ratio of $\alpha = \frac{J_2}{J_1} = -0.2925$ confirming the strong dimerization of the magnetic behaviour in this compound.

In this Chapter the thermal behaviour of the magnetic excitations in $BaCu_2V_2O_8$ is investigated using both experimental and theoretical techniques. As a highly dimerized spin$-1/2$ chain, $BaCu_2V_2O_8$ is a promising candidate to demonstrate strongly correlated behaviour at finite temperatures which was initially theoretically predicted for the spin$-1/2$ gapped antiferromagnets [121] and which contradicts to the conventional picture of thermal effects in quantum magnets [89]. Indeed, according to the conventional picture, at finite temperatures the magnetic excitations lose their coherence due to their uncorrelated collisions with each other which reduces their lifetime and, as a consequence, leads to the symmetric Lorentzian

broadening of their line shapes where the inverse of the Lorentzian width equals their lifetime [86; 122]. This behaviour was experimentally observed in two- and three-dimensional quantum magnets Rb_2MnF_4 and MnF_4 with gapless spin-wave excitations where the available states cover a big region of the phase space and the excitations do not interact with each other [87; 88]. However, recent theoretical research based on integrable quantum field theory [121] predicts that in strongly dimerized quantum magnets the magnetic excitations retain their coherence at elevated temperatures. These dimerized quantum magnets are characterized by a spin singlet ground state and an excited triplet state which are referred to as triplons [83]. These magnetic excitations are subject to the hard-core boson constraint so that only one excitation is allowed per dimer site [123]. At finite temperatures the thermally induced excitations partially occupy the available states and the creation of a new magnon requires the rearrangement of the thermally excited magnons within the system due to the hard-core constraint. This results in the strong correlations between the excitations which can be experimentally observed in an asymmetric thermal lineshape broadening of the magnetic excitations.

Because the coherence of the magnetic excitations at finite temperatures has potential applications for the quantum devices, this phenomenon was recently studied from both theoretical and experimental sides [36; 84; 85; 124; 125; 126]. First time strongly correlated behaviour at finite temperature was experimentally observed in 1D AFM copper nitrate [84]. This compound is a highly dimerized alternating chain where the ratio of the gap to the band width equals 3.9. At high temperatures the lineshapes were found to broaden asymmetrically which was interpreted as a signature of strong correlations between triplons and were modeled theoretically using the low-temperature expansion of the finite-temperature dynamical structure factor of the spin-$\frac{1}{2}$ alternating Heisenberg chain [124]. This theoretical approach reproduces the asymmetric broadening observed in the experimental data well only at relatively low finite temperatures because it is valid only at low particle density. At higher temperatures the asymmetric behaviour in copper nitrate was verified by the comparison of the experimental data to the exact diagonalization calculations [125]. In addition to the theoretical approaches, the fitting function was introduced to parametrize the asymmetric behaviour as a function of temperature [84]. Unfortunately this function can be hardly used to parametrize the asymmetric broadening because it behaves non-monotonically with respect to the parameters which describe an asymmetry.

Further experimental studies reveal strongly correlated behaviour at elevated temperatures in the 3-dimensional (3D) coupled-dimer antiferromagnet $Sr_3Cr_2O_8$, where the lineshape also becomes asymmetric and increasingly weighted towards the center of the band as temperature increases [36], confirming that this phenomenon is not restricted to 1-dimensional (1D) systems. The experimental data were compared to the results of the first order in the high-density $\frac{1}{z}$ expansion [126]. Although this theoretical approach achieves a remarkable agreement with the experimental data, some of its methodological aspects are still unclear

[127; 128].
This Chapter explores magnetic excitations in $BaCu_2V_2O_8$ at elevated temperatures to test strongly correlated behaviour in this compound. As a rare example of a AFM−FM alternating chain, $BaCu_2V_2O_8$ gives an unique opportunity to complement the investigation of the strongly correlated behaviour at elevated temperatures by the novel class of the dimerized systems with weak ferromagnetic coupling. In $BaCu_2V_2O_8$ the ratio of the gap to the band width equals to $\frac{\Delta}{B} = 3.6$ which is very close to the value of 3.9 in copper nitrate, where the strongly correlated behaviour was experimentally observed for the first time [84]. The energy scale of the magnetic excitations in $BaCu_2V_2O_8$ is higher with respect to the energy scale of the magnetic excitations in $Cu(NO_3)\cdot 2.5(D_2O)$ and $Sr_2Cr_2O_8$ that simplifies the experimental investigation of the strongly correlated phenomena in $BaCu_2V_2O_8$ and allows it to be explored over a wide temperature range.
In this Chapter the thermal behaviour of the line shapes of the magnetic excitations in $BaCu_2V_2O_8$ is precisely explored by the high resolution INS measurements at finite temperatures revealing the asymmetric lineshape broadening of the magnetic excitations with temperature increase. The experimental data were analyzed using a new fitting function which was introduced to parametrize the asymmetry observed in the experimental line shapes of the magnetic excitations. The fitting function is a convolution of the asymmetric Lorentzian and asymmetric Gaussian functions and takes into account the asymmetry of the instrumental resolution function. Additionally the experimental line shapes were compared to the results of two different theoretical approaches revealing a perfect qualitative and quantitative agreement with asymmetric behaviour observed in the experimental data.

7.2 Experimental settings

The strongly correlated behaviour in $BaCu_2V_2O_8$ at finite temperatures were explored via the analysis of the line shapes of the magnetic excitations at moderate temperatures.
The measurements of the high resolution constant wave-vector scans were performed in three separate experiments at the thermal triple−axis spectrometer PUMA which is located at FRM II at the Heinz Maier-Leibnitz Zentrum (MLZ), Garching, Germany [24]. The principle scheme of the thermal triple-axis spectrometer PUMA is shown (Fig.3.4) and discussed in Chapter 3.
For all experiments the same single crystal sample of $BaCu_2V_2O_8$ with mass of m=2.18 g was used. The sample was preoriented with the (H,0,L) plane as a horizontal scattering plane by using the Laue X-ray diffraction instrument in the laboratory for the X-ray experiments at HZB and then was fixed on the aluminium sample holder.
The sample holder with the preoriented sample was mounted into a closed-cycle cryostat that allows it to be cooled down to 3.5K. The temperature of 3.5K was base temperature in all three experiments except the second one, where base temperature was of 5K. Because both

these temperatures are less than 2% of the energy gap, they are assumed to be identically equivalent and in further analysis are both refered to as base temperature (BT).
In all three experiments the doubly−focussed single crystal copper monochromator (Cu (220)) with d-space of 1.28 Å was used together with the PG (002) filter (d-space of 3.35 Å) which allows the final wave vector k_f to be fixed at k_f = 1.97 $Å^{-1}$ (λ=3.189 Å) , k_f = 2.662$Å^{-1}$ (λ=2.36 Å) or k_f = 4.1$Å^{-1}$ (λ=1.532 Å). Two PG filters were placed between the sample and the analyser in order to prevent the contamination by high−order harmonics λ/n and a sapphire filter was placed into the beam before the monochromator in such way that the c-axis of the sapphire crystal was parallel to the beam direction in order to remove the fast neutron background.
The alignment of the sample in each experiment was checked at room temperature by elastic neutron scattering measurements of the (0,0,4) and (6,0,0) nuclear Bragg peaks. For these measurments the final wave vector was fixed at k_f = 4.1$Å^{-1}$. These particular nuclear Bragg peaks were chosen because (6,0,0) is the strongest in the diffraction pattern while the (0,0,4) has 50 % of the intensity of the strongest. During the alignment routine the lattice constants were optimized to the values of a = b = 12.5841 Å and c = 8.0664 Å which were the same for all experiments.
After alignment and corrections of the lattice constants the energy scans at different dispersion minima and maxima were performed at both base temperature and room temperature in order to check the intensity of the magnetic signal and background. For these scans the final wave vector was fixed at k_f = 2.662$Å^{-1}$ which is characterized by the calculated energy resolution value of ≈0.992 meV (at E=35 meV and Q=(3,0,4)) and provides high intensity neutron flux allowing the measurements to be performed quickly.
The high resolution constant wave-vector scans have been measured at the dispersion minima (601) and (800) at several temperatures over the temperature range of T=3.5K-200K and over the energy range of 30 meV-45 meV. In particular, the temperatures BT (expI, expII, expIII), 75K (expI, expII, expIII), 100K (expI, expIII), 125K (expI, expIII), 150K (expI, expIII), 175K (expI, expII, expIII), 200K (expI, expII, expIII) were explored.
These particular wave vectors (6,0,1) and (8,0,0) were chosen due to the following reasons. First, the dispersion minima and maxima are the most promising candidates to observe the asymmetric thermal line shape broadening behaviour [84]. Additionally, the thermal regime of the measurement requires that the investigated wave vectors have the high intensity of magnetic signal and low phonon background within the explored energy range of 30 meV-50 meV at base temperature. Moreover, only one of the two excited modes should have intensity at the explored wave vector otherwise the modes will be overlapped at high temperatures that complicates the analysis of their lineshapes. Finally, the instrument restrictions on the experimentally available range of the phase space should be taking into account. The several dispersion minima and dispersion maxima were tested and only dispersion minima at (6,0,1) and (8,0,0) were found to satisfy the conditions which are listed above. The measurements at

two equivalent wavevectors (6,0,1) and (8,0,0) are necessary in order to improve a statistic, to verify the results and to exclude an influence of other effects such as background.
The constant wave vector scans were conventionally performed changing the energy transfer by varying the wave vector of the incident beam k_i monochromator and keeping the final wave vector k_f of the analyser fixed. For the precise investigation of the line shape behaviour the high energy resolution was achieved by fixing the final wave vector to $k_f = 1.97\text{Å}^{-1}$ which is characterized by the calculated energy resolution value of 0.744 meV (at E=35 meV and Q=(6,0,1)).
The equivalence of the experimental settings of the different experiments was checked by the comparison of the constant wave-vector scans at (6,0,1) at BT which are plotted together in Fig. 7.1. The magnetic signal at (6,0,1) in the first experiment was found to be more intense with respect to the intensity of the magnetic signal at the same wave-vector in the second and third experiments. This difference was attributed to the changes of the monochromator settings and, in order to compare with the peaks at (6,0,1) in the second and third experiments, the peak at (6,0,1) in the first experiment was multiplied on the scaling factor of $\approx$ 0.8. After the scaling, the peaks at (6,0,1) for all three experiments are found to be identical confirming the equivalence of the experimental settings. The equivalence of the (6,0,1) and (8,0,0) dispersion minima was also confirmed by the comparison of the energy scans at these wave vectors which were found to be identical within the background error.
To check the thermal evolution of the band width, the energy scans at the dispersion maximum (6,0,2) have been done at a few temperatures of T=100K, 150K, 200K. Since this dispersion maximum is not useful for the analysis of the thermal lineshape broadening due to the presence of the second mode at the low energies, high resolution was not required. Therefore, for these measurements the final wave vector was fixed at $k_f = 2.662\text{Å}^{-1}$ giving the resolution of 1.6 meV in order to save counting time.

7.2.1 Background subtraction for the line shape analysis

The measurements at finite temperatures overlap with phonons excitations. The phonons depend on temperature and are increasing as temperature increases. Thus, their contribution should be taken into account especially during the analysis of the lineshapes of the magnetic excitations.
Figure 7.2(a)-(p) (black filled squares) shows the raw data of the constant wave vector scans at the (6,0,1) and (8,0,0) dispersion minima which were collected during experiments I- III at base and finite temperatures. To exclude a phonon contribution from the magnetic signal, each energy scans at each temperature was individually analyzed and the phonons background was subtracted. The Gaussian function was found to be suitable to reproduce the line shapes of the phonon excitations.
Figures 7.2(a) and 7.2(g) show the constant wave vector scans at (6,0,1) at base temperature

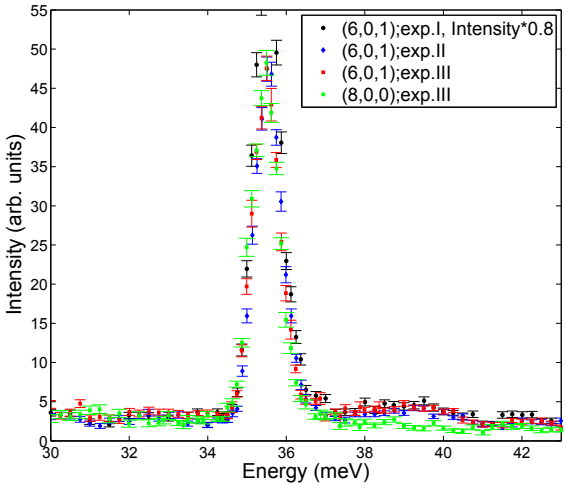

Figure 7.1: Constant wave-vector scans at (6,0,1) in the experiments I-III and at (8,0,0) in the experiment III at base temperature

performed in the Experiment I and Experiment II, respectively and reveal a complex background structure with two broad phonons at ≈32 meV and ≈39 meV. With the temperature increase no new phonons become visible and only flat part of the background increases. Thus, the background which was subtracted at base temperature (Fig. 7.2(a) solid red line) was also used for the higher temperature measurements and only slight modifications of the integrated intensity of the phonons (Fig. 7.2(b)-(f),(h)-(i) solid red lines) were applied. Figure 7.2(a)-(i) (blue filled squares) presents data after the background subtraction for experiments I and II.

Figure 7.2(j) shows the constant wave vector scan at (8,0,0) at base temperature which has much cleaner background with respect to the (6,0,1). Indeed, there are no features at the 32 meV and 39 meV. However, the background was found to increase strongly as temperature increased which was well described by using the cubic polynomial function in combination with Gaussian functions. The parameters of the cubic function were almost the same for all temperatures except the constant term. Figure 7.2(j)-(p) (blue filled squares) presents the raw data after the background subtraction.

7.2.2 Analytical description of the resolution function at PUMA

In the section 6.4 it was shown that the energy scans at the (8,0,0) and (6,0,1) dispersion minima at base temperature are primarily described by the asymmetric instrumental resolution function which was numerically computed using the RESCAL software while the intrinsic width of the magnetic excitations was found to tend to zero. This numerically computed instrumental resolution function is asymmetric when combined with the one-magnon dispersion and well reproduces the clearly experimentally observed asymmetry which weighted toward

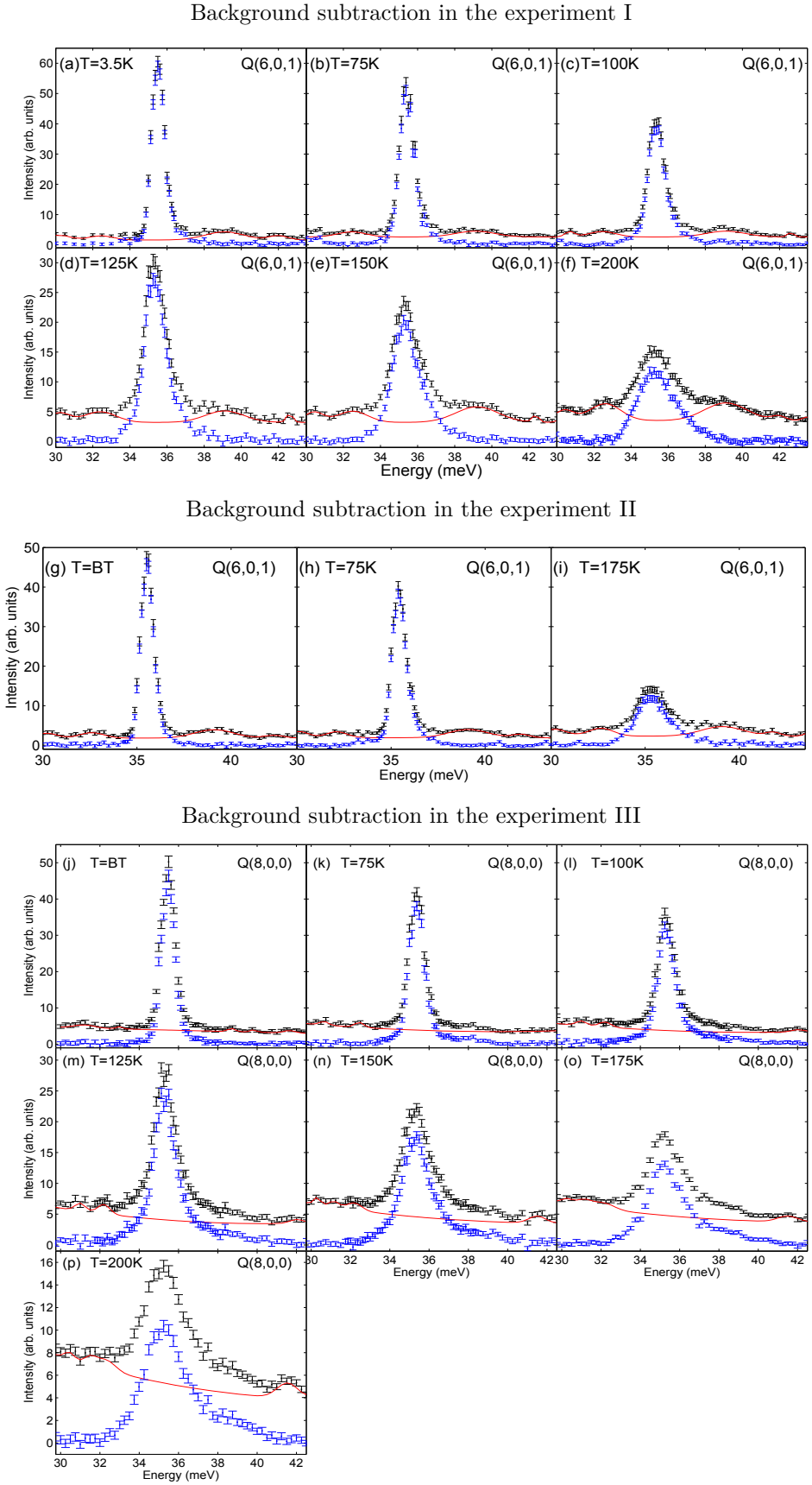

Figure 7.2: Background subtraction in the constant wave-vector scans (a)-(i) at (6,0,1) in the Experiment I-II and (j)-(p) at (8,0,0) in the Experiment III at base temperature. Black filled dots−raw data, solid red lines − fitted background by using the superposition of the Gaussian functions, blue filled dots−data after background subtraction.

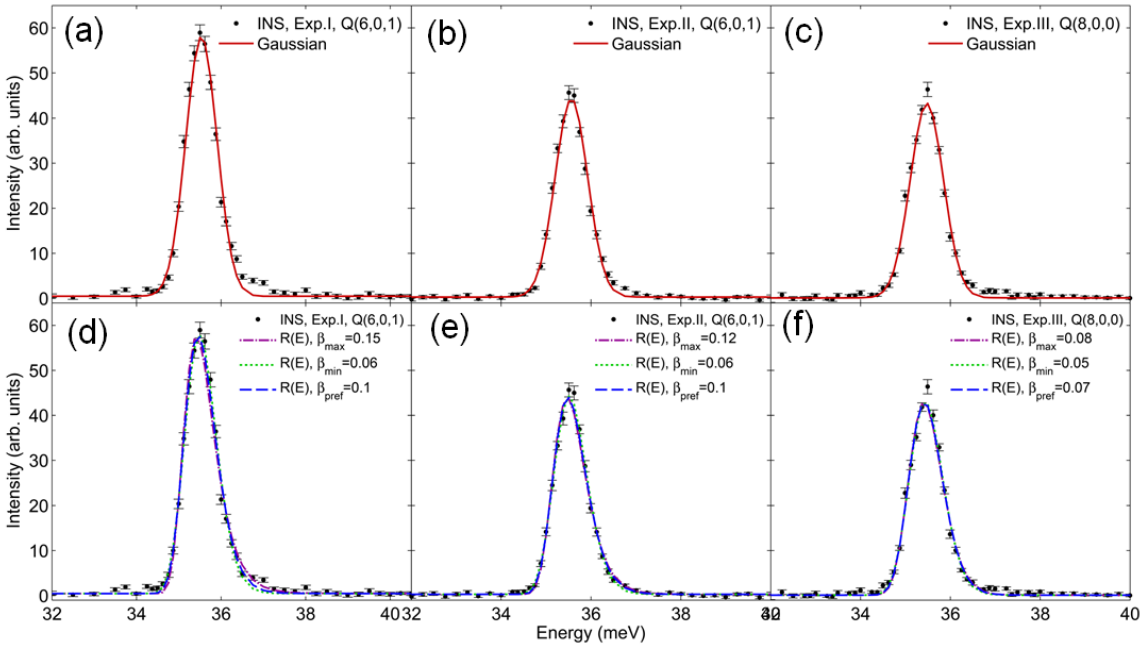

Figure 7.3: Fit analysis of the background-subtracted constant wave-vector scans at (6,0,1) and (8,0,0) measured at BT in experiments I-III using (a)-(c) symmetric Gaussian function, (d)-(e) R(E) function

to the higher energies of both constant wavevector scans at the (6,0,1) and (8,0,0) dispersion minima.

At elevated temperatures the lifetime of the magnetic excitations becomes finite which results in the intrinsic broadening of their lineshapes which can also be asymmetric while the instrumental resolution function is temperature independent. Therefore, the experimentally observed lineshapes of the magnetic excitations at finite temperatures are combination of intrinsic and resolution broadening so that for the analysis of the intrinsic lineshape it is important to distinguish the contribution of the asymmetric instrumental resolution broadening. This distinction can be realized by describing analytically the instrumental resolution function.

Conventionally the instrument resolution function is analytically described by the Gaussian function. Figures 7.3(a)-(c) shows the fit analysis of the energy scans at the dispersion minima at (8,0,0) and (6,0,1) at base temperature using the conventional symmetric Gaussian function. The extracted parameters of the full width at half maximum (W_G) and the peak position (E_0) are listed in the Table 7.1 (second column) .

Although the extracted values of W_G are in a good agreement with the calculated value of 0.74 meV, the conventional Gaussian function does not reproduce the asymmetry of the lineshape which arises from the convolution of the instrumental resolution function with the

Parameters of the resolution function in the experiments I-III				
Experiment I: (6,0,1)				
$\boldsymbol{\beta}$	Gaussian ($\beta = 0$)	R(E), $\beta_{pref} = 0.1$	R(E), $\beta_{max} = 0.15$	R(E), $\beta_{min} = 0.06$
WG_{FWHM}	0.8896 ± 0.0167	0.8929 ± 0.02	0.8843 ± 0.0166	0.87 ± 0.02
E_0	35.493 ± 0.008	35.47 ± 0.01	35.509 ± 0.008	35.53 ± 0.01
Experiment II: (6,0,1)				
$\boldsymbol{\beta}$	Gaussian ($\beta = 0$)	$\beta_{pref} = 0.1$	$\beta_{max} = 0.12$	$\beta_{min} = 0.06$
WG_{FWHM}	0.87 ± 0.0127	0.8712 ± 0.0149	0.8649 ± 0.0113	0.8532 ± 0.016
E_0	35.52 ± 0.008	35.5114 ± 0.006	35.536 ± 0.006	35.563 ± 0.008
Experiment III: (8,0,0)				
$\boldsymbol{\beta}$	Gaussian ($\beta = 0$)	$\beta_{pref} = 0.07$	$\beta_{max} = 0.08$	$\beta_{min} = 0.05$
WG_{FWHM}	0.8821 ± 0.0135	0.8836 ± 0.0142	0.8793 ± 0.0126	0.873 ± 0.026
E_0	35.447 ± 0.006	35.443 ± 0.006	35.4558 ± 0.006	35.476 ± 0.008

Table 7.1 The values of WG and E_0 parameters extracted from the fit analysis of the constant wave-vector scans at (6,0,1) and (8,0,0) at base temperature using the fitting function R(E) with different fixed values of the asymmetry parametr β.

one-magnon dispersion. Indeed, in Fig. 7.3(a)-(c) the fitted line does not clearly reproduce the asymmetric shoulder in the experimental data, which appears within the energy region of 36.5 meV - 37.5 meV.

An asymmetric Gaussian function R(E) was introduced in order to analytically describe the asymmetry of the instrumental resolution function:

$$R(E) = Gaussian\left(W_G + \beta(E - E_0), E\right) = \frac{\exp\left(\frac{-(E-E_0)^2}{2\left(\frac{W_G}{2\sqrt{2\ln(2)}} + \beta(E-E_0)\right)^2}\right)}{\sqrt{2\pi}\left(\frac{W_G}{2\sqrt{2\ln(2)}} + \beta(E - E_0)\right)}. \tag{7.2}$$

This function is based on a normalized Gaussian, where the full-width-at-half-maximum W_G is replaced by $W_G + \beta(E - E_0)$ and β describes the asymmetry of the instrumental resolution function. The parameters E_0 and A denote the peak position and the peak intensity, respectively.

The energy scans at the dispersion minima (6,0,1) and (8,0,0) at base temperature were fitted by the function R(E) to take into account the asymmetry of the resolution limited lineshape and the results are presented in Fig. 7.3(d)-(f). The data were fitted with β fixed at different values, so that only parameters W_G, A and E_0 were varied during the fit. The lower β_{min} and upper β_{max} limits of the parameter β which provides good agreement with the experimental data were determined and the optimum value of the asymmetry parameter β_{pref} was chosen within this range. The values of the W_G and E_0 parameters extracted from the fit analysis

for each fixed value of β_{min}, β_{max} and β_{pref} are listed in Table 7.1

7.2.3 Fitting function

At finite temperatures the intrinsic lineshape of the excitations broadens and becomes asymmetric. In order to parametrize the experimentally observed asymmetry, a customized fitting function F(E) was introduced:

$$F(E) = \frac{A}{\pi} \cdot L\left(W_L + \alpha(E - E_0), E\right) * R(E) =$$

$$= \frac{A}{\pi} \cdot (T) \int_{-\infty}^{\infty} \mathrm{d}t \frac{\frac{W_L(T)+\alpha(T)(t-E_0(T))}{2}}{(t - E_0(T))^2 + \left(\frac{W_L(T)+\alpha(T)(t-E_0(T))}{2}\right)^2} \times \frac{\exp\left(\frac{-(E-t)^2}{2\left(\frac{W_G}{2\sqrt{2\ln(2)}}+\beta(E-t)\right)^2}\right)}{\left(\frac{W_G}{2\sqrt{2\ln(2)}} + \beta(E-t)\right)} \tag{7.3}$$

This function is an convolution of the asymmetric resolution function R(E) with the asymmetric Lorentzian function $L(W_L + \alpha(E - E_0), E)$, where the Lorentzian width W_L is replaced by $W_L + \alpha(E - E_0)$ where α is an asymmetry parameter and E_0 is the center of the peak position. The parameter A is an integrated area of the peak. The asymmetric Lorentzian function is used to parameterize the intrinsic asymmetric lineshape broadening while the resolution function $R(E)$ takes into account the asymmetry due to the instrumental resolution function with parameters fixed to the values extracted at low temperatures (see Table 7.1). The function F(E) is different from a function I(E)=G(W_G,E)*L_{mod}(t,α,γ) which was used to parametrize the asymmetry of the line shape of magnetic excitations in copper nitrate and strontium chromate [84]. The previously used function I(E) is a convolution of the conventional symmetric Gaussian function G(W_G,E) with the modified Lorentzian function $L_{mod}(t)=\frac{1}{1+(t-\alpha t^2+\gamma t^3)^2}$ where the conventionally scaled argument t is replaced by a third-order polynomial t-αt^2+γt^3 whose coefficients α and γ describe an asymmetry of the lineshape. The function $L_{mod}(t,\alpha,\gamma)$ is not a monotonic function with respect to the parameters α and γ because it is a third-order polynomial function. It means that $L_{mod}(t_0,\alpha_1,\gamma_1)$ can be either larger or smaller than $L_{mod}(t_0,\alpha_2,\gamma_2)$ even if $\alpha_1>\alpha_2$ and $\gamma_1>\gamma_2$. Thus, the increase of the values of the α and γ parameters cannot unambiguously indicates the increase of the asymmetry of the line shape. In contrast, F(E) is a monotonic function of the asymmetry parameter α and, therefore, is more suitable to parametrize the asymmetric lineshape broadening with temperature increase.
The function $F(E)$ was created using the MatLab 2012b Software and was verified by fitting a test data set which was simulated in Origin 9.0 software using an inbuilt Voigt function.

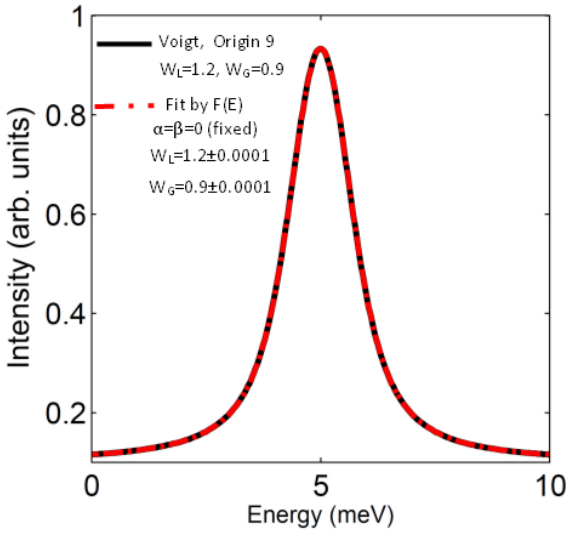

Figure 7.4: Solid black line is the Voigt function simulated in Origin 9 software and fitted then by the function F(E) with asymmetry parameters α and β fixed to zero.

Note, that the infinite integral in Eq. 7.3 is not necessary and can be replaced by the defined integral with relatively large limits of -10 0meV and 100 meV.
Figure 7.4 shows the test data set which was fitted by the function F(E) with the asymmetry parameters β and α fixed to zero. The extracted values of W_L=1.2±0.0001 and W_G=0.9±0.0001 are the same with the parameters which were used for the creating of this data set in the Origin software. This result confirms that the Lorentzian and Gaussian parts of the function F(E) were convoluted correctly.

7.3 Results and Analysis

In order to explore the thermal behaviour of the magnetic excitations at elevated temperatures in the highly dimerized 1D AFM-FM quantum magnet $BaCu_2V_2O_8$, first the temperature dependence of the line shape of magnetic excitations in $BaCu_2V_2O_8$ was explored. The background subtracted high resolution constant wave-vector scans measured at the dispersion minima (6,0,1) and (8,0,0) over the temperature range of 3.5K-200K were analysed using the fitting function F(E) introduced in the previous section. The extracted width and asymmetry parameters were compared with the results of analytical and numerical theoretical approaches. One approach is based on the diagrammatic Brückner approach combined with the method of Continuous Unitary Transformations (DBA-CUT) while the other is based density-matrix renormalization group (DMRG) computations combined with linear prediction. The thermal narrowing of the band width as a function of temperature was also explored and compared with the results of the theoretical predictions of the density-matrix renormal-

ization group (DMRG) computations allowing the temperature dependence of the dominant intradimer magnetic exchange coupling to be extracted. Finally the thermally induced low energy intraband mode was explored by performing the high-resolution energy scans at the vicinity of the theoretically predicted dispersion minimum at (3,0,1).

7.3.1 Asymmetric thermal lineshape broadening

Figure 7.5 shows the constant wave vector scans at the (6,0,1) and (8,0,0) dispersion minima (black-filled dots) and reveals that the excitations clearly broaden with increasing temperature. At the highest temperatures the lineshapes appear asymmetric and weighted towards higher energies.

In order to parametrize the observed asymmetric thermal lineshape broadening, the data at each elevated temperature were fitted using the function F(E) (solid red line) which was introduced in the previous section. The parameters of the instrumental resolution function W_G and β were fixed to the values which were extracted at base temperature (Table 7.1) while the parameters α and W_L, which are responsible for the intrinsic Lorentzian broadening, were freely varied and the extracted values are listed in the Table 7.2 and Table 7.3. Because the asymmetry parameter β of the instrumental resolution function lies within the range $\beta_{min} < \beta < \beta_{max}$, the data sets at each temperature were fitted with parameter β fixed to $\beta = \beta_{min}$, $\beta = \beta_{max}$ and $\beta = \beta_{pref}$. The extracted values of α and W_L at each temperature were averaged so that the error due to the uncertainty in the instrumental resolution function is included to the final error of the extracted values. This was done using formulas:

$$\Delta W_{L_T} = \sqrt{\Delta W^2_{L,\beta_{pref}} + \frac{(W_{L_T,\beta_{pref}} - W_{L_T,\beta_{max}})^2 + (W_{L_T,\beta_{pref}} - W_{L_T,\beta_{min}})^2}{2}} \tag{7.4}$$

$$\Delta \alpha_T = \sqrt{\Delta \alpha^2_{T,\beta_{pref}} + \frac{(\alpha_{T,\beta_{pref}} - \alpha_{T,\beta_{max}})^2 + (\alpha_{T,\beta_{pref}} - \alpha_{T,\beta_{min}})^2}{2}}$$

The extracted asymmetry parameters α and Lorentzian width W_L are plotted as a function of temperature in Fig. 7.5 which reveals that both increase with increasing temperature.

In order to further demonstrate the asymmetry, the data were also fitted by F(E) with the Lorentzian asymmetry parameter α fixed to zero and only the Lorentzian width varied (dashed blue line in Fig. 7.5). While the line shapes of the excitations below 150K are fitted well both with or without asymmetry, the lineshapes at 175K and 200K are in much better agreement with the asymmetric Lorentzian profile.

The asymmetric line shape observed in $BaCu_2V_2O_8$ at finite temperatures is similar to the previously observed asymmetric thermal line shape broadening in the 1D and 3D dimerized compounds of copper nitrate and strontium chromate. Unfortunately the quantitatively comparison of the extracted asymmetry parameters cannot be done because copper nitrate and

strontium chromate where parameterized by a different analytical equation. The asymmetry thermal line shape broadening in $BaCu_2V_2O_8$ can be attributed to strong correlations between the excitations as for copper nitrate and strontium chromate.

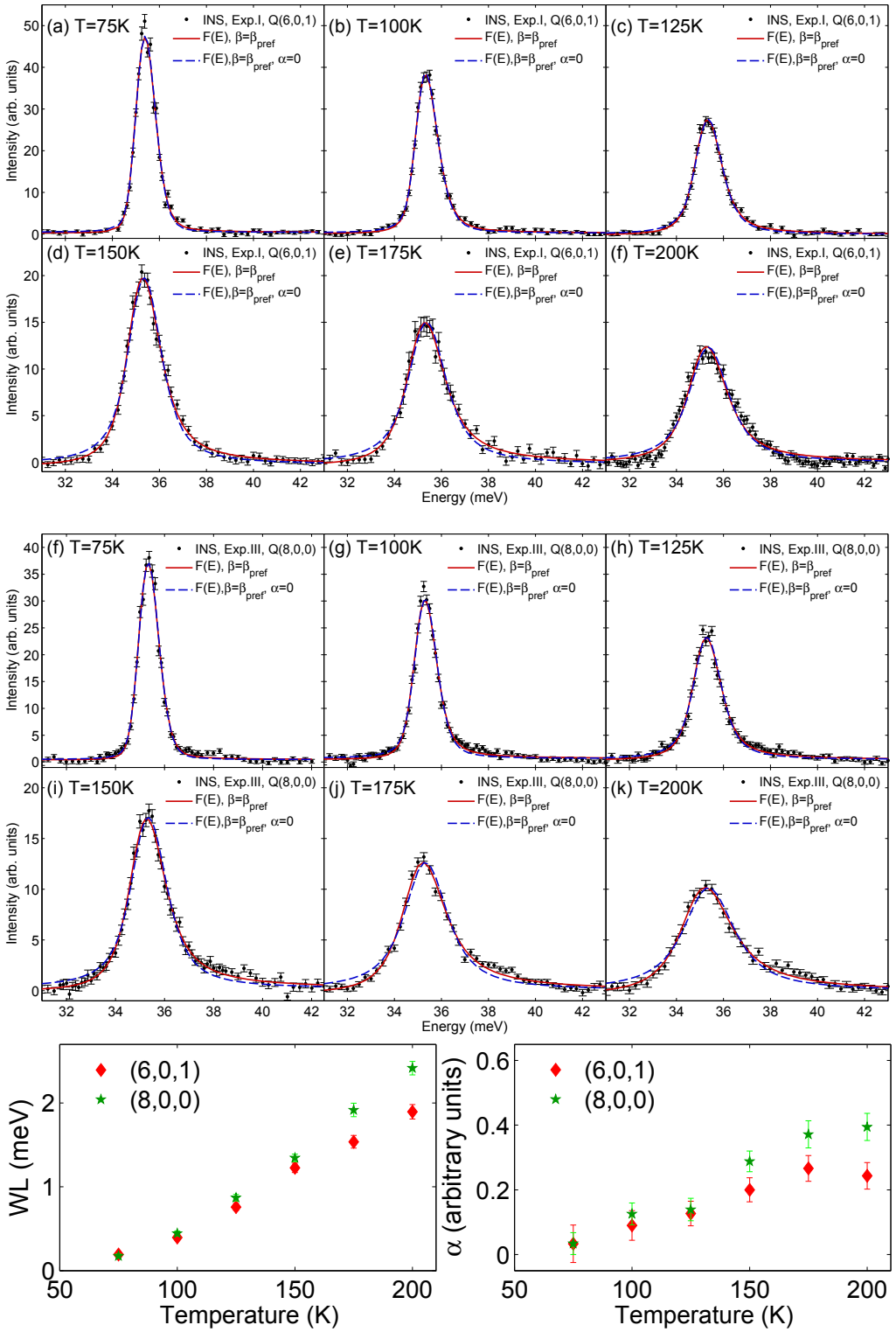

Figure 7.5: Fit analysis of the background subtracted constant wave-vector scans at (6,0,1) and (8,0,0) using introduced F(E) function with all Lorentzian parameters varied (solid red line) and with the asymmetry parameter α fixed to $\alpha = 0$ (dashed blue line)

Extracted fitted parameters at (6,0,1) (Experiments I,II)				
$\boldsymbol{T = 75K}$ **(Exp. I)**	$\boldsymbol{\beta_{pref} = 0.1}$	$\beta_{max} = 0.15$	$\beta_{min} = 0.06$	Averaged
$\boldsymbol{E_0}$	35.384 ± 0.011	35.38 ± 0.01	35.39 ± 0.011	
$\boldsymbol{W_L}$	0.193 ± 0.023	0.1811 ± 0.0238	0.2 ± 0.024	0.193 ± 0.025
$\boldsymbol{\alpha}$	0.0332 ± 0.03	0.0241 ± 0.03	0.076 ± 0.031	0.033 ± 0.058
$\boldsymbol{W_L(\alpha = 0)}$	0.1878 ± 0.0228	0.1856 ± 0.0223	0.1939 ± 0.024	
$\boldsymbol{T = 75K}$ **(Exp. II)**	$\boldsymbol{\beta_{pref} = 0.1}$	$\beta_{max} = 0.15$	$\beta_{min} = 0.06$	Averaged
$\boldsymbol{E_0}$	35.407 ± 0.008	35.4 ± 0.008	35.416 ± 0.01	
$\boldsymbol{W_L}$	0.18 ± 0.017	0.176 ± 0.016	0.1908 ± 0.0204	0.18 ± 0.018
$\boldsymbol{\alpha}$	0.0292 ± 0.023	0.0086 ± 0.0216	0.0704 ± 0.0273	0.0292 ± 0.0231
$\boldsymbol{W_L(\alpha = 0)}$	0.176 ± 0.017	0.1749 ± 0.0155	0.1826 ± 0.0211	
$\boldsymbol{T = 100K}$ **(Exp. I)**	$\boldsymbol{\beta_{pref} = 0.1}$	$\beta_{max} = 0.15$	$\beta_{min} = 0.06$	Averaged
$\boldsymbol{E_0}$	35.3254 ± 0.009	35.3114 ± 0.009	35.3384 ± 0.01	
$\boldsymbol{W_L}$	0.3957 ± 0.0226	0.3768 ± 0.0221	0.412 ± 0.024	0.396 ± 0.028
$\boldsymbol{\alpha}$	0.09 ± 0.026	0.046 ± 0.026	0.123 ± 0.0273	0.09 ± 0.046
$\boldsymbol{W_L(\alpha = 0)}$	0.3823 ± 0.0243	0.369 ± 0.022	0.3976 ± 0.0273	
$\boldsymbol{T = 125K}$ **(Exp. I)**	$\boldsymbol{\beta_{pref} = 0.1}$	$\beta_{max} = 0.15$	$\beta_{min} = 0.06$	Averaged
$\boldsymbol{E_0}$	35.3 ± 0.01	35.2766 ± 0.0102	35.3184 ± 0.0108	
$\boldsymbol{W_L}$	0.759 ± 0.03	0.7262 ± 0.0286	0.7821 ± 0.0315	0.759 ± 0.041
$\boldsymbol{\alpha}$	0.1268 ± 0.028	0.0947 ± 0.0269	0.1471 ± 0.029	0.127 ± 0.038
$\boldsymbol{W_L(\alpha = 0)}$	0.7451 ± 0.034	0.7156 ± 0.03	0.7673 ± 0.037	
$\boldsymbol{T = 150K}$ **(Exp. I)**	$\boldsymbol{\beta_{pref} = 0.1}$	$\beta_{max} = 0.15$	$\beta_{min} = 0.06$	Averaged
$\boldsymbol{E_0}$	35.287 ± 0.012	35.2574 ± 0.012	35.31 ± 0.012	
$\boldsymbol{W_L}$	1.227 ± 0.043	1.1844 ± 0.0394	1.2547 ± 0.0457	1.227 ± 0.056
$\boldsymbol{\alpha}$	0.2 ± 0.03	0.176 ± 0.029	0.2143 ± 0.0329	0.2 ± 0.037
$\boldsymbol{W_L(\alpha = 0)}$	1.207 ± 0.0558	1.165 ± 0.052	1.2346 ± 0.0595	
$\boldsymbol{T = 175K}$ **(Exp. II)**	$\boldsymbol{\beta_{pref} = 0.1}$	$\beta_{max} = 0.15$	$\beta_{min} = 0.06$	Averaged
$\boldsymbol{E_0}$	35.29 ± 0.02	35.2763 ± 0.020	35.316 ± 0.020	
$\boldsymbol{W_L}$	1.537 ± 0.0725	1.521 ± 0.072	1.5635 ± 0.0737	1.5371 ± 0.0725
$\boldsymbol{\alpha}$	0.2662 ± 0.0443	0.26 ± 0.044	0.276 ± 0.045	0.2662 ± 0.04
$\boldsymbol{W_L(\alpha = 0)}$	1.4853 ± 0.0867	1.4698 ± 0.0244	1.5109 ± 0.0888	
$\boldsymbol{T = 200K}$ **(Exp. I)**	$\boldsymbol{\beta_{pref} = 0.1}$	$\beta_{max} = 0.15$	$\beta_{min} = 0.06$	Averaged
$\boldsymbol{E_0}$	35.2766 ± 0.022	35.237 ± 0.022	35.3 ± 0.022	
$\boldsymbol{W_L}$	1.895 ± 0.076	1.845 ± 0.075	1.923 ± 0.077	1.897 ± 0.086
$\boldsymbol{\alpha}$	0.2433 ± 0.04	0.23 ± 0.04	0.25 ± 0.04	0.243 ± 0.041
$\boldsymbol{W_L(\alpha = 0)}$	1.839 ± 0.0823	1.7838 ± 0.0799	1.8576 ± 0.0837	

Table 7.2 The extracted parameters from the fit analysis of the background-subtracted constant wave-vector scan at (6,0,1) using F(E) function.

Extracted fitted parameters at (8,0,0) (Experiments III)				
$\boldsymbol{T = 75K}$ **(Exp. I)**	$\boldsymbol{\beta_{pref} = 0.07}$	$\beta_{max} = 0.08$	$\beta_{min} = 0.05$	Averaged
$\boldsymbol{E_0}$	35.3366 ± 0.0112	35.3348 ± 0.0112	35.34 ± 0.011	
$\boldsymbol{W_L}$	0.1745 ± 0.0235	0.172 ± 0.0237	0.179 ± 0.023	0.1745 ± 0.02378
$\boldsymbol{\alpha}$	0.0336 ± 0.0297	0.023 ± 0.03	0.0542 ± 0.0293	0.0336 ± 0.034
$\boldsymbol{W_L(\alpha = 0)}$	0.172 ± 0.0233	0.17 ± 0.0234	0.1756 ± 0.0234	
$\boldsymbol{T = 100K}$ **(Exp. I)**	$\boldsymbol{\beta_{pref} = 0.07}$	$\beta_{max} = 0.08$	$\beta_{min} = 0.05$	Averaged
$\boldsymbol{E_0}$	35.282 ± 0.0124	35.2788 ± 0.0112	35.2882 ± 0.0112	
$\boldsymbol{W_L}$	0.444 ± 0.030	0.44 ± 0.03	0.453 ± 0.031	0.444 ± 0.03
$\boldsymbol{\alpha}$	0.1255 ± 0.0318	0.1176 ± 0.0318	0.14 ± 0.032	0.1255 ± 0.0338
$\boldsymbol{W_L(\alpha = 0)}$	0.4282 ± 0.0329	0.4241 ± 0.0325	0.4358 ± 0.0338	
$\boldsymbol{T = 125K}$ **(Exp. I)**	$\boldsymbol{\beta_{pref} = 0.07}$	$\beta_{max} = 0.08$	$\beta_{min} = 0.05$	Averaged
$\boldsymbol{E_0}$	35.253 ± 0.0136	35.2482 ± 0.0136	35.2628 ± 0.0136	
$\boldsymbol{W_L}$	0.8702 ± 0.0387	0.8642 ± 0.0387	0.8807 ± 0.0389	0.8702 ± 0.04
$\boldsymbol{\alpha}$	0.139 ± 0.0339	0.1338 ± 0.0339	0.1487 ± 0.0340	0.139 ± 0.0347
$\boldsymbol{W_L(\alpha = 0)}$	0.8482 ± 0.0412	0.8426 ± 0.0409	0.8580 ± 0.0418	
$\boldsymbol{T = 150K}$ **(Exp. I)**	$\boldsymbol{\beta_{pref} = 0.07}$	$\beta_{max} = 0.08$	$\beta_{min} = 0.05$	Averaged
$\boldsymbol{E_0}$	35.277 ± 0.013	35.2708 ± 0.012	35.2892 ± 0.0136	
$\boldsymbol{W_L}$	1.3445 ± 0.0446	1.338 ± 0.0446	1.3553 ± 0.0447	1.3445 ± 0.045
$\boldsymbol{\alpha}$	0.2877 ± 0.0316	0.284 ± 0.0317	0.2945 ± 0.0316	0.2877 ± 0.032
$\boldsymbol{W_L(\alpha = 0)}$	1.2797 ± 0.06	1.2734 ± 0.06	1.29 ± 0.06	
$\boldsymbol{T = 175K}$ **(Exp. II)**	$\boldsymbol{\beta_{pref} = 0.07}$	$\beta_{max} = 0.08$	$\beta_{min} = 0.05$	Averaged
$\boldsymbol{E_0}$	35.2416 ± 0.023	35.2344 ± 0.023	35.2554 ± 0.023	
$\boldsymbol{W_L}$	1.9165 ± 0.08	1.9099 ± 0.0789	1.9276 ± 0.08	1.9165 ± 0.08
$\boldsymbol{\alpha}$	0.3714 ± 0.042	0.3693 ± 0.042	0.3751 ± 0.042	0.3714 ± 0.042
$\boldsymbol{W_L(\alpha = 0)}$	1.7973 ± 0.1088	1.7907 ± 0.1083	1.8085 ± 0.11	
$\boldsymbol{T = 200K}$ **(Exp. I)**	$\boldsymbol{\beta_{pref} = 0.07}$	$\beta_{max} = 0.08$	$\beta_{min} = 0.05$	Averaged
$\boldsymbol{E_0}$	35.28 ± 0.023	35.2744 ± 0.03	35.2748 ± 0.03	
$\boldsymbol{W_L}$	2.4161 ± 0.08	2.4102 ± 0.08	2.4127 ± 0.08	2.4161 ± 0.08
$\boldsymbol{\alpha}$	0.3943 ± 0.042	0.393 ± 0.042	0.3941 ± 0.042	0.3943 ± 0.042
$\boldsymbol{W_L(\alpha = 0)}$	2.2697 ± 0.13	2.2642 ± 0.13	2.2665 ± 0.13	

Table 7.3 The extracted parameters from the fit analysis of the background-subtracted constant wave-vector scan at (8,0,0) using F(E) function.

7.3.2 Comparison with the results of the theoretical approaches

In order to complete the investigation of the asymmetric thermal lineshape broadening of the magnetic excitations in $BaCu_2V_2O_8$, the experimentally observed results were compared with the results of the two different complementary theoretical approaches. The first approach is based on the numerical density-matrix renormalization group (DMRG) techniques and has been done by Alexander Tiegel from the theory department of Georg-August-Universität in Göttingen under supervision of Dr. S.R. Manmana, Prof. Dr. A. Honecker and Prof. Dr. T. Pruschke [110]. The second approach is the analytical diagrammatic Brückner approach implemented in the method of Continuous Unitary Transformations (DBA-CUT) which have been done by Benedikt Fauseweh under supervision of Prof. Dr. G. S. Uhrig from Technische Universität Dortmund [110].
Both approaches were performed for the S=1/2 alternating AFM-FM chain model which is characterized by the Heisenberg Hamiltonian given by the Equation 7.1. Both approaches compute the dynamic structure factor (DSF) at the dispersion minima at finite temperatures taking into account the symmetric Gaussian resolution broadening of W_G=0.87 meV that makes possible to directly compare the theoretical results with the experimental data even though the asymmetry of the resolution function is not included.
The results of both approaches unambiguously reproduce the asymmetric thermal broadening of the lineshape of the magnetic excitations at the dispersion minimum in $BaCu_2V_2O_8$ confirming the experimentally observed results. Figure 7.6(a)-(l) presents the comparison of the experimental data with the results of the DBA-CUT computations of the dynamic structure factor at the dispersion minimum for the temperatures of T=75K, 100K, 125K, 150K, 175K and 200K convolved with the symmetric Gaussian resolution function with W_G=0.87meV. Because the DBA-CUT approach does not control the peak position at finite temperatures, the theoretically predicted peak positions are slightly offset with respect to the experimental data at elevated temperatures (dashed magenta lines in Fig. 7.6(a)-(l)). The computed dynamic structure factors are artificially shifted for comparison to the experimental lineshapes (solid magenta lines in Fig. 7.6(a)-(l)).
The line shapes of the DSF simulated using DBA-CUT approach clearly display asymmetric lineshape broadening to the direction of the higher energies and agree well with the experimental data for all simulated temperatures.
To determine the predicted values of the asymmetry parameter α and the Lorentzian width at finite temperatures by the DBA-CUT theory, the simulated DSF were fitted by the function F(E) where the resolution parameters were fixed to W_G=0.86 and β=0. The extracted values of α and W_L are listed in Table 7.4 and are plotted as a function of temperature in Fig. 7.6(m) and 7.6(n) demonstrating remarkable quantitative agreement with the experimentally observed values.
Figure 7.7(a)-(f)(solid blue line) shows the computed dynamic structure factor at the disper-

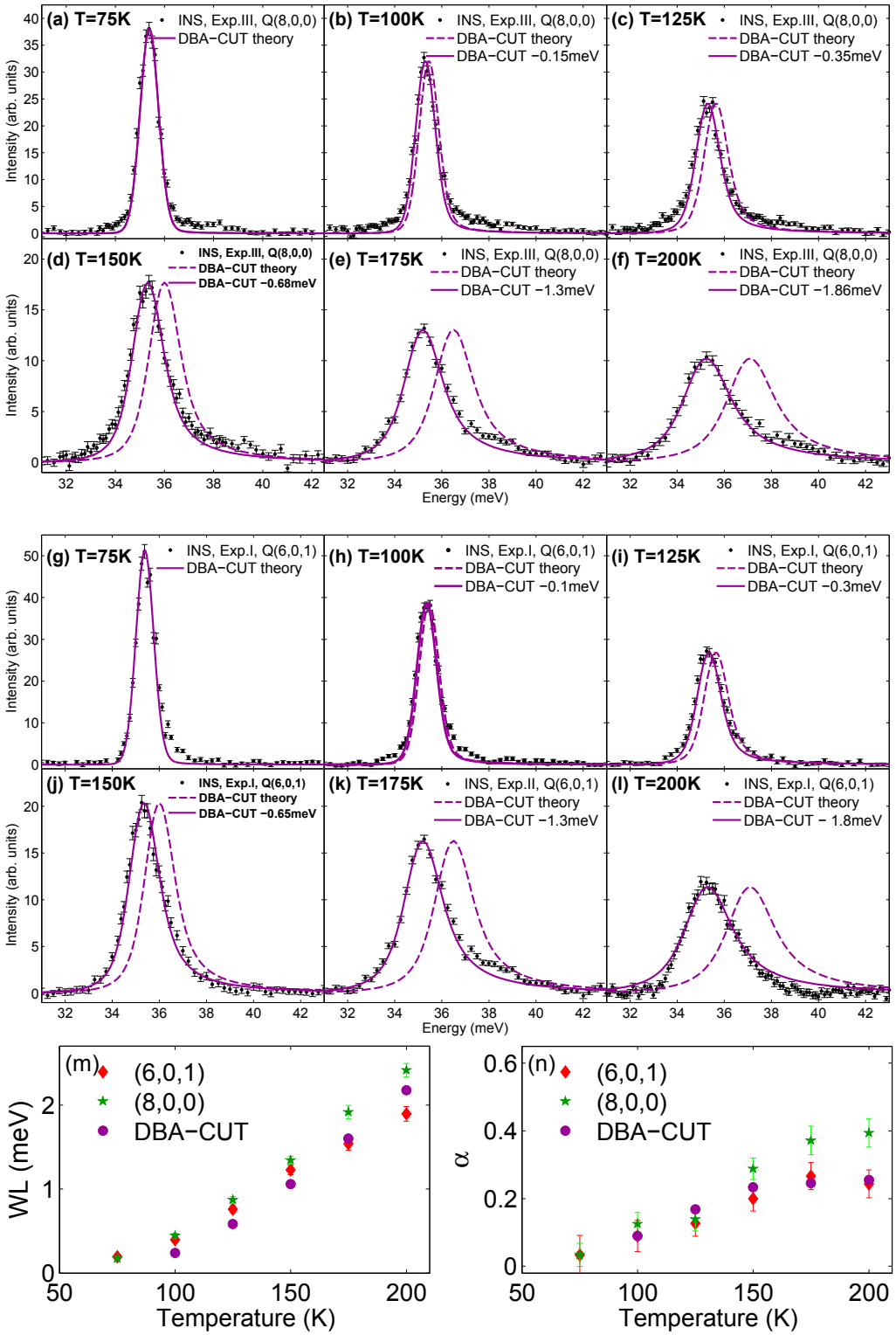

Figure 7.6: Results of the DBA-CUT computations of the dynamic structure factor at T=75K, 100K, 125K, 150K, 175K and 200K plotted over the (a)-(f) (8,0,0) and (g)-(l) (6,0,1) constant wave-vector scans at corresponding temperatures. The computations of DSF were performed by Benedikt Fausseweh. The temperature dependence of the (m) Lorentzian width W_L and (n) asymmetry parameter α exctracted from the fit analysis by the F(E) function of the computed DSF.

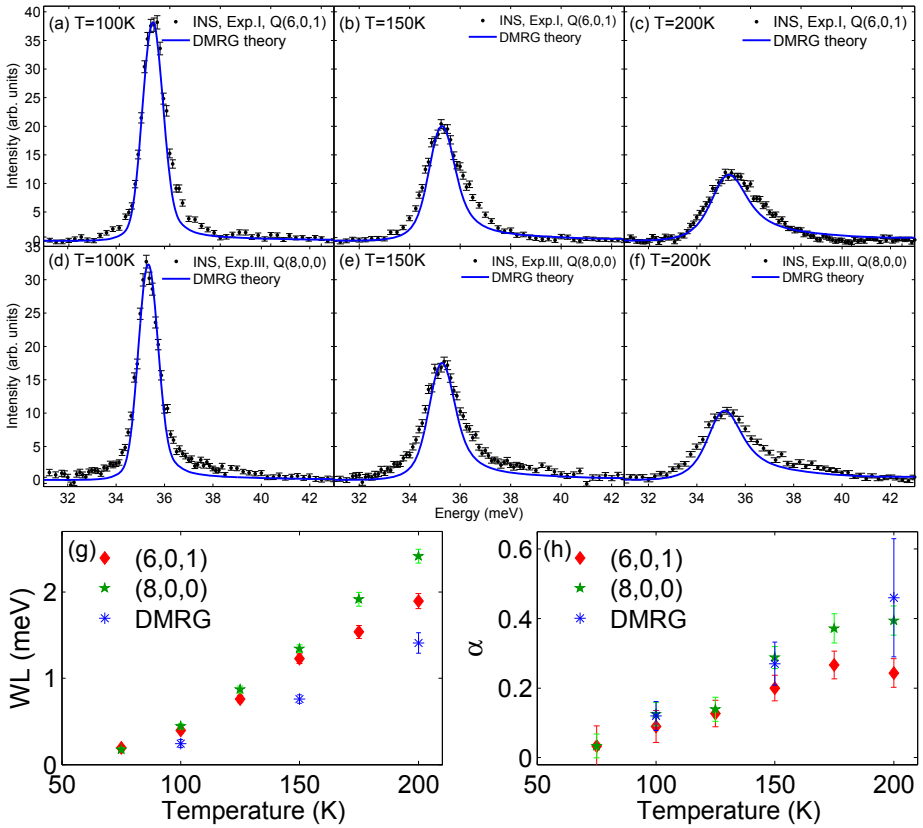

Figure 7.7: Results of the DMRG computations of the dynamic structure factor at T=100K, 150K and 200K plotted over the (a)-(c) (6,0,1) and (d)-(f) (8,0,0) constant wave-vector scans at corresponding temperatures. The DMRG computations of DSF performed by Alexander Tiegel. The temperature dependence of the (g) Lorentzian width W_L and (h) asymmetry parameter α exctracted from the fit analysis by the F(E) function of the computed DSF (solid blue line). The fit analysis of the simulated DSF was done together with A. Tiegel.

sion minima for the temperatures of T=100K, 150K and 200K using the DMRG approach. The simulated curves match the energy positions of the experimental peaks assuming that the intradimer coupling changes slightly as temperature increase which is discussed in the next subsection in detail. The lineshapes of the DSF simulated using DMRG approach clearly predict asymmetric thermal broadening weighted towards higher energies as observed for the experimental data.

To extract the values of the asymmetry parameter α and Lorentzian width W_L the simulated lineshapes were also fitted by the function F(E) at each temperature again using the resolution parameters fixed to W_G=0.86 and β=0. The extracted values of α and W_L are plotted as a function of temperature in Fig. 7.7. Although the absolute values of α and W_L from the DMRG simulations are not exactly the same as the experimental values, they increase with temperature indicating the same behaviour observed in the experiment.

Extracted experimental and theoretical fitted parameters					
Par.Temp.	$\mathbf{100}\boldsymbol{K}$	$\mathbf{125}\boldsymbol{K}$	$\mathbf{150}\boldsymbol{K}$	$\mathbf{175}\boldsymbol{K}$	$\mathbf{200}\boldsymbol{K}$
$\boldsymbol{\alpha}$(Q(6,0,1))	0.09±0.046	0.1268±0.038	0.2±0.037	0.2662±0.04	0.2433±0.041
$\boldsymbol{\alpha}$(Q(8,0,0))	0.1255±0.0338	0.139±0.0347	0.2877±0.032	0.3714±0.042	0.3943±0.042
$\boldsymbol{\alpha}$ (BDA-CUT)	0.09±0.001	0.1683±0.001	0.2333±0.0012	0.246±0.0015	0.255±0.0015
$\boldsymbol{\alpha}$ (DMRG)	0.12±0.0415		0.27±0.062		0.46±0.17
$\boldsymbol{W_L}$ (Q(6,0,1))	0.3957±0.0286	0.759±0.041	1.227±0.056	1.537±0.0757	1.895±0.086
$\boldsymbol{W_L}$ (Q(8,0,0))	0.44±0.03	0.87±0.04	1.3445±0.045	1.9165±0.08	2.416±0.08
$\boldsymbol{W_L}$ (BDA-CUT)	0.2386±0.001	0.585±0.001	1.06±0.0012	1.6±0.0015	2.178±0.0015
$\boldsymbol{W_L}$ (DMRG)	0.2436±0.0467		0.759±0.048		1.409±0.119

Table 7.4 The extracted averaged parameters from the fit analysis of the experimental data using F(E) function and the extracted fitted parameters from the analysis of the DMRG and DBA-CUT simulated dynamic structure factors.

7.3.3 Thermal band narrowing

To complement to the constant wave-vector scans at the dispersion minimum at (6,0,1) the constant wave-vector scans at the dispersion maximum (6,0,2) have been measured at several temperatures of T=BT, 100K, 150K and 200K in order to investigate the evolution of the bandwidth with temperature increase. The results are plotted together with the constant wave-vector scans at the dispersion minimum at (6,0,1) at the corresponding temperatures in Fig. 7.8(a), note that the peaks are much wider at (6,0,2) because they have been measured with the lower energy resolution.

In order to precisely determine a peak position at each temperature the data were fitted by the function F(E) where the parameters of the resolution function were fixed to the values which were extracted at base temperature at the two wavevectors (6,0,1) and (6,0,2). The results reveal that the low energy peaks are almost at the same energy position for all temperatures while the upper mode is shifting to lower energies with temperature increase. This result is opposite to the priviously observed thermal behaviour at the energy peak positions of the dispersion minimum and maximum in the dimerized quantum antiferromagnet strontium chromate where both peaks shifted significantly to the centre of the band. However, using the dimensionless energy scale units of E/E_{cb} where the E_{cb} is the centre of the band at each temperature both the dispersion maximum at (6,0,2) and the dispersion minimum at (6,0,1) now shift to the centre of the band width with temperature increase (Fig. 7.8(b)) which is consistent with the previously observed results. At the same time the centre of the band shifts toward lower energies with temperature increase which can be attributed to a slight

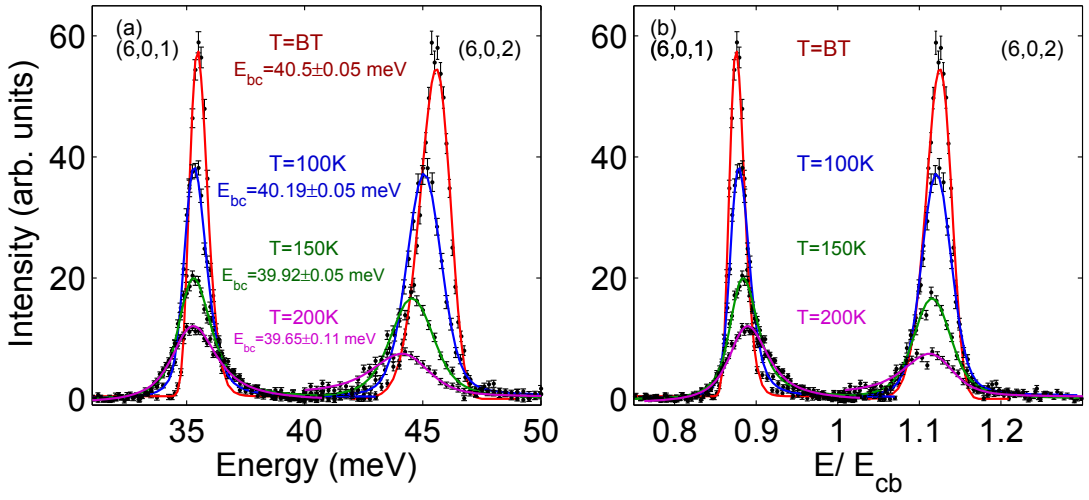

Figure 7.8: Constant energy scans at the (6,0,1) and (6,0,2) at the temperatures of T=BT, 100K, 150K and 200K with the energy scale in (a) meV and (b) units of E/E_{cb} where the solid lines correspond to the fit analysis using F(E) function.

weakening of the intradimer magnetic exchange constant.

7.3.4 Temperature dependence of the intrachain magnetic exchange coupling

In the previous subsection it was shown that the minimum and the maximum of the dispersion are shifting to the center of the band with temperature increase while the absolute value of the centre of the band is shifted toward lower energies at elevated temperatures. This thermal behaviour of the dispersion energy range can be attributed to the combination of i) the thermal effects and ii) the possible slight changes of the intrachain magnetic exchange constants due to the thermal lattice expansion.

In order to distinguish the contribution of each of these effects to the thermally induced energy shift of the peak positions at finite temperatures, the experimentally observed data were compared with the results of the DMRG computations at elevated temperatures which were performed by A. Teigel from Göttingen university [110]. The DMRG computations have been done for the S=1/2 Heisenberg Hamiltonian (eq. 7.1) at finite temperatures with fixed alternating ratio of J_2/J_1=-0.29 for all temperatures, so that the intradimer magnetic exchange interaction J_1 is only the scaling factor and was not involved in the computation routine. The DMRG simulations do not take into account the temperature dependence of the intrachain magnetic exchange coupling but they predict the energy shifts due to the thermal effects to high accuracy. Figure 7.9(a) shows the results of the DMRG computations which are plotted in the dimensionless units of the intradimer magnetic exchange coupling. Note that the computed dynamic structure factor (DSF) at (6,0,2) is much broader than the computed DSF at (6,0,1) because the resolution of the DMRG computations at the dispersion maximum is much lower.

Figure 7.9(b) shows the comparison of the experimental data with the results of the DMRG computations which are plotted in meV units assuming that the intradimer magnetic exchange coupling J_1 is temperature independent and equal to base temperature value of J_1=40.92 meV. This comparison reveals that the both simulated DSF at the dispersion minimum and at the dispersion maximum are shifted toward to higher energies with respect to the experimental data. Since both offsets are shifted in the same direction they cannot be associated with the thermal effects. Because the DMRG simulations take into account the thermal effects, the observed offsets of the predicted centre of the band can be attributed to the incorrect value of the scaling factor J_1 which was used for the scaling of the simulated data. Assuming that the positions of the centre of the band of the simulated DSF should match the experimentally observed values at each temperature, the predicted positions of the centre of the band in units of J_1 were compared to the experimentally observed values and the corresponding scaling factors J_1 were extracted for each temperature (Table 7.5). Figure 7.9(c) shows the comparison of the experimental data with the simulated dynamic structure factors which are scaled in meV units using the deduced values of J_1(T) (Table 7.5). Figure 7.9 shows that the simulations with the new scaling factor are in good agreement with the experimental data while the tiny shift of the simulated peaks with respect to the experimental peak position positions (by 0.15 meV) can be caused either by the resolution effects or by the slight changes of the alternating ratio.

The changes of the alternating ratio is estimated using folowing way. The DMRG computations reveal the value of the energy shift of the peak position due to the thermal effect in the dimesionless scale of the E/J_1 where J_1 is the dominant intradimer magnetic exchange interaction. Therefore, using the extracted values of J_1(T) at each particular temperature, the expected peak position, which would be at the base temperature assuming that this J_1 is temperature independent, is estimated by the subtruction of the predicted for this temperature energy shift from the experimentally observed peak position at finite temperature. Since the expected peak position at base temperature for particular J_1 is known, the alternating ratio α can be exctracted using the 5th order expansion (eq. 6.9) for each particular J_1(T). In Table 7.5 the estimated values of α(T) are summarized. These results imply that the intradimer magnetic exchange interaction J_1(T) and alternating ratio α(T) decrease slightly with temperature increase which can be associated with thermal expansion of the crystal lattice.

7.3.5 Discussion

The series of INS experiments on the single crystal of the alternating highly dimerized AFM-FM chain $BaCu_2V_2O_8$ at elevated temperatures reveal the presence of the strong correlations and show that the FM coupling has no specific effects on the asymmetric broadening. Indeed, as for the AFM-AFM alternating chain compound copper nitrate, the line shape of the

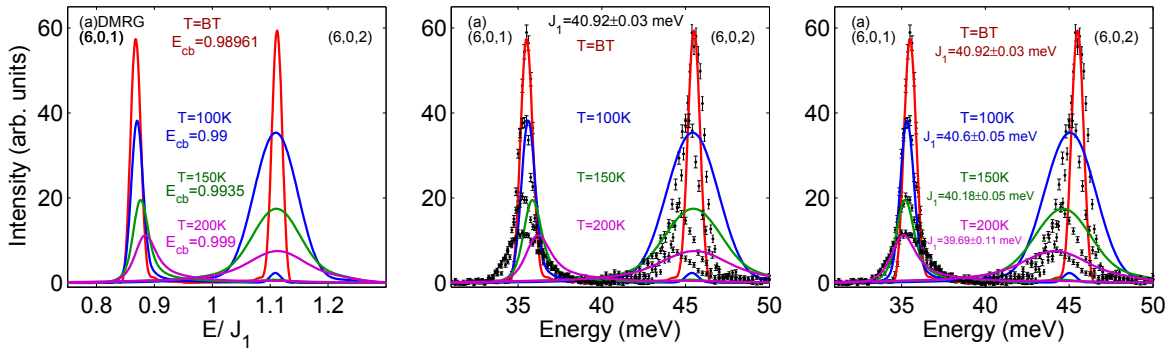

Figure 7.9: (a) DMRG simulations in the dimensionless scale of E/J_1, (b) the comparison of the background-subtracted constant wave-vector scans at (6,0,1) and (6,0,2) with the DMRG simulations scaled using J_1=40.92 meV for all temperatures, (c) the comparison of the background-subtracted constant wave-vector scans at (6,0,1) and (6,0,2) with the DMRG simulations scaled using the temperature dependent value of J_1 from the Table 7.5

magnetic excitations in $BaCu_2V_2O_8$ was found to broaden asymmetrically with increasing temperature rather than as a symmetric Lorentzian as observed for conventional magnets. Because the observed asymmetric thermal line shape broadening in $BaCu_2V_2O_8$ was parameterized by the new introduced fitting function F(E) direct quantitative comparison with the asymmetric behaviour recently explored in an AFM-AFM alternating chain copper nitrate and AFM 3D dimer compound strontium chromate is complicated, nevertheless the qualitative comparison can be done. $BaCu_2V_2O_8$ was explored over the temperature range of T=BT-200K which corresponds to the temperature range of T=0-0.48Δ in the units of the energy gap Δ. The temperature dependence of the asymmetry parameter α in $BaCu_2V_2O_8$ reveals that the asymmetry does not reach its maximum within the explored temperature range but continues to increase at the highest temperatures of T=175K (0.42Δ) and T=200K (0.48Δ). This is in an agreement with the asymmetric thermal behaviour which was observed in strontium chromate where the asymmetry parameter rapidly increases within the temperature range of 0-0.38Δ and then slowdowns within the range of 0.38Δ-0.5Δ achieving its maximum value at $\approx$ 0.55Δ-0.63Δ. In copper nitrate the maximum value of the asymmetry parameter was achieved at an even higher temperature of 1.2Δ. Therefore, one can expect that the observed strongly correlated behaviour in $BaCu_2V_2O_8$ will persist beyond the explored temperature range and the symmetric thermal lineshape broadening will keep on increasing at least up to the room temperature ($\approx$0.726Δ).

The observed band narrowing in $BaCu_2V_2O_8$ apparently contradicts to the conventional picture according to which the minimum and the maximum of the band should shift toward to the centre of the band with temperature increase as can clearly be observed for strontium chromate. In $BaCu_2V_2O_8$ the dispersion minimum is almost temperature independent in the absolute energy scale with temperature increase while the maximum of the dispersion shifts toward lower energies at elevated temperatures. However, the comparison with the theoretical

Temperature dependence of values of the centre of the band				
Temperature	CB experiment	CB DMRG	$J_1(T)$	α(T)
3.5	40.495 ± 0.03	0.98961	40.92±0.03	-0.2925Å±0.002
100	40.19 ± 0.05	0.99	40.6 ± 0.05	-0.29Å±0.002
150	39.92 ± 0.05	0.9935	40.18 ± 0.05	-0.283Å±0.004
200	39.65 ± 0.1	0.999	39.69 ± 0.1	-0.2761Å±0.004

Table 7.5 Temperature-dependent values of the J_1(T) and α(T) determined from the comparison of the centre of the band (CB) extracted from the experimental data in units of meV with the centre of the band predicted by DMRG simulations in dimensionless units. The α(T) is determined from the analysis of the energy shift due to the thermal effects predicted by the DMRG simulations and exctracted values of the J_1(T) (see details in the text).

predictions of the numerical DMRG computations reveals that this behaviour can be caused by the competition of the thermal effects with the effects of a slight reduction in the magnetic exchange coupling due to the thermal expansion of the crystal lattice . Indeed, because $BaCu_2V_2O_8$ was measured over the large temperature range, the crystal lattice expands at finite temperatures with respect to base temperature which results to the decreasing of the magnetic exchange interactions. Particularly, the decrease of J_1 with temperature increase results in the energy shift of the centre of the band to low energy and, as consequence, leads to the energy shift of both dispersion minimum at (6,0,1) and the dispersion maximum at (6,0,2) to lower energy. At the same time the thermal effects shift the dispersion minimum (6,0,1) in the opposite direction to higher energies which compensate the lower energy shift due to the decreasing value of J_1, thus, in experimental data the peak at (601) seems to be independent of temperature. In the case of the dispersion maximum at (6,0,2) both effects shift the peak to lower energies resulting to the huge experimentally observed energy shift of the dispersion maximum with temperature increase.

7.4 Conclusions

In this Chapter the thermal behaviour of the magnetic excitations in $BaCu_2V_2O_8$ was explored by the single crystal INS technique. The results reveal the asymmetric thermal line shape broadening of the magnetic excitations at elevated temperatures which is associated with the presence of strongly correlated behaviour in $BaCu_2V_2O_8$ at finite temperatures. The observed asymmetry was parameterized by a new fitting function F(E) which allows the asymmetry and underlying strongly correlated behaviour in $BaCu_2V_2O_8$ to be quantitatively described. In addition, the experimentally observed results were compared with the predictions of the analytical and numerical approaches and demonstrate a good quantitative agreement with both of them confirming the presence of the strong correlation phenomena at finite temperatures. The experimentally observed unconventional thermal band narrowing

was analysed and assigned to the combination of the thermal effects with the changes of the magnetic exchange coupling due to the thermal lattice expansion which was confirmed by the comparison with the results of the theoretical computations.

8 Conclusions and perspectives

In this thesis the magnetic properties of two novel compounds $BaNi_2V_2O_8$ and $BaCu_2V_2O_8$ were explored at both base and finite temperatures using a wide variety of experimental techniques and theoretical approaches. Both compounds are rare examples of model magnetic systems and are promising candidates to display intriguing magnetic phenomena at finite temperatures such as the Berezinskii - Kosterlitz - Thouless topological vortex phase and strongly correlated behaviour at elevated temperatures, respectively. Both compounds were grown at the in-house Crystal Laboratory at HZB. Investigation of both compounds started with the detailed characterization of their magnetic properties at base temperature to solve their Hamiltonians for the first time. Their behaviours at finite temperatures were then explored over wide temperature ranges. The presented research is based on the results of experiments which were performed at the in-house laboratories and also at external neutron scattering facilities. In particular, thermodynamic measurements of both compounds were performed in the Laboratory for Magnetic Measurement in HZB while the inelastic neutron scattering data were collected on different instruments located at FRM2 (Munich), PSI (Switzerland), Rutherford Appleton Laboratory (UK) and ILL (Grenoble). Triple-axis spectroscopy was the main neutron experimental technique due to its precise, high resolution access to the (Q,ω) space.

The first compound, $BaNi_2V_2O_8$, is a honeycomb S=1 antiferromagnet which is found to be a good physical realization of the 2D XXZ Heisenberg model. In this compound the S=1 Ni^{2+} magnetic ions develop long-range magnetic order below the ordering temperature T_N=47.75K$\pm$0.5K and the ordered state is characterized by the propagation vector (1,0,1/2). The single crystal DC susceptibility measurements performed for a magnetic field of 1T applied parallel and perpendicular to the c-axis reveal no obvious signature of the transition to long-range magnetic order although they do display strong planar anisotropy below T=80K. Below the temperature of T=52K the anisotropy becomes more pronounced and the susceptibility data display the behaviour of the 2D XXZ Heisenberg model as predicted by Quantum Monte Carlo Simulations [40].

The single crystal inelastic neutron scattering measurements of $BaNi_2V_2O_8$ reveal the spin-wave magnetic excitation spectrum which consists of two gapped modes with energy gaps of E_1=0.41meV$\pm$0.03meV and E_2=3.25meV$\pm$0.03meV, respectively. Both modes disperse up 25meV within the honeycomb plane but are completely dispersionless along the c-axis confirming the two-dimensional magnetic behaviour of this compound. The analysis of the directional

dependence of the relative intensities of these modes shows that the higher energy gape is due to the XY anisotropy D_{XY}=0.0695meV±0.0015meV of the spin fluctuations while the lower energy gap is caused by the presence of the weak easy-axis in-plane anisotropy $D_{inplane}$=-0.0009meV±0.00015meV . The values of these anisotropies were extracted from the fit analysis of the magnetic excitation spectrum of $BaNi_2V_2O_8$ at base temperature within a linear spin-wave theory approach which also allowed the Hamiltonian of $BaNi_2V_2O_8$ to be solved. The extracted Hamiltonian reveals that the dominant term in the Hamiltonian is the first-neighbor magnetic exchange interaction within the honeycomb plane which is antiferromagnetic and varies within the range 10.9meV⩽J_n⩽13.35meV. The second-neighbour magnetic exchange interaction J_{nn} is much weaker and lies within the range 0.85meV⩽J_{nn}⩽1.65meV however it is required to reproduce the modulation on top of the dispersion observed in the experimental magnetic excitation spectrum. The third-neighbour magnetic interaction J_{nnn} is not obligatory, but if it is present in the Hamiltonian it can be either antiferromagnetic or ferromagnetic and lies within the range -0.1meV⩽J_{nnn}⩽0.4meV. Although the magnetic system displays long-range magnetic order the fit analysis reveals that the interplane magnetic exchange coupling is 10^{-5}-10^{-4} times weaker than the dominant magnetic exchange interaction J_n and that the transition to the ordered state is most likely driven by the combination of the interplane coupling and easy-axis in-plane anisotropy.

The critical phenomena of $BaNi_2V_2O_8$ were explored by performing neutron diffraction at finite temperatures, both below and above the ordering temperature T_N. The results reveal that $BaNi_2V_2O_8$ behaves as a two-dimensional antiferromagnet over the whole explored temperature range but undergoes several crossovers first from 2D Ising like to 2D XY and then to 2D Heisenberg magnetic behaviour with increasing temperature. These crossovers are associated with the complexity of the Hamiltonian of $BaNi_2V_2O_8$ where only the dominant isotropic first-neighbour term J_n plays a role at high temperatures but when temperature decreases the weaker terms such as the D_{XY} and $D_{inplane}$ anisotropies start to effect the magnetic behaviour. In particular, the analysis of the temperature dependence of the spontaneous magnetization below T_N displays a crossover of the critical exponent from the value of β=0.21 (46.3K⩽T⩽47.7K), which is close to the predicted value for the 2D XY model, to β=0.172 (T⩽46K) which is similar to 2D Ising like criticality and indicates the influence of the easy-axis anisotropy. The analysis of the thermal decay of the correlation length above the ordering temperature T_N shows that at temperatures above T=52K $BaNi_2V_2O_8$ behaves as a 2D Heisenberg antiferromagnet. The thermal decay of the correlation length just above the ordering temperature T_N but below T=52K is found to be described well only by the Berezinskii - Kosterlitz - Thouless theory suggesting the presence of free vorticies. In an ideal 2D XY magnet these vorticies would pair below the Kosterlitz - Thouless transition temperature whose value is predicted to be T_{BKT}=45.56K±0.18K in $BaNi_2V_2O_8$. The transition to long-range antiferromagnetic order which occurs at higher temperature of T_N=47.75K due to the interplane coupling and easy axis anisotropy however destroys the vorticies and prevents

the Berezinskii - Kosterlitz - Thouless transition.
These result suggest that $BaNi_2V_2O_8$ is a promising candidate to detect the Berezinskii - Kosterlitz - Thouless behaviour within the temperature range of $T_N<T<52K$ where $BaNi_2V_2O_8$ behaves as a purely 2D XXZ Heisenberg magnetic system without conventional long-range magnetic order and where the free vortex excitations are present. In the future, direct observation of the free vortex excitations will be attempted using the small angle neutron scattering technique (SANS). Although this technique was not used for the investigation of the BKT phase transition so far, it was successfully applied to detect a vortex solid-liquid transition in type-II superconductor [129]. An analogy of the flux of the unbounded BKT vortex excitations to the vortex-liquid phase in type-II superconductor makes SANS a promising technique to explore a dynamic of the free vorticies in $BaNi_2V_2O_8$. The signature of the free vortex excitations can be also detected in AC susceptibility data but for the data analysis the comparison with theoretical simulations of the AC susceptibility data is required [130]. Finally, the spin-vortices in $BaNi_2V_2O_8$ can be investigated and visualized using magnetic exchange force microscopy (MExFM) technique which allows the spin-arrangement in the antiferromagnetic isolators to be resolved in the atomic scale [131]. Recently, MExFM technique was successfully tested to resolve simultaneously the nickel ions and thier spins in nickel oxide [132] which makes MExFM a promising technique to visualize vortex-excitations in $BaNi_2V_2O_8$.
The second compound explored in this work is $BaCu_2V_2O_8$ which is found to be a physical realisation of the $S=\frac{1}{2}$ dimerized alternating Heisenberg chain model. This compound has a tetragonal crystal structure where $S=\frac{1}{2}$ magnetic Cu^{2+} ions are arranged into double-copper oxygen plaquettes which rotate by 90° with respect to each other forming screw chains along the c-axis. There are four screw chains per unit cell two of which are characterized by clockwise rotation and two by anticlockwise rotation. The single crystal DC susceptibility measurements of $BaCu_2V_2O_8$ reveal a non-magnetic ground state and the data were fitted well by the dimer-model. The extracted values of the intra- and interdimer magnetic exchange constants respectively equal J_{intra}=39.80meV±0.13meV and J_{inter}=-9.87meV±2.64meV implying that the antiferromagnetic dimers are weakly coupled by a ferromagnetic inter-dimer exchange interaction.
The single crystal inelastic neutron scattering data reveal that the magnetic excitation spectrum consists of two gapped excitation branches which both disperse between 35.37meV±0.05meV and 45.56meV±0.05meV along the L-direction but are completely dispersionless within the tetragonal plane implying that the dimers are coupled one-dimensionally along the c-axis. Both modes are characterized by the same periodicity, size of energy gap and bandwidth, but are shifted with respect to each other by half a period along L. The presence of these two modes was attributed to the doubling of the magnetic Brillouin zone along the $c^\star$-axis due to the presence of two dimers per unit cell which leads to the observation of the second shadow mode in the magnetic excitation spectrum.
The observed dispersion was analysed using the one-magnon dispersion relation of an alter-

nating chain calculated up to 5^{th} order which allows the dimer periodicity and intrachain magnetic exchange interactions to be extracted. Each mode was analysed independently because there was unclear which particular branch corresponds to the one-magnon excitation mode and which one is the shadow mode. The fit analysis of the two modes reveals that there are two possible solutions for the Hamiltonian of the alternating chain model which both are agree equally well with the experimental data. The first solution (AFM-AFM) suggests that both intra- and interdimer magnetic exchange interactions are antiferromagnetic and respectively equal J_{intra}=40.75meV$\pm$0.05meV and $J_{inter}=\alpha J_{intra}$ where α=0.225 is the alternation ratio. The second solution (AFM-FM) also implies that the dominant intradimer exchange interaction is antiferromagnetic and equals J_{intra}=40.92meV but in contrast suggests that the weaker interdimer exchange interaction is ferromagnetic and equals $J_{inter}=\alpha J_{intra}$ where α=-0.2925. The extracted value of the dimer periodicity equals half of the unit cell for both excitation branches which exactly corresponds to the proposed screw chain model.
Both solutions for the J_{intra} and J_{inter} exchange interactions were used in theoretical simulations of the magnetic excitation spectrum of $BaCu_2V_2O_8$ at base temperature. The comparison of the theoretical computations with the experimental data reveals that only the AFM-FM solution gives the correct intensity distribution of the magnetic excitation spectrum of $BaCu_2V_2O_8$. The magnetic exchange paths which are responsible for the J_{intra} and J_{inter} magnetic exchange coupling were distinguished by analysing the intensity distribution of the magnetic excitation spectrum using the first moment sum rule relation. The results reveal that the dominant AFM J_{intra} interaction is realized via a Cu-O-V-O-Cu super-super-exchange path while the weak FM J_{inter} interaction is within the copper-oxygen plaquettes and is in full agreement with the Goodenough-Kanamori-Anderson rules for super-exchange coupling.
The presence of strongly correlated behaviour that persist at moderately high temperatures in $BaCu_2V_2O_8$ was revealed by analysing the line shape of the magnetic excitations at several finite temperatures up to the highest temperature of T $\approx 0.5\Delta$ where Δ=35.37meV$\pm$0.05meV is the observed energy gap of the dispersion in $BaCu_2V_2O_8$. The analysis was performed using a newly developed fitting function which is based on the asymmetric Lorentzian function but also takes into account the contribution of the instrumental resolution function. The extracted temperature dependence of the asymmetry parameter in this fitting function reveals that the line shape of the magnetic excitations in $BaCu_2V_2O_8$ start to broaden asymmetrically with increasing temperature in contrast to the conventional symmetric Lorentzian broadening usually observed. This was attributed to the strongly correlated behaviour of the magnetic excitations at moderately high temperatures.
The experimental data were compared with the results of two different theoretical approaches which compute the dynamic structure factor of $BaCu_2V_2O_8$ at finite temperatures using the alternating ratio α=-0.29 extracted from the analysis of the magnetic excitation spectrum of $BaCu_2V_2O_8$ at base temperature. The line shapes of the dynamic structure factor simulated

using the analytical DBA-CUT approach completely reproduce the line shapes of the experimental data. The temperature dependences of the asymmetry parameters extracted from the fit analysis of the simulated and experimental data are in perfect agreement with each other confirming the presence of strongly correlated behaviour in $BaCu_2V_2O_8$. The dynamic structure factor of $BaCu_2V_2O_8$ at finite temperatures simulated using the numerical DMRG theoretical technique reproduce only qualitatively the tendency of the asymmetric line shape broadening with temperature increase. However these DMRG computations precisely reproduce the peak positions of the dispersion minimum and maximum and can account for their energy shift due to thermal effects. The comparison of the predicted peak positions of the dispersion minimum and maximum by DMRG computations with the corresponding positions which were experimentally observed reveal the thermal band narrowing due to a small decrease of the dominant J_{intra} exchange interaction with temperature increase.
This research proves using both experimental and theoretical techniques that the magnetic properties of $BaCu_2V_2O_8$ are described well by the S=$\frac{1}{2}$ 1D alternating chain model where the antiferromagnetic dimers are ferromagneticly coupled into the screw chain. The strong interactions between the excitations due to the hardcore constraint in combination with the limited bandwidth of the dispersion allow the retention of coherence with increasing temperature which is observed experimentally as an asymmetric energy broadening of their lineshapes. Apart from the extraordinary coherence of the magnetic excitations at finite temperatures, $BaCu_2V_2O_8$ is promising candidate for the observation of the thermal intraband scattering which is caused by the rearrangement of the thermally induced magnetic excitations within the band and is expected to appear over the energy range of 0meV-10meV at finite temperatures. Because the intraband scattering has weak intensity which is comparable with the phonon background experimental measurements of this thermal effect require longer counting times with respect to the investigation of the strongly correlated behaviour presented here.

Bibliography

[1] K. H. J. Buschow and F. R. de Boer, *Physics of Magnetism and Magnetic Materials* (Springer, United States of America, 2003).

[2] A. Messiah, *Quantum Mechanics* (North Holland, Netherlands, 1975).

[3] C. Timm, "Theory of Magnetism," `https://www.physik.tu-dresden.de/~timm/personal/teaching/thmag_w09/lecturenotes.pdf` (2015).

[4] W. A. Harrison, *Elementary Electronic Structure* (World Scientific Publishing Company, Singapore, 2004).

[5] K. Yosida, *Theory of Magnetism* (Springer, Germany, 2001).

[6] M. Roy, "The N-electron wavefunction," `http://www2.le.ac.uk/departments/physics/people/mervynroy/lectures/pa4311/quantum-chemistry-summary.pdf` (2015).

[7] S. Blundell, *Physics of Magnetism and Magnetic Materials* (Oxford University Press, Great Britain, 2001).

[8] J. Keeling, "Quantum Magnetism," `https://www.st-andrews.ac.uk/~jmjk/keeling/teaching/magnetism-notes.pdf`.

[9] J. Kanamori, J. Phys. Chem. Solids **10**, 87 (1959).

[10] J. B. Goodenough, Phys. Rev. **117**, 1442 (1960).

[11] L. Onsager, Phys. Rev. **65**, 117 (1944).

[12] N. D. Mermin and H. Wagner, Phys. Rev. Lett. **17**, 1133.

[13] B. Simons, "Phase Transitions and Collective Phenomena: Topological Phase Transitions," `http://www.tcm.phy.cam.ac.uk/~bds10/phase.html` (1997).

[14] J. M. Kosterlitz and D. J. Thouless, J. Phys. C: Solid Statte Phys. **6**, 1181.

[15] J. M. Kosterlitz, J. Phys. C: Solid Statte Phys. **7**, 1046.

[16] V. L. Berezinskii, Soviet Physics Jetp **32**, 493 (1971).

[17] V. L. Berezinskii, Soviet Physics Jetp **34**, 610 (1972).

[18] C. Kittel, *Introduction to Solid State Physics* (John Wiley Sons, United States of America, 2004).

[19] D. L. Q. Castro, PhD Thesis, Technical University Berlin (2011).

[20] R. Kleiner, D. Koelle, F. Ludwig, and J. Clarke, Proc. IEEE **92**, 1534 (2004).

[21] G. Shirane, S. M. Shapiro, and J. M. Tranquada, *Neutron Scattering with a Triple-Axis Spectrometer: Basic Techniques* (Cambridge University Press, United Kingdom, 2006).

[22] G. L. Squires, *Thermal Neutron Scattering* (Dover Publications, New York, 1996).

[23] S. W. Lovesey, *The Theory of Neutron Scattering from Condensed Matter* (Clarendon Press, United Kingdom, 1986).

[24] O. Sobolev and J. T. Park, Journal of large-scale research facilities **5**, A13 (2015).

[25] J. G. Bednorz and K. A. Müller, Z. Physik B - Condensed Matter **64**, 189 (1986).

[26] D. G. Hinks, L. Soderholm, D. W. Capone, J. D. Jorgensen, I. Schuller, C. U. Serge, K. Zhang, and J. D. Grace, Appl. Phys. Lett. **50**, 1688 (1987).

[27] T. Hanaguri, C. Lupien, Y. Kohsaka, D.-H. Lee, M. Azuma, M. Takano, H. Takagi, and J. C. Davis, Nature **430**, 1001 (2004).

[28] K. Binder and A. P. Young, Rev. Mod. Phys. **58**, 801 (1986).

[29] P. W. Anderson, Mat. Res. Bull. **8**, 153 (1973).

[30] B. Keimer, N. Belk, R. J. Birgeneau, A. Cassanho, C. Y. Chen, M. Greven, M. A. Kastner, A. Aharony, Y. Endoh, R. W. Erwin, and G. Shirane, Phys. Rev. B. **46**, 14034 (1992).

[31] V. Y. Pomjakushin, A. A. Zakharov, A. Amato, V. N. Duginov, F. N. Gygax, D. Herlach, A. N. Ponomarev, and A. Schenck, Physica C **272**, 250 (1996).

[32] S. M. Hayden, *Neutron Scattering in Layered Copper-Oxide Superconductors*, edited by A. Furrer (Springer, Netherlands, 1998).

[33] T.-H. Han, J. S. Helton, S. Chu, D. G. Nocera, J. A. Rodrigueza-Rivera, C. Broholm, and Y. S. Lee, Nature **492**, 406.

[34] C. Balz, B. Lake, A. T. M. Nazmul Islam, Y. Singh, J. A. Rodriguez-Rivera, T. Guidi, E. M. Wheeler, G. G. Simeoni, and H. Ryll, Phys. Rev. B **95**, 174414 (2017).

[35] A. Banerjee, C. A. Bridges, J.-Q. Yan, A. A. Aczel, L. Li, M. B. Stone, G. E. Granroth, M. D. Lumsden, Y. Yiu, J. Knolle, S. Bhattacharjee, D. L. Kovrizhin, R. Moessner, D. A. Tennant, D. G. Mandrus, and S. E. Nagler, Nature (2016).

[36] D. L. Quintero-Castro, B. Lake, A. T. M. N. Islam, E. M. Wheeler, C. Balz, M. Månsson, K. C. Rule, S. Gvasaliya, and A. Zheludev, Phys. Rev. Lett. **109**, 127206 (2012).

[37] Y. Xu and C. Zhang, Phys. Rev. Lett **114**, 110401 (2015).

[38] R. Scheider, A. G. Zaitsev, D. Fuchs, and H. Löhneysen, J. Phys. Cond. Matt. **26**, 455701 (2014).

[39] U. Tutsch, B. Wolf, S. Wessel, L. Postulka, Y. Tsui, H. Jeschke, I. Opahle, T. Saha-Dasgupta, R. Valenti, A. Brühl, K. Removic-Langer, T. Kretz, H.-W. Lerner, M. Wagner, and M. Lang, Nature Comm. **5**, 6169 (2014).

[40] A. Cuccoli, T. Roscilde, V. Tognetti, R. Vaia, and P. Verrucchi, Phys. Rev. B **67**, 104414.

[41] Z. He, T. Taniyama, and M. Itoh, J. Magn. Magn. Mater. **306**, 277 (2006).

[42] K. Ghoshray, B. Pahari, B. Bandyopadhyay, R. Sarkar, and A. Ghoshray, Phys. Rev. B **71**, 214401 (2005).

[43] C. S. Lue and B. X. Xie, Phys. Rev. B **72**, 052409 (2005).

[44] A. Islam, E. S. Klyushina, and B. Lake, in preparation .

[45] T. Barnes, J. Riera, and D. A. Tennant, Phys. Rev. B **59**, 11384 (1999).

[46] L. P. Regnault and J. Rossat-Mignod, *Magnetic Properties of Layered Transition Metal Compounds*, edited by L. J. d. Jongh (Kluwer Academic Publishers, Netherlands, 1990).

[47] N. Rogado, Q. Huang, J. W. Lyun, A. P. Ramirez, D. Huse, and R. J. Cava, Phys. Rev. B **65**, 144443 (2002).

[48] G. Rushbrook and P. Wood, International Journal at the Interface Between Chemistry and Physics **1**, 257 (1958).

[49] M. Heinrich, H.-A. Krug von Nidda, A. Loidl, N. Rogado, and R. J. Cava, Phys. Rev. Lett **91**, 137601 (2003).

[50] A. Chernyshev, M. E. Zhitomirsky, N. Martin, and L.-P. Regnault, Phys. Rev. Lett. **109**, 097201 (2012).

[51] G. Shirane, S. Shapiro, and J. Tranquada, *Neutron Scattering with a triple-axis spectrometer* (Cambredge University Press, United Kingdom, 2002).

[52] S. Toth and B. Lake, Journal of Physics: Condensed Matter **27**, 166002 (2015).

[53] W. Knafo, C. Meingast, K. Grube, S. Drobnik, P. Popovich, P. Schweiss, P. Adelmann, T. Wolf, and H. v. Lohneysen, Phys. Rev. Lett. **99**, 137206 (2007).

[54] L. P. Regnault, J. P. Boucher, J. Rossat-Mignod, J. Bouillot, R. Pynn, J. Y. Henry, and J. P. Renard, Physica B+C **136**, 329 (1986).

[55] H. E. Stanley and T. A. Kaplan, Phys. Rev. Lett. **17**, 913 (1966).

[56] J. M. Nabarro, *Theory of crystal dislocations* (Oxford University Press, Great Britain, 1967).

[57] A. Jelic and L. F. Cugliandolo, J. Stat. Mech. Theor. Exp. **2**, P02032.

[58] D. J. Bishop and J. D. Reppy, Phys. Rev. Lett. **40**, 104414.

[59] D. J. Resnik, J. C. Garland, S. Boyd, J. T. Shoemaker, and R. Newrock, Phys. Rev. Lett. **47**, 1542 (1981).

[60] W. Zhao, Q. Wang, M. Liu, W. Zhang, Y. Wang, M. Chen, Y. Guo, K. He, X. Chen, Y. Wang, J. Wang, X. Xie, Q. Niu, L. Wang, X. Ma, J. K. Jain, M. H. W. Chan, and Q.-K. Xue, Solid State Communications **165**, 59 (2013).

[61] A. I. Safonov, S. A. Vasilyev, I. S. Yasnikov, I. I. Lukashevich, and S. Kaakkola, Phys. Rev. Lett. **81**, 4545 (1998).

[62] Z. Hadzibabic, P. Krüger, M. Cheneau, B. Battelier, and J. Dalibard, Nature **441**, 1118 (2006).

[63] D. Waibel, G. Fisher, T. Wolf, H. Löhneysen, and B. Pilawa, Phys. Rev. B **91**, 214412 (2015).

[64] M. M. Hall, V. G. Veeraraghavan, and H. Rubin, J. Appl. Cryst. **10**, 66 (1977).

[65] S. T. Bramwell and P. C. W. Holdsworth, J. Phys.: Condens. Mat. **5**, L53 (1993).

[66] K. Hirakawa and H. Ikeda, J. Phys. Soc. Jpn. **35**, 1328 (1973).

[67] K. Koyama, N. Terata, and M. M., J. Phys. Soc. Jpn. **54**, 2708 (1985).

[68] K. M. Diederix, J. P. Groen, L. S. J. M. Henkens, T. O. Klaassen, and N. J. Poulis, Physica B **93**, 99 (1978).

[69] J. Skalyo, G. Shirane, and S. A. Friedberg, Phys. Rev. **188**, 1037 (1969).

[70] K. Koyama, H. Nobumasa, and M. Matsuura, J. Phys. Soc. Jpn. **56**, 1553 (1987).

[71] A. Wildes, H. M. Rønnow, B. Roessli, M. J. Harris, and K. W. Godfrey, J. Magn. Magn. Mater. **310**, 1221 (2007).

[72] H. M. Rønnow, A. R. Wildes, and S. T. Bramwell, Physica B **676**, 276 (2000).

[73] A. R. Wildes, H. M. Rønnow, B. Roessli, M. J. Harris, and K. W. Godfrey, Phys. Rev. B. **74**, 0994422 (2006).

[74] L. P. Regnault, J. Rossat-Mignod, and J. Y. Henry, J. Phys. Soc. Jpn. (Suppl) **52**, 1 (1983).

[75] B. Simons, "Phase Transitions and Collective Phenomena: Scaling Theory," `http://www.tcm.phy.cam.ac.uk/~bds10/phase.html` (1997).

[76] S. Chakravarty, B. I. Halperin, and D. R. Nelson, Phys. Rev. B **39**, 2344 (1989).

[77] J. Igarashi, Phys. Rev. B **46**, 10763 (1992).

[78] K. Nakajima, K. Yamada, S. Hosoya, Y. Endoh, M. Greven, and R. J. Birgeneau, Z. Phys. B **96**, 479 (1995).

[79] S. Hikami and T. Tsuneto, Prog. Theor. Phys. **63**, 387 (1980).

[80] T. Ota, I. Tsukada, I. Terasaki, and K. Uchinokura, Phys. Rev. B **50**, 3363 (1994).

[81] L. Miu, G. Jakob, P. Haibach, T. Kluge, U. Frey, P. Voss-de Haan, and H. Adrian, Phys. Rev. B **57**, 3144 (1998).

[82] Y. Matsuda, S. Komiyama, T. Onogi, T. Terashima, K. Shimura, and Y. Bando, Phys. Rev. B **48**, 10498 (1993).

[83] K. P. Schmidt and G. S. Uhrig, Phys. Rev. Lett. **90**, 227204 (2003).

[84] D. A. Tennant, B. Lake, A. J. A. James, F. H. L. Essler, S. Notbohm, H.-J. Mikeska, J. Fielden, P. Kögerler, P. C. Canfield, and M. T. F. Telling, Phys. Rev. B **85**, 014402 (2012).

[85] F. Groitl, T. Keller, K. Rolfs, D. A. Tennant, and K. Habicht, Phys. Rev. B **93**, 134404 (2016).

[86] S. Tyč and B. I. Halperin, Phys. Rev. B **42**, 2096 (1990).

[87] T. Huberman, D. A. Tennant, R. A. Cowley, R. Coldea, and C. D. Frost, J. Stat. Mech.: Theor. and Exp. **2008**, P05017 (2008).

[88] S. P. Bayrakci, T. Keller, K. Habicht, and B. Keimer, Science **312**, 1926 (2006).

[89] S. P. Bayrakci, D. A. Tennant, P. Leininger, T. Keller, M. C. R. Gibson, S. D. Wilson, R. J. Birgeneau, and B. Keimer, Phys. Rev. Lett. **111**, 017204 (2013).

[90] S. E. Sebastian, PhD thesis, Stanford University (2006).

[91] M. Jaime, V. F. Correa, N. Harrison, C. D. Batista, N. Kawashima, Y. Kazuma, G. A. Jorge, R. Stern, I. Heinmann, S. A. Zvyagin, Y. Sasago, and K. Uchinokura, Phys. Rev. Lett. **3**, 087203 (2004).

[92] C. Rüegg, D. F. McMorrow, B. Normand, H. M. Rønnow, S. E. Sebastian, I. R. Fisher, C. D. Bastita, and S. N. Gvasaliya, Phys. Rev. Lett. **98**, 017202 (2007).

[93] A. Oosawa, T. Kato, H. Tanaka, K. Kakurai, M. Müller, and H.-J. Mikeska, Phys. Rev. B **65**, 094426 (2002).

[94] C. Rüegg, N. Cavadini, A. Furrer, H.-U. Güdel, K. Krämer, H. Mutka, A. Wildes, K. Habicht, and P. Vorderwisch, Nature **423**, 62.

[95] A. A. Aczel, Y. Kohama, C. Marcenat, F. Weickert, O. E. Ayala-Valenzuela, M. Jaime, R. D. McDonald, S. D. Selesnic, H. A. Dabkowska, and G. M. Luke, Phys. Rev. Lett. **103**, 207203 (2009).

[96] B. Willenberg, H. Ryll, K. Kiefer, D. A. Tennant, F. Groitl, K. Rolf, P. Manuel, D. Khaluavin, K. C. Rule, A. U. B. Wotter, and S. Süllow, Phys. Rev. B(R) **91**, 060407 (2015).

[97] Z. He, T. Kyômen, and M. Itoh, Phys. Rev. B **69**, 220407(R) (2004).

[98] H.-J. Koo and M.-H. Whangbo, Inorg. Chem. **45**, 4440 (2006).

[99] R. Vogt and H. Müller-Buschbaum, Z. Anorg. Allg. Chem **591**, 167.

[100] Z. He, T. Kyômen, and M. Itoh, J. Cryst. Growth **274**, 486 (2005).

[101] S. S. Salunke, A. V. Mahajan, and I. Dasgupta, Phys. Rev. B **77**, 012410 (2008).

[102] J. Laughier and A. Filhol, J. Appl. Cryst. **16**, 281 (1983).

[103] S. Shamoto, M. Sato, J. M. Tranguada, B. J. Sternlieb, and G. Shiran, Phys. Rev. B **48**, 13817 (1993).

[104] Y. Singh and D. C. Johnston, Phys. Rev. B **76**, 012407 (2007).

[105] D. C. Johnston, *Handbook of Magnetic Materials*, edited by K. H. J. Buschow, Vol. 10 (Elsevier Science, Netherlands, 1997).

[106] M. Troyer, H. Tsunetsugu, and D. Würtz, Phys. Rev. B **50**, 13515 (1994).

[107] D. C. Johnston, R. K. Kremer, M. Troyer, X. Wang, A. Klümper, S. l. Bud'ko, and P. S. Panchula, A. F. Canfield, Phys. Rev. B **61**, 9558.

[108] S. A. Zvyagin, J. Wosnitza, J. Krzystek, R. Stern, M. Jaime, Y. Sasago, and K. Uchinokura, Phys. Rev. B **73**, 094446 (2006).

[109] J. C. Bonner, S. A. Friedberg, H. Kobayashi, D. L. Meier, and H. Blöte, Phys. Rev. B **27**, 248 (1983).

[110] E. S. Klyushina, A. Tiegel, B. Fauseweh, A. T. M. N. Islam, J. T. Park, B. Klemke, A. Honecker, G. S. Uhrig, S. R. Manmana, and B. Lake, Phys. Rev. B **93**, 241109(R) (2016).

[111] H. Tanaka, K. Takatsu, W. Shiramura, and T. Ono, J. Phys. Soc. Jpn. **65**, 1945 (1996).

[112] T. Kato, K. Takatsu, H. Tanaka, W. Shiramura, M. Mori, K. Nakajima, and K. Kakurai, J. Phys. Soc. Jpn. **67**, 752 (1998).

[113] M. Lax, *Symmetry principles in Solid State and molecular Physics* (Wiley, J. and Sons, New York, 1974).

[114] I. Cabrere, J. D. Thompson, R. Coldea, D. Prabhakaran, R. I. Bewley, T. Guidi, J. A. Rodriguez-Rivera, and C. Stock, Phys. Rev. B **90**, 014418 (2014).

[115] D. Tennant and D. McMorrow, "Rescal for Matlab: a computational package for calculating neutron TAS resolution functions," https://www.ill.eu/instruments-support/computing-for-science/cs-software/all-software/matlab-ill/rescal-for-matlab/ (1995).

[116] P. C. Hohenberg and W. F. Brinkman, Phys. Rev. B. **10**, 128 (1974).

[117] Y. Zhu, ed., *Magnetic Neutron Scattering: and Recent Developments in Triple Axis Spectroscop in," Modern Techniques for Characterizing Magnetic Materials* (Springer, Hidelberg, New York, 2005).

[118] H. Rosner, M. D. Johannes, S.-L. Drechsler, M. Schmitt, O. Janson, W. Schelle, W. Liu, Y.-X. Huang, and R. Kniep, Sci. Technol. Adv. Mater. **8**, 352 (2007).

[119] G. Xu, C. Broholm, D. H. Reich, and M. A. Adams, (2000).

[120] P. W. Anderson, Phys. Rev. **79**, 350 (1950).

[121] F. H. L. Essler and R. M. Konik, Phys. Rev. B **78**, 100403 (2008).

[122] A. B. Harris, D. Kumar, B. I. Halperin, and P. C. Hohenberg, Phys. Rev. B **3**, 961 (1971).

[123] S. U. Sachdev, Nature Physics **4**, 173 (2008).

[124] A. J. A. James, F. H. L. Essler, and R. M. Konik, Phys. Rev. B **78**, 094411 (2008).

[125] A. J. A. James, PhD thesis, University of Oxford (2008).

[126] J. Jensen, D. L. Quintero-Castro, A. T. M. N. Islam, K. C. Rule, M. Månsson, and B. Lake, Phys. Rev. B **89**, 134407 (2014).

[127] B. Fauseweh and G. S. Uhrig, Phys. Rev. B **92**, 214417 (2015).

[128] B. Fauseweh, J. Stolze, and G. S. Uhrig, Phys. Rev. B **90**, 024428 (2014).

[129] X. Ling, S. Park, B. A. McClain, S.-M. Choi, D. Dender, and J. Lynn, Phys. Rev. Lett. **86**, 712 (2001).

[130] U. Tutsch, B. Wolf, S. Wessel, L. Postulka, Y. Tsui, H. Jeschke, I. Opahle, T. Saha-Dasgupta, R. Valenti, A. Brühl, K. Removí Langer, T. Kretz, H.-W. Lerner, M. Wagner, and M. Land, Nature Communications **5**, 5169 (2014).

[131] R. Wiesendanger, Rev. Mod. Phys. **81**, 1495 (2009).

[132] U. Kaiser, A. Schwarz, and R. Wiesendanger, Nature (London) **446**, 522 (2007).

Eidesstattliche Versicherung

Hiermit versichere ich an Eides Statt, dass ich meine Dissertation mit dem Titel:

"Unconventional magnetic properties of low-dimensional antiferromagnets $BaNi_2V_2O_8$ and $BaCu_2V_2O_8$"

selbstständig verfasst habe. Alle benutzten Hilfsmittel und Quellen sind in der Arbeit aufgeführt.

Berlin, den 09.01.2017 Ekaterina Klyushina